UNIVERSITY OF SOUTHAMPTON

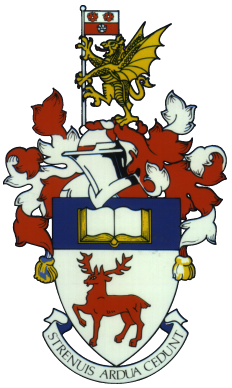

Near-field Acoustic Assessment of Open Rotor Aero-Engines

by

Prathiban Sureshkumar

EngD Thesis

Acoustics Group
Institute of Sound and Vibration Research
Faculty of Engineering and the Environment

January 2017

P Sureshkumar,
Acoustics Group,
Institute of Sound and Vibration Research,
Faculty of Engineering and the Environment,
University of Southampton,
Southampton. SO17 1BJ.
United Kingdom.

Typeset in LaTeX. All page, figure, table and bibliographic references in the contents lists and main body of text are hyperlinked.

UNIVERSITY OF SOUTHAMPTON

ABSTRACT

FACULTY OF ENGINEERING AND THE ENVIRONMENT
Institute of Sound and Vibration Research

Engineering Doctorate

Near-field Acoustic Assessment of Open Rotor Aero-Engines

by Prathiban Sureshkumar

The focus of this research, part sponsored by *Rolls-Royce plc.*, is to both model and gain an understanding of the acoustics in the near-field of the open rotor aero-engine concept. The eventual aim of such work is to develop accurate and fast prediction models which can be used to optimise engine design and operation, so that the noise produced by the open rotor can be minimised to sit well under regulation noise levels. This work will also be used to help understand the results of important experimental testing of the open rotor. Finally, such work may be useful for understanding what cabin noise levels may be, which is a strong factor in passenger comfort and is therefore another consideration for the client.

Outlined in this thesis are a number of tools and methods aimed at helping to predict the open rotor's acoustic near-field in a fast and reliable fashion. As a primer, analytical models for the tonal noise of an open rotor in the free-field are first derived. The models are based on frequency domain methods, such as those proposed by Hanson in the 1980s. All models in this thesis may be used during engine development to make acoustic predictions at various operating conditions and gain insight into how certain rotor geometric features and operating conditions affect the generated noise level and propagation. Methods for projecting noise levels from the near-field to the far-field are also presented, which is useful when validating noise measurements from experiments. The effect of scattering from the open rotor centrebody and the effect of reverberation when contained in a closed test-section wind tunnel are also modelled. Centrebody scattering and tunnel reverberation have been shown from data analysis to have an impact on open rotor acoustic measurements. The analysis presented in this thesis has led to some novel mitigation techniques and suggestions for improved open rotor experiment design. Some limited comparisons to scaled open rotor experiments are provided, in order to validate the models and highlight further issues that would occur during real engine operation.

The business case for and the environmental benefits of the open rotor are clear. Efficient operation is a key driver in the development of aircraft propulsion technologies, since it can significantly drive down operational costs and the open rotor aero-engine promises a step change improvement in fuel efficiency. Another important objective during engine development is mitigating the generation of unwanted noise, in order to meet aircraft noise regulations.

Contents

List of Figures

Declaration of Authorship

I, PRATHIBAN SURESHKUMAR, declare that the thesis entitled 'Near-field Acoustic Assessment of Open Rotor Aero-Engines' and the work presented in the thesis are both my own, and have been generated by me as a result of my own original research. I confirm that:

- this work was done wholly or mainly while in candidature for a research degree at this University;
- where any part of this thesis has previously been submitted for a degree or any other qualification at this University or any other institution, this has been clearly stated;
- where I have consulted the published work of others, this is always clearly attributed;
- where I have quoted the work of others, the source is always given. With the exception of such quotations, this thesis is entirely my own work;
- I have acknowledged all main sources of help;
- where the thesis is based on work done by myself jointly with others, I have made it clear what was done by others and what I have contributed myself.

Signed:.....
Date:.....

Acknowledgements

This Engineering Doctorate (EngD) was funded and sponsored by the Engineering and Physical Sciences Research Council (EPSRC) and Rolls-Royce plc. The research was conducted at the Rolls-Royce University Technology Centre (UTC) for Gas Turbine Noise, at the University of Southampton, within the Institute of Sound and Vibration Research. I would respectfully like to thank all these institutions for their role during this research doctorate, in particular for the financial sponsorship that was required.

I am grateful to my academic supervisor, Dr Michael Kingan, who has always made time for guidance and support during this project and has been a great mentor throughout. I am indebted for everything he has taught me through the course of my study. All the staff and colleagues at the Rolls-Royce UTC for Gas Turbine Noise are due thanks as well, for the support, discussions and wonderful working environment they established. I believe at some point I have had useful technical discussions with all the members of academic staff, which have been great for my learning. Particular thanks are due to Dr Rod Self and Dr Alan McAlpine. I am very fortunate to have worked with everyone at the UTC.

The EngD's industrial supervisor, Dr Anthony Parry, is also due my utmost gratitude and I thank him for all his support during my research. His expertise was always useful and he was instrumental in creating the collaborative effort that was required with Rolls-Royce plc. for this work to be conducted. I would also like to thank Rolls-Royce staff who I was in direct contact with through the course of this research; Dr Peter Hopkins, Dr Kevin Britchford and Dr Howoong Namgoong from the Noise team and Dr Clive Lockwood from the Compressor Aerodynamics team. The numerous telephone conversations and the discussions I had during my many visits to Derby were very insightful and I am thankful for their time.

Finally I thank my family, in particular my father, mother and sister, for their continued support through all the challenges we have faced and their patience while I completed my thesis.

Chapter 1

Introduction

In recent years, there has been a renewed interest in the open rotor aero-engine concept. Compared to the current generation of aircraft propulsors, the potential for step change improvements in fuel efficiency with this concept look promising (Parker, 2011). A schematic of *Rolls-Royce's* open rotor aero-engine concept is shown in Figure 1.1. The open rotor consists of two co-axial and contra-rotating propeller-fans, driven by a gas-turbine contained within its centrebody. This arrangement, which notably does not include the external nacelle seen on turbofan engines, has two key benefits. It allows for a higher effective bypass ratio than that obtained by ducted turbofan engines, increasing the engine's propulsive efficiency. The second contra-rotating propeller also converts some of the residual swirl downstream of the front propeller into additional axial thrust, again improving the efficiency of the concept. Studies have shown that the inclusion of a counter-rotation propeller (CRP) is expected to achieve an 8% improvement in fuel efficiency over an equivalent single rotation propeller (SRP) (Parry, 1988).

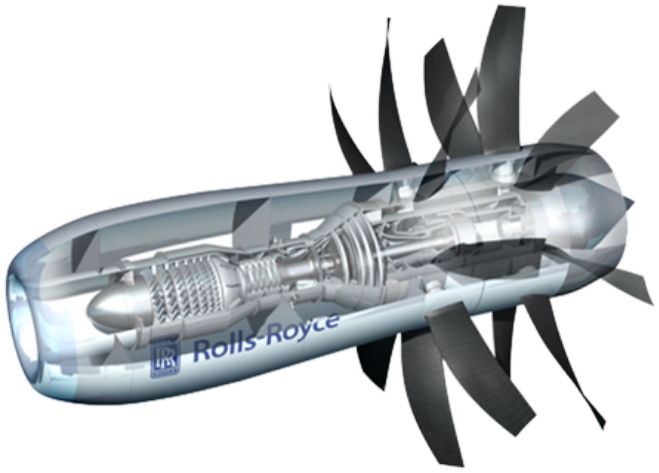

FIGURE 1.1: Cutaway schematic of the open rotor. Picture courtesy of Rolls-Royce.

Conventional propeller designs are known to be more efficient than turbofan engines although this is dependent on the operating conditions of the engine, such as the forward flight speed. Current aircraft are typically designed to cruise (the high altitude flight regime in which aircraft spend the largest proportion of operation) at Mach numbers of around 0.8. Normally, propellers approaching this speed see a rapid reduction in efficiency. The open rotor is designed to overcome this by the use of thin, highly swept blades which can maintain somewhat efficient operation at transonic (or even supersonic) blade speeds (Parry, 1988). The main differences between earlier open rotor concepts and those currently being proposed include significant material and structural improvements and the use of rotor blades which are both aerodynamically and aeroacoustically optimised. This means that modern open rotor concepts are both safer and more efficient than their predecessors.

A number of unique and challenging noise mechanisms are inherent in the design of an open rotor. Furthermore, the traditional methods of noise mitigation in aero-engines are not applicable here (for example, the use of acoustic liners on the inner wall of a turbofan's nacelle). In this chapter, the historical development of the open rotor aero-engine is outlined, along with the progress of relevant research. The current industrial climate is also highlighted (in order to set the context of the work presented in this thesis) and this chapter is concluded with an outline of the content of the following chapters, summarising the key research objectives and findings in each.

1.1 Context of Research

Rapid growth in air travel

Figures from the International Civil Aviation Organization (ICAO) and the World Bank suggest that approximately 3.4 billion passengers were carried by air transport in 2015. Forecasts estimate that the demand for commercial air travel will follow an exponential growth in the near future, primarily due to rapid development in emerging economies. It has been suggested that the global fleet of aircraft is expected to roughly triple in the period from 2007 to 2020 (ACARE, 2001). Concurrently, the human impact on the environment is gaining public traction as a major societal issue and, subsequently, the aviation industry is under continuous pressure from regulatory and public bodies to reduce its environmental footprint. There has already been a progressive effort to reduce the impact of aircraft, with respect to the effect they have on air quality, climate change and noise (Parker, 2011). Issues such as air quality and noise are a particular problem for the communities around airports, where the impact of aircraft is most significant. The impact to the environment is further compounded by the aforementioned expectation of exponential growth. Therefore, in light of the pressing need to address the environmental performance of aircraft (in the context of this work, aviation noise), a

number of recommendations have been made for aviation stakeholders in the UK by regulating bodies (CAA, 2014, Chapter 10). Airframe and aero-engine manufacturers can accomplish such aims by the evolution of new aircraft and aircraft component concepts tailored to include these concerns.

Recently, there has been clear evidence of aero-engine developments for environmental objectives in particular; the recent adaptations of successful airframes by Airbus (A320neo) and Boeing (737 MAX) to include improved aero-engines is a clear example. Government regulation, alongside performance and cost targets, set the competitive landscape in the aero-engine industry. Regulatory bodies can greatly influence the development of future concepts; the International Civil Aviation Organisation (ICAO) has historically set noise certification limits, which all future aircraft designs are expected to adhere to (IATA, 2004). Studies have shown that the open rotor aero-engine could obtain up to 30% gains in fuel efficiency (Parker, 2011) when compared to a baseline turbofan engine. Commercial interest in the open rotor concept is significant, but this is not only due to the potential cost savings achieved by the improved fuel burn. Importantly, an improved fuel burn also reduces the environmental impact of the engine, particularly in terms of carbon emissions. With the introduction of carbon taxes and international accords in place to address climate change, aero-engine carbon emissions is a consideration of increasing importance for the aviation industry.

Increasingly strict noise regulation

It is expected that the modern design iteration of Rolls-Royce's open rotor will produce certification noise levels lower than those of current aero-engines meaning that the current regulation would be satisfied. However it should be noted that the open rotor is a future aero-engine concept and so would not be in commercial operation within the short-term. It is therefore necessary to minimise open rotor noise to account for further reductions in noise regulations, which will inevitably occur over time. The latest set of standards, known as Chapter 4, came into effect in 2006. It is expected that these standards will again be redefined and lowered in the near future (Dickson, 2013). This upcoming set of regulatory standards are referred to as Chapter 14. Chapter 14 regulation will be introduced in two phases, depending on the weight class of the aircraft. The first phase will not be introduced until 2018, is expected to demand a reduction of 7 EPNdB and will only affect aircraft of weight greater than approx. 55 tonnes. The second phase, for aircraft weights below 55 tonnes, may require a reduction of up to 10 EPNdB but will not come into effect any earlier than 2021. Further recommended targets have been set by the Advisory Council for Aeronautics Research in Europe (ACARE) (ACARE, 2001); an organisation which aims to reduce the impact of aircraft on the environment by 2020 with the following standards for new aircraft: a 50% reduction in CO_2 emissions per passenger kilometre, an 80% reduction in NO_x emissions and a

50% reduction in perceived noise. Achieving all these targets in unison is especially challenging because new technologies often present trade-offs between at least two of these targets. Note that ACARE is already in the process of arranging targets for 2050 in preparation for recommending further improvements still.

1.2 Historical Open Rotor Research

Although a number of components in the open rotor aero-engine may generate noise, the dominant components of noise are generated by the rotating blades and engine core. Broadly, the focus of this thesis is to contribute to the current understanding of the noise mechanisms generated by propellers in flow. Identifying methods by which the noise emissions of an open rotor engine can be reduced is a useful outcome for the industrial sponsor of this project, *Rolls-Royce plc.* For this reason, it is worthwhile understanding the generation and propagation mechanisms of noise during engine operation, and in addition obtaining sufficient capability to predict those mechanisms. An open rotor aero-engine produces both tone and broadband noise. There are numerous sources of tone and broadband noise, which makes accurate noise prediction a difficult task. Historically, much research and development has focused on characterising and minimising the tonal component of propeller noise. The research in this thesis will also focus on open rotor tone noise, putting forward modelling improvements which may help generate more accurate estimates to better understand this phenomenon. A typical open rotor noise frequency spectrum from a rig test is shown in Figure 1.2.

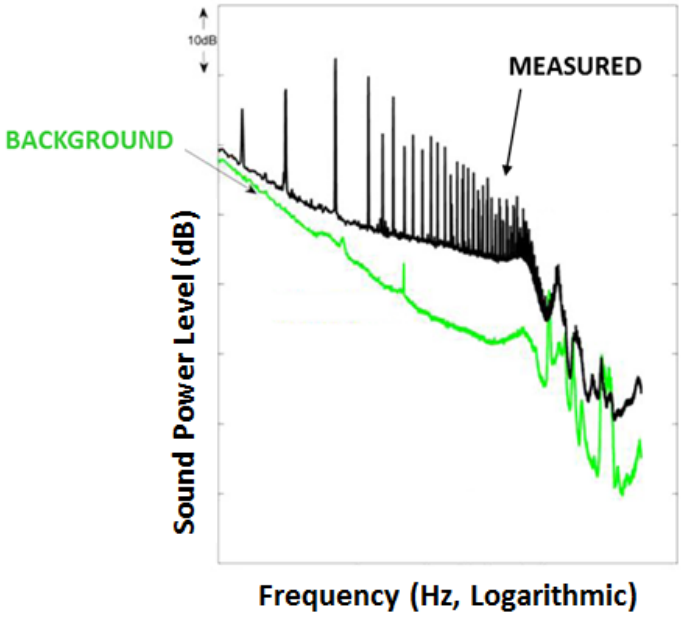

FIGURE 1.2: A typical sound pressure level (SPL) frequency spectrum (adapted from (Parry et al., 2011)).

Much of the previous industrial focus has also largely concerned acoustic emissions observed in the far-field. Regulatory assessment distances are all located at far-field positions, mirroring the communities around airports, who experience most of the burden of aircraft noise. Some of the acoustic formulae that have been derived for open rotor noise are quite complex and can be difficult to evaluate exactly. However simplifications can be applied to these formulae, significantly reducing the evaluation time. Asymptotic approximations applied to the acoustic radiation formulae have been documented as saving up to 95% in evaluation times (Parry, 1988), whilst maintaining solution accuracy. However, these approximations limit the validity of these formulae to the far-field only. A full evaluation of the exact formulae would allow for the prediction and understanding of near-field open rotor noise.

The near-field acoustics of propellers in general were first studied in part because of the discomfort that passengers of propeller driven aircraft felt due to noise passing into the fuselage cabin (Garrick and Watkins, 1954). Despite a number of design iterations and the use of modern aero-engine and airframe technologies, the issue of passenger cabin noise might still be considerable for the open rotor, perhaps more so if the engine is placed under the aircraft wing, in what is known as a puller configuration. Considering the near-field noise of an open rotor when coupled with engine installation effects adds another level of complexity to acoustic prediction. Such installation effects include the refraction and reflection of noise emitted from the engine, either by nearby aircraft structures (e.g. wings and pylons), which may provide useful noise shielding effects, or by flow distortions (e.g. boundary layers and wakes) into the open rotor caused by said structures. Including these effects would enhance the accuracy of any open rotor noise predictions and such issues form the topic of much of the current research in this particular field.

As well as addressing some of these issues with prediction, the research presented here will also be used as a tool to supplement the acoustic testing of the open rotor. The project sponsor, *Rolls-Royce plc.* (primarily a propulsion systems manufacturer), will assess any new designs of the open rotor through rigorous experimental testing of the concept, but such work can be expensive and time consuming. Therefore, quick and reliable analytical methods (similar to those proposed in this body of work) are a useful aid for design and operation optimisation, and for obtaining further understanding of the results from experiments. A portion of this thesis is dedicated to the data analysis of results from Rolls-Royce's acoustic experiments for open rotors. Results from campaigns such as these would ultimately be used to validate any final designs. A physical understanding of open rotor near-field noise becomes particularly relevant because much of the analysed noise data is collected in the test rig's near-field.

Open Rotor Prediction Methods

A number of methods may be used to predict the noise produced by various open rotor designs, ranging from simple analytical methods to high fidelity CFD/CAA methods. The simple analytic models might be useful for quick design iteration and optimisation studies, as demonstrated in Parry and Vianello (2012), whilst the CFD/CAA would be much more useful for design validation (due to comparatively reduced modelling assumptions).

A part of the challenge in deriving expressions for radiated noise is to obtain an accurate description of the sources. Methods of varying fidelity may be used, from low fidelity, analytic descriptions to high fidelity and relatively expensive CFD generated sources. Parry (1988) and Whitfield et al. (1990) describe, in depth, some simple analytic methods which rely purely on geometric, operational and rotor aerodynamic performance parameters. As an example, in these simple models the problem is reduced to the response of the rotor blade to individual 'gusts' (Fourier components of the incoming flow) and the unsteady loading that is then induced, which is described by models in Amiet (1974); Parry (1988); Sears (1941). The models predict both rotor alone and rotor-rotor interaction noise due to 'thickness' and 'loading' type sources, however no description of the volume quadrupole source is provided. Employing higher fidelity source calculations, the works of Colin, Blanc, Caruelle, Barrois and Djordjevic (2012), Colin, Carazo, Caruelle, Node-Langlois and Parry (2012), Colin, Caruelle and Parry (2012) and Sharma and Chen (2013) describe computational strategies combining CFD and CAA for predicting open rotor tone noise in the far-field.

Many of the aeroacoustic prediction methods available in the literature have their roots in the seminal paper by Ffowcs-Williams and Hawkings (1969), which describes a method to calculate the noise produced by a non-stationary and impermeable surface. For example, in this work, such a surface might describe the open rotor's blades - the blades are typically deconstructed as surface distributions of 'thickness' and 'loading' sources. The work may also be extended to consider a volume distribution of quadrupole type sources. Further discussion into these source types is provided in Chapter 2, where rotor tone noise analytic expressions are generated for the most prevalent sources.

The source representation described in Ffowcs-Williams and Hawkings (1969) can be extended to generate expressions describing the radiation of near- and far-field open rotor tone noise. Typically, the radiation is either calculated in the time domain, as demonstrated in the works of Farassat (Farassat, 1981, 1986; Farassat and Myers, 1987), or in the frequency domain in methods largely investigated by Hanson. Hanson has provided models for near-field SRP tones (SRP tones are also referred to as rotor-alone tones) (Hanson, 1985*a*), far-field SRP tones (Hanson, 1980*a*), and far-field CRP tones (tones produced by the contra-rotation of two propellers, also referred to as rotor-rotor interaction tones) (Hanson, 1985*b*). Time domain methods, such as those proposed by

Farassat (1981); Farassat and Brentner (1998); Farassat et al. (1992), are advantageous because they can directly evaluate the emitted acoustic waveform from the suggested distribution of sources. These methods have been extended to include non-axial inflow, periodic loading and are even capable of including aeroelastic effects through iterative processes (Farassat et al., 1992). On the other hand, frequency domain methods, as proposed by Hanson (1983, 1985*a*, 1992), evaluate contributions from each frequency individually.

Open Rotor Tone Noise

Only a brief overview of tone noise is provided here, since the following chapters will elaborate on this in further detail. Frequency domain methods similar to those proposed by Hanson are described in the body of this work. Although generation of a converged, time-accurate noise signal from the open rotor would be computationally expensive (waveforms could technically be replicated by evaluating a fundamental tone frequency along with a large number of its harmonics), the method is particularly suited to deconstructing the acoustics into individual frequencies. Generally, it is the fundamental frequency (of SRPs) and lower order harmonics of open rotor tones that produce the most significant noise. Therefore it is more straightforward and efficient to consider the acoustics in the frequency domain when attempting tone noise predictions. Obtaining a noise prediction in the frequency domain and in the near-field of the open rotor requires calculation of a spatial Fourier transform, which is typically evaluated numerically. The associated integrand could be very oscillatory and thus expensive to compute. The method of stationary phase has been used to approximate this integral in the far-field, which can significantly reduce the computational expense. Papers by Crighton and Parry (1991, 1992); Parry and Crighton (1989) make further simplifications, where the radial integral in Hanson's far-field formulation is evaluated by asymptotic techniques. Parry (1988) describes how these techniques may be used to simplify the noise generated by the interaction of two (contra-rotating) rotors and Peake and Crighton (1991) have developed asymptotic methods which apply for near-field noise radiation of steady 'loading' and 'thickness' noise sources (corresponding to rotor-alone tones).

Open Rotor Broadband Noise

Open rotor broadband noise is not addressed in this thesis. However, as the other major type of open rotor noise, for completeness a short summary is provided here. In the works of Parry et al. (2011), a significant proportion of the sound energy was shown to be contained in open rotor broadband noise sources. In fact, when compared to open rotor tone noise levels in third-octave bands (particularly relevant for noise regulation), the analysis shows near equivalent proportions (see Figure 1.3). Indeed, at certain conditions perhaps even higher levels of broadband noise are found towards the

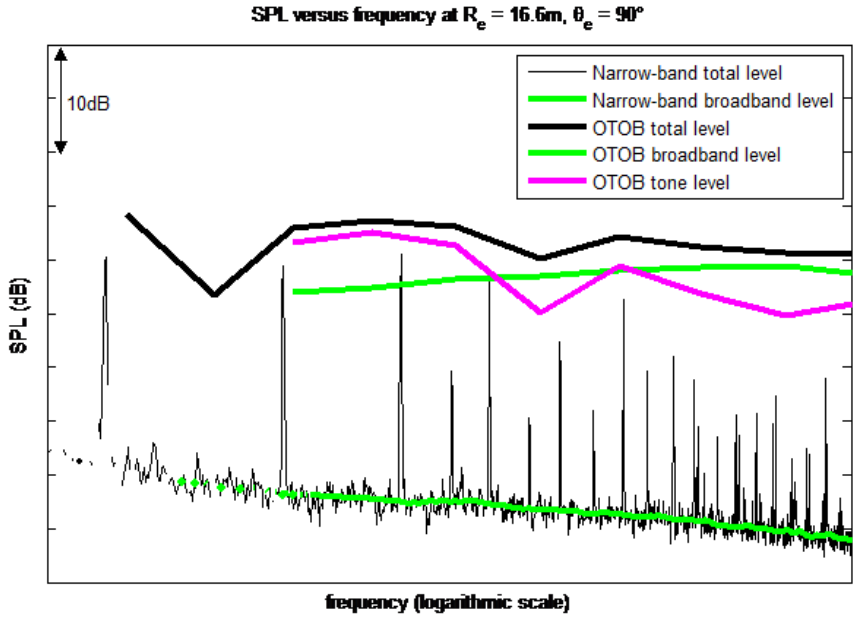

FIGURE 1.3: Spectral comparison of open rotor tone and broadband noise (adapted from (Parry et al., 2011)).

higher end of the frequency spectrum. Note that this analysis was conducted on an aeroacoustically optimised open rotor design, in which case improvements in tone noise levels might have led to the unmasking of the broadband noise sources.

Open rotor broadband noise is challenging to predict because it is difficult to estimate or even measure the unsteady flow and turbulence characteristics required to model the noise sources. There are a number of broadband noise sources, for which also exist a number of models predicting the radiated broadband noise levels. Rotor self-noise, produced by trailing edge diffraction of either turbulence in the rotor blade boundary layer or rotor blade near-wake, has also been studied in the context of helicopter rotors and wind turbines and has been modelled in papers by Kim and George (1982); Sinayoko et al. (2013); Zhou and Joseph (2006). Atmospheric turbulence ingestion noise is generated by rotor blades chopping through atmospheric turbulence. The papers of Amiet (1977); Paterson and Amiet (1982) both present and validate a model for this noise source. Other models also exist which include the effect of turbulent stretching through the inclusion of rapid distortion theory (Amiet, 1989; Majumdar and Peake, 1998). Finally, rotor-rotor interaction noise, which is produced by turbulence in a rotor wake interacting with a downstream (and contra-rotating) rotor, was first modelled by Blandeau and Joseph (2010) and later this model was adjusted and extended by Kingan (2012) to include axial flow. A further model to consider, pylon-rotor interaction (a non-rotating pylon wake containing turbulence replaces the rotor wake), is also included in that work. Many of the models rely on simple and empirical models for the turbulence

statistics which would add a level of error to the final noise prediction. Since measurement and corroboration of even the empirical turbulence models at the right flow conditions is arduous, validating open rotor broadband noise has proved difficult.

1.3 Thesis Objectives

The main aim of this research is to provide improved modelling methods for open rotor noise in the near-field of an open rotor aero-engine test rig, specifically methods which would account for installation or operational effects encountered by the project sponsor during open rotor experimental campaigns. The focus of this engineering doctorate thesis is in general to develop methods applicable and beneficial to the industrial research conducted by *Rolls-Royce plc.*. The clearest example of industrial benefit is that prediction methods of near-field open rotor noise may be useful in determining the pressure on the surface of an aircraft fuselage, which in turn could be used to help determine noise levels in the passenger cabin. Chapter 2 describes some simple analytic models which are valid in the near-field and could be used to derive primary estimates for this purpose.

However much of the research presented in this thesis also proves a useful tool in examining and understanding acoustic test rig data better. The results obtained from experimentation could be the most reliable data set for estimating the noise generated by the open rotor in true flight conditions, and so drawing understanding from test data is invaluable to an engine manufacturer. A number of *Rolls-Royce's* open rotor rig tests were conducted in high flow speeds, which required the use of wind tunnels. In facilities capable of high flow speeds, the wind tunnel test sections are usually limited in cross-sectional area, due to the expense and difficulty that arises when shifting large volumes of air at high speed. This means that acoustic measurements are often in the near-field of the test rig by default. Chapter 3 outlines Rolls-Royce's cruise regime (i.e. high flow speed) experiments and explains in more detail the effect that measurement in the near-field has on the noise levels.

Further experimental data analysis concluded that near-field noise testing in closed environments is challenging, perhaps even to the point of being impractical. The noise data may be contaminated by a number of experimental effects, such as tunnel reverberation and tunnel flow distortions. The problem of tunnel reverberation is investigated in Chapter 4, with the free-field models being modified to generate more accurate predictions for open rotor noise under these circumstances. The outcomes of this research demonstrate under what conditions reverberation may occur and provides conclusions on mitigating the contamination of the direct noise field.

Analysis using the simple near-field models leads, in part, to the investigation of open rotor centrebody scattering. An objective of this work was to consider improvements

to the accuracy of the analytic models, and modelling of the centrebody may in certain cases provide improvement on a free-field model. The insight into near-field acoustic propagation had led to the understanding that specific open rotor tones could, under certain conditions, strongly radiate noise towards the centrebody. This work is presented in Chapter 5. This is further shown to be an improbable feature of noise generated by standard SRPs and so this behaviour is unique to an open rotor aero-engine. This work was further extended to show how, theoretically, an open rotor centrebody could be acoustically lined to mitigate this component of noise.

Chapter 2

Analytic Models for Open Rotor Tone Noise

The tonal component of noise generated by an open rotor aero-engine is largely dependent on its operation and geometry. Variations in geometric features or operating conditions will adjust the frequency and amplitude of these tones. However, in all cases, it is clear that the tones will form a significant component of the noise. In this chapter we discuss the 'rotor alone' and 'interaction' tones produced by the open rotor and present analytic models for their prediction. A brief discussion is put forward on the generation mechanisms and propagation behaviour of these tones. The derivation of the theoretical expressions makes a number of assumptions (outlined later in this chapter), the most prominent being that the open rotor is considered to be operating in the free-field, i.e. with no interference from any nearby structures (including features on the engine itself). This is the simplest case to consider and will set the basis for modelling adaptations in later chapters. Note that the work presented in this chapter is not original itself, but lays the necessary groundwork for original research presented in later chapters.

Literature Survey

The rotor-alone tones of an open rotor are equivalent to the tones produced by a single rotation propeller (SRP), which are well defined in existing literature. Research on propeller acoustics dates back to the early 20^{th} century, when Gutin (1936) first gave a description for the noise caused by loading forces on a propeller in a static medium. This description used approximations that limited its use to the far-field, but an exact form was evaluated by Hubbard and Regier (1950), to understand the near-field problem in further detail. The motivation of this work was to investigate pressures in the critical region near the propeller tip which would in turn be used to estimate fuselage cabin pressures. The work of Gutin was extended to include axial flow by Garrick and Watkins

(1954), and further realistic improvements have been made over time, such as inclusion of chordwise non-compactness effects by Watkins and Durling (1956), which can cause rapid cancellations due to phase variations across the blade chord, an important consideration in the near-field.

Tones are also produced by interactions between the forward and aft rotors on the open rotor. Interaction tone noise has been covered extensively in literature, particularly in research that is specifically oriented towards the open rotor concept (Brouwer, 2010; Kingan and Self, 2011; Parry, 1988). The interaction tone mechanism is essentially analogous to the well established rotor-stator interaction described by Tyler and Sofrin (1962) in turbofan aero-engine compressors.

The operating conditions of an open rotor will also affect the presence of interaction tones. Interaction tones are prevalent in regimes of high loading such as take-off (Parry, 1988). The directivity of the interaction tone is different to that for rotor-alone tones. They radiate into the forward and rearward arcs, as opposed to in the plane of the rotor (Brouwer, 2010). However they do not radiate along the axis of the rotor, unless the order of Bessel function is zero (leading to the generation of what is similar to plane wave "siren" noise), which is only likely to occur at combinations of higher rotor harmonic indices or if the blade number for each rotor is the same.

2.1 Solutions of the convected wave equation

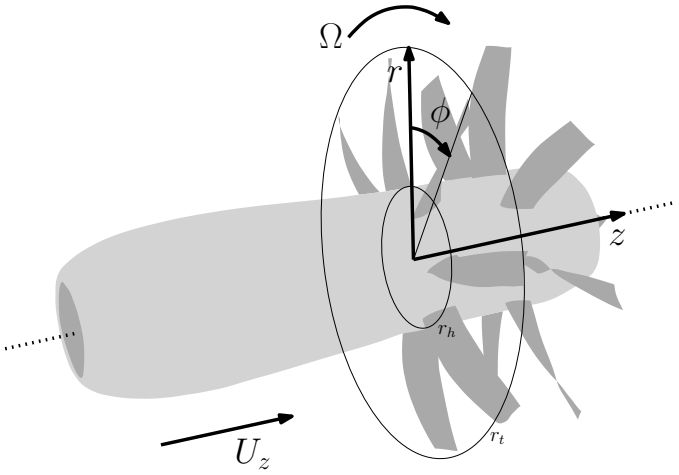

FIGURE 2.1: A schematic of the open rotor and the cylindrical coordinate system.

Figure 2.1 depicts the rotor coordinate system used in the following models. The coordinate system origin is placed at the engine centreline and in the 'rotor disc' plane of the rotor at which sound is generated. For convenience, the handedness of the coordinate system is chosen such that the rotor which generates the sound is rotating in

the positive ϕ direction. In other words, the positive ϕ direction would flip between sound generation models based on the front and rear rotor. Observer position coordinates are identified with the subscript o while the subscript s describes source position coordinates. The formulation starts with the wave equation, defined in terms of source co-ordinates $\mathbf{y} = \{z_s, \phi_s, r_s\}$ and τ.

$$\left[\nabla_y^2 - \frac{1}{c_0^2}\frac{\mathrm{D}_0^2}{\mathrm{D}\tau^2}\right] p\left(\mathbf{y}, \tau\right) = -\gamma\left(\mathbf{y}, \tau\right) \tag{2.1}$$

where ∇_y^2 is a Laplacian derivative. The acoustic pressure is denoted by p and γ represents an arbitrary source function. The material derivative is defined as

$$\frac{\mathrm{D}_0}{\mathrm{D}\tau} = \frac{\partial}{\partial\tau} + \mathbf{U}\cdot\nabla_y \tag{2.2}$$

The vector $\mathbf{U}$ represents the mean flow and in all of the following analysis the flow is assumed to be purely axial, i.e. $\mathbf{U} = \{U_z, 0, 0\}$. The ambient speed of sound is assigned to c_0.

As shown in Goldstein (1976, eq. 1.66), for sources located in a fluid of infinite extent (with no scattering surfaces) the acoustic pressure is given by

$$p\left(\mathbf{x}, t\right) = \int_{-\infty}^{\infty}\int_{\nu} \gamma\left(\mathbf{y}, \tau\right) G\left(\mathbf{y}, \tau \,|\, \mathbf{x}, t\right)\, \mathrm{d}\mathbf{y}\, \mathrm{d}\tau. \tag{2.3}$$

where here ν represents the volume of fluid. The Fourier transform of an arbitrary function f, is defined as

$$\tilde{f}\left(\omega\right) = \frac{1}{2\pi}\int_{-\infty}^{\infty} f\left(\tau\right)\exp\left\{-\mathrm{i}\omega\tau\right\}\, \mathrm{d}\tau \tag{2.4}$$

and the corresponding inverse Fourier transform is

$$f\left(\mathbf{y}, \tau\right) = \int_{-\infty}^{\infty} \tilde{f}\left(\mathbf{y}, \omega\right)\exp\left\{\mathrm{i}\omega\tau\right\}\, \mathrm{d}\omega. \tag{2.5}$$

The Green's function associated with eq. (2.1) may be expressed as follows (see Appendix 2.A)

$$G\left(\mathbf{y}, \tau \,|\, \mathbf{x}, t\right) = \int_{-\infty}^{\infty} \tilde{G}_\omega\left(\mathbf{y} \,|\, \mathbf{x}\right)\frac{\exp\left\{\mathrm{i}\omega\left(t-\tau\right)\right\}}{2\pi}\, \mathrm{d}\omega. \tag{2.6}$$

Applying these transformations to eq. (2.3) results in

$$p(\mathbf{x},t) = \int_{-\infty}^{\infty} \int_{\nu} \int_{-\infty}^{\infty} \int_{-\infty}^{\infty} \tilde{\gamma}(\mathbf{y},\omega') \frac{\tilde{G}_{\omega}}{2\pi} \exp\left\{\mathrm{i}\omega'\tau - \mathrm{i}\omega\tau + \mathrm{i}\omega t\right\} \mathrm{d}\omega' \,\mathrm{d}\omega \,\mathrm{d}\mathbf{y} \,\mathrm{d}\tau. \tag{2.7}$$

Evaluating the τ integral gives

$$\int_{-\infty}^{\infty} \exp\left\{\mathrm{i}\left(\omega' - \omega\right)\tau\right\} \mathrm{d}\tau = 2\pi\delta\left(\omega' - \omega\right) \tag{2.8}$$

and thus, when the ω' integral is solved as well, the final expression is

$$p(\mathbf{x},t) = \int_{\nu} \int_{-\infty}^{\infty} \int_{-\infty}^{\infty} \tilde{\gamma}(\mathbf{y},\omega) \tilde{G}_{\omega} \exp\left\{\mathrm{i}\omega t\right\} \mathrm{d}\omega \,\mathrm{d}\mathbf{y}. \tag{2.9}$$

A complete derivation of the frequency domain Green's function is presented in Appendix 2.B. That derivation results in the following expression

$$\tilde{G}_{\omega}(\mathbf{y} \,|\, \mathbf{x}) = \sum_{n} \exp\left\{-\mathrm{i}n\phi_s\right\} \left(\int_{-\infty}^{\infty} \mathrm{i}J_n(\Gamma r_<) H_n^{(2)}(\Gamma r_>) \frac{\exp\left\{-\mathrm{i}k_z z_o + \mathrm{i}n\phi_o\right\}}{8\pi} \exp\left\{\mathrm{i}k_z z_s\right\} \mathrm{d}k_z \right), \tag{2.10}$$

where

$$\begin{aligned} r_< &= a, \quad r_> = r_o \quad \text{if} \quad a < r_o \\ r_< &= r_o, \quad r_> = a \quad \text{if} \quad a > r_o. \end{aligned} \tag{2.11}$$

2.2 Acoustic Source Functions

Two types of acoustic source are considered here: the monopole and the dipole. A third, the quadrupole, may also be considered in the context of rotor tone noise, however accurate prediction is difficult due to the complexity in measuring or predicting the flow features which generate this type of noise. The operating regime in which quadrupole noise is considered significant is quite limited when compared to the other two source types and even in these regimes the other sources are typically expected to dominate.

Envia (2015) includes predictions of open rotor quadrupole noise sources in his high speed open rotor noise analysis. A short discussion on quadrupole noise in the context of open rotor tone noise follows later in this chapter.

Expressions for the sound generated by rotors are expressed in the more convenient cylindrical coordinate system. For monopole and dipole noise, the sources are considered as being attached to the rotating blade of an open rotor. Therefore it is also convenient to express the sources as translating in a rotating ring centered around the rotor axis, similar to a ring source. In this section we derive expressions for the acoustic source in such a format.

By the conclusion of this chapter, we shall arrive at expressions for unsteady pressure which are in essence equivalent to two of the terms in Goldstein (1976, eq. 4.10), but applied specifically to open rotor noise. This expression in Goldstein in general describes observed density perturbations caused by distributions of the aforementioned sources immersed in a uniformly moving medium.

2.2.1 Rotating Point Monopole

First consider the acoustic pressure produced by a single rotating monopole. In this case

$$\gamma\left(\mathbf{y},\tau\right)=\rho_0\frac{\mathrm{D}_0 Q}{\mathrm{D}\tau}=\rho_0\left[\frac{\partial}{\partial\tau}+U\frac{\partial}{\partial z_s}\right]Q_0\delta_3\left(\mathbf{y}-\mathbf{y}_0\right) \tag{2.12}$$

where $\mathbf{y}_0=\{z_0,\phi_0,r_0\}$ is a source offset vector. To account for rotation of the rotor we set $\phi_0=\Omega\tau$, where Ω is the angular velocity of the rotor, and $r_0=a$, a being the source rotation radius. Q_0 is referred to as the volume displacement velocity. Note that, with these prescribed source offsets, increasing source time now causes the source to move around the rotor axis in a ring, as desired. The three-dimensional spatial delta function δ_3 is expressed in cylindrical coordinates as

$$\delta_3\left(\mathbf{y}-\mathbf{y}_0\right)=\delta\left(z_s-z_0\right)\delta\left(\phi_s-\phi_0\right)\frac{\delta\left(r_s-r_0\right)}{r_s}. \tag{2.13}$$

The delta function in ϕ may be expressed as an infinite summation of exponentials

$$\delta\left(\phi_s-\phi_0\right)=\sum_{m=-\infty}^{\infty}\frac{\exp\left\{-\mathrm{i}m\left(\phi_s-\phi_0\right)\right\}}{2\pi}. \tag{2.14}$$

and combining these definitions, the source function is now

$$\gamma = \sum_m \frac{\rho_0 Q_0}{2\pi r_s}\left[\mathrm{i}m\Omega + U\frac{\partial}{\partial z_s}\right]\exp\left\{-\mathrm{i}m\phi_s + \mathrm{i}m\Omega\tau\right\}\delta\left(z_s - z_0\right)\delta\left(r_s - a\right). \tag{2.15}$$

Taking the Fourier transform of the source function

$$\tilde{\gamma}\left(\mathbf{y},\omega'\right) = \sum_m \frac{\rho_0 Q_0}{4\pi^2 r_s}\int_{-\infty}^{\infty}\left[\mathrm{i}m\Omega + U\frac{\partial}{\partial z_s}\right] \times \exp\left\{-\mathrm{i}m\phi_s + \mathrm{i}m\Omega\tau - \mathrm{i}\omega'\tau\right\}\delta\left(z_s - z_0\right)\delta\left(r_s - a\right)\,\mathrm{d}\tau \tag{2.16}$$

and evaluating the τ integral results in

$$\tilde{\gamma}\left(\mathbf{y},\omega'\right) = \sum_m \frac{\rho_0 Q_0}{2\pi r_s}\left[\mathrm{i}m\Omega + U\frac{\partial}{\partial z_s}\right]\exp\left\{-\mathrm{i}m\phi_s\right\}\delta\left(z_s - z_0\right)\delta\left(r_s - a\right)\delta\left(\omega' - m\Omega\right). \tag{2.17}$$

2.2.2 Rotating Point Dipole

The source function for a dipole is represented by

$$\gamma\left(\mathbf{y},\tau\right) = \mathbf{f}\cdot\nabla_y\delta_3\left(\mathbf{y} - \mathbf{y}_0\right). \tag{2.18}$$

where $\mathbf{f} = \{f_z, f_\phi, f_r\}$ is a force vector. Expressing the gradient in cylindrical polar coordinates then yields

$$\mathbf{f}\cdot\nabla_y = \left[f_z\frac{\partial}{\partial z_s} + \frac{f_\phi}{r_s}\frac{\partial}{\partial\phi_s} + f_r\frac{\partial}{\partial r_s}\right], \tag{2.19}$$

and applying the same expansions and definitions for offset co-ordinates as in the previous derivation for rotating monopoles leads to the following expression for the dipole source function

$$\gamma\left(\mathbf{y},\tau\right) = \sum_m \left[f_z\frac{\partial}{\partial z_s} - \frac{\mathrm{i}mf_\phi}{r_s} + f_r\frac{\partial}{\partial r_s}\right]\frac{\exp\left\{-\mathrm{i}m\phi_s + \mathrm{i}m\Omega\tau\right\}}{2\pi r_s}\delta\left(z_s - z_0\right)\delta\left(r_s - a\right). \tag{2.20}$$

Taking the Fourier transform and solving the τ integral then leads to

$$\tilde{\gamma}\left(\mathbf{y},\omega'\right)=\sum_{m}\left[f_z\frac{\partial}{\partial z_s}-\frac{\mathrm{i}mf_\phi}{r_s}+f_r\frac{\partial}{\partial r_s}\right]\frac{\exp\left\{-\mathrm{i}m\phi_s\right\}}{2\pi r_s}\delta\left(z_s-z_0\right)\delta\left(r_s-a\right)\delta\left(\omega'-m\Omega\right). \tag{2.21}$$

In terms of rotor forcing, f_r corresponds to radial forces on the rotor blades. It may be assumed that these forces are much smaller than the other force vector components and thus in the following analyses they will be neglected (i.e. $f_r=0$).

2.3 Acoustic Pressure Generated by Rotating Sources

2.3.1 Expression for Rotating Monopole

To obtain an expression for the unsteady pressure generated by a rotating point monopole we can replace eq. (2.17) in eq. (2.9)

$$p\left(\mathbf{x},t\right)=\int_{\nu}\int_{-\infty}^{\infty}\tilde{G}_\omega\sum_{m}\frac{\rho_0Q_0}{2\pi r_s}\left[\mathrm{i}m\Omega+U\frac{\partial}{\partial z_s}\right]$$
$$\times\exp\left\{-\mathrm{i}m\phi_s\right\}\delta\left(z_s-z_0\right)\delta\left(r_s-a\right)\delta\left(\omega'-m\Omega\right)\exp\left\{\mathrm{i}\omega' t\right\}\,\mathrm{d}\omega'\,\mathrm{d}\mathbf{y}. \tag{2.22}$$

In cylindrical polar co-ordinates $\mathrm{d}\mathbf{y}=r_s\,\mathrm{d}r_s\,\mathrm{d}\phi_s\,\mathrm{d}z_s$ and so, using the properties of the delta functions, we might evaluate the integrals in this expression, such that

$$p\left(\mathbf{x},t\right)=\int_{0}^{2\pi}\tilde{G}_\omega\left(z_0,\phi_s,a\,|\,\mathbf{x}\right)\sum_{m}\frac{\rho_0Q_0}{2\pi}\left[\mathrm{i}m\Omega+U\frac{\partial}{\partial z_s}\right]\exp\left\{-\mathrm{i}m\phi_s\right\}\exp\left\{\mathrm{i}m\Omega t\right\}\,\mathrm{d}\phi_s. \tag{2.23}$$

Combining eqs. (2.23) and (2.10) (noting different summation indices) gives

$$p\left(\mathbf{x},t\right)=\sum_{m}\sum_{n}\int_{-\infty}^{\infty}\int_{0}^{2\pi}-\frac{\rho_0Q_0c_0}{16\pi^2}\left[\kappa-k_zM\right]J_n\left(\Gamma r_<\right)H_n^{(2)}\left(\Gamma r_>\right)$$
$$\exp\left\{\mathrm{i}k_zz_s-\mathrm{i}k_zz_o\right\}\exp\left\{\mathrm{i}n\phi_o\right\}\exp\left\{-\mathrm{i}\left(m+n\right)\phi_s\right\}\exp\left\{\mathrm{i}m\Omega t\right\}\,\mathrm{d}\phi\,\mathrm{d}k_z. \tag{2.24}$$

The ϕ integral can now be evaluated as follows

$$\sum_m \sum_n \int_0^{2\pi} \exp\left\{-\mathrm{i}\left(m+n\right)\phi_s\right\}\,\mathrm{d}\phi_s = 2\pi\delta_{n,-m} \tag{2.25}$$

Therefore the solution for acoustic pressure becomes

$$p\left(\mathbf{x},t\right) = -\frac{\rho_0 Q_0 c_0 I_{k_z}}{8\pi}\exp\left\{-\mathrm{i}m\phi_o + \mathrm{i}m\Omega t\right\} \tag{2.26}$$

where, using the definitions in eq. (2.11),

$$I_{k_z} = \int_{-\infty}^{\infty}\left[\kappa - k_z M\right] J_{-m}\left(\Gamma r_<\right) H_{-m}^{(2)}\left(\Gamma r_>\right)\exp\left\{\mathrm{i}k_z z_0 - \mathrm{i}k_z z_o\right\}\,\mathrm{d}k_z. \tag{2.27}$$

2.3.2 Expression for Rotating Dipole

A similar expression for the unsteady pressure generated by a rotating point dipole may be derived, this time by inserting eqs. (2.21) and (2.10) into eq. (2.9) to yield

$$p\left(\mathbf{x},t\right) = \sum_m \sum_n \int_{-\infty}^{\infty}\int_0^{2\pi} -\frac{J_n\left(\Gamma r_<\right) H_n^{(2)}\left(\Gamma r_>\right)}{16\pi^2}\left[f_z k_z - \frac{m f_\phi}{a}\right] \exp\left\{\mathrm{i}k_z z_0 - \mathrm{i}k_z z_o + \mathrm{i}n\phi_o - \mathrm{i}\left(m+n\right)\phi_s + \mathrm{i}m\Omega t\right\}\,\mathrm{d}\phi_s\,\mathrm{d}k_z. \tag{2.28}$$

Expanding the volume integral again means that, after solving several integrals (including the ϕ integral as in eq. (2.25), we arrive at the expression

$$p\left(\mathbf{x},t\right) = -\frac{I_{k_z}}{8\pi}\exp\left\{-\mathrm{i}m\phi_o + \mathrm{i}m\Omega t\right\} \tag{2.29}$$

where

$$I_{k_z} = \int_{-\infty}^{\infty}\left[f_z k_z - \frac{m f_\phi}{r}\right] J_{-m}\left(\Gamma r_<\right) H_{-m}^{(2)}\left(\Gamma r_>\right)\exp\left\{\mathrm{i}k_z z_s - \mathrm{i}k_z z_o\right\}\,\mathrm{d}k_z \tag{2.30}$$

and $r_<$ and $r_>$ are defined as in eq. (2.11).

2.4 Distributed Sources for Rotor Noise

The point source expressions can be integrated over a (closed) surface to arrive at expressions for the sound generated by a distributed source region. Thus it is a simple extension to convert the expressions at the close of subsections 2.3.1 and 2.3.2 into ones which may be used to predict the noise generated by steady thickness and steady loading open rotor tone noise. The necessary steps are described in the following section.

2.4.1 Conversion to blade coordinates

The following forms of tone noise may be described by distributions of either dipole or monopole sources on the rotor blade surface. Thus it is convenient if the sources can be described in a coordinate system aligned to the rotor blade, i.e. with chordwise and chord-normal co-ordinates. Figure 2.2 visualises the relation of these co-ordinates to the original cylindrical co-ordinate system aligned to the rotor axis.

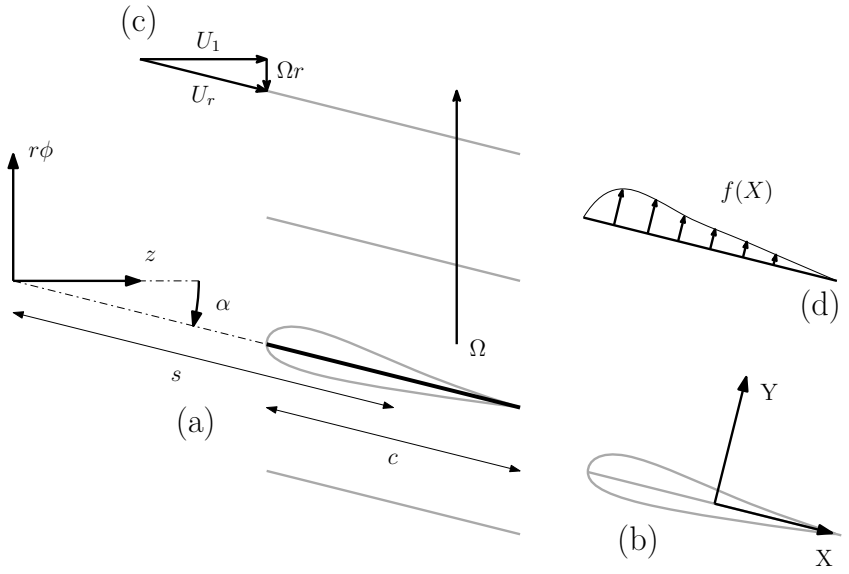

FIGURE 2.2: A schematic on an annular surface, showing the coordinate systems and some of the parameters used for modelling.

We are no longer accounting for sources at just a single source radius, a, but on radii over the total span of the blade, thus r_0 is set equal to r, a blade radius co-ordinate. When converting to the blade co-ordinate system, a number of blade parameters are introduced, such as the blade stagger angle α, the blade sweep s and the blade chordwise co-ordinate X (see Figure 2.2 (a) and (b)). It is assumed that the magnitude of blade thickness (and possibly lean) is significantly smaller than the typical wavelengths of rotor-locked tone noise being assessed. In such a case, the distributed source may be considered acoustically compact in the chord-normal direction. For this reason, one can reduce the distributed sources over the blade surface to equivalent sources on the blade planform

(an infinitely thin surface on the blade chord at every span). Note that the blade stagger, blade sweep and blade chord-length c may all be a function of radius.

In blade co-ordinates, the axial source offset co-ordinate z_0 may be expressed as

$$z_0 = (s + X)\cos\alpha \tag{2.31}$$

and the azimuthal co-ordinate ϕ_0 as

$$\phi_0 = \Omega\tau + \frac{2\pi k}{B} - (s + X)\frac{\sin\alpha}{r} \tag{2.32}$$

where the second term in this expression places the k^{th} of B sources spaced equally around the azimuth. To include B sources, a summation from $k = 1$ to B is also included. In the final expressions for rotor noise, B will represent the number of rotor blades. The integral over the close surface S which describes the original source region is now simply over the blade planform Σ, which can be expressed in blade coordinates with appropriate limits (where r_h is the blade hub radius and r_t the blade tip radius).

$$\int_{\Sigma} \mathrm{d}\Sigma = \int_{-c/2}^{c/2}\int_{r_h}^{r_t} \mathrm{d}r\,\mathrm{d}X \tag{2.33}$$

2.4.2 Steady Thickness

In our following formulation for steady thickness, which starts from eq. (2.26), the monopole strength per unit area is equal to $U_r b\frac{\mathrm{d}h}{\mathrm{d}X}$ where U_r is the blade relative velocity (see Figure 2.2 (c)), b is a non-dimensional maximum blade thickness at a given span and $h(X, r)$ is a measure of the blade thickness. Replacing this along with eqs. (2.31) and (2.32) and integrating over the blade planform results in

$$p(\mathbf{x}, t) = \sum_m \sum_n \sum_{k=1}^{B} \int_{-\infty}^{\infty}\int_{0}^{2\pi}\int_{r_h}^{r_t}\int_{-c/2}^{c/2} -\frac{\rho_0 c_0 b U_r}{16\pi^2}\frac{\mathrm{d}h}{\mathrm{d}X}\left[\kappa - k_z M\right] J_n(\Gamma r_<)\, H_n^{(2)}(\Gamma r_>)$$
$$\exp\left\{-\mathrm{i}k_z z_o + \mathrm{i}n\phi_o - \mathrm{i}(m+n)\phi_s + 2\pi\mathrm{i}\frac{mk}{B} + \mathrm{i}m\Omega t + \mathrm{i}\left[k_z\cos\alpha - \frac{m\sin\alpha}{r}\right](s+X)\right\}$$
$$\mathrm{d}X\,\mathrm{d}r\,\mathrm{d}\phi_s\,\mathrm{d}k_z. \tag{2.34}$$

The ϕ_s integral may be solved as before (eq. (2.25)) but it is simple to show that the exponential in k only results in a solution when the index m is a multiple of B. Thus we introduce $\nu = -mB$ and $\omega_m = mB\Omega$ and therefore

$$p(\mathbf{x},t) = -\sum_m \int_{r_h}^{r_t} \frac{\rho_0 c_0 b B U_r}{8\pi} \int_{-\infty}^{\infty} \int_{-c/2}^{c/2} \frac{\mathrm{d}h}{\mathrm{d}X} \left[\kappa - k_z M\right] J_\nu(\Gamma r_<) H_\nu^{(2)}(\Gamma r_>) \exp\left\{-\mathrm{i}k_z z_o + \mathrm{i}\nu\phi_o + \mathrm{i}\omega_m t + \mathrm{i}k_s + \mathrm{i}k_X \tilde{X}\right\} \mathrm{d}X\, \mathrm{d}k_z\, \mathrm{d}r \quad (2.35)$$

where

$$k_X = \left[k_z \cos\alpha + \nu \frac{\sin\alpha}{r}\right] c, \quad k_s = \frac{k_X s}{c}, \quad \tilde{X} = \frac{X}{c}. \quad (2.36)$$

We may combine the thickness variation along the chord of the blade with the chordwise phase term and integral, and so

$$\int_{-\frac{1}{2}}^{\frac{1}{2}} \frac{\mathrm{d}h}{\mathrm{d}X} \exp\left\{-\mathrm{i}k_X \tilde{X}\right\} \mathrm{d}\tilde{X} = \left[h \exp\left\{-\mathrm{i}k_X \tilde{X}\right\}\right]_{-\frac{1}{2}}^{\frac{1}{2}} + \mathrm{i}k_X \Psi_T, \quad \Psi_T = \int_{-\frac{1}{2}}^{\frac{1}{2}} h \exp\left\{-\mathrm{i}k_X \tilde{X}\right\} \mathrm{d}\tilde{X} \quad (2.37)$$

where the expression in the square brackets is zero. For certain blade shapes it is possible to solve the integral in Ψ_T analytically. The final equation for acoustic pressure due to blade thickness sources then becomes

$$p(\mathbf{x},t) = -\sum_m \int_{r_h}^{r_t} \frac{\rho_0 c_0 b c B U_r}{8\pi} \exp\left\{\mathrm{i}\nu\phi_o + \mathrm{i}\omega_m t\right\} I_{k_z}\, \mathrm{d}r \quad (2.38)$$

$$I_{k_z} = \int_{-\infty}^{\infty} \left[\kappa - k_z M\right] J_\nu(\Gamma r_<) H_\nu^{(2)}(\Gamma r_>) \exp\left\{-\mathrm{i}k_z z_o + \mathrm{i}k_s\right\} \mathrm{i}k_X \Psi_T\, \mathrm{d}k_z \quad (2.39)$$

2.4.3 Steady Loading

Steady loading noise occurs as a result of the loading forces generated by the blade. The force produced by a blade element onto the air is given by the force vector $\mathbf{f} = \{f_z, f_\phi, 0\}$ (as before, the radial forces are assumed negligible). This force usually lies normal to the blade surface. For sources lying on the blade planform, which is assumed to be aligned

to the local flow direction, the force is always chord normal. Therefore, expressing the blade force $\mathbf{f}$ in components of the cylindrical co-ordinate system gives

$$f_z = F\sin\alpha, \quad f_\phi = \frac{F\cos\alpha}{r} \tag{2.40}$$

where F is a force magnitude and, for an elemental area on the rotor blade,

$$F = \frac{1}{2}\rho_0 U_r^2 c C_L f\left(\tilde{X}\right)\,\mathrm{d}X\,\mathrm{d}r. \tag{2.41}$$

The blade co-efficient of lift is represented by C_L and $f\left(\tilde{X}\right)$ is a dimensionless chordwise force distribution (see Figure 2.2 (d)) such that

$$\int_{-\frac{1}{2}}^{\frac{1}{2}} f\left(\tilde{X}\right)\,\mathrm{d}\tilde{X} = 1. \tag{2.42}$$

Here we can start with the expression obtained during derivation of the single radius rotating point force (eq. (2.28)) and redefine the source terms in blade co-ordinates with eqs. (2.31) and (2.32). Then, integrating over the blade planform and around the azimuth (see eq. (2.25)), reducing the summation over B sources and replacing eqs. (2.40) and (2.41) results in

$$p\left(\mathbf{x},t\right) = -\sum_m \int_{r_h}^{r_t} \frac{\rho_0 U_r^2 C_L c}{16\pi} \int_{-\infty}^{\infty} \left[k_z\sin\alpha - \frac{\nu\cos\alpha}{r}\right] J_\nu\left(\Gamma r_<\right) H_\nu^{(2)}\left(\Gamma r_>\right) \exp\left\{-\mathrm{i}k_z z_o + \mathrm{i}\nu\phi_o + \mathrm{i}\omega_m t + \mathrm{i}k_s\right\}\,\mathrm{d}k_z\,\mathrm{d}r \tag{2.43}$$

where

$$\Psi_L = \int_{-1/2}^{1/2} f\left(\tilde{X}\right)\exp\left\{\mathrm{i}k_X\tilde{X}\right\}\,\mathrm{d}\tilde{X} \tag{2.44}$$

The loading distribution Ψ_L accounts for chordwise non-compactness and may be defined arbitrarily. Depending on the distribution chosen, it may be evaluated either analytically or numerically. As before, $\nu = -mB$, $\omega_m = mB\Omega$ and now

$$\frac{\mathrm{d}L}{\mathrm{d}r} = \frac{1}{2}\rho_0 U_r^2 c C_L \Psi_L \tag{2.45}$$

so that the final expression is, when again using the definitions in eqs. (2.11) and (2.36),

$$p\left(\mathbf{x},t\right)=\frac{B}{8\pi}\sum_{m=-\infty}^{\infty}\int_{r_h}^{r_t}\exp\left\{\mathrm{i}\nu\phi_o+\mathrm{i}\omega_m t\right\}I_{k_z}\,\mathrm{d}r \tag{2.46}$$

where

$$I_{k_z}=\int_{-\infty}^{\infty}\left[k_z\sin\alpha-\frac{\nu\cos\alpha}{r}\right]J_\nu\left(\Gamma r_<\right)H_\nu^{(2)}\left(\Gamma r_>\right)\exp\left\{-\mathrm{i}k_z z_o+\mathrm{i}k_s\right\}\,\mathrm{d}k_z. \tag{2.47}$$

2.4.4 Viscous Wake Interaction

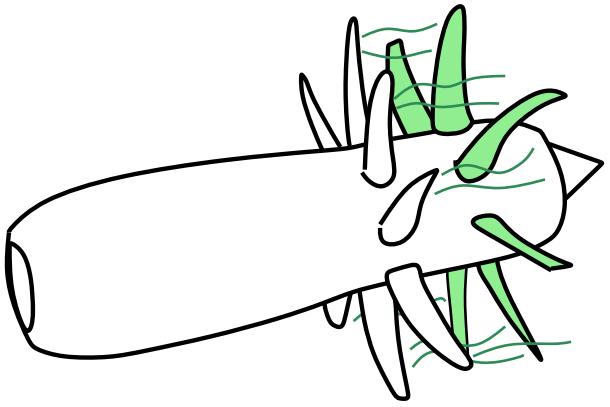

FIGURE 2.3: Representation of the rotor-rotor interaction.

Figure 2.3 is a simplified schematic of the rotor-wake interaction noise source. Generally, interaction tones are created by the unsteady blade loading generated by some form of periodic distortion. The loading is unsteady in that it is time varying in the blade relative frame of reference (in the previous cases the loading was stationary in this frame). Since the mechanisms of noise generation leading to interaction tones are no longer locked to the rotor, these tones will typically occur at different frequencies and with different circumferential mode orders (no longer at multiples of the blade number B) to the rotor alone noise sources. The formulation can still be derived in a similar manner; the Green's function remains the same as we are still considering free-field radiation, however the definition of the source function changes, as shown in this subsection. For rotor parameters, the subscripts 1 and 2 correspond to the front and rear rotor respectively, i.e. B_2 is the blade count of the rear rotor. Note that the definition of ν depends on whether a sum (ν_+) or difference (ν_-) interaction tone is being considered. Generally speaking, it is the difference interaction tone that is of interest, since the sum interaction

tone is in most cases not an efficient propagator of noise, which may be determined by the relatively large circumferential mode order ν.

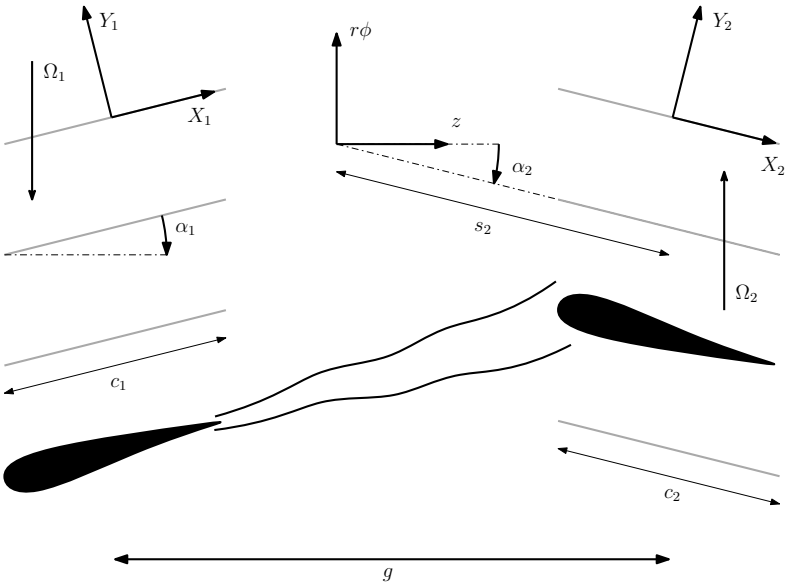

FIGURE 2.4: A schematic on an annular surface, showing some of the modelling parameters for the rotor-rotor interaction.

An expression for tone noise generated by the unsteady loading on the blades of the rear rotor, caused by contra-rotating wakes generated by the front rotor, is now presented. The unsteady loading on an individual reference blade on the rear rotor, here indexed by $k = 0$, is first expressed as a Fourier Series

$$F^{(0)}\left(X^{(0)}, r, \tau\right) = \sum_{m_1=-\infty}^{\infty} F_{m_1}^{(0)}\left(X^{(0)}, r\right) \exp\left\{\mathrm{i}m_1 B_1 \left(\Omega_1 + \Omega_2\right)\tau\right\} \tag{2.48}$$

where

$$F_{m_1}^{(0)}\left(X^{(0)}, r\right) = \frac{1}{T}\int_0^T F^{(0)}\left(X^{(0)}, r, \tau\right) \exp\left\{-\mathrm{i}m_1 B_1 \left(\Omega_1 + \Omega_2\right)\tau\right\}\, \mathrm{d}\tau \tag{2.49}$$

and the period of the distortion $T = 2\pi/\left(B_1\left(\Omega_1 + \Omega_2\right)\right)$. Note that the loading on the k^{th} blade is related to the reference blade by

$$\begin{aligned} F^{(k)}\left(X^{(k)}, r, \tau\right) &= F^{(0)}\left(X^{(k)}, r, \tau + \frac{2\pi k}{B_2\left(\Omega_1 + \Omega_2\right)}\right) \\ &= \sum_{m_1=-\infty}^{\infty} F_{m_1}^{(0)}\left(X^{(k)}, r\right) \exp\left\{\mathrm{i}m_1 B_1 \left(\Omega_1 + \Omega_2\right)\tau + 2\pi \mathrm{i}k m_1 \frac{B_1}{B_2}\right\} \end{aligned} \tag{2.50}$$

and the Fourier transform of this function would be

$$\begin{aligned}\tilde{F}^{(k)}\left(X^{(k)},r,\omega\right) &= \frac{1}{2\pi}\int_{-\infty}^{\infty}\sum_{m_1=-\infty}^{\infty} F_{m_1}^{(0)}\left(X^{(k)},r\right) \\ &\quad\times\exp\left\{-\mathrm{i}\left(\omega-m_1B_1\left(\Omega_1+\Omega_2\right)\right)\tau+2\pi\mathrm{i}km_1\frac{B_1}{B_2}\right\}\mathrm{d}\tau \\ &= \sum_{m_1=-\infty}^{\infty} F_{m_1}^{(0)}\left(X^{(k)},r\right)\exp\left\{2\pi\mathrm{i}km_1\frac{B_1}{B_2}\right\}\delta\left(\omega-m_1B_1\left(\Omega_1+\Omega_2\right)\right) \quad (2.51)\end{aligned}$$

The formulation now continues as before for a dipole type source but that, in effect, the source function is now defined as

$$\begin{aligned}\gamma\left(\mathbf{y},\omega\right) &= \sum_{k=1}^{B_2}\sum_{m_2}\left[\sin\alpha\frac{\partial}{\partial z_s}-\frac{\mathrm{i}m_2\cos\alpha}{r}\right]\frac{F^{(k)}\left(X^{(k)},r,\tau\right)}{2\pi r} \\ &\quad\times\exp\left\{-\mathrm{i}m_2\phi_s+\mathrm{i}m_2\Omega_2\tau+2\pi\mathrm{i}\frac{m_2k}{B_2}+\mathrm{i}\left[k_z\cos\alpha_2-\frac{m_2\sin\alpha_2}{r}\right]\left(s+X\right)\right\}\mathrm{d}X\,\mathrm{d}r\end{aligned} \quad (2.52)$$

where we have included the summation in k (representing B_2 blades) and the conversion to rear rotor blade coordinates. The summation over k can be solved by noting that a solution only exists when $m_2 \to \nu = m_2B_2 - m_1B_1$ and so

$$\sum_{k=1}^{B_2}\sum_{m_1}\sum_{m_2}\exp\left\{2\pi\mathrm{i}k\left(\frac{m_1B_1+m_2}{B_2}\right)\right\}f\left(m_2\right)=B_2\sum_{m_1}\sum_{m_2}f\left(\nu\right) \quad (2.53)$$

where here f is a function representing the remainder of the expression. Using this source function in eq. (2.9) and following the same process as before (but including the variable change outlined in eq. (2.53)) results in an expression for the sound pressure, p, emitted from the rear rotor, due to an unsteady blade loading caused by interactions with the front rotor wake

$$p=-\sum_{m_1}\sum_{m_2}\frac{B_2}{8\pi}\int_{r_h}^{r_t}\exp\left\{-\mathrm{i}\nu\phi_o+\mathrm{i}\omega_{m_1m_2}t\right\}I_{k_z}\,\mathrm{d}r \quad (2.54)$$

where

$$I_{k_z} = \int_{-\infty}^{\infty} \left[k_z \sin\alpha_2 - \frac{\nu \cos\alpha_2}{r} \right] J_\nu\left(\Gamma r_<\right) H_\nu^2\left(\Gamma r_>\right) \exp\left\{-\mathrm{i}k_z z_o + \mathrm{i}k_s\right\} \Psi_{VW}\, \mathrm{d}k_x \quad (2.55)$$

$$\Psi_{VW} = \int_{-\frac{1}{2}}^{\frac{1}{2}} F_{m_1} \exp\left\{\mathrm{i}k_X X_2\right\}\, \mathrm{d}X_2 \quad (2.56)$$

and the definitions in eqs. (2.11) and (2.36) are again used but now the circumferential mode order ν and tone frequency $w_{m_1 m_2}$ are defined as

$$\nu = m_2 B_2 - m_1 B_1 \quad (2.57)$$

$$\omega = m_1 B_1 \Omega_1 + m_2 B_2 \Omega_2 \quad (2.58)$$

As before Ψ_{VW} is a loading distribution that includes the chordwise phase variation and the unsteadiness is described by an infinite number of harmonic gusts of index m_1. The distribution may be described analytically or numerically. An analytic description would be dependant on the features of the wake as it impacts the blade and the blade response itself. A number of modelling options for this type of loading are discussed in detail in Parry (1988).

2.4.5 Quadrupole Noise

For completeness we mention the quadrupole noise component of rotor-alone tones. Whilst steady loading and thickness components are considered to dominate rotor-alone tone noise in most cases, it could also be important to consider quadrupole noise at higher axial flow speeds, which are typical of the cruise regime. The evaluation of quadrupole noise requires calculation of a volume integral encapsulating the flow around the blades, which adds considerably to the complexity of the problem.

A quadrupole noise prediction scheme has not been developed here. It has in fact been suggested in some literature that quadrupole source terms could be neglected for prop-fans (Parry, 1988). On top of this, the addition of blade sweep to the propeller can reduce the transonic effects that are likely to appear on comparatively straight-bladed propellers (Metzger and Rohrbach, 1979). Design features such as sweep (which aid the reduction of this noise source) are included in the modern, optimised blades considered in the majority of this work.

2.4.6 Rotor-rotor Potential Field Interaction

The strongly bound potential fields of the blades in each rotor may induce an upwash on the other rotor, creating an unsteady lift force on those blades, which would again lead to the generation of radiated noise. In this sense the mechanism is similar to the viscous wake interaction noise source, however note here that there can be upstream interactions due to the potential field originating from the downstream rotor as well. Potential field interaction noise may thus be emitted from the upstream and the downstream rotor. The strength of the potential field has been shown to be strongly dependant on certain rotor parameters, such as blade count, blade loading and rotor gap, g (see Figure 2.4). Since the mechanism is analogous to viscous wake interaction the noise is generated at identical frequencies and circumferential mode orders. However only the tones due to the interaction of the lowest harmonics is expected to be significant and indeed modern open rotor aero-engine designs are expected to have parameters selected to mitigate the level of this noise source entirely. As such a similar expression for the acoustic pressure due to potential field interaction has not been presented, but is essentially identical to the form of the viscous wake interaction expression.

2.5 Far-field Approximation

In full, the near-field expressions derived for rotor-alone tones (eqs. (2.46) and (2.38)) can require large amounts of computational power, especially when considering several harmonics.

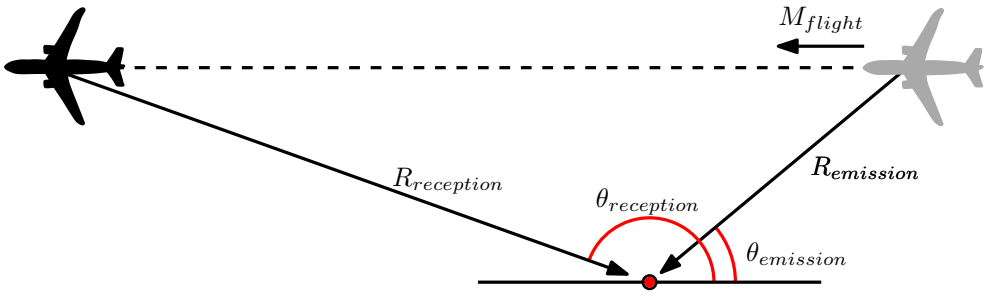

FIGURE 2.5: Reception and emission polar coordinates for a flyover case. θ is the meridional angle, R is the radius and M_{flight} is the flight Mach number.

It should be highlighted that a change from reception co-ordinates (used in the near-field) to emission coordinates may be applied when simulating far-field noise. The latter is considered a more useful coordinate system for understanding far-field noise. Figure 2.5 shows propagation paths of an acoustic wave and its description in both reception and emission coordinates. The use of emission co-ordinates introduces two new variables - the meridional angle, θ and a propagation radius, $R = |\mathbf{x}|$.

The conversion between emission and reception coordinates is simple and the procedure is presented in Appendix 2.D. Note that in flyover cases, using emission coordinates gives a better understanding of the directivity of noise as they account for the effects of aircraft speed. However in wind tunnel tests, the 'observers' are fixed relative to the engine and thus receive noise in reception coordinates. Thus a conversion procedure between reception and emission coordinates is useful for the analysis of results. A derivation of the far-field approximation that is applied to the expressions presented in this chapter is outlined in appendix 2.C.

Returning to the expression for steady loading noise given in eqs. (2.46) and (2.47), the approximation for the k_z integral using the method of stationary phase is

$$I_{k_z} \sim \frac{-2\mathrm{i}}{|\mathbf{x}|(1-M\cos\theta)}\left[\frac{\kappa\cos\theta\sin\alpha}{(1-M\cos\theta)}+\frac{\nu\cos\alpha}{r}\right]\frac{\mathrm{d}L}{\mathrm{d}r} \times J_{-\nu}(\beta r)\exp\left\{-\mathrm{i}\left(\frac{\nu\pi}{2}+k_s+\kappa|\mathbf{x}|\right)\right\} \quad (2.59)$$

and thus the far-field approximation for steady loading noise is

$$p\left(\mathbf{x},t\right)=\sum_{m=-\infty}^{\infty}\frac{-\mathrm{i}B}{4\pi|\mathbf{x}|(1-M\cos\theta)}\exp\left\{\mathrm{i}\nu\left(\phi_o-\frac{\pi}{2}\right)+\mathrm{i}\omega_m\left(t-\frac{|\mathbf{x}|}{c_0}\right)\right\} \int_{r_h}^{r_t}\left[\frac{\kappa\cos\theta\sin\alpha}{(1-M\cos\theta)}+\frac{\nu\cos\alpha}{r}\right]\frac{\mathrm{d}L}{\mathrm{d}r}J_{-\nu}(\beta r)\exp\left\{-\mathrm{i}k_s\right\}. \quad (2.60)$$

For the expression for thickness noise, using the method of stationary phase means the k_x integral approximates to

$$I_{k_z} \sim \frac{-2\mathrm{i}\kappa}{|\mathbf{x}|(1-M\cos\theta)^2}J_{-\nu}(\beta r)\exp\left\{-\mathrm{i}\left(\frac{\nu\pi}{2}+k_s+\kappa|\mathbf{x}|\right)\right\}\mathrm{i}k_X\Psi_V$$

and the far-field approximation for thickness noise is

$$p\left(\mathbf{x},t\right)=\sum_{m=-\infty}^{\infty}\frac{-\rho\kappa Bc_0}{4\pi|\mathbf{x}|(1-M\cos\theta)^2}\exp\left\{\mathrm{i}\nu\left(\phi_o-\frac{\pi}{2}\right)+\mathrm{i}\omega_m\left(t-\frac{|\mathbf{x}|}{c_0}\right)\right\} \int_{r_h}^{r_t}bk_XU_r\Psi_VJ_{-\nu}(\beta r)\exp\left\{-\mathrm{i}k_s\right\}\,\mathrm{d}r. \quad (2.61)$$

Both the above far-field expressions are equivalent to those derived by Hanson (1980*b*) and later by Parry (1988). Note that a similar process can be used to generate expressions for the acoustic pressure in the far-field of any of the source types considered in this chapter.

The expressions for near-field and far-field rotor-alone tone noise (eqs. (2.46), (2.38), (2.60) and (2.61)) can be used to make predictions based on realistic open rotor operating conditions and blade geometries. In the following subsection, comparisons of these models are made in both the near- and far-field to display the extent of near-field effects.

The operating conditions and blade geometries are provided by Rolls-Royce. In the following figures a take-off case is considered, for which the flow Mach number, M, is roughly 0.2. In this case, blade loading is high, relative to other regimes of flight.

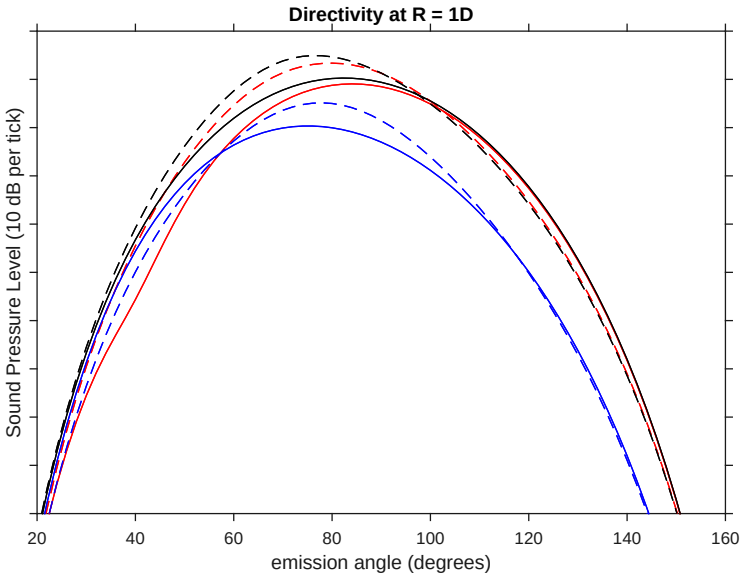

FIGURE 2.6: {1,0} tone directivities produced by the near-field (dashed) and far-field (solid) prediction methods. Both steady loading (red) and thickness (blue) noise source are included as well as the sum of the sources (black). The tone directivities are evaluated at a fixed emission radius in the near-field.

Figure 2.6 shows a tone directivity at a fixed emission radius that is a single rotor diameter away from the rotor hub. Directivities are evaluated for both components of rotor alone noise and a coherent sum is presented as well. Note that in the forward arc ($> 90°$) the total noise is less than the steady loading component. This is due to a phase difference between the two components. Note also that, at this emission radius, the predicted near-field peak sound pressure levels are higher than the equivalent values predicted by the far-field models. The near-field models are capable of predicting rotor near-field effects, where the far-field models cannot.

If we now increase the rotor observer separation distance, as in Figure 2.7, where the observer is now located approximately thirty rotor diameters from the rotor hub we see

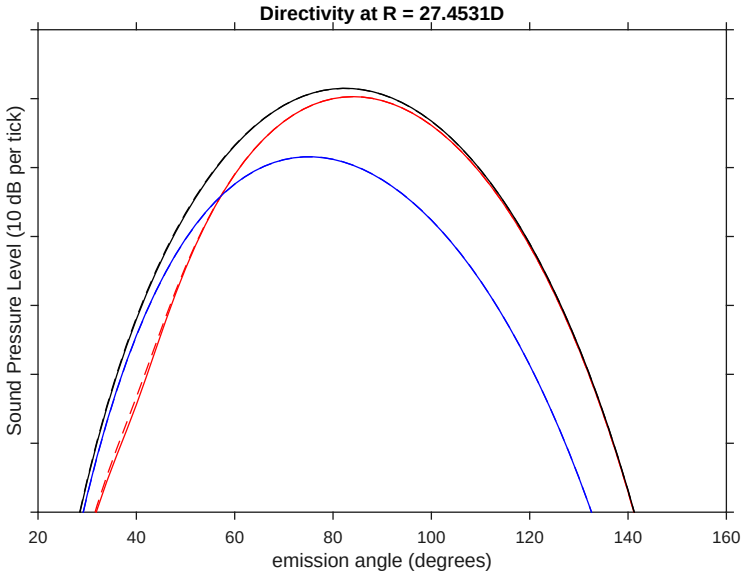

FIGURE 2.7: {1,0} tone directivities produced by the near-field (dotted) and far-field (solid) prediction methods. Both steady loading (red) and thickness (blue) noise source are included as well as the sum of the sources (black). The tone directivities are evaluated at a fixed emission radius in the far-field.

that these near-field effects are minimised. It is clear that the observer is in the far-field and this is proved by the high correlation of results between both formulations. There is nearly no variation in the evaluated pressures.

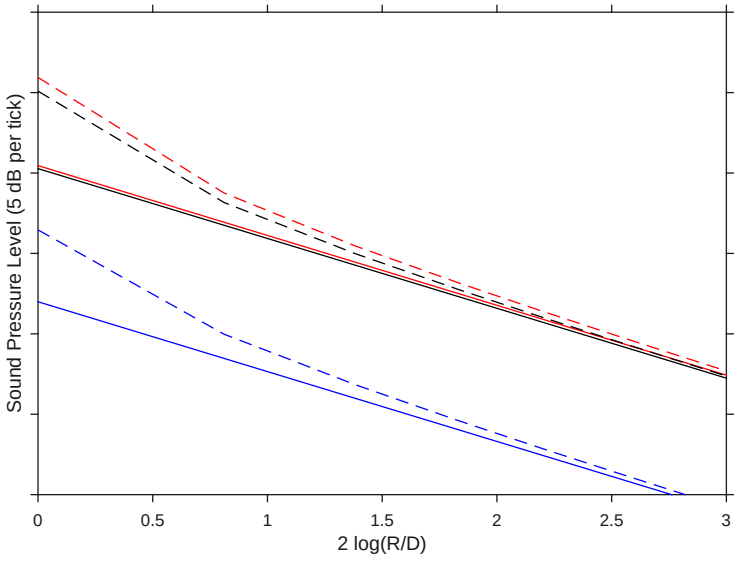

FIGURE 2.8: Log-log plot showing SPL variation with emission radius for the near-field (dotted) and far-field (solid) prediction methods. Both steady loading (red) and thickness (blue) noise source are included as well as the sum of the sources (black). The radius, R, has been made non-dimensional by the rotor diameter, D.

To illustrate this point further we can fix the emission angle and vary the rotor observer separation distance. This relationship is shown in Figure 2.8. A log-log plot has been

used to demonstrate that the far-field model predicts acoustic propagation that is spherically spreading in nature. This figure demonstrates the inability of the far-field model to capture radiation behaviour in the near-field. As the emission radius is increased, the accuracy of the far-field method improves. In this case, by a distance roughly three rotor diameters away from the source, the far-field model is a very good match to the near-field model. Far-field models have been useful in the engineering design of open rotors since they are significantly less expensive to run in terms of computational power yet maintain accuracy everywhere except in the near-field.

When compared to rotor-alone tones, interaction tones are less sensitive to near-field effects. This behaviour is seen in Figure 2.9. The counter rotating wake essentially produces a higher effective mode phase speed which allows sound to propagate more efficiently. This change in behaviour could be thought of as analogous to duct modes which are 'cut on'. Therefore, in many interaction tone simulations it may prove acceptable to use a far-field prediction model (especially in lieu of the relative computational expense). Interaction tone prediction methods have been covered extensively in the literature, most notably in Parry (1988).

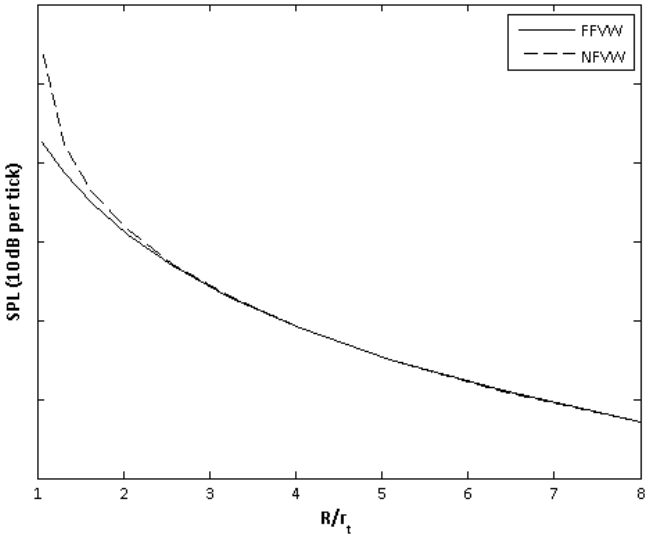

FIGURE 2.9: Comparison of a simplified near- and far-field viscous wake prediction code. The near-field and far-field rapidly converge with increasing sideline since near-field effects can be much less pronounced in interaction tones.

2.6 Open Rotor Aerodynamics Prediction

Many of these acoustic models require a description of either the rotor blade forced response or the flow aerodynamics around the open rotor blades in order to correctly quantify source strengths. The details of aerodynamic modelling of open rotors is not the main objective of the research here and is beyond the scope of this thesis. The

required aerodynamic parameters for the most part have been provided by the sponsor *Rolls-Royce* plc. *Rolls-Royce* supply rotor blade lift and drag coefficients by using any one of a suite of in house aerodynamic prediction tools. Due to its rapid evaluation time, WAKEA, an aerodynamic strip theory code, has been the tool of choice for supplying the necessary steady aerodynamic parameters for the majority of the work presented here i.e. in the development of the acoustic models. However, in some parts of the work presented, the accuracy of the acoustic prediction was particularly important. For these calculations, the aerodynamic parameters were provided by a steady Reynolds-averaged Navier Stokes (RANS) prediction tool. These simulations were conducted using the code MPROP, a RANS Computation Fluid Dynamics (CFD) code dedicated to the prediction of exposed rotor aerodynamics. Both the tools WAKEA and MPROP are owned by the sponsor *Rolls-Royce*. Situations where a more accurate noise prediction were required include comparisons of noise predictions to measurements from experimental campaigns, and involvement in the EU project NINHA where noise predictions were shared with a number of project partners.

MPROP

MPROP is one of the tools used by *Rolls-Royce* for prediction of open rotor aerodynamic performance. MPROP was developed specifically for the prediction of open rotor or propeller aerodynamics. MPROP is a derivative of a larger turbomachinery aerodynamic prediction tool, MULTALL. The calculation mesh is defined in a blade to blade passage (i.e. in the blade spacing between the upper surface of one blade and the lower surface of the adjacent blade) and typically from the engine (or first rotor) inlet to the engine (or last rotor) exit. A steady full-annulus solution is easily obtained from this solution. Mixing planes are used at the boundary between each bladerow. For the open rotor there are two rotor bladerows to model. The rotor blade geometries are required to define the calculation mesh for MPROP. This information was again supplied by the sponsor *Rolls-Royce*. The results from the MPROP solution contain a definition for the grid as well as some evaluated flow parameters on each grid point - typically pressure, density and a velocity vector. Further flow parameters are evaluated from these fundamental parameters.

Application to acoustic modelling

In order to generate acoustic predictions, the aerodynamic solutions generated by MPROP require further post processing, in order to identify spanwise blade lift and drag coefficients generated by the steady flow solution. The acoustic models may be trivially adapted such that a blade loading distribution or a rotor blade wake can be approximated from these parameters. Although no validation work was conducted directly for this thesis, the project sponsor established that the RANS simulations generated by

MPROP provide better predictions for the necessary aerodynamic parameters, particularly at high speed, through internal assessments of their CFD tools.

For all distributed source models, both spanwise and chordwise distribution profiles are required for the source definition. In the following chapters, for any distributed source calculations, spanwise variation is captured by the aeordynamic modelling and blade span integrals are evaluated numerically. On the other hand, chordwise variation is typically defined by an analytic function, allowing for, in most cases, analytic evaluation of the chordwise integral. Analytic definition of the chordwise variation reduces the necessary computation time.

2.7 Conclusions

In this chapter, analytical models for the tone noise generated by the open rotor in a free-field environment and which are valid in the near-field have been presented. The models are not original work, however such techniques for rotor noise prediction lay the foundation for original work presented in the following chapters. Models for a number of tone noise sources have been derived and these models have been used to understand the free-field radiation of open rotor tones. Specifically, models for steady loading, steady thickness and rotor wake interaction have been discussed in detail. The models can account for a uniform axial flow and also consider the effects of blade geometry such as sweep and chordwise variation. It would be possible to model other sources, such as potential field interaction, in a similar fashion, however for brevity only models for the dominant sources are included in this work. Other three-dimensional blade geometry features such as lean may be modelled in a similar fashion, however the use of thin blades and the frequencies of interest renders the source distribution compact in this dimension. A free-filed Green's function is presented here - much of the work in the next chapter will use modified Green's functions to develop valid near-field noise models.

Appendices

2.A Green's Function Transform

The Green's function G satisfies the equation

$$\left[\nabla_y^2 - \frac{1}{c_0^2}\frac{\mathrm{D}_0^2}{\mathrm{D}\tau^2}\right] G\left(\mathbf{y}, \tau \,|\, \mathbf{x}, t\right) = -\delta_3\left(\mathbf{x} - \mathbf{y}\right)\delta\left(t - \tau\right) \tag{2.62}$$

where δ_3 is a three-dimensional delta function. First take the Fourier transform of eq. (2.62), which yields

$$\left[\nabla_y^2 - \frac{1}{c_0^2}\left[\mathrm{i}\omega + U_z\frac{\partial}{\partial z_s}\right]^2\right]\tilde{G}\left(\mathbf{y},\omega\,|\,\mathbf{x},t\right) = \frac{1}{2\pi}\int_{-\infty}^{\infty} -\delta_3\left(\mathbf{x}-\mathbf{y}\right)\delta\left(t-\tau\right)\exp\left\{-\mathrm{i}\omega\tau\right\}\,\mathrm{d}\tau. \quad (2.63)$$

Using properties of the delta function, the τ integral on the left hand side (LHS) can be evaluated, so that

$$\left[\nabla_y^2 - \frac{1}{c_0^2}\left(\mathrm{i}\omega + U_z\frac{\partial}{\partial z_s}\right)^2\right]\tilde{G}\left(\mathbf{y},\omega\,|\,\mathbf{x},t\right) = -\delta_3\left(\mathbf{x}-\mathbf{y}\right)\frac{\exp\left\{-\mathrm{i}\omega t\right\}}{2\pi}. \quad (2.64)$$

Taking the conjugate of eq. (2.64) gives

$$\left[\nabla_y^2 - \frac{1}{c_0^2}\left(-\mathrm{i}\omega + U_z\frac{\partial}{\partial z_s}\right)^2\right]\tilde{G}^* = -\delta_3\left(\mathbf{x}-\mathbf{y}\right)\frac{\exp\left\{\mathrm{i}\omega t\right\}}{2\pi} \quad (2.65)$$

and then let

$$\tilde{G}^* = \tilde{G}_\omega\left(\mathbf{y}\,|\,\mathbf{x}\right)\frac{\exp\left\{\mathrm{i}\omega t\right\}}{2\pi} \quad (2.66)$$

such that now

$$\left[\nabla_y^2 - \frac{1}{c_0^2}\left(-\mathrm{i}\omega + U_z\frac{\partial}{\partial z_s}\right)^2\right]\tilde{G}_\omega\left(\mathbf{y}\,|\,\mathbf{x}\right) = -\delta_3\left(\mathbf{x}-\mathbf{y}\right). \quad (2.67)$$

Therefore, the frequency domain transformation for the Green's function is

$$G\left(\mathbf{y},\tau\,|\,\mathbf{x},t\right) = \int_{-\infty}^{\infty}\tilde{G}^*\left(\mathbf{y},\omega\,|\,\mathbf{x},t\right)\exp\left\{-\mathrm{i}\omega\tau\right\}\,\mathrm{d}\omega = \int_{-\infty}^{\infty}\tilde{G}_\omega\left(\mathbf{y}\,|\,\mathbf{x}\right)\frac{\exp\left\{\mathrm{i}\omega\left(t-\tau\right)\right\}}{2\pi}\,\mathrm{d}\omega. \quad (2.68)$$

2.B Derivation of Frequency Domain Green's Function

In order to determine the free-field Green's function, we will now solve the differential equation for which this Green's function is a solution. Starting with the frequency domain convected wave equation in cylindrical coordinates gives

$$\left[\frac{\partial^2}{\partial z_s^2}+\frac{1}{r_s^2}\frac{\partial^2}{\partial \phi_s^2}+\frac{\partial^2}{\partial r_s^2}+\frac{1}{r_s}\frac{\partial}{\partial r_s}-\frac{1}{c_0^2}\left(\mathrm{i}\omega-U_z\frac{\partial}{\partial z_s}\right)^2\right]\tilde{G}_\omega\left(\mathbf{y}\,|\,\mathbf{x}\right)=-\delta_3\left(\mathbf{x}-\mathbf{y}\right) \quad (2.69)$$

We define a Fourier transform of $\tilde{G}_\omega$ in both z_s and ϕ_s

$$\tilde{G}_\omega^{110}\left(k_z,m,r_s\,|\,\mathbf{x}\right)=\frac{1}{(2\pi)^2}\int_{-\infty}^{\infty}\int_{0}^{2\pi}\tilde{G}_\omega\left(\mathbf{y}\,|\,\mathbf{x}\right)\exp\left\{-\mathrm{i}k_z z_s+\mathrm{i}m\phi_s\right\}\,\mathrm{d}\phi_s\,\mathrm{d}z_s \quad (2.70)$$

and a corresponding inverse Fourier transform as

$$\tilde{G}_\omega=\sum_m\left(\int_{-\infty}^{\infty}\tilde{G}_\omega^{110}\left(k_z,m,r_s\,|\,\mathbf{x}\right)\exp\left\{\mathrm{i}k_z z_s\right\}\,\mathrm{d}k_z\right)\exp\left\{-\mathrm{i}m\phi_s\right\}. \quad (2.71)$$

The inhomogeneous wave equation in eq. (2.69) is subjected to the transformation in eq. (2.70) and the expression becomes

$$\left[\frac{\partial^2}{\partial r_s^2}+\frac{1}{r_s}\frac{\partial}{\partial r_s}-\frac{m^2}{r_s^2}-k_z^2+\kappa^2-2\kappa M k_z+M^2k_z^2\right]\tilde{G}_\omega^{110}\left(k_z,m,r\,|\,\mathbf{x}\right)$$
$$=\int_{-\infty}^{\infty}\int_{0}^{2\pi}-\delta_3\left(\mathbf{x}-\mathbf{y}\right)\frac{\exp\left\{-\mathrm{i}k_z z_s+\mathrm{i}m\phi_s\right\}}{4\pi^2}\,\mathrm{d}\phi_s\,\mathrm{d}z_s. \quad (2.72)$$

where $\kappa=\omega/c_0$ is referred to as the acoustic wavenumber and $M=U_z/c_0$ is a Mach number. The right hand side (RHS) of this expression can again be evaluated using the properties of the delta function since

$$\delta_3\left(\mathbf{x}-\mathbf{y}\right)=\delta\left(z_o-z_s\right)\frac{\delta\left(r_o-r_s\right)}{r_s}\delta\left(\phi_o-\phi_s\right) \quad (2.73)$$

and so

$$\int_{-\infty}^{\infty}\int_{0}^{2\pi} -\delta_3\left(\mathbf{x}-\mathbf{y}\right)\exp\left\{-\mathrm{i}k_z z_s + \mathrm{i}m\phi\right\}\,\mathrm{d}\phi\,\mathrm{d}z_s$$
$$= -\frac{\delta\left(r_o - r_s\right)}{4\pi^2 r_s}\exp\left\{-\mathrm{i}k_z z_o + \mathrm{i}m\phi_o\right\}. \quad (2.74)$$

The homogeneous form of this differential equation is known as Bessel's Differential Equation,

$$\left[\frac{\partial^2}{\partial r_s^2} + \frac{1}{r_s}\frac{\partial}{\partial r_s} + \left(\Gamma^2 - \frac{m^2}{r_s^2}\right)\right]\tilde{G}_\omega^{110}\left(k_z, m, r_s \,|\, \mathbf{x}\right) = 0 \quad (2.75)$$

where Γ is a radial wavenumber, defined by the dispersion relation

$$\Gamma^2 = \kappa^2 - 2\kappa M k_z - \beta^2 k_z^2 \quad (2.76)$$

and β is the Prandtl-Glauert factor $\sqrt{1-M^2}$. The expression in eq. (2.76) provides two possible values of Γ, either the positive or negative root. The root to use will depend on the sign of the frequency ω as well as the form of the solution that is taken.

$J_m\left(\Gamma r\right)$, $Y_m\left(\Gamma r\right)$, $H_m^{(1)}\left(\Gamma r\right)$ and $H_m^{(2)}\left(\Gamma r\right)$ are all linearly independent solutions of Bessel's equation. The Hankel functions, H, are defined as

$$H_m^{(1)}\left(\Gamma r\right) = J_m\left(\Gamma r\right) + \mathrm{i}Y_m\left(\Gamma r\right) \quad (2.77)$$
$$H_m^{(2)}\left(\Gamma r\right) = J_m\left(\Gamma r\right) - \mathrm{i}Y_m\left(\Gamma r\right) \quad (2.78)$$

The domain of r is from $0 \leq r \leq \infty$. There are boundary conditions imposed at each of the limits of this domain - firstly, at $r = 0$ the solution must be finite and secondly, that at $r = \infty$ the solution must be bounded and outgoing. The latter condition is known as Sommerfeld's radiation condition. Only the Bessel function of the first kind, J_m, meets the boundary condition at $r = 0$. Sommerfeld's radiation condition is in our case satisfied by the Hankel function of the second kind, $H_m^{(2)}$.

The Hankel function that meets the exterior boundary condition is dependant on the time convention used. The validity of the solution can be simply assessed by considering the Hankel function's asymptotic limit for large arguments. According to Abramowitz and Stegun (1972, eq. 9.2.4) as $r \to \infty$

$$H_m^{(2)}(\Gamma r) \sim \sqrt{\frac{2}{\pi\Gamma r}} \exp\left\{-\mathrm{i}\left(\Gamma r - \frac{m\pi}{2} - \frac{\pi}{4}\right)\right\}. \tag{2.79}$$

but only when $k_z^2 < (\kappa - Mk_z)^2$. For the case when $k_z^2 > (\kappa - Mk_z)^2$ the root becomes imaginary and the wave is evanescent. The root must be selected such that we obtain a wave that decays as $r \to \infty$. Since we would like to maintain using the Hankel function of the second kind, we use the negative imaginary root of Γ for all positive ω i.e.

$$\Gamma = \begin{cases} \operatorname{sgn}(\kappa)\sqrt{(\kappa - Mk_z)^2 - k_z^2} & \text{if } k_z^2 < (\kappa - Mk_z)^2 \\ -\mathrm{i}\sqrt{(\kappa - Mk_z)^2 - k_z^2} & \text{if } k_z^2 > (\kappa - Mk_z)^2 \\ 0 & \text{if } k_z^2 = (\kappa - Mk_z)^2 \end{cases}$$

(Note that $\Gamma = 0$ would produce a standing wave and thus does not propagate sound). Thus our solutions to the differential equation take the form

$$y_1 = \tilde{\tilde{G}}_\omega^- = A_m J_m(\Gamma r) \tag{2.80}$$

$$y_2 = \tilde{\tilde{G}}_\omega^+ = B_m H_m^{(2)}(\Gamma r). \tag{2.81}$$

The co-efficients A_m and B_m can be determined by using the Wronskian method. First, we convert the differential equation expressed in eq. (2.72) to its Sturm-Liouville form by multiplying through by r, thus

$$\left[r\frac{\partial^2}{\partial r^2} + \frac{\partial}{\partial r} + r\Lambda\right]\tilde{G}_\omega^{110}(k_z, m, r \,|\, \mathbf{x}) = \left[\frac{\partial}{\partial r}\left(r\frac{\partial}{\partial r}\right) + r\Lambda\right]\tilde{G}_\omega^{110}(k_z, m, r \,|\, \mathbf{x}) = \\ -\delta(r_o - r)\frac{\exp\{-\mathrm{i}k_z z_o + \mathrm{i}m\phi_o\}}{4\pi^2} \tag{2.82}$$

where

$$\Lambda = \Gamma^2 - \frac{m^2}{r^2} \tag{2.83}$$

Next, take this form of the differential equation and integrate on r over a small interval around r_o - this results in

$$\int_{r_o-\epsilon}^{r_o+\epsilon}\left[\frac{\partial}{\partial r}\left(r\frac{\partial}{\partial r}\right)+r\Lambda\right]\tilde{G}_{\omega}^{110}\left(k_z,m,r\,|\,\mathbf{x}\right)\,\mathrm{d}r=-\int_{r_o-\epsilon}^{r_o+\epsilon}\delta\left(r_o-r\right)\frac{\exp\left\{-\mathrm{i}k_z z_o+\mathrm{i}m\phi_o\right\}}{4\pi^2}\,\mathrm{d}r \tag{2.84}$$

$$r\frac{\partial\tilde{\tilde{G}}_{\omega}}{\partial r}\bigg|_{r_o-\epsilon}^{r_o+\epsilon}+\int_{r_o-\epsilon}^{r_o+\epsilon}r\Lambda\tilde{\tilde{G}}_{\omega}\,\mathrm{d}r=-\frac{\exp\left\{-\mathrm{i}k_z z_o+\mathrm{i}m\phi_o\right\}}{4\pi^2} \tag{2.85}$$

The integral in the second term on the expression's LHS will evaluate to 0, since (it is assumed that) the functions within this integral are continuous on r i.e.

$$r_o\Lambda\left(r_o\right)\tilde{\tilde{G}}_{\omega}^{+}-r_o\Lambda\left(r_o\right)\tilde{\tilde{G}}_{\omega}^{-}=0 \tag{2.86}$$

Thus the first term on the LHS of this expression must be discontinuous at r_o and equivalent in magnitude to the RHS, i.e.

$$r_o\frac{\partial\tilde{\tilde{G}}_{\omega}^{+}}{\partial r}-r_o\frac{\partial\tilde{\tilde{G}}_{\omega}^{-}}{\partial r}=-\frac{\exp\left\{-\mathrm{i}k_z z_o+\mathrm{i}m\phi_o\right\}}{4\pi^2} \tag{2.87}$$

There are now two boundary conditions as well as two expressions at $r=r_o$ which $\tilde{\tilde{G}}_{\omega}$ must satisfy. We can use the two expressions at $r=r_o$ (eqs. (2.86) and (2.87)) to determine the co-efficients A_m and B_m, provided the Wronskian of the two solutions ($W\left(y_2,y_1\right)$) is non-zero, that is, the solutions are linearly independent.

For simplicity, formulate these conditions as a matrix problem

$$\mathbf{Y}\cdot\mathbf{A}=\mathbf{C} \tag{2.88}$$

where $\mathbf{Y}$ is a 2×2 matrix and contains the solutions in eqs. (2.80) and (2.81) and their radial derivatives; $\mathbf{A}$ is a column matrix containing co-efficients A_m and B_m, and $\mathbf{C}$ represents the RHS of the two conditions specified, i.e.

$$\begin{pmatrix}H_m^{(2)} & -J_m\\ \frac{\partial H_m^{(2)}}{\partial r} & -\frac{\partial J_m}{\partial r}\end{pmatrix}\begin{pmatrix}B_m\\ A_m\end{pmatrix}=\begin{pmatrix}0\\ C_m\end{pmatrix} \tag{2.89}$$

and

$$C_m=-\frac{\exp\left\{-\mathrm{i}k_z z_o+\mathrm{i}m\phi_o\right\}}{4\pi^2 r_o}. \tag{2.90}$$

Using the Wronskian, the co-efficients are defined by

$$B_m = -\frac{J_m(\Gamma r)\exp\{-\mathrm{i}k_z z_o + \mathrm{i}m\phi_o\}}{r_o W\left(H_m^{(2)}, J_m\right)} \tag{2.91}$$

$$A_m = -\frac{H_m^{(2)}(\Gamma r)\exp\{-\mathrm{i}k_z z_o + \mathrm{i}m\phi_o\}}{r_o W\left(H_m^{(2)}, J_m\right)} \tag{2.92}$$

where the Wronskian of the two solutions is simply $\det(\mathbf{Y})$ and is evaluated as follows

$$W\left(H_m^{(2)}, J_m\right) = J_m \frac{\partial H_m^{(2)}}{\partial r} - H_m^{(2)} \frac{\partial J_m}{\partial r} \tag{2.93}$$

The derivatives with respect to r are evaluated by noting that

$$\frac{\partial H_m^{(2)}}{\partial r} = \frac{\partial Z}{\partial r} H_m^{(2)\prime}(Z) = \Gamma H_m^{(2)\prime}(\Gamma r_o) \tag{2.94}$$

$$\frac{\partial J_m}{\partial r} = \frac{\partial Z}{\partial r} J_m'(Z) = \Gamma J_m'(\Gamma r_o). \tag{2.95}$$

Using these expressions and the definition of the Hankel function provided in eq. (2.78) gives

$$\begin{aligned} W\left(H_m^{(2)}, J_m\right) &= \Gamma\left[J_m\left\{J_m' - \mathrm{i}Y_m'\right\} - \left\{J_m - \mathrm{i}Y_m\right\}J_m'\right] = \mathrm{i}\Gamma\left[J_m' Y_m - Y_m' J_m\right] \\ &= \mathrm{i}\Gamma\left[W(J_m, Y_m)\right]. \end{aligned} \tag{2.96}$$

Then, referring to Abramowitz and Stegun (1972, eq. 9.1.16),

$$W\left(H_m^{(2)}, J_m\right) = \mathrm{i}\Gamma\frac{2}{\pi\Gamma r_o} = \frac{2\mathrm{i}}{\pi r_o}. \tag{2.97}$$

The co-efficients A_m and B_m can now be expressed and so now the solutions arising from eqs. (2.80) and (2.81) are

$$y_1 = \frac{\mathrm{i}}{8\pi} J_m(\Gamma r)\, H_m^{(2)}(\Gamma r_o) \exp\{-\mathrm{i}k_z z_o + \mathrm{i}m\phi_o\} \tag{2.98}$$

$$y_2 = \frac{\mathrm{i}}{8\pi} H_m^{(2)}(\Gamma r)\, J_m(\Gamma r_o) \exp\{-\mathrm{i}k_z z_o + \mathrm{i}m\phi_o\} \tag{2.99}$$

where y_1 is valid in the domain $r \leq r_o$ and y_2 is valid in the domain $r \geq r_o$, or

$$\tilde{G}_\omega^{110}(k_z, m, r_s \,|\, \mathbf{x}) = \mathrm{i}J_m(\Gamma r_<)\, H_m^{(2)}(\Gamma r_>) \frac{\exp\{-\mathrm{i}k_z z_o + \mathrm{i}m\phi_o\}}{8\pi} \tag{2.100}$$

and

$$r_< = r_s, \quad r_> = r_o \quad \text{if} \quad r_s < r_o \tag{2.101}$$

$$r_< = r_o, \quad r_> = r_s \quad \text{if} \quad r_s > r_o. \tag{2.102}$$

Finally, the inverse Fourier transform of $\tilde{G}_\omega^{110}(k_z, m, r_s \,|\, \mathbf{x})$ is now taken (as defined in eq. (2.71)), resulting in an expression for the free-field frequency domain Green's function

$$\tilde{G}_\omega(\mathbf{y} \,|\, \mathbf{x}) = \sum_m \exp\{-\mathrm{i}m\phi_s\} \left(\int_{-\infty}^{\infty} \mathrm{i}J_m(\Gamma r_<)\, H_m^{(2)}(\Gamma r_>) \frac{\exp\{-\mathrm{i}k_z z_o + \mathrm{i}m\phi_o\}}{8\pi} \exp\{+\mathrm{i}k_z z_s\}\, \mathrm{d}k_z \right). \tag{2.103}$$

2.C Derivation of Far-field Expressions

Far-field expressions are derived as follows. A large argument approximation for the Hankel function of the second kind may be used - its asymptotic form is given in Abramowitz and Stegun (1972).

$$H_{-\nu}^2(\Gamma r_o) \approx \sqrt{\frac{2}{\pi \Gamma r_o}} \exp\left\{ \mathrm{i}\left(\frac{\pi}{4} - \Gamma r_o - \frac{\nu\pi}{2} \right) \right\}$$

The next step is to change from reception co-ordinates (used in the near-field) to emission coordinates. The latter is considered a more useful coordinate system for understanding far-field noise. This introduces two new variables - the meridional angle, θ and a propagation radius, $R = |\mathbf{x}|$. The method of stationary phase is then used to approximate the

integrals with respect to k_z in eqs. (2.39) and (2.47). A change in integration variable is made to γ by defining

$$\kappa\gamma = k_z$$

Our integral is then of the form

$$I_{k_z} = \int_{-\infty}^{\infty} g(\gamma) \exp\left\{\mathrm{i}\kappa|\mathbf{x}|h(\gamma)\right\} \, \mathrm{d}\gamma.$$

For both expressions for steady loading and thickness

$$h(\gamma) = -\gamma(M - \cos\theta) - \frac{\Gamma}{\kappa}\sin\theta, \quad \tfrac{\Gamma}{\kappa} = \sqrt{(1-\gamma M)^2 - \gamma^2} \tag{2.104}$$

The integral may then be approximated to

$$I_{k_z} = \tilde{g}(\gamma_s)\sqrt{\frac{2\pi}{\kappa|\mathbf{x}|h''(\gamma_s)}} \exp\left\{\mathrm{i}\left(\frac{\pi}{4} + \kappa|\mathbf{x}|h(\gamma_s)\right)\right\}$$

where γ_s is the stationary point and

$$\gamma_s = \frac{-\cos\theta}{1 - M\cos\theta}.$$

Therefore

$$h(\gamma_s) = -1, \quad h'(\gamma_s) = 0, \quad h''(\gamma_s) = \frac{(1 - M\cos\theta)^3}{\sin^2\theta}$$

2.D Conversion from Reception to Emission Coordinates

The open rotor coordinate system may be expressed in terms of reception (or physical) and emission coordinates. The convention here is to express reception coordinates using a cylindrical polar coordinate system and emission coordinates as a spherical polar coordinate system. Typically, reception coordinates are used for near-field results or data collected in a wind tunnel. Emission coordinates are used for far-field results or results collected form flyover experiments. The axial coordinate in both coordinate systems is coaxial with the engine axis.

The reception coordinate system is defined so that x is positive in the direction of the flow. r and ϕ represent a sideline radius and azimuthal co-ordinate respectively. The emission coordinate system instead uses R for radius and θ and ϕ as a polar and azimuthal angle respectively. Note that θ is defined as zero when the emission vector is pointing upstream, against the flow direction. It is useful to be able to convert between the two coordinate systems, so that comparisons can be made between both near- and far-field results. Conversions towards both coordinate systems (and any derivations) are presented here. Consider that in time τ an acoustic wave will have propagated distance R at the speed of sound c_0. In the same time the effect of the flow U_z will have caused the acoustic wavefront to have translated in the direction of the flow by a distance Δ. Thus

$$\tau = \frac{R}{c_0} = \frac{\Delta}{U_z}. \tag{2.105}$$

Reception coordinates x and r may be defined in terms of emission coordinates as

$$x = -R\cos\theta + \Delta = R\left(M - cos\theta\right) \tag{2.106}$$

$$r = R\sin\theta \tag{2.107}$$

since $M = U_z/c_0$ and therefore $\Delta = MR$. To convert from physical to emission co-ordinates, consider that

$$R^2 = (x - \Delta)^2 + r^2 = (x - MR)^2 + r^2 \tag{2.108}$$

which gives rise to the quadratic equation

$$\left(M^2 - 1\right)R^2 - 2xMR + \left(x^2 + r^2\right) = 0. \tag{2.109}$$

Solving this for R yields

$$R = \frac{xM \pm \sqrt{x^2M^2 - \left(M^2 - 1\right)\left(x^2 + r^2\right)}}{M^2 - 1} \tag{2.110}$$

Although there are two solutions, only the single root which yields positive values for R consistently is used; negative values of R are not physical here. Also, it may be shown that

$$\theta = \cos^{-1}\left(\frac{MR - x}{R}\right) \tag{2.111}$$

since, for the domain being considered ($0^\circ \leq \theta \leq 180^\circ$) the inverse function of cosine is used since it is exact.

Chapter 3

Model Scale Open Rotor Testing

In this chapter, a summary of the work conducted in collaboration with Rolls-Royce plc. is presented. Contributions from Rolls-Royce are highlighted where appropriate in this body of work. The model development presented here is the work of the author (which has been credited by citation when based on the work of others), however experimental data analysis was a collaborative effort. Certain data analysis may have been repeated at both the academic and industrial institutions for verification - however all analysis and figures presented in this chapter are original creations of the author. Much of this work has been published in Sureshkumar and Kingan (2012) and Parry et al. (2012).

3.1 Open Rotor Experiments

Rolls-Royce have conducted a number of scaled open rotor tests throughout the development phase of the open rotor. In some of these tests, near-field acoustic measurements are collected in a high speed wind tunnel at the Aircraft Research Association (ARA) test facility in Bedford, UK. It is necessary to collect data in the near-field due to the size of the tunnel. A photograph of the facility and one of Rolls-Royce's scaled open rotor test rigs, Rig 145, is shown in Figure 3.1. Collecting experimental acoustic data is a challenging task and there are many factors to take into account, such as effects of flow, reflections from nearby structures, reverberation and background noise. The experimental data is therefore analysed and interpreted in such a fashion that it may be made more comparable with the free-field prediction schemes. Measurement data collected from these tests has been used as part of the model validation process.

Much of the information regarding the tests, particularly specific information regarding blade designs, is the intellectual property of *Rolls-Royce* and thus cannot be disclosed in

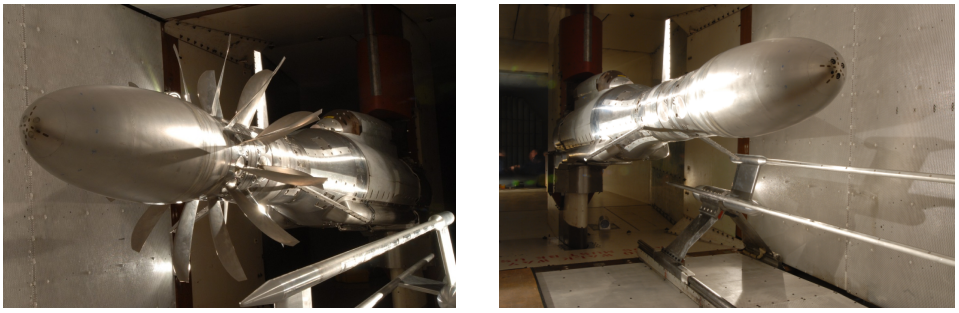

(A) (B)

FIGURE 3.1: Testing of Rig 145 Build 1 in the high speed ARA test facility.

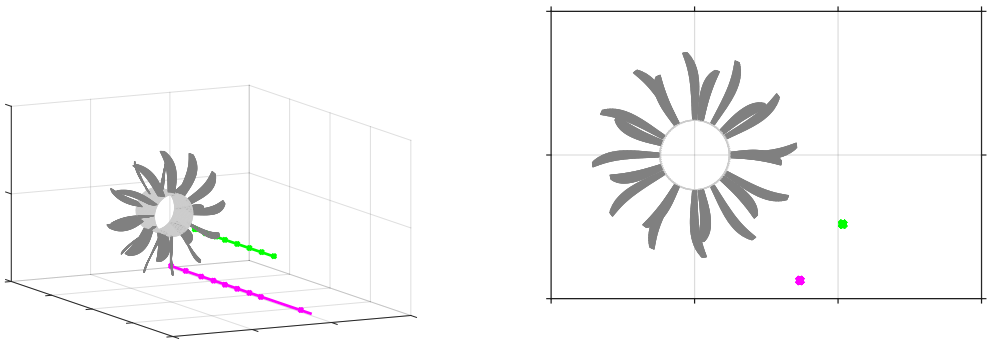

(A) (B)

FIGURE 3.2: Microphone positions in ARA Rig 145 Build 1 (2008) tests.

detail in this work. Results have been sanitised where there is a requirement to, however it is still possible to determine parametric relationships and general trends.

Data from ARA tests of Rig145 'Build 1' and 'Build 2' has been analysed. Rig 145 is a 1/6 scale open rotor test rig developed and operated by Rolls-Royce for aerodynamic and acoustic open rotor testing. Build 1 denotes a datum set of blades, which have since been aeroacoustically optimised and redesigned, remanufactured and labelled as Build 2.

The Build 1 tests used two microphone arrays at a fixed sideline distance from the open rotor, axially spanning upstream and downstream of both rotors (see Figure 3.2). The Rig 145 Build 2 tests had three microphone arrays (Figure 3.3), again at a fixed sideline distance from the open rotor with microphones spanning in both upstream and downstream directions from the open rotor test rig. The sideline distances of each microphone array are typically placed at points of interest to *Rolls-Royce*, such as the expected distance of a puller or pusher open rotor from the fuselage.

Further experiments were also conducted by *Rolls-Royce* and industrial partners in tests at the German-Dutch Wind Tunnels (DNW) test facility (see Figure 3.4). Data from

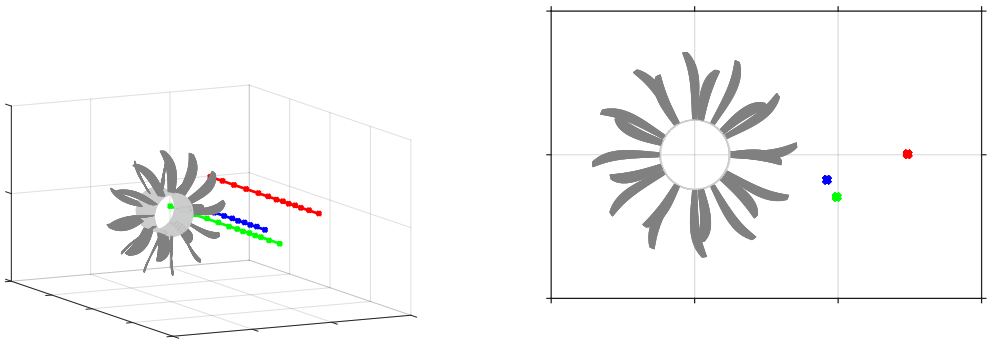

(A) (B)

FIGURE 3.3: Microphone positions in ARA Rig 145 Build 2 (2011) tests.

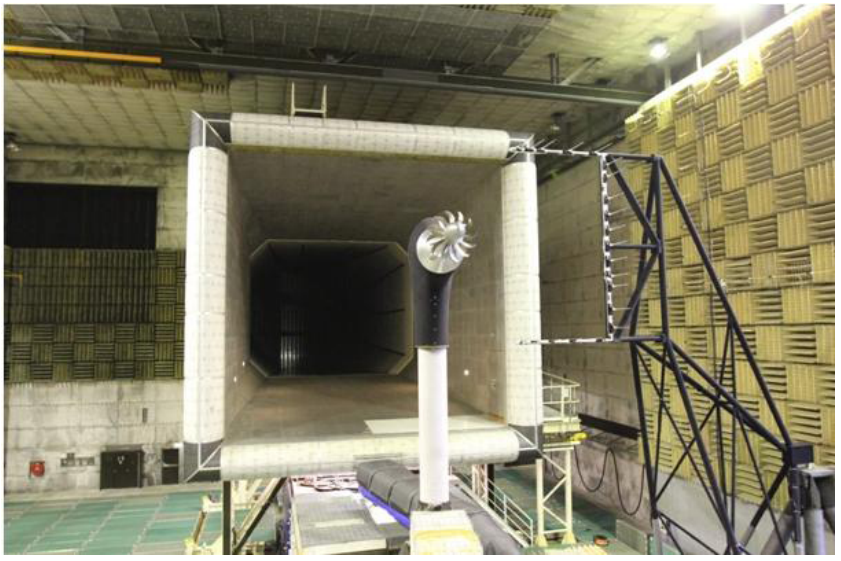

FIGURE 3.4: Testing of Rig 145 Build 1 in the low speed German-Dutch Wind Tunnels (DNW) test facility.

these tests will also be used for validation. These wind tunnel tests were used to study engine operation in the take-off and approach flight regimes, i.e. at lower flow speeds than ARA. Far-field and near-field flow data is available from these tests. The tests themselves have given significant insight into the acoustics of open rotors, as has been described in existing literature (see Parry et al., 2011). This experimental data will also be used with extrapolation methods derived later in this chapter as part of the data analysis.

3.2 Validation of Prediction Models

Model Implementation

The models described in Chapter 2 were found to be analytically similar to the formulations for near-field propeller noise provided in Parry (1988) and Hanson (1985*a*); it is a trivial process to recast a similar model described in this work to the expressions provided in those references since the formulations are essentially similar. As described in the previous chapter, the far-field models, which are generally used by the project sponsor and other associated research institutions, are analytically similar to the near-field expressions bar the use of a far-field approximation, which serves only to limit the far-field model's range of validity. As a verification for the implementation of the near-field models, results were compared with models implemented in independent research using far-field models generated using similar derivation techniques (Kingan and Self, 2011; Parry, 1988). An example of one such implementation is the noise prediction suite used by the project sponsor. In all test cases, the results were found to be quantitatively similar. Figure 2.7 is an example of one such comparison, but using a far-field model implemented by the thesis author. A similar comparison with independent models produced exactly similar results. These outcomes are an indication that the analytic models presented in Chapter 2 were implemented as expected, before use in the following analysis.

All the near-field models described in Chapter 2 require numerical evaluation of an infinite integral in k_x, the axial wavenumber (this integral may be evaluated analytically when the far-field approximation is used). In order to solve this integral, the formulations were coded into MATLAB and an adaptive Gauss-Kronod quadrature routine was used to solve the integral. This variant of Gaussian quadrature allows for error approximation and can also evaluate integrals with singular endpoints. This method of numerical integration is efficiently implemented in MATLAB as the *quadgk* function. Gauss-Kronod quadrature has been efficiently implemented and is readily available in other languages, for example it is available in QUADPACK and NAG Numerical Libraries for use with C and FORTRAN. The inevitable singularities in the integrand of the axial wavenumber integral mean that the numerical evaluation is actually the sum of three integrals, with the infinite limits and the two singularities forming the limits of each integration. In most cases, the integral limited by the two singularities is the biggest contribution to the sum, however this is not always the case so it is important to include the contribution from the other two integrals as well. The integrand tends to zero at each infinite limit.

Since Gauss-Kronod quadrature is adaptive, performance and error margins are dependent on the integrand being solved. Generally, an error tolerance of $1 \times 10^{-12}\mathrm{m}^{-2}$ was used when implementing the numerial integration routines for these near-field models in

MATLAB. The performance was thus conditional on the integrand itself which, depending on modelling parameters, might become highly oscillatory and thus take longer to solve with the requested error tolerance. In some cases during testing, the error tolerance was increased to $1 \times 10^{-6}\mathrm{m}^{-2}$, so as to improve performance, however performance was largely not an issue since, at the frequencies and operating conditions of interest, most free-field near-field computations solved in a reasonable time (at the most 2 or 3 minutes per observer point for the distributed source models). Varying the error tolerance one or two orders of magnitude from $1 \times 10^{-12}\mathrm{m}^{-2}$ had no noticeable difference on the result, thus the integration error tolerance was considered sufficient.

The following analyses in this chapter make use of noise measurements from the open rotor test rig experiments. Thus, the distributed source models (eqs. (2.38) (2.46) and (2.55)) are used for comparison. Note that these models also require integration over the distributed source region. As discussed in Section 2.6, broad parameters for the blade aerodynamics (e.g. lift and drag coefficients) are used in most cases and the thin blades are assumed to behave in a manner consistent with flat plate theory. In most cases, a half sinusoid lift distribution is applied, which makes the chord-wise integral analytically solvable, however it is trivial to solve this integral numerically for an arbitrary lift distribution. The radial integral is solved using a simple quadrature routine, again available as a function in MATLAB. Generally, during the bulk of this research, all comparisons with data and all results which required an accurate prediction made use of the distributed source model. Point source models were used to help understand propagation mechanisms and generate insight. For rotor-alone tones, a combination of the steady loading and thickness models are used. It is assumed shear noise is negligible for modern open rotor designs, particularly when the blades incorporate sweep (Peake and Parry, 2012). For interaction tones, only the viscous wake interaction model is applied, based on the assumption that potential field interaction is relatively weak for modern open rotor designs (Parry and Vianello, 2012; Peake and Parry, 2012).

Validation of Near-field Models

Data collected from the open rotor experimental campaigns described in the previous section are now used towards model validation. Predictions are made using blade geometries and rotor operating conditions tested during the campaign. In general, experimental and predicted sound levels appear to be similar but only for a specific range of the conditions tested and definitely only for a limited range of observer positions or tones. This leads to the conclusion that the main mechanisms of noise generation and propagation may be captured by these models, but that there are very likely some unmodelled assumptions or parameters which impedes the accuracy of the comparison. A description of potential unmodelled factors is provided alongside the data comparisons.

Note that, since the data represents noise from a test rig propeller, the analytic models used in the comparison are from the distributed source formulations. Conclusions from the data comparisons in this chapter lay the foundations for the reasoning behind research conducted in the later chapters of this thesis.

The near-field models will be validated against the high speed experimental data obtained at ARA. Only data from the Rig 145 Build 1 tests have been used for validation.

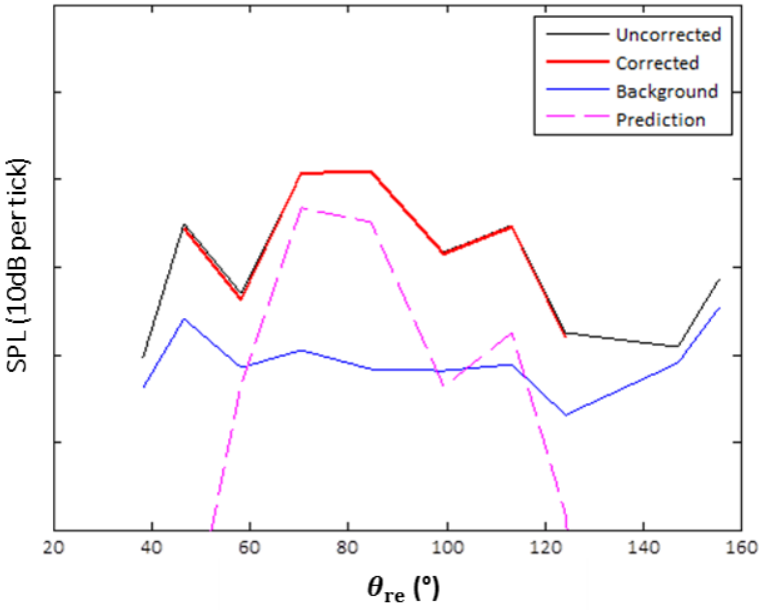

FIGURE 3.5: $\{1, 0\}$ tone SPL directivity for a climb-cruise regime transition case. Predictions are compared with experiments.

Figure 3.5 through Figure 3.8 show rotor alone tone sound pressure level (SPL) directivities from two different experiment test cases. The cases relate to an end of climb engine condition and cruise regime engine condition, meaning that different blade pitches, axial flow Mach numbers and thrusts are required in each case. The measured directivities produced from experimental data have been corrected for background noise and are shown along with a background noise directivity and the original (uncorrected) data.

In both cases, it was noted that the background noise level was as high as the broadband noise level from the measured spectra itself, so it is assumed that the wind tunnel background noise is louder than rotor broadband noise. It is likely that flow induced noise is the dominant component of background noise. Figure 3.9 shows measured and flow-only (background noise) spectra at various microphone positions for the end of climb case. The same set of data is presented for the cruise case in Figure 3.10. The data was corrected by deleting the broadband noise level, which was obtained using a moving median filter. Note, that if background noise is within 5dB of the noise measurement level, then the result is considered contaminated and removed from the corrected directivity.

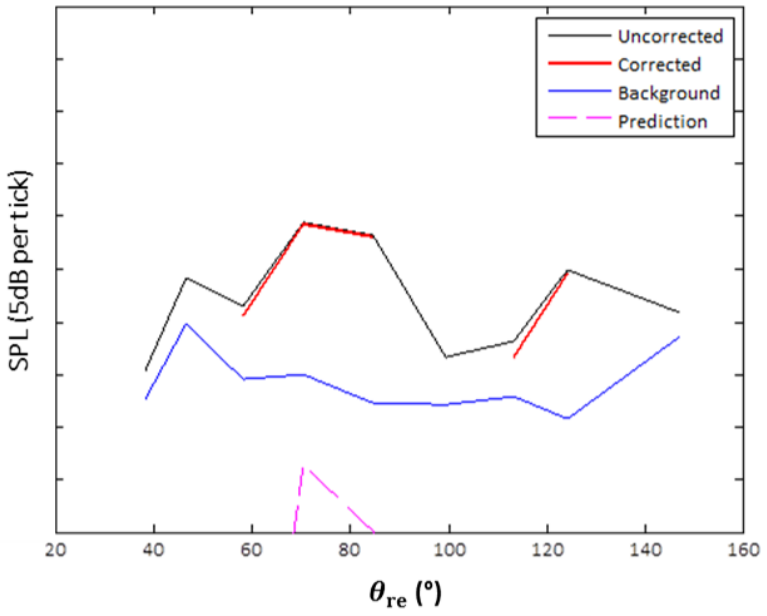

FIGURE 3.6: $\{2,0\}$ tone SPL directivity for a climb-cruise regime transition case. Predictions are compared with experiments.

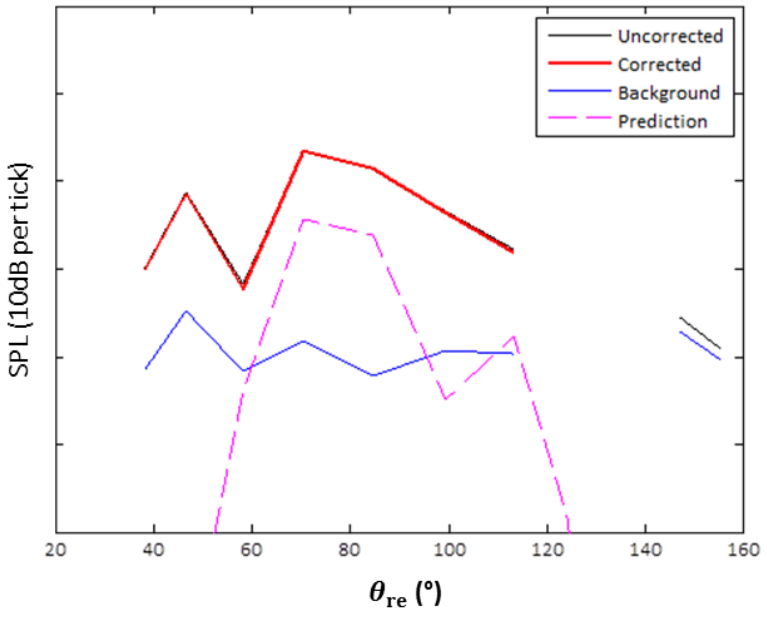

FIGURE 3.7: $\{1,0\}$ tone SPL directivity for a climb regime case. Predictions are compared with experiments.

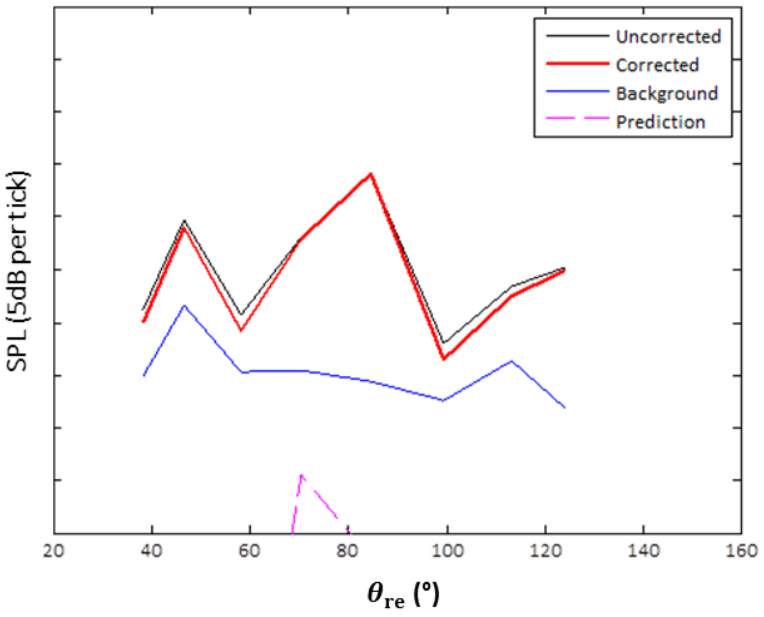

FIGURE 3.8: $\{2,0\}$ tone SPL directivity for a climb regime case. Predictions are compared with experiments.

Figure 3.5 shows the directivity of the first, front rotor alone tone for an end of climb regime test case, for which there is an axial flow Mach number of 0.57. Figure 3.6 shows the second, front rotor alone tone for the same case. There is a discrepancy between prediction and experiments for both cases, which is significantly larger for the second harmonic tone. For the fundamental tone the directivity is quite similar, particularly at measurement points close to the plane of the rotor (where the discrepancy is at a minimum). Note that the second harmonic tone is at a higher frequency. It is speculated that a) the increased frequency reduces the near-field region of this tone and so b) a number of the measurement positions are sat in the reverberant field of the wind tunnel, which is more prevalent outside the near-field region. This also explains the increasing discrepancy away from the plane of the rotor and the relatively flat shape of the directivity from measurements (presumably due to cut-on noise).

The same behaviour is noted in the results from the cruise regime case, for which there is an axial flow Mach number of 0.75. Figures 3.7 and 3.8 show the first and second front rotor alone tone SPL directivities respectively. The prediction for the first front rotor-alone tone is a much better match to experiments when compared with the second rotor alone tone. However, a slightly larger discrepancy is noted than in the previous lower Mach number case. Note that the directivities are best matched in shape and level in the region around the plane of the rotor. These differences due to flow Mach number and emission angle, as well as the discrepancy in general, could again be explained by tunnel reverberation. The higher speed case would again have a reduced near-field region, perhaps explaining the greater discrepancy, since measurement positions may show more contamination as a result of a more equal ratio between the level of the

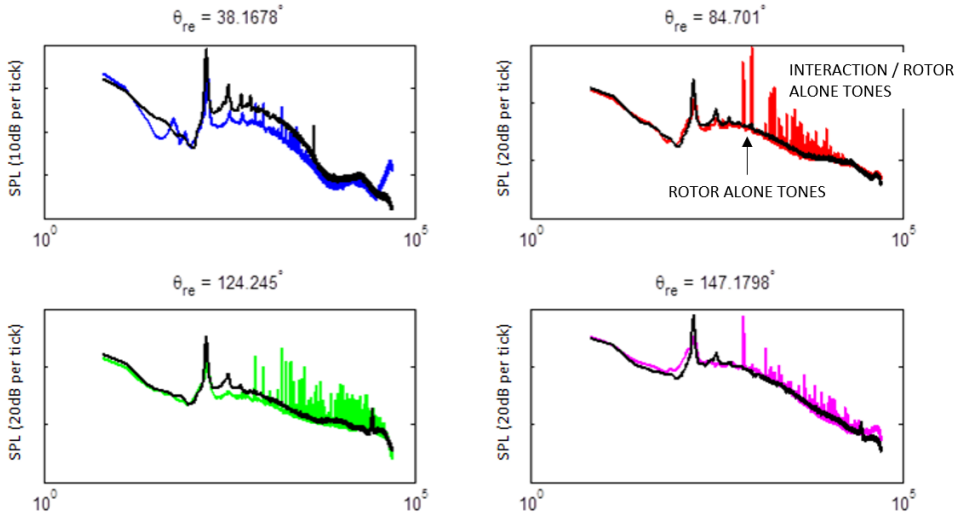

(A)

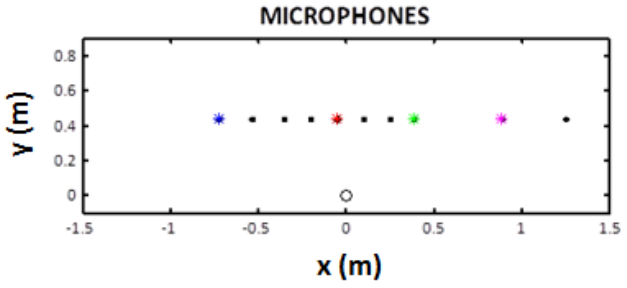

(B)

FIGURE 3.9: Measured spectra at various microphone position for the climb-cruise regime transition case. The spectra are coloured to match the microphone they relate to and are compared with the appropriate flow-only spectra (shown in black).

direct noise field and reverberant noise field. This explanation is discussed in much more detail in Chapter 4, which specifically concerns wind tunnel reverberation.

Figure 3.11 shows the first rear rotor alone tone for the cruise regime case. In these results, the prediction actually over-predicts the levels seen from experiments. It is speculated that this could be due to inaccuracies in the aerodynamic input, which is harder to predict for the rear rotor. The rear rotor has a complex flow structure impinging on it yet in this case is calculated by a relatively simple aerodynamic tool. It is plausible that if improved aerodynamic input were available a better match between predicted and experimental noise levels could be achieved.

The discrepancies seen between measured and predicted noise levels could also be due to a number of other factors. Flow distortions caused by other objects in the wind tunnel or from a non-uniform axial inflow could cause unmodelled effects on the measured sound field. As stated previously, reverberation from the wind tunnel walls could also have an effect on the noise levels recorded in experiments. Acoustic lining was used on the

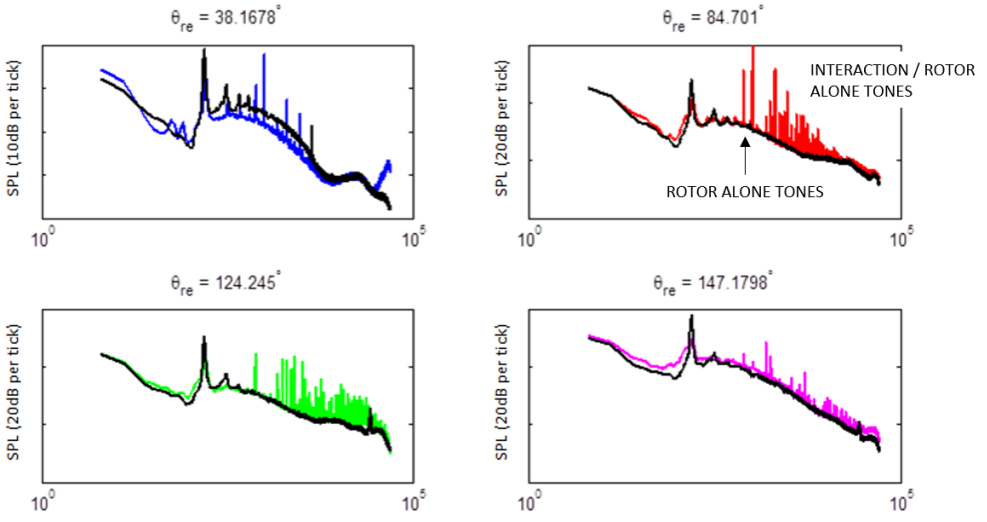

(A)

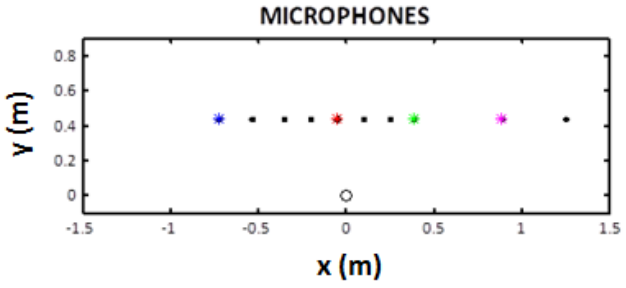

(B)

FIGURE 3.10: Measured spectra at various microphone position for the cruise regime case. The spectra are coloured to match the microphone they relate to and are compared with the appropriate flow-only spectra (shown in black).

walls of the test section at ARA when Rolls-Royce conducted their experiments. It was specifically designed for this purpose (Wood and Newman, 1990) and used for the first set of scale open rotor tests conducted in the late 1980s (Kirker, 1990). However, analysis outlined in Wood and Newman (1990) suggests that the lining could become less effective with increasing axial inflow Mach numbers. Note that an analytic model to predict noise in a reverberant rectangular duct is presented in Chapter 4 in order to assess if reverberation is a problem in the ARA test facility, and how much of an effect this could have on the measured sound field.

Validation of Far-field Models

Measurement data from the experimental campaigns at DNW has been used to validate far-field models. Tone directivity comparisons between far-field noise prediction methods and two experimental data cases are presented. Both cases are on the same working line, however relate to a take-off and approach engine condition.

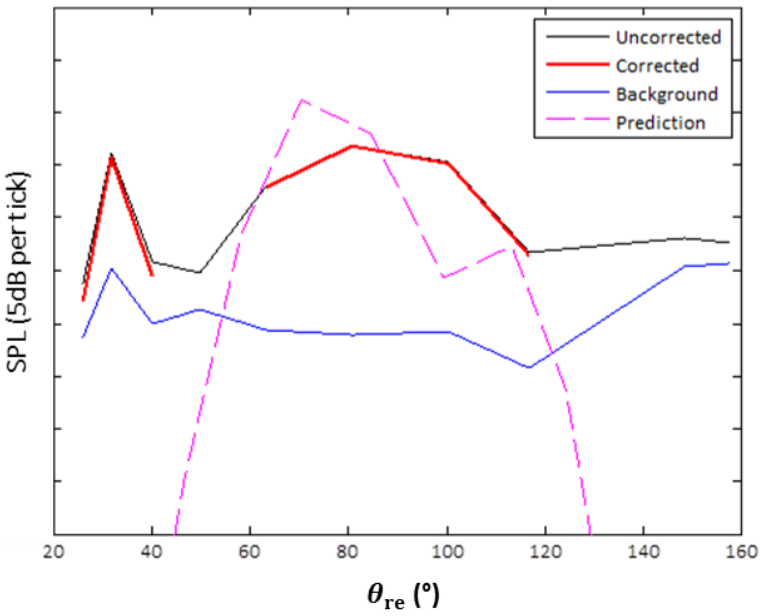

FIGURE 3.11: $\{0, 1\}$ tone SPL directivity for a cruise regime case. Predictions are compared with experiments.

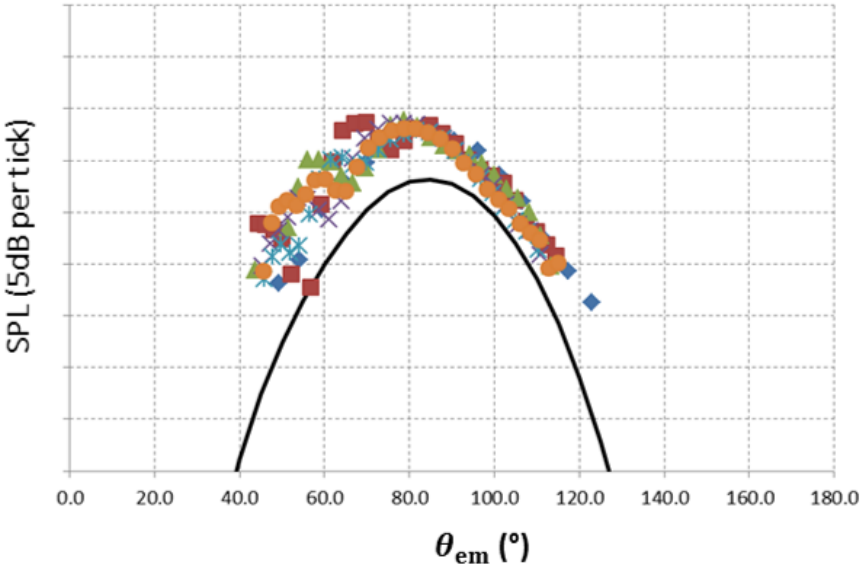

FIGURE 3.12: $\{1, 0\}$ tone SPL directivity for a take-off case. Predictions are compared with experiments. Markers represent measured data polar directivities, with each marker typre representing a different azimuthal position. A solid black line represents a rotor alone tone prediction.

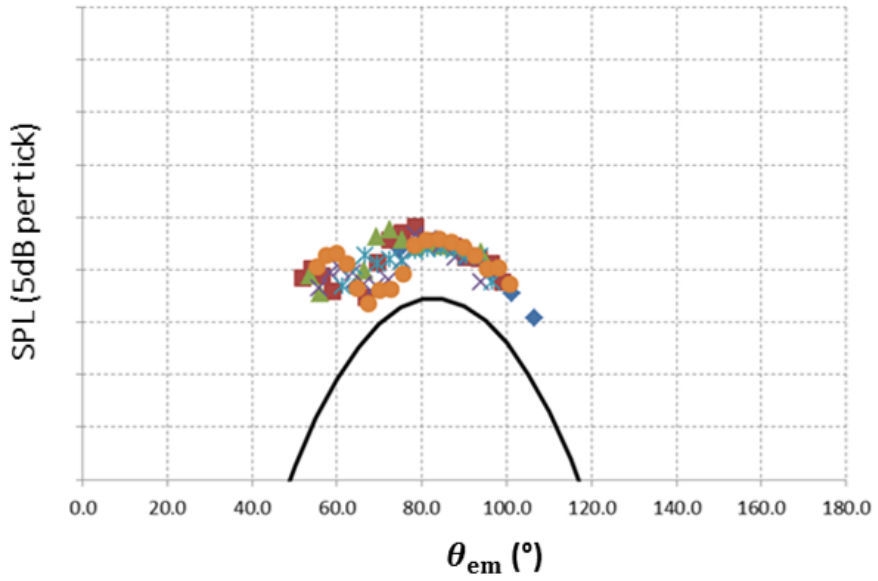

FIGURE 3.13: $\{1,0\}$ tone SPL directivity for a cutback case. Predictions are compared with experiments. Markers represent measured data polar directivities, with each marker typre representing a different azimuthal position. A solid black line represents a rotor alone tone prediction.

These directivities are observed at a far-field observer array. Figures 3.12 and 3.13 show first front rotor-alone tone directivities for a take-off and cutback case respectively. The directivities for both experiments and predictions are similar, although there is some discrepancy between the levels. The discrepancy could be a result of inaccurate aerodynamic data used as input to the code or due to unmodelled factors affecting the final result, for example factors such as centrebody scattering, pylon wake interaction and inflow distortion.

Comparisons are also made with interaction tone directivities. Figures 3.14 and 3.15 show the predicted and measured directivities for the $\{1,2\}$ interaction tone for the same cases. Figure 3.14 relates to the take-off case. The fieldshapes are in general a good match but again there are minor discrepancies for the levels. Again such errors could be due to an inaccurate estimation of aerodynamic performance. Accurate estimation or calculation of the aerodynamics is necessary since much of the noise is generated by viscous wake interactions, which in turn affect the blade loading. It is also possible that there are unmodelled factors to consider - the prediction methods do not take account for centrebody scattering, which has shown to be a significant component of noise for some interaction tones in Chapter 5. Centrebody scattering seems a plausible factor for the discrepancy in the interaction tone directivities because the shape of the directivity has changed, which could be caused by the interference of the direct and reflected noise fields at these observer points. It is also plausible there are other scattering effects to consider, including shear layer diffraction (a large shear layer exists between the tunnel jet and ambient medium in the remainder of the facility). This factor is made more plausible by the fact that the large discrepancy exists only in the forward arc of the propeller, where

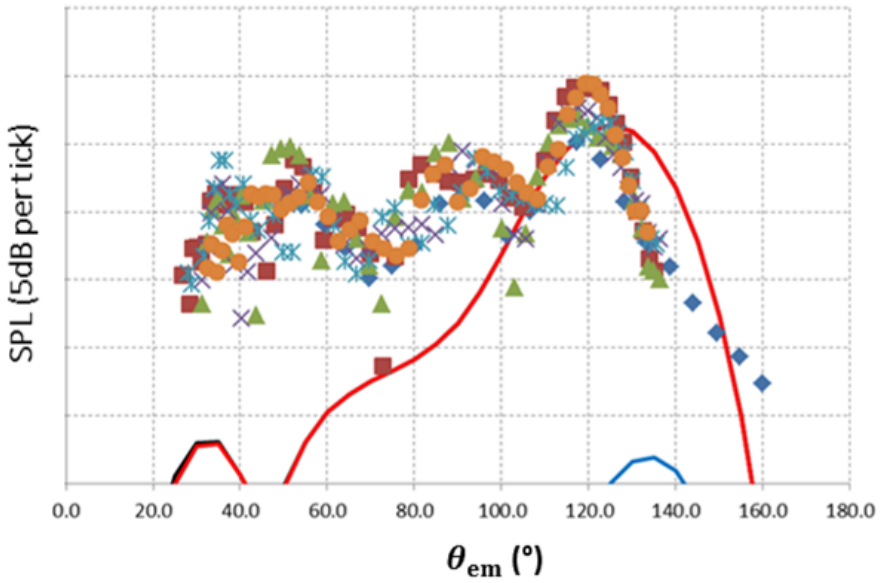

FIGURE 3.14: $\{1, 2\}$ tone SPL directivity for a take-off case. Predictions are compared with experiments. Markers represent measured data polar directivities, with each marker typre representing a different azimuthal position. A solid red line represents a viscous wake interaction tone prediction, found to be the dominant interaction noise source.

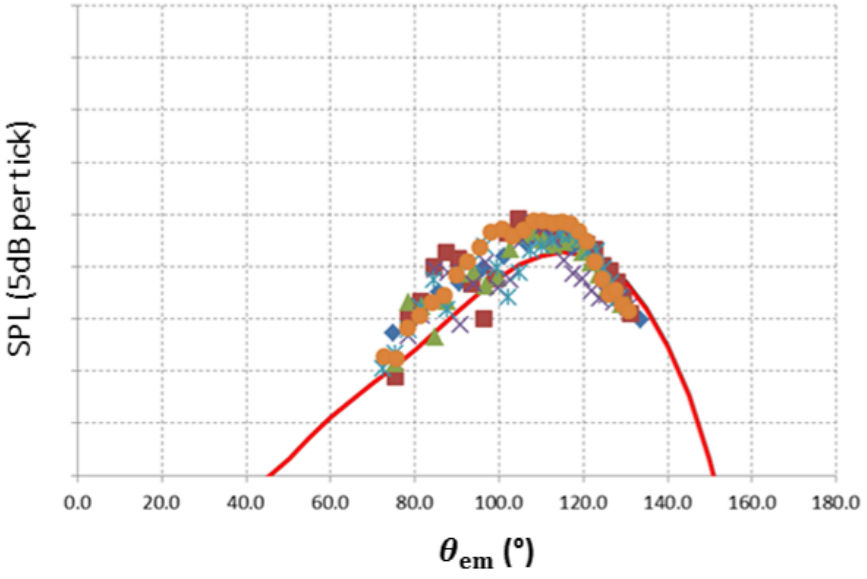

FIGURE 3.15: $\{1, 2\}$ tone SPL directivity for a cutback case. Predictions are compared with experiments. Markers represent measured data polar directivities, with each marker typre representing a different azimuthal position. A solid red line represents a viscous wake interaction tone prediction, found to be the dominant interaction noise source.

noise would propagate into the flow which would further exacerbate any shear layer diffraction effects. Note these are all merely suggestions for why the analytic models and experimental data are not similar across the whole directivity.

3.2.1 Projection methods

A method for projecting rotor tone acoustic pressures from one location to another, and valid in the rotor near-field, is now presented. This is a useful technique since data from computations or experiments may only be captured in the near-field — the projection methods can be used to predict what the sound may instead be at far-field distances. A special method is required, since sound pressure in the near-field does not decay with distance in a similar fashion as in the far-field (proportional to r). There are high amplitude, rapidly decaying pressures in the near-field which these projection methods take account of. Two extrapolation methods are presented and compared.

The measurement data from open rotor experimental campaigns shall again be used to validate and test the proposed methods. Much of the analysis will focus on tests conducted at the ARA, where the limited size of the wind tunnel means acoustic results were collected in the near-field. As previously mentioned, collecting acoustic data experimentally is fraught with many complications and there are many factors to consider, such as effects of flow distortions, reflections from nearby structures, reverberation and background noise.

The ARA tests are the only available source of experimental data at cruise conditions available to the author and so developing an accurate projection method is necessary in order to assess cruise noise in the far-field. Extrapolation to the far-field provides a metric which may be easily subjected to spherical spreading type propagation, used as input for aircraft structure interaction models or even passed into atmospheric propagation models, which may ultimately be used to calculate en-route noise. The methods are also useful in comparing results from Build 1 and Build 2 tests conducted at ARA, since one must account for the possible differences in microphone positions used between each test.

The ‘Approximate’ Transfer Function

Peake and Boyd (1993) suggest the use of a transfer function to project acoustic pressures to an alternate observer location. It is shown in Parry and Crighton (1989) that the noise from a propeller is dominated by contributions in the region of a single radial station — and in subsonic operating conditions this station is located at the blade tip. This approximation for subsonic operating conditions is acceptable for the tone created at the blade passing frequency and the range of the contributing region diminishes with

increasing harmonics, meaning the approximation becomes even more accurate when considering them.

In light of this, an exact point force method is used for comparison with near-field data. The strength of the point force F is kept variable so that it may be adjusted to best match the data to be projected. The force strength obtained from the data fit is then used in a point force method with a different observer position to establish an estimate pressure at that particular location. A far-field point force expression derived using asymptotic methods can be used with credible results if the projection is to be made into (or from) the far-field. This would be used in place of the equivalent near-field expression. Derivations of free-field point force expressions can be found in Section 2.3. Note that using a point force for the transfer function makes the assumption that steady loading is the dominant contributor to rotor-alone tones, which holds in many cases.

In order to define a suitable transfer function, an equivalent force strength should be determined. The appropriate value of F is determined by performing an unconstrained search for the minimum of a simple cost function

$$E = \sum_{n=1}^{N} \left(P_m^n - F P_{upf}^n \right)^2$$

where P_m denotes the acoustic pressure obtained from measurements, P_{upf} denotes the acoustic pressure due to a representative unit point force and the index n determines a particular microphone of N microphones. In this way both a single microphone or an array of data can be used for force strength matching. In the analysis performed on experimental data in this chapter, the sound pressure is matched to each microphone in turn. This is then projected to the required sideline distance, at a constant reception angle. The Mach radius is a function of observer angle and should be conserved, so that the dominant source radius does not change (see Section 3.B).

Point Forces and Point Acoustic Doublets

The application of rotating point forces at a single radius is a good approximation for steady loading noise sources. However when one considers the approximation of thickness noise sources, it is more appropriate to use rotating acoustic doublets at a single radius and aligned parallel with the rotor blade. Derivations of free-field rotating point sources are presented in Section 2.3. The expression for an acoustic doublet may be derived by taking the expression for a rotating monopole (see eq. (2.26)) and taking the (non-dimensional) chordwise derivative so that

$$\frac{\partial p}{\partial \tilde{X}} = \frac{\partial p}{\partial z_s} \cos\alpha + \frac{\partial p}{\partial \phi_s} \frac{\sin\alpha}{r_s} = \left[\frac{\mathrm{i}m \sin\alpha}{r_s} - \mathrm{i}k_z \cos\alpha \right] p \tag{3.1}$$

which means, after following through the formulation, the final expression would be

$$\frac{\mathrm{d}p}{\mathrm{d}\tilde{X}}(\mathbf{x},t) = \frac{\mathrm{i}\rho_0 Q_0 c_0 I_{k_z}}{8\pi} \exp\left\{-\mathrm{i}m\phi_o + \mathrm{i}m\Omega t\right\} \tag{3.2}$$

where

$$I_{k_z} = \int_{-\infty}^{\infty} \left[\kappa - k_z M\right] \left(k_z \cos\alpha - \frac{m\sin\alpha}{r_s}\right) J_{-m}\left(\Gamma r_<\right) H^{(2)}_{-m}\left(\Gamma r_>\right) \exp\left\{\mathrm{i}k_z z_0 - \mathrm{i}k_z z_o\right\} \mathrm{d}k_z. \tag{3.3}$$

(A) (B)

FIGURE 3.16: A "source" and "sink" monopole of infinitesimal separation (a) are axially aligned with the blade stagger angle (b) (as is the incoming flow). The figure in (a) is a representation of what has been termed here an acoustic doublet, with the arrows schematically indicating plausible streamlines between the "source" and "sink" monopoles.

An acoustic doublet is essentially the co-location of a source and sink monopole, since flow around a blade can be said to consist of source monopoles along the section of the chord with increasing thickness and sink monopoles when the thickness is decreasing. Figure 3.16 represents this approximation.

The expressions for rotating acoustic doublets and rotating point forces are compared to full steady loading and blade thickness source distributions in Figure 3.17. Realistic geometries and flow conditions are used. The graphs show that the acoustic doublet approximation is a better match for thickness sources, whereas the point force approximation is better suited for steady loading. The discrepancies between the relevant approximation and evaluation pair are due to phase interferences between sources in the full distribution, which slightly alter the overall directivity.

The 'Exact' Transfer Function

Brouwer (2010) notices that the formulations for acoustic pressures contain only a single term which is reliant on the sideline distance co-ordinate, r_o. Exploiting this property allows a term independent of r_o to be defined, which can be used in turn to project

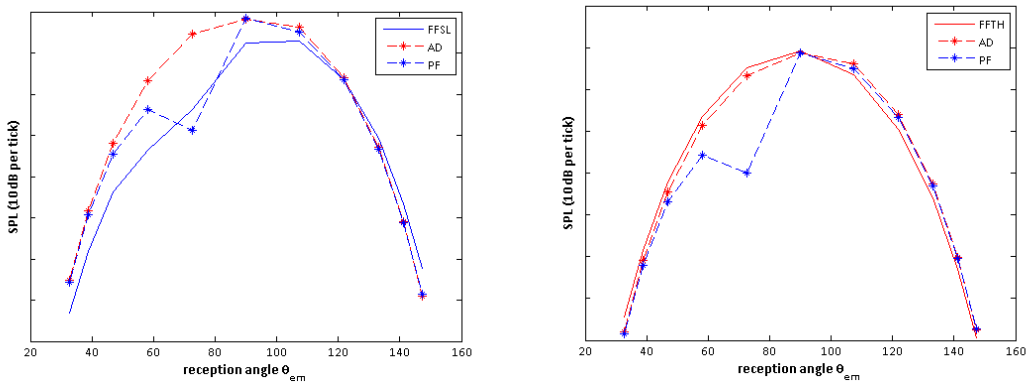

(A) (B)

FIGURE 3.17: Comparison of directivities of an acoustic doublet and point force with (a) a full far-field steady loading expression and (b) a full far-field thickness expression. The graphs show that a point force is better suited to approximating steady loading noise, whereas the acoustic doublet yields better approximations for thickness noise.

any data from one sideline distance to another. Note that this method does not limit the source definition, and therefore is not limited to a specific or even combination of specific sources. However the method does require the spatial Fourier transform of data across the infinite span of the propeller axis and thus limiting this range or discretizing the data will clearly affect the accuracy of the method.

As an example, the method is applied to an exact formulation for propeller thickness noise. Starting with a formula for thickness acoustic pressure (eq. (2.38)) valid outboard of the propeller tip we have

$$p\left(\mathbf{x},t\right)=\frac{\rho c_0 BbU_r}{8\pi}\sum_{m=-\infty}^{\infty}\int_{r_h}^{r_t}\exp\left\{\mathrm{i}\nu\phi_o\right\}\exp\left\{\mathrm{i}\omega_m t\right\}I_{k_z}\,\mathrm{d}r$$

$$I_{k_z}=\left[\kappa-k_z M\right]J_{-\nu}\left(\Gamma r_s\right)H_{-\nu}^{(2)}\left(\Gamma r_o\right)\exp\left\{-\mathrm{i}k_z z_o\right\}\exp\left\{-\mathrm{i}k_s\right\}\mathrm{i}k_z\Psi_T\,\mathrm{d}k_z.$$

Note that, for a specific value of m, this formula is of the form

$$p_m\left(\mathbf{x},t\right)=\frac{1}{2\pi}\int_{-\infty}^{\infty}\tilde{p}_m\left(k_z,\phi_o,r_o,t\right)\exp\left\{-\mathrm{i}k_z z_o\right\}\,\mathrm{d}k_z$$

where

$$\tilde{p}_m(k_z,t) = \frac{\rho c_0 BbU_r}{4} \int_{r_h}^{r_t} \exp\{\mathrm{i}\nu\phi_o\} \exp\{\mathrm{i}\omega_m t\} [\kappa - k_z M] \\ J_{-\nu}(\Gamma r_s) H_{-\nu}^{(2)}(\Gamma r_o) \exp\{-\mathrm{i}k_s\} \mathrm{i}k_z \Psi_T \, \mathrm{d}k_z \quad (3.4)$$

which describes a spatial Fourier transform of pressure in the axial direction. At a single frequency, for a pressure observation at any given observer location A, p_m^A, and observer location B, p_m^B, the formulae are essentially the same except for in the argument of the Hankel function. Therefore we can say

$$\frac{\tilde{p}_m^A}{H_{-\nu}^{(2)}(\beta r_o^A)} = \frac{\tilde{p}_m^B}{H_{-\nu}^{(2)}(\beta r_o^B)}$$

Clearly then, if the spatial Fourier transform of the pressure at one location is available then this can be used to derive a value at another location, which in turn may be used to calculate the acoustic pressure levels by an inverse Fourier transform. Essentially we can write that

$$p_m^B(\mathbf{x},t) = \frac{1}{2\pi} \int_{-\infty}^{\infty} \tilde{p}_m^A(k_z,t) \frac{H_{-\nu}^{(2)}\left(\beta r_o^B\right)}{H_{-\nu}^{(2)}(\beta r_o^A)} \exp\{-\mathrm{i}k_z z_o\} \, \mathrm{d}k_z$$

The inverse Fourier transform is given by

$$\tilde{p}_m(k_z,\phi_o,r_o,t) = \int_{-\infty}^{\infty} p_m(\mathbf{x},t) \exp\{\mathrm{i}k_z z_o\} \, \mathrm{d}z_o.$$

A simple study is presented, using the two extrapolation methods. The methods have been used on a near-field point force prediction, the results of which are shown in Figure 3.18. Both are then compared to a near-field prediction at the same projection distance, and as might be expected both methods have projected the data very accurately. However to assess the robustness of both methods they are now tested using input data of varying quality.

The robustness of each of the methods is assessed using data derived from theoretical methods. This data was adjusted to include randomly generated noise, since it is expected that any experimental data could be contaminated by various sources of noise and other acoustic effects. A number of parameters were assessed, such as the strength of background noise, the number of axial points of data available, measurement or signal noise and the axial range of recorded data. As part of the assessment, near-field data was

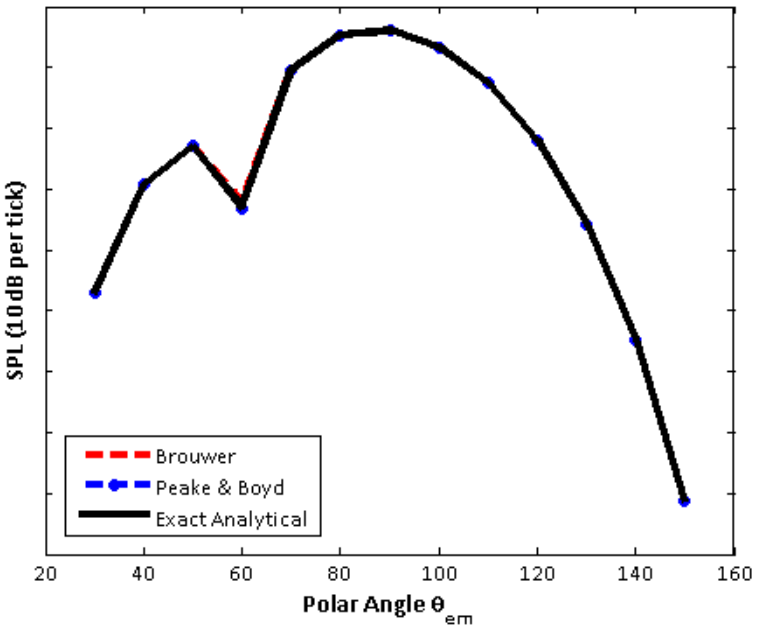

FIGURE 3.18: Comparison of the methods based on Peake and Boyd's approximate transfer function, Brouwer's exact transfer function and an analytical point force method evaluated at the projected observer locations.

calculated using the models described earlier, at a sideline distance one rotor diameter from the hub. Predictions were made for the tone noise generated by a generic propeller in isolation. A number of calculations were made at this sideline distance and with varying axial location, which would be equivalent to the position of observers or microphones in this 'virtual' experiment. Background noise was added to a level approximately 20db below the peak 'measured' noise. This limited the range of data that would remain sufficiently uncontaminated and thus be suitable for projection. Figure 3.19 shows the theoretical prediction of a rotor-alone tone directivity and its contamination.

A threshold is applied at 3dB above the sound pressure level of background noise, to remove data that was seriously contaminated by noise. The remaining data was then passed to the two projection methods as input. Both the range and smooth nature of the original tone directivity have been diminished by these adjustments.

The results of projecting this data to the far-field, using both methods is shown in Figure 3.18. In this particular case, both projection methods have worked well, since the directivities largely match. In this case, a high number of locations were used as input, representing a large number of microphones, a small amount of signal noise was applied and the background noise was 20dB lower than the peak, which is relatively small. All of these conditions are actually quite favourable.

In fact, when varying these conditions, it was found that the ability of these methods to match predictions significantly reduced. The point force approximation method is very

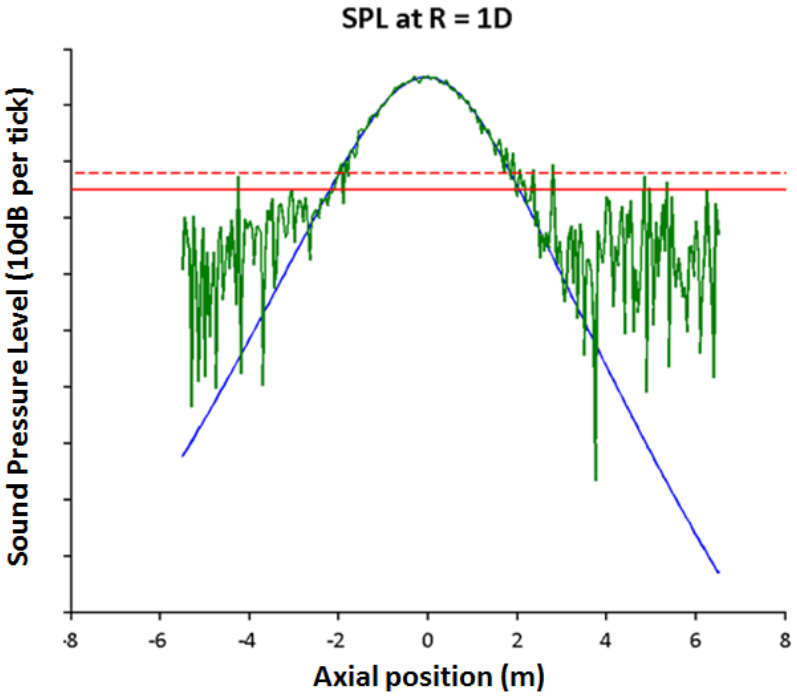

FIGURE 3.19: Theoretical prediction for a rotor-alone tone. The original directivity is shown in blue. Noise has been overlayed so as to simulate imperfect data (green). The mean level of background noise is shown (red), as well as a selected threshold (dashed red) which was used to filter out highly contaminated data.

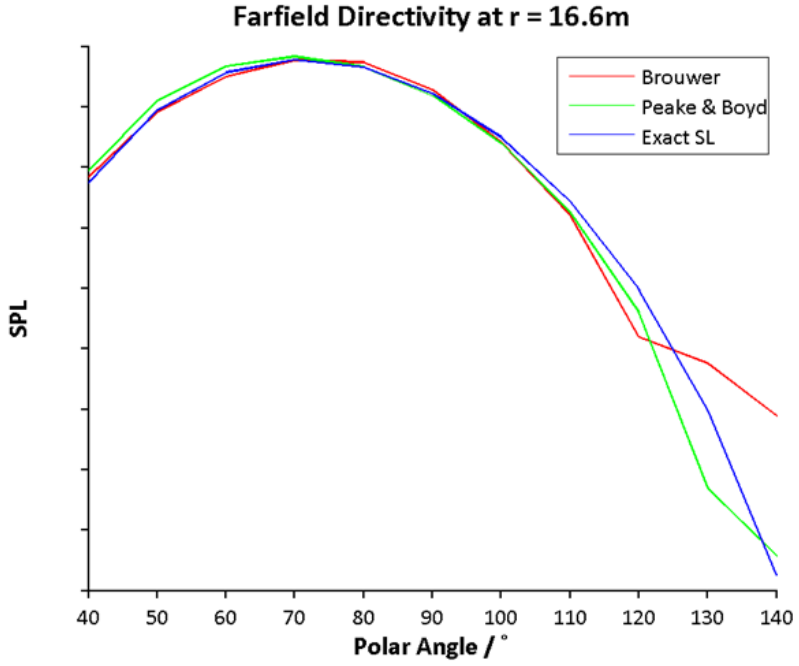

FIGURE 3.20: Projections to the far-field using each of the projection methods, along with an equivalent far-field prediction for steady loading noise.

robust, as increases in noise and reductions in the range and amount of input data in most cases do not prevent the method from matching to far-field prediction levels. The method is suited to producing estimates particularly when input data is low quality and sparse. The method does not account for a distribution of sources and in fact the use of a point force assumes that loading terms are the most dominant contribution. In some cases it could be the thickness component that dominates, and thus an acoustic doublet should be used instead.

The exact method, as indicated by Brouwer (2010), can effectively project an exact description of sources, since sources do not need to be defined. However, this means other noise sources, such as background noise, or reflections, will be projected as well. For this reason, the method does not cope well with high levels of background or measurement noise. The method also struggles with data that does not have a large axial extent or is very sparse, since this will in turn affect the accurate computation of the axial Fourier transform that is required. Although this method should technically be able to produce more accurate results after projection, it is expected that the method will fail to produce reasonable estimates when projecting experimental data, for which background noise is high and microphones are sparsely positioned. The method also requires instantaneous acoustic pressures, which is lost when data is converted to sound pressure levels. Currently, data from experiments is only available as sound pressure levels which prevents appropriate use of this projection method at this time. Further analysis of this method will be conducted as more data becomes available.

3.3 Projection of Measured Data

The effectiveness of the extrapolation method described by Peake and Boyd's 'approximate' transfer function is demonstrated on experimental data. We consider data at three different sideline distances, which coincide with the location of axially aligned microphone rails from ARA Build 2 open rotor experiments. These microphone locations are shown in Figure 3.3.

In the first instance, we consider projections of the $\{1, 0\}$ rotor-alone tone. Projections are made using a point force located at the blade tip and with a matched force strength. Applying the projection method to the original experimental data yields the results shown in Figure 3.21.

Experimental data is displayed with stars connected by a solid line, whilst projected data is shown with circles connected by a dashed line. The colours indicate a rail at a particular sideline distance, and in fact match the rail colourings shown in Figure 3.3, the 3D plot of microphone locations in ARA Build 2 tests. The colour of the projected data indicates the rail towards which the projection was made, i.e. projection data in

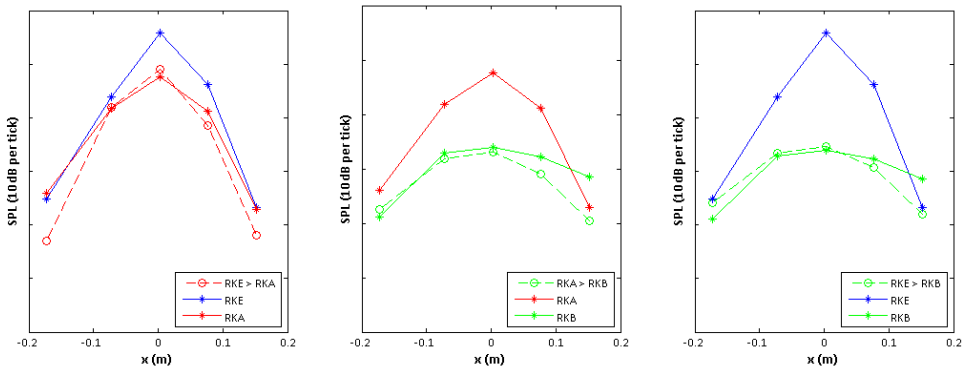

(A) (B) (C)

FIGURE 3.21: Rotor-alone tone directivities from ARA Build 2 experiments. It is assumed steady loading is the dominant source of noise. The diagrams show experimental data (starred markers and solid line) and projections (circular markers and dashed line). Projections are coloured according to the rail they are projected to. Each of the colours reflects the rails depicted in Figure 3.3. (a) Projection from rail RKA to RKE, (b) projection from rail RKE to RKB and (c) projection from rail RKA to RKB.

red indicates a projection made to rail RKA, whereas experimental data captured at RKA is also coloured in red.

It is expected that discrepancies between projected and measured values are due to reverberation effects present in the wind tunnel. However the projected directivity is on the whole a good estimate of the measured equivalent. Note the limited axial extent of the projected arrays - it is expected that with axial distances further from the rotor plane, tunnel reverberation effects would be more prominent and thus the projected estimates may not be as accurate. Determining the effects of reverberation or any flow distortions in the wind tunnel is not the focus here, however a study to determine its importance is included in Chapter 4. Projections are also made using the levels for the $\{1, 1\}$ interaction tone. In this case, the dominant component of noise is expected to be a result of the viscous wake of the front rotor impinging on the rear rotor. A near-field point force expression similar to the one outlined above, but with a loading distribution appropriate for viscous wake calculations, was thus derived. Due to the counter-rotation of the propellers, the effective mode speed of the tone can be much higher and thus the Mach radius could be located inboard of the propeller tips. If the Mach radius lies on the propeller blade, this becomes the dominant source radius and thus the radius to use for the point force transfer function. It is also apt to point out that the Mach radius is a function of the observer angle. When evaluating different positions and hence observer angles, the Mach radius (and thus dominant source radius) will change. Projections must be made with a point force transfer function defined using the appropriate source radius.

In some cases, the Mach radius may move inboard of the propeller hub, where it becomes difficult to determine a single dominant source radius. Determining a dominant radius

becomes more complicated because for these particular cases the field scattered by the hub becomes an important consideration as well. However, as the Mach radius moves further inboard, towards the origin, near-field effects become more negligible. It becomes acceptable to use a far-field expression. Pressure evaluated by the far-field expression is inversely proportional with radius and so this relationship can be used to project the pressure to an alternate sideline.

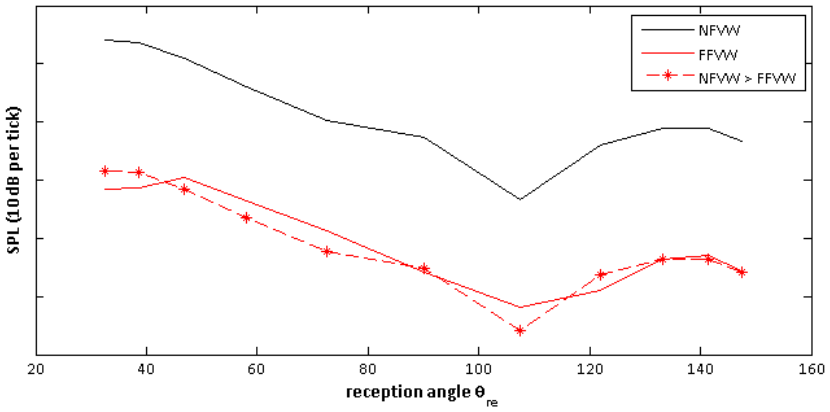

FIGURE 3.22: Prediction of the viscous wake component of interactions tones. Both the incident and centrebody scattered field have been included. Predictions have been produced with a near-field model and then a far-field model at points further afield. A point force method has been used to project between the near-field and far-field data points, which assumes a far-field rate of decay i.e. 1/r.

This approximation has been demonstrated on predictions for a {1,1} interaction tone. Interaction tones are typically expected to display minimal near-field effects, which can be explained by the location of the Mach radius. Figure 3.22 shows predictions at two different sideline distances along with a projection from one sideline array to the other. The projection is displayed with starred markers and a dashed line, where the colour indicates the array to which the projection was made. Since the Mach radius is well inboard of the hub for this case, a decay rate proportional to $1/r$ has been used, and as the graph shows this is a suitable approximation to make. To further clarify the suitability of this approximation, refer to Figure 2.9, which shows the far-field and near-field solutions of acoustic pressure from a viscous wake interaction source, and its relationship with increasing sideline distance.

Projections were also made using experimental data for the {1,1} interaction tone, which are shown in Figure 3.23. Data that is too close to background noise levels have been considered contaminated with noise and removed from the directivities.

The same convention as previously has been used to visualise the data. Gaps in the experimental data exist where tone smearing correction methods and filters have not allowed data through, due to contamination by background noise levels. Despite this, projected and experimental directivities still show good agreement to each other. Again

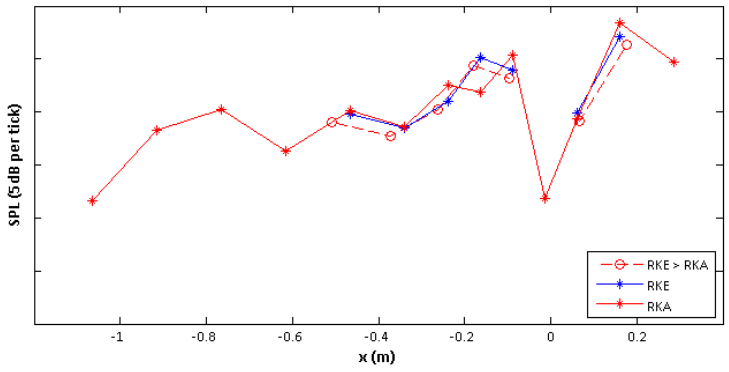

(A)

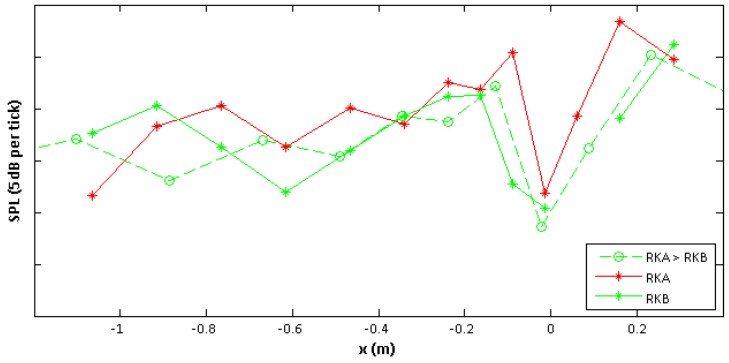

(B)

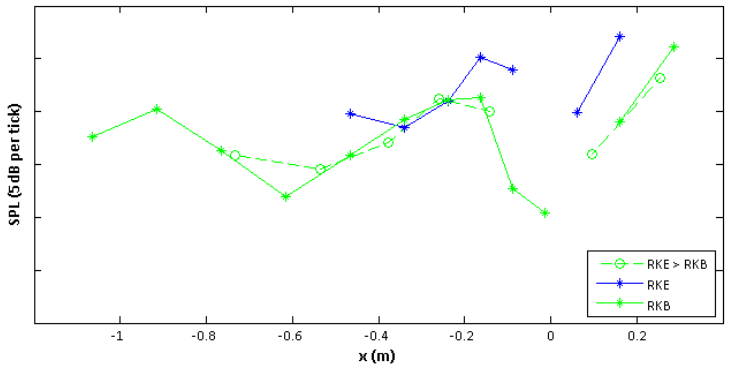

(C)

FIGURE 3.23: Interaction tone directivities from ARA Build 2 experiments. It is assumed viscous wake interactions are the dominant source of noise. The diagrams show experimental data (starred markers and solid line) and projections (circular markers and dashed line). Projections are coloured according to the rail they are projected to. Each of the colours reflects the rails depicted in Figure 3.3. (a) Projection from rail RKA to RKE, (b) projection from rail RKE to RKB and (c) projection from rail RKA to RKB.

discrepancies are likely to exist due to flow distortions and possible reverberation effects in the tunnel, on top of the obvious approximations assumed by this method.

The extrapolation methods can also be used to validate parameter studies and confirm general design trends. Figure 3.24 shows the variation of SPL with inflow Mach number at single microphones from each of the rails. Using the extrapolation methods, the data has been projected to the same observer locations, and it is clear from the figure that the data has collapsed to a single trend - there is some data scatter present which is to be expected from experiments. Confirmation of such trends is a useful technique for improving designs in order to minimise noise.

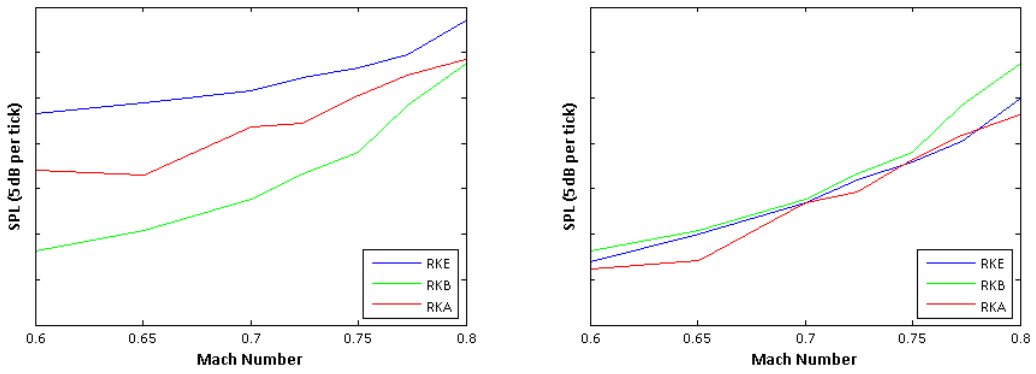

(A) (B)

FIGURE 3.24: SPL against axial inflow Mach number. The thrust has not been kept constant between test cases. Experimental data collected at rails RKE (blue), RKA (red) and RKB (green) have been used. The data has been corrected for sideline position using Peake and Boyd's 'approximate' transfer function. SPL v Mach number (a) uncorrected for observer location and (b) corrected for observer location.

The extrapolation techniques can also be used to compare like for like cases from different tests. Similar cases were run in ARA Build 1 and Build 2 tests, with the only difference being that aeroacoustically optimised blades were used in the latter tests. Figures 3.2 and 3.3 show the microphone positions for each test respectively. Due to differing positions the tests are not directly comparable, but using the extrapolation methods derived here, data can be projected to a common observer sideline distance. Figure 3.25 shows such a comparison between Build 1 and Build 2 data. $\{1, 0\}$ tone directivities have been plotted and the data has been corrected for observer position. The Build 1 blades, represented by a dashed line, are louder than all pitch variations of Build 2 blades, showing that in terms of the noise production for this tone and under these specific operating conditions, the Build 2 blades perform better. Quantifying design improvement is a much more complicated procedure, however this application demonstrates the use that can be derived from such extrapolation techniques.

The methods outlined in this chapter have been used by the research sponsor Rolls-Royce to conduct a basic parametric study. Further details of the study can be found

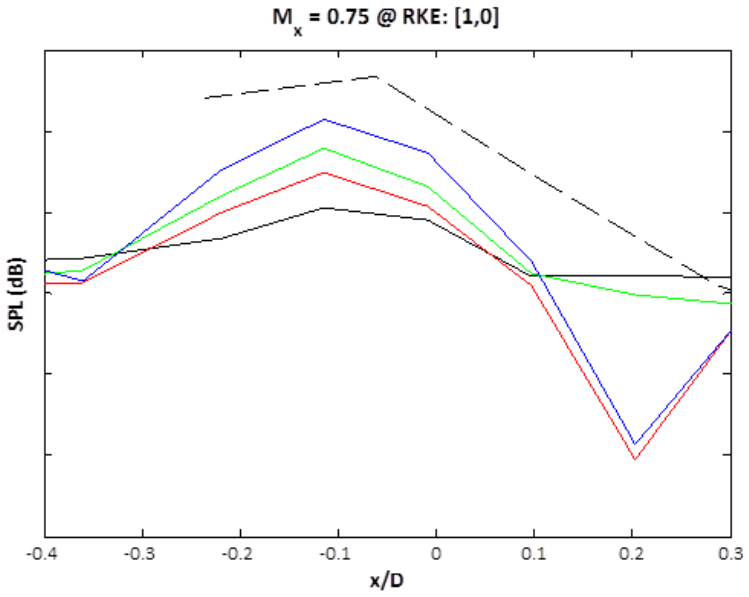

FIGURE 3.25: $\{1, 0\}$ tone directivities from both ARA Build 1 (dashed line) and ARA Build 2 (solid lines) experiments. Different solid line types represent different blade pitches of ARA Build 2 — under these conditions ARA Build 1 seems to underperform compared to all ARA Build 2 cases.

in Parry et al. (2012). The study uses the methods outlined here to compare results collected at different observer locations.

3.4 Conclusions

Data analyses from a number of open rotor experimental campaigns have been presented in this chapter. The experiments were conducted by Rolls-Royce plc. A number of test points, conditions and tones were interrogated from the experiments; only a very small subset has been presented here for demonstrative purposes. This value of these data analyses to the work in this thesis is that it was used for validation of the simple analytical models presented in the previous chapter. These comparisons highlighted a mismatch between experiment and prediction at particular operating conditions and observer positions. The inaccuracies in the simple free-field models as shown in this chapter adds relevance to the research presented in the following chapters, where the research presented is undertaken in part to correct for these discrepancies. Also, in order to discern more information from the acoustic measurement data, further analysis techniques have been implemented on those measurement data sets. Specifically, extrapolation methods were implemented to compare acoustic measurements from different observation locations.

The benefit from such methods to the sponsor is as follows. At some conditions and for particular tones, the near-field models have been shown to be somewhat valid for

a number of operating conditions and importantly in the near-field of the propeller. If required, the sponsor could incorporate such models into any quick noise prediction tools used for iterative design of the open rotor. The implementation of extrapolation methods to the data set has been quite useful. It has allowed the sponsor to compare results from different data sets and accounts for differences in observer position. It was shown that when measurements from different data sets are made comparable, measurements obtained from the aeroacoustically optimised blade are quieter than a previous generation design, at all blade pitches. This result would contribute to a validation for the expected acoustic performance of the new design, at the operating conditions which were compared.

Appendices

3.A Conversion between model and full scale open rotors

The rotor advance ratio, J, is a non-dimensional parameter that quantifies the rotor forward speed based on its rotation speed and diameter. The advance ratio is essentially a measure of rotor pitch, i.e. the direction from which the flow hits the leading edge of the rotor blade.

$$J = \frac{V}{nD} \tag{3.5}$$

where V is the ambient flow speed, n is the rate of rotation of the rotor and D is the rotor diameter.

The rotor coefficient of thrust, C_T, is a non-dimensional value for the thrust produced by that rotor.

$$C_T = \frac{T}{\rho n^2 D^4} \tag{3.6}$$

where T is the rotor thrust and rho is the ambient flow density.

When comparing results between model and full scale open rotors, one should ensure the non-dimensional parameters C_T, M and J are conserved. Note that M is the flow Mach number and

$$M = \frac{V}{c_0} \tag{3.7}$$

and the ambient speed of sound, c_0 is defined as

$$c_0 = \sqrt{\gamma R \Theta} \tag{3.8}$$

where γ is the ratio of specific heats for air, R is the specific gas constant for air and Θ is the ambient temperature.

3.A.1 Thrust Conversion

For example, let us suppose that we wish to simulate a full scale open rotor operating at cruise thrust. The equivalent thrust requirement for a model scale open rotor is now determined, where the subscript M indicates model scale parameters and the subscript F indicates full scale parameters. Using eq. (3.7) we can show that

$$M = \frac{V_M}{\sqrt{\gamma R \Theta_M}} = \frac{V_F}{\sqrt{\gamma R \Theta_F}} \tag{3.9}$$

$$V_M = V_F \sqrt{\frac{\Theta_M}{\Theta_F}}. \tag{3.10}$$

then, using eq. (3.5) we have

$$J = \frac{V_M}{n_M D_M} = \frac{V_F}{n_M D_M} \sqrt{\frac{\Theta_M}{\Theta_F}} = \frac{V_F}{n_F D_F} \tag{3.11}$$

$$\frac{1}{n_F D_F} = \frac{1}{n_M D_M} \sqrt{\frac{\Theta_M}{\Theta_F}} \tag{3.12}$$

Pressure is related to temperature by the ideal gas law

$$p = \rho R \Theta. \tag{3.13}$$

where p is the ambient pressure. This can be replaced into eqs. (3.6) and (3.12) to yield

$$C_T = \frac{T_F}{\rho n_F^2 D_F^4} = \frac{T_F}{\rho D_F^2} \frac{1}{n_M^2 D_M^2} \frac{p_M}{p_F} = \frac{T_M}{\rho n_M^2 D_M^4} \tag{3.14}$$

$$T_M = T_F \frac{p_M}{p_F} \left(\frac{D_M}{D_F} \right)^2 \tag{3.15}$$

3.A.2 Frequency Conversion

A similar change must be made to the rotor rotational frequency when converting between model and full scale. Combining eqs. (3.12) and (3.13) shows that

$$n_M = n_F \frac{D_F}{D_M} \sqrt{\frac{p_M}{p_F}}. \tag{3.16}$$

3.B The Mach Radius

The idea of the Mach radius was first presented in Parry (1988). Consider a source rotating with angular speed Ω at fixed radius r_s and translating along the axis of rotation with Mach number M. For a given angular speed the Mach radius is the radius at which the maximum speed in the direction of the observer would be precisely sonic (see Figure 3.26, where the source is identified as the propeller tip).

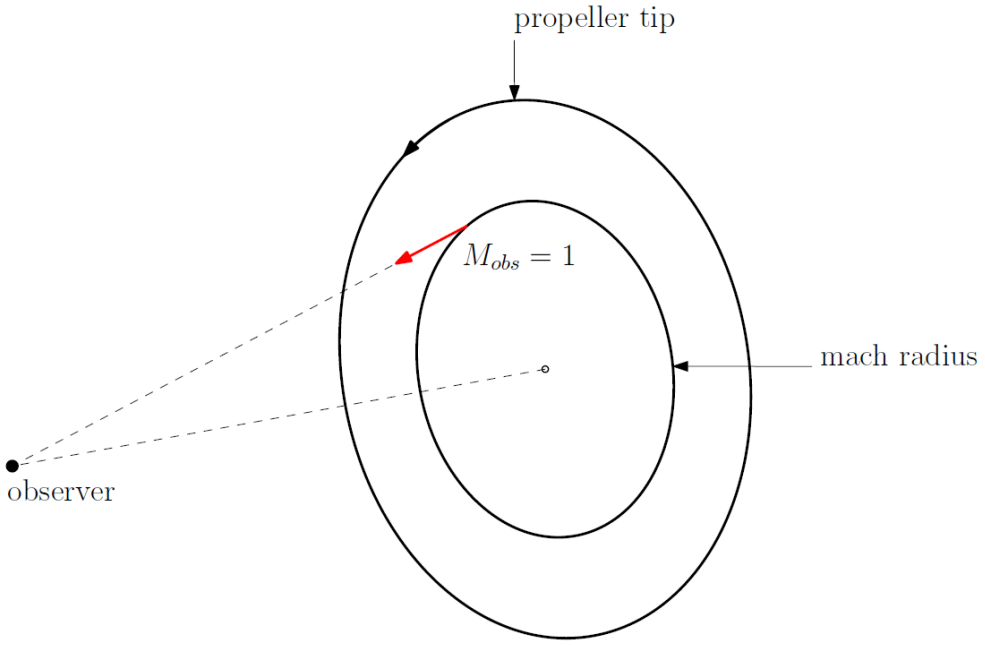

FIGURE 3.26: The Mach radius; the radius at which the source would be moving towards the observer at exactly unit Mach.

The Mach radius will be denoted r^* and will also be defined in terms of a non-dimensional radius $z^* = r^*/r_s$. For a stationary (non-translating) rotating source, in the plane of the rotor the Mach radius reduces to $z^* = 1/M_s$, which is often referred to as the sonic radius. M_s is the rotation Mach number of the source. However the Mach radius incorporates observer angles which are off the rotor plane as well as axial flow and in such a case is defined by

$$r^* = \frac{r_s\sqrt{1-(M\sin\theta_{\rm re})^2}}{M\sin\theta_{\rm re}} = \frac{r_s\left(1-M\cos\theta_{\rm em}\right)}{M_s\sin\theta_{\rm em}} \tag{3.17}$$

where M_s is the source rotation Mach number and θ is the observer angle; the subscripts re and em correspond to reception and emission coordinates respectively.

Chapter 4

Wind Tunnel Reverberation

4.1 Introduction

This chapter describes theoretical models for open rotor noise that include tunnel reverberation effects. Wind tunnels that might typically be used for high speed Open Rotor testing are modelled in order to assess the impact of reverberation in these tunnel setups. Understanding the effect would allow the industrial partner, Rolls-Royce, to improve the accuracy of their estimates for Open Rotor cruise noise. Only the tonal noise component of Open Rotors is considered here and the frequency domain methods popularised in Hanson (1985*a*,*b*, 1992) are the basis for rotor tone noise prediction.

In Section 4.2 the procedure to derive the relevant theoretical models is outlined. The wind tunnel Green's functions for a rectangular cross-section and circular cross-section wind tunnel are presented, with further derivation showing how expressions for rotor loading sources might be obtained. The application of Graf's addition theorem to the expression for a rectangular cross-section wind tunnel is presented in Section 4.2.1. This step in the procedure simplifies the expression and has the benefit of reducing the computational cost of evaluating the final expression. Section 4.3 describes analysis of open rotor tone noise in wind tunnel environments using the proposed models. The models are specifically used to assess and understand the impact of tunnel reverberation. A comparison is made between a free-field model and a wind tunnel with an impedance boundary condition at the walls. The comparison shows how under certain conditions predictions based in a wind tunnel can theoretically be similar to those made in the free-field. However obtaining similar results in a test campaign is not practical. The differences in the acoustic field generated in rectangular and circular cross-section wind tunnels is also investigated. Finally, simulations of open rotor tone noise in two existing wind tunnel setups are presented. The analyses provide rudimentary insight into the impact that tunnel reverberation might have when testing at these facilities. The two facilities are the Transonic Wind Tunnel (TWT) at the Aircraft Research Association

(Bedford, UK) and ONERA's S1MA wind tunnel (Modane, France). The former of the two has a rectangular cross-section in the test section whilst the latter is circular.

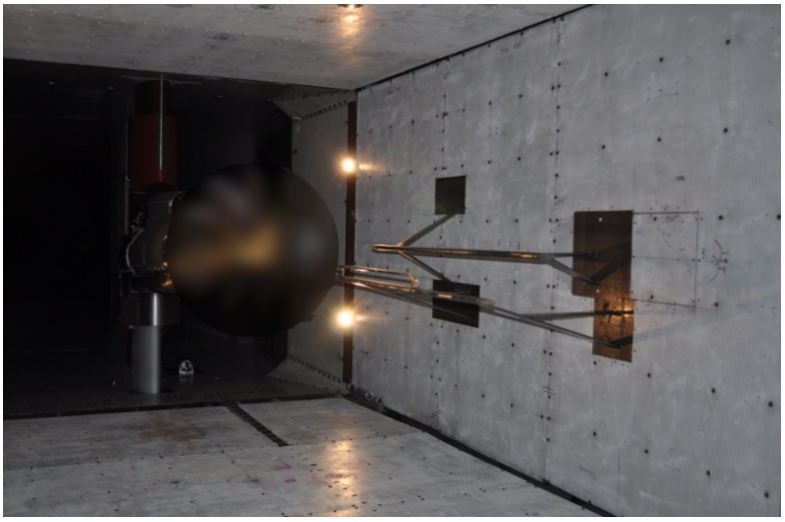

FIGURE 4.1: A photograph of recent model scale open rotor tests conducted at the ARA's transonic wind tunnel in Bedford, UK. Some of the noise measurements were made using microphone rails placed at fixed sidelines to the test rig.

Literature Survey

Kirker (1990) describes the testing of Rolls-Royce's Rig 140 (a model scale Open Rotor test rig) in the Aircraft Research Association's (ARA) Transonic Wind Tunnel. This tunnel has a rectangular cross section and rigid walls. Wood and Newman (1990) describe the development and implementation of a removable acoustic liner designed specifically for this tunnel's test section. The purpose of this liner was to reduce the effect of reverberation in the test section over a range of frequencies. The liner was optimised for Rolls-Royce's propeller testing requirements at the time. Installing the liner meant that acoustic measurements could be more readily undertaken. Therefore, during noise measurement test points, the liner was installed in the test-section of the wind tunnel. Commissioning tests showed that the liner was only reliably effective for flow Mach numbers below approximately 0.6 and a degradation in liner performance was noted at higher wind tunnel flow speeds. Parry et al. (2012) later describe the high-speed testing of Rolls-Royce's refurbished scale Open Rotor test rig, Rig 145, in the ARA's Transonic Wind Tunnel. Similarly, the noise measurements from these tests are suspected to be contaminated for the cases simulating cruise conditions, despite the use of the acoustic liner. A photograph of the tunnel test section during these tests is presented in Figure 4.1. In their paper a significant number of experimental acoustic measurements are presented but because of concerns over reverberation effects in the tunnel, these were confined to a region close to the rotor disc planes, where the effect seems less prevalent. It is suggested here that this is because maximum performance of the acoustic liner is achieved near to the plane of the rotor, where the vector of acoustic

intensity is directed normal to to the tunnel wall. A further analysis of this is presented later in the chapter.

The approach used in this chapter is to derive an analytic Green's function to account for the scattering caused by the wind tunnel walls. Generating Green's functions for ducts with internal flows, rotational sources and acoustic treatments at the boundary has been the subject of many research papers and texts, and has been covered in impressive detail. A number of these papers (Alonso and Burdisso, 2007; Brambley and Peake, 2006; Rienstra and Tester, 2008) typically cite the application of noise inside the nacelle of a turbofan aero-engine and therefore usually present models for circular or annular cross-sections that do not extend much beyond the rotor disc area. A similar method for noise prediction is proposed in this chapter but the geometries considered reflect typical wind tunnel setups. In a wind tunnel, the cross-sectional area is much larger relative to the rotor disc area. In this analysis the near-field region of the source is also of significant interest. Both of these requirements means that a significantly larger number of modes must be included in the calculation in order to achieve a converged solution and thus the computational cost increases proportionally.

4.2 Formulation

The wind tunnel is assumed infinitely long and so in this analysis end reflections are ignored. If the tunnel setup is sufficiently long enough to allow cut-off modes to decay, reflections of these modes from the ends of the wind tunnel should be insignificant. The analysis in this paper considers sufficiently high frequencies, duct radii and only purely real impedances, such that end reflections of most modes are not likely to impact the solution. Also, the tunnel's boundaries do not vary along the tunnel axis. The axial co-ordinate is denoted by the subscript 1 and is positive downstream. This analysis is also limited to the consideration of simple rectangular and circular cross sections. In all models the rotational axis of the source and the wind tunnel centreline are parallel. In the circular cross section model the two axes are collinear, however the formulation of the rectangular cross section model allows the origin of the co-ordinate system to be placed anywhere within the tunnel cross section, provided the plane of rotation remains normal to the tunnel axis and boundaries. It is also assumed that an impedance boundary condition would be sufficient to model the presence of an acoustic liner on the tunnel's boundaries.

The dominant source of noise is assumed to be produced by loading on the rotor blades. Therefore only a formulation for dipole sources is presented. However, the method could be extended in the same manner to consider the noise due to monopole or quadrupole sources, which may also contribute to rotor tone noise. It is assumed the blade loading

is purely due to interactions with the hydrodynamic field and any acoustic scattering from the rotor blades is ignored.

The tunnel mean flow velocity is constant and uniform across the tunnel cross section. This is a crude assumption, especially since it is thought that at high speed the boundary layer may modify the impedance of the tunnel liner. However, the plug flow assumption leads to simpler expressions which are quicker to solve. It is thought that the wavelengths of the tone harmonics of interest may be larger than the thickness of the tunnel wall boundary layers but this cannot be confirmed without measurement of the tunnel wall boundary layer. In such a case it should be plausible to ignore acoustic refraction in the wall boundary layer. The flow only has an axial component. Finally, the effects of flow distortions induced by the open rotor itself and acoustic scattering from any other structures in the tunnel (such as the open rotor's centrebody) are ignored.

The flow is assumed to be isentropic, therefore $p = \rho c_0^2$ where p denotes a pressure perturbation, ρ is the density perturbation and c_0 is the speed of sound. Introducing the isentropic assumption into Goldstein (1976, eq. 4.13) gives the following expression, which we use to determine the unsteady pressure at location $\mathbf{x} = \{x_1, x_2, x_3\}$ and time t produced by the loading forces which would be generated at the open rotor's blades.

$$p(\mathbf{x}, t) = \int_{-T}^{T} \int_{S_b(\tau)} f_i(\mathbf{y}, \tau) \frac{\partial}{\partial y_i} g(\mathbf{y}, \tau \,|\, \mathbf{x}, t) \, \mathrm{d}S(\mathbf{y}) \, \mathrm{d}\tau. \tag{4.1}$$

Note that $-T < \tau < T$ is the interval of time over which sound is emitted and is assumed to be infinitely large. g is a Green's function which satisfies the convected wave equation

$$\left[\frac{\partial^2}{\partial y_1^2} + \frac{\partial^2}{\partial y_2^2} + \frac{\partial^2}{\partial y_3^2} - \frac{1}{c_0^2} \left(\frac{\partial}{\partial \tau} + U \frac{\partial}{\partial y_1} \right)^2 \right] g(\mathbf{y}, \tau \,|\, \mathbf{x}, t) = -\delta \left(t - \tau \right) \delta \left(\mathbf{y} - \mathbf{x} \right), \tag{4.2}$$

where U is the mean flow velocity in the wind tunnel and is aligned with the tunnel's axial co-ordinate. f_i is the force per unit area exerted by the blades on the air, which is assumed to be dominated by the lift force on the blades. We choose Green's functions that simulate the following two conditions; either a wind tunnel with rigid walls and purely axial flow, or a wind tunnel with acoustically lined walls and no flow. Either condition will give rise to a different boundary condition which the Green's function must also satisfy and these are provided at the relevant point in the paper. A wind tunnel with acoustically lined walls and flow is more complicated to consider because of the requirement to calculate an additional set of 'surface' modes. Due to the difficulty

in accurately predicting these extra modes, the conditions that allows them to arise is not explored in this paper.

The blades will be modelled as being infinitely thin so that the integration over the blade surface S_b can be replaced by an integration over the blade planform area and f_i replaced by $L^{(b)}n_i$ where $L^{(b)}$ is the lift force per unit area on the b^{th} blade and n_i is now a unit vector in the direction of the local 'lift' force exerted by the blades on the fluid. It will be more convenient to work in cylindrical coordinates $\{y_1, r, \phi\}$ where r and ϕ are co-ordinates for the radius and azimuthal angle.

Also, $n_i \frac{\partial}{\partial y_i}$ can be written in cylindrical coordinates as

$$n_i \frac{\partial}{\partial y_i} = n_1 \frac{\partial}{\partial y_1} + n_\phi \frac{1}{r} \frac{\partial}{\partial \phi} + n_r \frac{\partial}{\partial r}, \tag{4.3}$$

where n_r and n_ϕ are the radial and azimuthal components of the unit vector $\mathbf{n}$. The blades rotate at Ω rad/s and the lift force is assumed to be aligned normal to the local flow direction. Therefore the components of the unit vector may be defined as

$$n_1 = \sin\alpha, n_\phi = \cos\alpha, n_r = 0, \tag{4.4}$$

where $\tan\alpha = \Omega r/U$.

The rotor is assumed to have B identical, evenly spaced blades. If $S_p^{(b)}$ denotes the planform area of the b^{th} rotor blade, eq. (4.1) can be rewritten as follows.

$$p(\mathbf{x}, t) = \sum_{b=0}^{B-1} \int_{-\infty}^{\infty} \int_{S_p^{(b)}(\tau)} L^{(b)} \left[\sin\alpha \frac{\partial g}{\partial y_1} + \frac{\cos\alpha}{r} \frac{\partial g}{\partial \phi} \right] \mathrm{d}S(\mathbf{y}) \, \mathrm{d}\tau \tag{4.5}$$

It will be convenient to express the lift force per unit area on the planform of the b^{th} blade in terms of its radial and chordwise blade coordinates r and $X^{(b)}$ i.e. $L^{(b)}\left(X^{(b)}, r, \tau\right)$. The location of a point on the b^{th} blade can be expressed in terms of the cylindrical coordinate system using the equations below.

$$y_1 = \left(s + X^{(b)}\right) \cos\alpha \tag{4.6}$$

$$\phi = \Omega\tau - \left(s + X^{(b)}\right) \frac{\sin\alpha}{r} + \frac{2\pi b}{B} \tag{4.7}$$

The hub and the tip of the blades are located at radius R_h and R_t respectively. The chordwise coordinate $X^{(b)}$ has its origin at the mid-chord such that $-c/2 < X^{(b)} < c/2$

where c denotes the blade chord length. Note that s denotes the blade 'sweep'. Eq. (4.5) becomes

$$p(\mathbf{x},t) = \sum_{b=0}^{B-1} \int_{-\infty}^{\infty} \int_{R_h}^{R_t} \int_{-c/2}^{c/2} L^{(b)} \left[\sin\alpha \frac{\partial g}{\partial y_1} + \frac{\cos\alpha}{r} \frac{\partial g}{\partial \phi} \right] \mathrm{d}X^{(b)}\, \mathrm{d}r\, \mathrm{d}\tau. \tag{4.8}$$

The Green's function is given by

$$g(\mathbf{y},\tau \,|\, \mathbf{x},t) = \frac{-\mathrm{i}}{4\pi} \sum_{n_2} \sum_{n_3} \int_{-\infty}^{\infty} \frac{\Psi_{n_2,n_3}(y_2,y_3)\, \Psi_{n_2,n_3}(x_2,x_3)}{k_{n_2,n_3} \Gamma_{n_2,n_3}} \times \exp\left\{ \mathrm{i}\omega(t-\tau) - \mathrm{i}\frac{M\kappa}{\beta^2}(y_1-x_1) - \mathrm{i}\frac{k_{n_2,n_3}}{\beta^2}|y_1-x_1| \right\} \mathrm{d}\omega \tag{4.9}$$

where $\kappa = \omega/c_0$, $k_{n_2,n_3}^2 = \kappa^2 - \beta^2 \varkappa_{n_2,n_3}^2$, $\beta^2 = 1 - M^2$, $M = U/c_0$ and $\varkappa_{n_2,n_3}$ and Ψ_{n_2,n_3} are an eigenvalue/eigenfunction pair which satisfy the following two-dimensional Helmholtz equation

$$\left(\frac{\partial^2}{\partial y_2^2} + \frac{\partial^2}{\partial y_3^2} + \varkappa_{n_2,n_3}^2 \right) \Psi_{n_2,n_3} = 0, \tag{4.10}$$

as well as whichever of the boundary conditions is relevant for the case being modelled. The Green's function is transformed to the frequency domain by

$$g(\mathbf{y},\tau \,|\, \mathbf{x},t) = \int_{-\infty}^{\infty} G_\omega(\mathbf{y} \,|\, \mathbf{x}) \frac{\exp\{\mathrm{i}\omega(t-\tau)\}}{2\pi} \mathrm{d}\omega \tag{4.11}$$

and so

$$G_\omega(\mathbf{y} \,|\, \mathbf{x}) = \frac{-\mathrm{i}}{2} \sum_{n_2} \sum_{n_3} \frac{\Psi_{n_2,n_3}(y_2,y_3)\, \Psi_{n_2,n_3}(x_2,x_3)}{\Gamma_{n_2,n_3} k_{n_2,n_3}} \exp\left\{ -\mathrm{i}\frac{M\kappa}{\beta^2}(y_1-x_1) - \mathrm{i}\frac{k_{n_2,n_3}}{\beta^2}|y_1-x_1| \right\} \tag{4.12}$$

Also,

$$\Gamma_{n_2,n_3} = \int_A \Psi_{n_2,n_3}^2(y_2,y_3)\, \mathrm{d}A, \tag{4.13}$$

where A is the cross sectional area of the wind tunnel.

Note that this frequency domain Green's function G_ω must also satisfy the appropriate boundary conditions. If the tunnel surfaces are rigid, G_ω would satisfy

$$n_i \frac{\partial G_\omega}{\partial y_i} = 0 \tag{4.14}$$

where n_i is a unit vector normal to the tunnel wall surfaces, pointing out of the tunnel volume. In the frequency domain, the acoustic impedance Z is defined by $Z = \tilde{p}/\tilde{u_n}$, where $\tilde{u_n}$ is the acoustic velocity normal to the wind tunnel wall and the normal is directed out of the wind tunnel volume. Defining the specific acoustic admittance Λ as

$$\Lambda = \frac{\rho_0 c_0}{Z} = \frac{\rho_0 c_0 \tilde{u_n}}{\tilde{p}} \tag{4.15}$$

and coupling this with the linearised Euler equation for momentum results in the following formulation of the no-flow impedance boundary condition

$$n_i \frac{\partial G_\omega}{\partial y_i} = -\mathrm{i}\kappa\Lambda_i G_\omega. \tag{4.16}$$

where the subscript i can be either 2 or 3 and corresponds to the tunnel transverse coordinates. Note that the no flow impedance boundary condition should be solved in conjunction with the wave equation that is obtained by setting $U = 0$ in eq. (4.2).

In sections 4.2.1 and 4.2.2 formulations for wind tunnels with rectangular and circular cross sections are derived. A schematic of these cross-sections is presented in Figure 4.2.

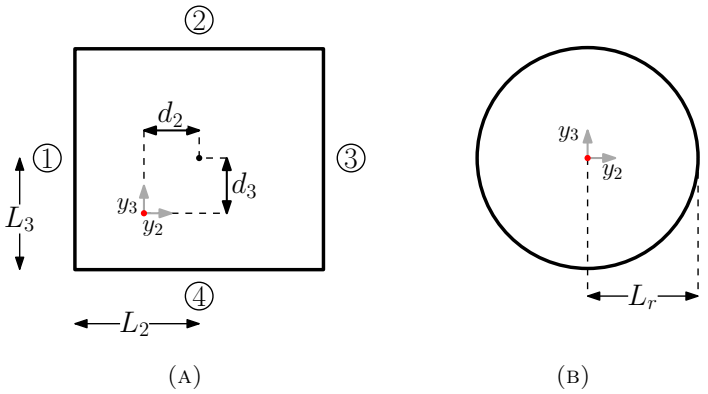

(A) (B)

FIGURE 4.2: Schematic of (a) a rectangular and (b) a circular cross section wind tunnel. The parameters defining the shape and size of the tunnel cross-section are shown. For the rectangular cross-section schematic, the parameters describing the offset of the wind tunnel centreline from the origin of the co-ordinate system are also shown.

4.2.1 Rectangular Cross-Section Wind Tunnel

The following definitions are used in our formulation for a rectangular wind tunnel.

$$\Psi_{n_2,n_3} = \psi_{n_2}(y_2)\,\psi_{n_3}(y_3) \quad \psi_{n_i} = \begin{cases} \cos\left(\dfrac{\pi k_{n_i}}{2L_i}(y_i - d_i)\right) & \text{when} \quad n_i = 0, 2, 4... \\ \sin\left(\dfrac{\pi k_{n_i}}{2L_i}(y_i - d_i)\right) & \text{when} \quad n_i = 1, 3, 5... \end{cases} \tag{4.17}$$

and

$$\Gamma_{n_2,n_3} = \gamma_{n_2}\gamma_{n_3} \qquad \gamma_{n_i} = \begin{cases} L_i\left[1 + \operatorname{sinc}(k_{n_i})\right] & \text{when} \quad n_i = 0, 2, 4... \\ L_i\left[1 - \operatorname{sinc}(k_{n_i})\right] & \text{when} \quad n_i = 1, 3, 5... \end{cases} \tag{4.18}$$

L_2 and L_3 are the half-width and half-height of the wind tunnel respectively whilst the parameters d_2 and d_3 are used to describe the offset of the origin from the wind tunnel centreline (see Figure 4.2) and

$$-L_i \leq d_i \leq L_i. \tag{4.19}$$

From eq. (4.10) we can obtain a definition for the eigenvalue set in terms of the transverse wavenumbers k_{n_2} and k_{n_3}

$$\varkappa^2_{n_2,n_3} = \left(\frac{\pi k_{n_2}}{2L_2}\right)^2 + \left(\frac{\pi k_{n_3}}{2L_3}\right)^2. \tag{4.20}$$

For rigid walls, the transverse wavenumbers are defined as

$$k_{n_i} = n_i. \tag{4.21}$$

To calculate the transverse wavenumbers for a wind tunnel with an impedance boundary, we solve the following expressions, derived from eq. (4.16) at each of the tunnel walls. For reference, a number has been assigned to each wall as presented in Figure 4.2. At walls 1 and 3

$$\frac{\partial G_\omega}{\partial y_2} = \pm \mathrm{i}\kappa\Lambda_2 G_\omega \qquad \text{at} \quad y_2 = d_2 \mp L_2 \tag{4.22}$$

and at walls 2 and 4

$$\frac{\partial G_\omega}{\partial y_3} = \mp \mathrm{i}\kappa\Lambda_3 G_\omega \qquad \text{at} \quad y_3 = d_3 \pm L_3 \tag{4.23}$$

In this following analysis we shall set $\Lambda_2 = \Lambda_3 = \Lambda$. Therefore, for a rectangular wind tunnel with impedance boundaries, the transverse wavenumbers can be determined using the following set of expressions

$$\hat{k}_i \tan \hat{k}_i + \mathrm{i}\kappa\Lambda L_i = 0 \quad \text{when} \quad n_i = 0, 2, 4, ... \tag{4.24}$$

$$\hat{k}_i \cot \hat{k}_i - \mathrm{i}\kappa\Lambda L_i = 0 \quad \text{when} \quad n_i = 1, 3, 5, ... \tag{4.25}$$

where $\hat{k}_i = \pi k_{n_i}/2$. The transverse wavenumbers for a tunnel with an impedance boundary condition at its walls are complex and are not solved for analytically. The solutions are obtained by using a root finding technique and continuation from the rigid wall solution (where $\Lambda_i = 0$) to the desired wall admittance. In the limit $\Lambda_i \to \infty$ the wavenumber is once again real-valued and would be equivalent to that required for a pressure release boundary. This iterative procedure, also known as a shooting method, has been discussed and used elsewhere (McAlpine and Wright, 2006; Rienstra and Tester, 2008).

Graf's Addition Theorem

It will now be shown that the eigenfunctions specified in eq. (4.17) can be rewritten in cylindrical coordinates using Graf's addition theorem for Bessel functions (Abramowitz and Stegun, 1972). This simplification provides a new expression for the Green's function which is convenient for evaluating the sound field produced by rotating sources. This new expression is then substituted into eq. (4.12) in order to determine the tonal noise produced by the blades of an open rotor in a rectangular wind tunnel with rigid walls.

Firstly, the eigenfunctions are expanded using the following relationships

$$\cos\left(\frac{\pi k_{n_i}}{2L_i}(y_i - d_i)\right) = \frac{1}{2}\left[\exp\left\{\mathrm{i}\frac{\pi k_{n_i}}{2L_i}y_i - \mathrm{i}\frac{\pi k_{n_i}}{2L_i}d_i\right\} + \exp\left\{-\mathrm{i}\frac{\pi k_{n_i}}{2L_i}y_i + \mathrm{i}\frac{\pi k_{n_i}}{2L_i}d_i\right\}\right], \tag{4.26}$$

$$\sin\left(\frac{\pi k_{n_i}}{2L_i}\left(y_i - d_i\right)\right) = \frac{1}{2\mathrm{i}}\left[\exp\left\{\mathrm{i}\frac{\pi k_{n_i}}{2L_i}y_i - \mathrm{i}\frac{\pi k_{n_i}}{2L_i}d_i\right\} - \exp\left\{-\mathrm{i}\frac{\pi k_{n_i}}{2L_i}y_i + \mathrm{i}\frac{\pi k_{n_i}}{2L_i}d_i\right\}\right]. \tag{4.27}$$

Then, converting to cylindrical polar co-ordinates and making use of the Jacobi-Anger expansions (Abramowitz and Stegun, 1972) yields the following identities

$$\exp\left\{\pm\mathrm{i}\frac{\pi k_{n_2}}{2L_2}r\cos\phi\right\} = \sum_{q_2=-\infty}^{\infty} J_{q_2}\left(\frac{\pi k_{n_2}r}{2L_2}\right)\exp\left\{\mathrm{i}q_2(\phi \pm \pi/2)\right\} \tag{4.28}$$

$$\exp\left\{\pm\mathrm{i}\frac{\pi k_{n_3}}{2L_3}r\sin\phi\right\} = \sum_{q_3=-\infty}^{\infty} J_{q_3}\left(\frac{\pi k_{n_3}r}{2L_3}\right)\exp\left\{\pm\mathrm{i}q_3\phi\right\}, \tag{4.29}$$

where J is a Bessel function of the first kind. Using eqs. (4.26)-(4.29), each of the terms in the double series of eigenfunctions can now be expressed as a series where each term is a combination of Bessel and exponential functions, taking the form of the following four expansions

$$\cos\left(\frac{\pi k_{n_2}}{2L_2}\left(y_2 - d_2\right)\right) = \frac{1}{2}\sum_{q_2=-\infty}^{\infty} J_{q_2}\left(\frac{\pi k_{n_2}r}{2L_2}\right)\exp\left\{\mathrm{i}q_2\phi\right\} \times\left[\exp\left\{\mathrm{i}\frac{\pi q_2}{2} - \mathrm{i}\frac{\pi k_{n_2}}{2L_2}d_2\right\} + \exp\left\{-\mathrm{i}\frac{\pi q_2}{2} + \mathrm{i}\frac{\pi k_{n_2}}{2L_2}d_2\right\}\right], \tag{4.30}$$

$$\sin\left(\frac{\pi k_{n_2}}{2L_2}\left(y_2 - d_2\right)\right) = \frac{1}{2\mathrm{i}}\sum_{q_2=-\infty}^{\infty} J_{q_2}\left(\frac{\pi k_{n_2}r}{2L_2}\right)\exp\left\{\mathrm{i}q_2\phi\right\} \times\left[\exp\left\{\mathrm{i}\frac{\pi q_2}{2} - \mathrm{i}\frac{\pi k_{n_2}}{2L_2}d_2\right\} - \exp\left\{-\mathrm{i}\frac{\pi q_2}{2} + \mathrm{i}\frac{\pi k_{n_2}}{2L_2}d_2\right\}\right], \tag{4.31}$$

$$\cos\left(\frac{\pi k_{n_3}}{2L_3}\left(y_3 - d_3\right)\right) = \frac{1}{2}\sum_{q_3=-\infty}^{\infty} J_{q_3}\left(\frac{\pi k_{n_3}r}{2L_3}\right)\exp\left\{\mathrm{i}q_3\phi\right\} \times\left[\exp\left\{-\mathrm{i}\frac{\pi k_{n_3}}{2L_3}d_3\right\} + \exp\left\{\mathrm{i}\pi q_3 + \mathrm{i}\frac{\pi k_{n_3}}{2L_3}d_3\right\}\right], \tag{4.32}$$

$$\sin\left(\frac{\pi k_{n_3}}{2L_3}\left(y_3-d_3\right)\right)=\frac{1}{2\mathrm{i}}\sum_{q_3=-\infty}^{\infty}J_{q_3}\left(\frac{\pi k_{n_3}r}{2L_3}\right)\exp\left\{\mathrm{i}q_3\phi\right\}\times\left[\exp\left\{-\mathrm{i}\frac{\pi k_{n_3}}{2L_3}d_3\right\}-\exp\left\{\mathrm{i}\pi q_3+\mathrm{i}\frac{\pi k_{n_3}}{2L_3}d_3\right\}\right]. \quad (4.33)$$

Therefore

$$\psi_{n_2}=\frac{1}{2}\sum_{q_2=-\infty}^{\infty}J_{q_2}\left(\frac{\pi k_{n_2}r}{2L_2}\right)\exp\left\{\mathrm{i}q_2\phi\right\}Q_{n_2,q_2} \quad (4.34)$$

where

$$Q_{n_2,q_2}=\begin{cases}\left[\exp\left\{\mathrm{i}\frac{\pi q_2}{2}-\mathrm{i}\frac{\pi k_{n_2}}{2L_2}d_2\right\}+\exp\left\{-\mathrm{i}\frac{\pi q_2}{2}+\mathrm{i}\frac{\pi k_{n_2}}{2L_2}d_2\right\}\right] & \text{when} \quad n_2=0,2,4...\\ -\mathrm{i}\left[\exp\left\{\mathrm{i}\frac{\pi q_2}{2}-\mathrm{i}\frac{\pi k_{n_2}}{2L_2}d_2\right\}-\exp\left\{-\mathrm{i}\frac{\pi q_2}{2}+\mathrm{i}\frac{\pi k_{n_2}}{2L_2}d_2\right\}\right] & \text{when} \quad n_2=1,3,5...\end{cases} \quad (4.35)$$

and

$$\psi_{n_3}=\frac{1}{2}\sum_{q_3=-\infty}^{\infty}J_{q_3}\left(\frac{\pi k_{n_3}r}{2L_3}\right)\exp\left\{\mathrm{i}q_3\phi\right\}\hat{Q}_{n_3,q_3} \quad (4.36)$$

where

$$\hat{Q}_{n_3,q_3}=\begin{cases}\left[\exp\left\{-\mathrm{i}\frac{\pi k_{n_3}}{2L_3}d_3\right\}+\exp\left\{\mathrm{i}\pi q_3+\mathrm{i}\frac{\pi k_{n_3}}{2L_3}d_3\right\}\right] & \text{when} \quad n_3=0,2,4...\\ -\mathrm{i}\left[\exp\left\{-\mathrm{i}\frac{\pi k_{n_3}}{2L_3}d_3\right\}-\exp\left\{\mathrm{i}\pi q_3+\mathrm{i}\frac{\pi k_{n_3}}{2L_3}d_3\right\}\right] & \text{when} \quad n_3=1,3,5...\end{cases} \quad (4.37)$$

Combining these expressions yields a new expression for the source eigenfunctions but in cylindrical co-ordinates:

$$\Psi_{n_2,n_3}=\frac{1}{4}\sum_{q_2=-\infty}^{\infty}\sum_{q_3=-\infty}^{\infty}J_{q_2}\left(\frac{\pi k_{n_2}r}{2L_2}\right)J_{q_3}\left(\frac{\pi k_{n_3}r}{2L_3}\right)\exp\left\{\mathrm{i}(q_2+q_3)\phi\right\}Q_{n_2,q_2}\hat{Q}_{n_3,q_3}. \quad (4.38)$$

We shift to using the summation index $q = q_3 + q_2$. Making use of the identity $J_{-\nu}(z) = J_\nu(z)\exp\{\mathrm{i}\nu\pi\}$ and the symmetry of the infinite summation in q_2 then yields the following altered expressions

$$\Psi_{n_2,n_3} = \frac{1}{4}\sum_{q_2=-\infty}^{\infty}\sum_{q=-\infty}^{\infty} J_{q_2}\left(\frac{\pi k_{n_2} r}{2L_2}\right) J_{q_2+q}\left(\frac{\pi k_{n_3} r}{2L_3}\right)\exp\{\mathrm{i}q\phi + \mathrm{i}q_2\pi\}\, Q_{n_2,-q_2}\hat{Q}_{n_3,q+q_2} \tag{4.39}$$

Note that Graf's Addition Theorem (Abramowitz and Stegun, 1972) states

$$\sum_{q_2=-\infty}^{\infty} J_{q_2}\left(\frac{\pi k_{n_2} r}{2L_2}\right) J_{q+q_2}\left(\frac{\pi k_{n_3} r}{2L_3}\right)\exp\{\pm\mathrm{i}q_2\pi/2\} = J_q\left(k_r r\right)\exp\{\pm\mathrm{i}q\chi\} \tag{4.40}$$

where

$$k_r = \sqrt{\left(\frac{\pi k_{n_2}}{2L_2}\right)^2 + \left(\frac{\pi k_{n_3}}{2L_3}\right)^2} = \varkappa_{n_2,n_3}, \tag{4.41}$$

$$\tan\chi = \frac{k_{n_2}}{k_{n_3}}\frac{L_3}{L_2}. \tag{4.42}$$

Combining all the terms that are dependent on the summation index q_2 and using Graf's addition theorem results in an expression for the eigenfunction that is only dependent on one summation index, q. For simplicity the remaining phase terms are combined into a single term, $\mathcal{Q}_{n_2,n_3,q}\left(\chi, d_2, d_3\right)$, where the form of $\mathcal{Q}$ will be dependent on whether n_i is odd or even. The expression for the eigenfunctions can now be redefined in terms of cylindrical source co-ordinates with only one summation,

$$\Psi_{n_2,n_3} = \frac{1}{4}\sum_{q=-\infty}^{\infty} J_q\left(k_r r\right)\exp\{\mathrm{i}q\phi\}\,\mathcal{Q}_{n_2,n_3,q}. \tag{4.43}$$

Substituting eq. (4.43) into eq. (4.12) yields the following new (and convenient) expression for the frequency domain Green's function of an infinitely long rectangular cross section wind tunnel which is suited to modelling rotor sources:

$$G_\omega\left(\mathbf{y}\,|\,\mathbf{x}\right) = \frac{-\mathrm{i}}{8}\sum_{n_2=0}^{\infty}\sum_{n_3=0}^{\infty}\sum_{q=-\infty}^{\infty}\frac{J_q\left(k_r r\right)\mathcal{Q}_{n_2,n_3,q}\Psi_{n_2,n_3}\left(x_2,x_3\right)}{\Gamma_{n_2,n_3}k_{n_2,n_3}} \exp\left\{\mathrm{i}q\phi - \mathrm{i}\frac{M\kappa}{\beta^2}\left(y_1 - x_1\right) - \mathrm{i}\frac{k_{n_2,n_3}}{\beta^2}|y_1 - x_1|\right\}. \tag{4.44}$$

This Green's function is equivalent to the original expression where the source co-ordinates were instead expressed using a rectangular co-ordinate system (obtained by substituting eq. (4.17) into eq. (4.12)).

Expressions for Rotor Loading Sources

We first introduce the following Fourier transform pair for the loading term $L^{(b)}$

$$L^{(b)}\left(X^{(b)},r,\tau\right)=\int_{-\infty}^{\infty}\tilde{L}^{(b)}\left(X^{(b)},r,\omega'\right)\exp\left\{\mathrm{i}\omega'\tau\right\}\,\mathrm{d}\omega', \tag{4.45}$$

$$\tilde{L}^{(b)}\left(X^{(b)},r,\omega'\right)=\frac{1}{2\pi}\int_{-\infty}^{\infty}L^{(b)}\left(X^{(b)},r,\tau\right)\exp\left\{-\mathrm{i}\omega'\tau\right\}\,\mathrm{d}\tau. \tag{4.46}$$

Then, combining the expressions given in eqs. (4.6), (4.7), (4.8), (4.11), (4.44) and (4.45) yields eq. (4.47) (after further simplification) for the acoustic pressure in the wind tunnel.

$$\begin{aligned}p(\mathbf{x},t)=\frac{-1}{8}\sum_{n_2=0}^{\infty}\sum_{n_3=0}^{\infty}\sum_{q=-\infty}^{\infty}\sum_{b=0}^{B-1}\int_{R_h}^{R_t}\int_{-c/2}^{c/2}\int_{-\infty}^{\infty}\tilde{L}^{(b)}\left(X^{(b)},r,\omega-q\Omega\right)\\ \left[\sin\alpha\left(\frac{M\kappa\pm k_{n_2,n_3}}{\beta^2}\right)-q\frac{\cos\alpha}{r}\right]\frac{J_q\left(k_r r\right)\mathcal{Q}_{n_2,n_3,q}\Psi_{n_2,n_3}\left(x_2,x_3\right)}{\Gamma_{n_2,n_3}k_{n_2,n_3}}\\ \exp\left\{\mathrm{i}\omega t+\mathrm{i}q\frac{2\pi b}{B}+\mathrm{i}\left(\frac{M\kappa\pm k_{n_2,n_3}}{\beta^2}\right)x_1-\mathrm{i}\left[\left(\frac{M\kappa\pm k_{n_2,n_3}}{\beta^2}\right)\cos\alpha+q\frac{\sin\alpha}{r}\right]\left(s+X^{(b)}\right)\right\}\\ \mathrm{d}\omega\,\mathrm{d}X^{(b)}\,\mathrm{d}r.\end{aligned} \tag{4.47}$$

This is a general equation which can be used to predict the pressure perturbation due to the lift forces on the blades of an open rotor installed in a rectangular cross-section wind tunnel and observed at a location $\mathbf{x}$ either upstream (upper sign) or downstream (lower sign) of the source.

The frequency domain pressure jump due to B evenly spaced rotating point forces of magnitude F newtons, located at radius a and aligned normal to the local flow direction can be expressed as

$$\tilde{L}^{(b)}\left(X^{m},r,\omega\right)=F\delta\left(r-a\right)\delta\left(X^{(b)}\right)\delta\left(\omega\right). \tag{4.48}$$

Substituting eq. (4.48) into eq. (4.47) and evaluating the summation over b yields the following expression

$$p(\mathbf{x},t) = -\frac{BF}{8}\sum_{n_2=0}^{\infty}\sum_{n_3=0}^{\infty}\sum_{q=-\infty}^{\infty}\left[\sin\alpha\left(\frac{M\kappa \pm k_{n_2,n_3}}{\beta^2}\right) - \nu\frac{\cos\alpha}{a}\right] \frac{J_\nu\left(k_r a\right)\mathcal{Q}_{n_2,n_3,\nu}\Psi_{n_2,n_3}\left(x_2,x_3\right)}{\Gamma_{n_2,n_3}k_{n_2,n_3}} \exp\left\{\mathrm{i}\nu\Omega t + \mathrm{i}\left(\frac{M\kappa \pm k_{n_2,n_3}}{\beta^2}\right)x_1\right\}. \quad (4.49)$$

where $\nu = qB$, $\kappa = \nu\Omega/c_0$ and we have arbitrarily set $s = 0$. Each value of q corresponds to a tone harmonic generated by the rotor source.

The general expression for rotor loading sources given in eq. (4.47) may also be used to calculate the noise generated by distributed sources which more accurately simulate a rotor. Eq. (4.47) is used here to calculate the noise generated by steady loading on the blades of an open rotor and by the unsteady loading due to interactions between the wakes emanating from an upstream contra-rotating rotor and the blades on a downstream rotor.

For the steady loading source, the Fourier transformed loading term is given by

$$\tilde{L}^{(b)}\left(X^m, r, \omega\right) = \frac{1}{2}\rho_0 U_r^2 C_L f\left(X^{(b)}\right)\delta\left(\omega\right). \quad (4.50)$$

where U_r is the speed of the rotor blade relative to the fluid, C_L is a function of blade radius and is the local lift coefficient of the blade section and here f is a dimensionless function which models the chord-wise distribution of lift. Substituting eq. (4.50) into eq. (4.47) and evaluating the summation over b will then yield

$$p(\mathbf{x},t) = \frac{-B\rho_0}{16}\sum_{n_2=0}^{\infty}\sum_{n_3=0}^{\infty}\sum_{q=-\infty}^{\infty}\frac{\mathcal{Q}_{n_2,n_3,\nu}\Psi_{n_2,n_3}\left(x_2,x_3\right)}{\Gamma_{n_2,n_3}k_{n_2,n_3}} \times \exp\left\{\mathrm{i}\nu\Omega t + \mathrm{i}\left(\frac{M\kappa \pm k_{n_2,n_3}}{\beta^2}\right)x_1\right\}\int_{R_h}^{R_t} J_\nu\left(k_r r\right)U_r^2 c C_L \Psi_L k_Y \exp\left\{-\mathrm{i}\phi_s\right\}\mathrm{d}r. \quad (4.51)$$

which is an expression for the acoustic pressure generated by steady loading forces on Open Rotor blades situated in a rectangular cross section wind tunnel. Here c is the rotor blade chord and is a function of blade radius, $\nu = qB$, $\kappa = \nu\Omega/c_0$, $\bar{X}^{(b)} = X^{(b)}/c$,

$$\phi_s = \left[\left(\frac{M\kappa \pm k_{n_2,n_3}}{\beta^2}\right)\cos\alpha + \nu\frac{\sin\alpha}{r}\right]s, \quad (4.52)$$

$$k_c = \left[\left(\frac{M\kappa \pm k_{n_2,n_3}}{\beta^2}\right)\cos\alpha + \nu\frac{\sin\alpha}{r}\right]c, \tag{4.53}$$

$$k_Y = \left[\left(\frac{M\kappa \pm k_{n_2,n_3}}{\beta^2}\right)\sin\alpha - \nu\frac{\cos\alpha}{r}\right], \tag{4.54}$$

and

$$\Psi_L = \int_{-1/2}^{1/2} f\left(X^{(b)}\right)\exp\left\{-\mathrm{i}k_c\bar{X}^{(b)}\right\}\,\mathrm{d}\bar{X}^{(b)}. \tag{4.55}$$

A model for noise generated by the unsteady loading on the blades of the rear rotor, which is caused by contra-rotating wakes generated at the front rotor, is now presented. The unsteady loading caused by the periodic distortion and on a single blade, here indexed by $b = 0$, is first expressed as a Fourier Series

$$L^{(0)}\left(X^{(0)}, r, \tau\right) = \sum_{k=-\infty}^{\infty} L_k^{(0)}\left(X^{(0)}, r\right)\exp\left\{\mathrm{i}kB_1\left(\Omega_1+\Omega_2\right)\tau\right\} \tag{4.56}$$

where

$$L_k^{(0)}\left(X^{(0)}, r\right) = \frac{1}{T}\int_0^T L^{(0)}\left(X^{(0)}, r, \tau\right)\exp\left\{-\mathrm{i}kB_1\left(\Omega_1+\Omega_2\right)\tau\right\}\,\mathrm{d}\tau \tag{4.57}$$

and the period $T = 2\pi/\left(B_1\left(\Omega_1+\Omega_2\right)\right)$.

Note that the loading on the b^{th} blade is related to the reference blade by

$$\begin{aligned} L^{(b)}\left(X^{(b)}, r, \tau\right) &= L^{(0)}\left(X^{(b)}, r, \tau + \frac{2\pi b}{B_2\left(\Omega_1+\Omega_2\right)}\right) \\ &= \sum_{k=-\infty}^{\infty} L_k^{(0)}\left(X^{(b)}, r\right)\exp\left\{\mathrm{i}kB_1\left(\Omega_1+\Omega_2\right)\tau + 2\pi\mathrm{i}bk\frac{B_1}{B_2}\right\} \end{aligned} \tag{4.58}$$

and so

$$\tilde{L}^{(b)}\left(X^{(b)},r,\omega\right)=\frac{1}{2\pi}\int_{-\infty}^{\infty}\sum_{k=-\infty}^{\infty}L_k^{(0)}\left(X^{(b)},r\right)\exp\left\{-\mathrm{i}\left(\omega-kB_1\left(\Omega_1+\Omega_2\right)\right)\tau+2\pi\mathrm{i}bk\frac{B_1}{B_2}\right\}\,\mathrm{d}\tau$$
$$=\sum_{k=-\infty}^{\infty}L_k^{(0)}\left(X^{(b)},r\right)\exp\left\{2\pi\mathrm{i}bk\frac{B_1}{B_2}\right\}\delta\left(\omega-kB_1\left(\Omega_1+\Omega_2\right)\right)\quad(4.59)$$

Replace eq. (4.59) into eq. (4.47) and evaluate the summation over b to obtain the expression for the acoustic pressure caused by the wake interaction source on an Open Rotor installed in a rectangular cross section wind tunnel

$$p(\mathbf{x},t)=\frac{-B_2}{8}\sum_{n_2=0}^{\infty}\sum_{n_3=0}^{\infty}\sum_{q=-\infty}^{\infty}\sum_{k=-\infty}^{\infty}\frac{\mathcal{Q}_{n_2,n_3,\nu}\Psi_{n_2,n_3}\left(x_2,x_3\right)}{\Gamma_{n_2,n_3}k_{n_2,n_3}}$$
$$\exp\left\{\mathrm{i}\left(qB_2\Omega_2+kB_1\Omega_1\right)t+\mathrm{i}\left(\frac{M\kappa\pm k_{n_2,n_3}}{\beta^2}\right)x_1\right\}\int_{R_h}^{R_t}J_\nu\left(k_r r\right)c\Psi_L k_Y\exp\left\{-\mathrm{i}\phi_s\right\}\,\mathrm{d}r.\quad(4.60)$$

Note that the original parameters in eq. (4.60) reference the rear rotor since this is where the sound is emitted from. Thus these parameters have been adjusted with the subscript 2 where necessary. For this expression, $\nu=qB_2-kB_1$, $\kappa=\left(qB_2\Omega_2+kB_1\Omega_1\right)/c_0$,

$$\Psi_L=\int_{-1/2}^{1/2}L_k^{(0)}\left(X^{(b)},r\right)\exp\left\{-\mathrm{i}k_c\bar{X}^{(b)}\right\}\,\mathrm{d}\bar{X}^{(b)}\quad(4.61)$$

and the other parameters are defined as before.

The benefit of using Graf's addition theorem arises from the potential improvements in speed or accuracy. Using a rectangular co-ordinate system for the Green's function results in an expression that contains an extra ϕ integral which would need to be evaluated numerically. By converting the expression to cylindrical co-ordinates, via Graf's addition theorem, the ϕ integral may instead be solved analytically. The benefits obtained in either speed or accuracy will thus arise from the margin of error to which the numerical integral is evaluated and ultimately is determined by the number of function calls that are required by the integration routine being used. Assuming an acceptable margin of error, the amount of speed up will also depend on a number of other modelling parameters as well, such as for example the observer position or evaluated mode count. As an example, a comparable calculation was conducted using both forms of the expression. An adaptive Gauss-Kronod quadrature routine implemented in MATLAB was used for numerical integration. When generating a pressure contour at constant axial position

near the plane of the rotor, such as those presented in this paper, a calculation speed up of three orders of magnitude was noted when using the expression formed by Graf's addition theorem.

4.2.2 Circular Cross-Section Wind Tunnel

Similar expressions may also be easily derived for a wind tunnel with a circular cross-section. A diagram representing this cross-section was also presented in Figure 4.2. In this case the rotor axis and wind tunnel axis are collinear. The frequency domain Green's function is still of similar form to that presented in eq. (4.12) but it is more convenient to formulate the expression in cylindrical co-ordinates, such that

$$G_\omega\left(\mathbf{y}\,|\,\mathbf{x}\right) = -\frac{\mathrm{i}}{2}\sum_m\sum_n \frac{\Psi^*_{mn}\left(\phi_x, r_x\right)\Psi_{mn}\left(\phi_y, r_y\right)}{\Gamma_{mn}k_{mn}} \times \exp\left\{-\mathrm{i}\left[\frac{M\kappa}{\beta^2}\left(y_1 - x_1\right) + \frac{k_{mn}}{\beta^2}|x_1 - y_1|\right]\right\} \quad (4.62)$$

where the summation indices n_2 and n_3 have been exchanged for m and n to differentiate them from the previous case and here we have allowed for the possibility of complex eigenfunctions. A derivation of this Green's function is presented in section 4.B. The eigenfunction Ψ_{mn} is again a solution to eq. (4.10) over the cross section of the duct and expressing this in cylindrical co-ordinates leads to

$$\left(\frac{1}{r_y^2}\frac{\partial^2}{\partial\phi_y^2} + \frac{1}{r_y}\frac{\partial}{\partial r_y} + \frac{\partial^2}{\partial r_y^2} + \varkappa_{mn}^2\right)\Psi_{mn} = 0 \quad (4.63)$$

As previously, a wall boundary condition must also be satisfied, which in this case is only dependant on the radial co-ordinate r. For example, for a rigid wall wind tunnel, the boundary condition is

$$\frac{\partial\Psi_{mn}}{\partial r} = 0. \quad (4.64)$$

For a cylindrical wind tunnel, we use the following definition for the eigenfunction set

$$\Psi_{mn}\left(r,\phi\right) = J_m\left(\varkappa_{mn}r\right)\exp\left\{\mathrm{i}m\phi\right\}. \quad (4.65)$$

As before $\varkappa_{mn}$ can be determined by using the boundary condition, so for the rigid wall case these are quite easily determined by finding the zeros of the derivative of the Bessel

function J. Note that for each order m of the Bessel function, there will be infinite zeros to find, which are specified by the index n. m and n respectively correspond to azimuthal and radial mode numbers. The zeros are found by using an iterative search routine (for example using a bi-section method), in a similar fashion to the method required for finding the eigenvalues of a rectangular wind tunnel with an impedance boundary. Also in this case, when the orthogonality condition is satisfied,

$$\Gamma_{mn} = \int_A \Psi_{mn}\Psi_{mn}^* \,\mathrm{d}A = \int_0^{L_r}\int_0^{2\pi} J_m\left(\varkappa_{mn} r_y\right) J_m^*\left(\varkappa_{mn} r_y\right) \exp\left\{\mathrm{i}\left(m-m\right)\phi_y\right\} r_y \,\mathrm{d}\phi_y \,\mathrm{d}r_y \tag{4.66}$$

and again making use of the rigid wall boundary condition to solve the integral over r (and the fact that in our analysis we only consider real values of $\varkappa_{mn}$) then yields

$$\begin{aligned}\Gamma_{mn} &= 2\pi \int_0^{L_r} J_m^2\left(\varkappa_{mn} r_y\right) r_y \,\mathrm{d}r_y = \left[\frac{r_y^2}{2}\left[J_m'\left(\varkappa_{mn} r_y\right)\right]^2 + \frac{r_y^2}{2}\left(1 - \frac{m^2}{\left(\varkappa_{mn} r_y\right)^2}\right)\left[J_m\left(\varkappa_{mn} r_y\right)\right]^2\right]_0^{L_r} \\ &= \frac{L_r^2}{2}\left(1 - \frac{m^2}{\left(\varkappa_{mn} L_r\right)^2}\right)\left[J_m\left(\varkappa_{mn} L_r\right)\right]^2 = \frac{L_r^2\varkappa_{mn}^2 - m^2}{2\varkappa_{mn}^2}\left[J_m\left(\varkappa_{mn} L_r\right)\right]^2 \end{aligned} \tag{4.67}$$

Replacing these terms into eq. (4.62) gives

$$G_\omega\left(\mathbf{y}\,|\,\mathbf{x}\right) = -\frac{\mathrm{i}}{2}\sum_{m=-\infty}^{\infty}\sum_{n=0}^{\infty}\frac{J_m\left(\varkappa_{mn} r_y\right) J_m\left(\varkappa_{mn} r_x\right)}{k_{mn}\Gamma_{mn}} \exp\left\{-\mathrm{i}\left[K^{\pm}\left(x_1 - y_1\right) - m\left(\phi_y - \phi_x\right)\right]\right\} \tag{4.68}$$

Expression for Rotor Loading Sources

Replacing eqs. (4.6), (4.7), (4.11), (4.68) and (4.45) into eq. (4.8) yields

$$p\left(\mathbf{x},t\right)=\frac{1}{2}\sum_{b=1}^{B}\sum_{m=-\infty}^{\infty}\sum_{n=0}^{\infty}\int_{r_h}^{r_t}\int_{-c/2}^{c/2}\int_{-\infty}^{\infty}\left[K_1^{\pm}\sin\alpha+\frac{m\cos\alpha}{r}\right]$$
$$\times\frac{\tilde{L}\left(X^{(b)},r,\omega-m\Omega\right)J_m\left(\varkappa_{mn}r_y\right)J_m\left(\varkappa_{mn}r_x\right)}{k_{mn}\Gamma_{mn}}$$
$$\times\exp\left\{\mathrm{i}\omega t-\mathrm{i}K^{\pm}x_1-\mathrm{i}m\phi_x+\frac{2\pi\mathrm{i}bm}{B}+\mathrm{i}\left[K_1^{\pm}\cos\alpha+\frac{m\sin\alpha}{r}\right]\left(s+X^{(b)}\right)\right\}\mathrm{d}\omega\,\mathrm{d}X\,\mathrm{d}r_y \tag{4.69}$$

This is a general loading expression. For a rotating point force, set s = 0 (zero sweep) and substitute eq. (4.48). Solving the remaining integrals and the summation over b gives

$$p\left(\mathbf{x},t\right)=\sum_{m=-\infty}^{\infty}p_m\exp\left\{\mathrm{i}\nu\Omega t\right\} \tag{4.70}$$

and

$$p_m=\frac{BF}{2}\sum_{n=0}^{\infty}\left[K_1^{\pm}\sin\alpha+\frac{\nu\cos\alpha}{a}\right]\frac{J_\nu\left(\varkappa_{mn}a\right)J_\nu\left(\varkappa_{mn}r_x\right)}{\Gamma_{mn}k_{mn}}$$
$$\times\exp\left\{-\mathrm{i}\nu\phi_x-\mathrm{i}K_1^{\pm}x_1\right\} \tag{4.71}$$

where $\nu=mB$ and $\kappa=\nu\Omega/c_0$. Each value of m corresponds to a tone harmonic generated by the rotor source.

The general expression given in eq. (4.69) may also be used to consider distributed (and more realistic) rotor loading sources placed in a circular cross section wind tunnel. An expression for the tonal noise generated by the steady loading rotor source can be used by replacing eq. (4.50) into eq. (4.69), which after some manipulation yields the following expression of acoustic pressure for each rotor tone harmonic m

$$p_m=\frac{B\rho_0}{4}\sum_{n=-\infty}^{\infty}\frac{J_\nu\left(\varkappa_{mn}r_x\right)}{\Gamma_{mn}k_{mn}}\exp\left\{-\mathrm{i}\left(\frac{-M\kappa\pm k_{mn}}{\beta^2}\right)x_1-\mathrm{i}\nu\phi_x\right\}$$
$$\times\int_{R_h}^{R_t}\left[K_1^{\pm}\sin\alpha+\frac{\nu\cos\alpha}{r_y}\right]J_\nu\left(\varkappa_{mn}r_y\right)cU_r^2C_L\Psi_L\exp\left\{-\mathrm{i}\phi_s\right\}\mathrm{d}r_y \tag{4.72}$$

where ν and κ are defined as before, but k_c has changed from its previous definition

$$k_c = \left[K_1^{\pm} \cos\alpha + \frac{\nu \sin\alpha}{r} \right] c \tag{4.73}$$

and now $\phi_s = k_c s/c$. An expression for the acoustic pressure caused by unsteady loading on the rear rotor, which in turn is due to wakes generated by the front rotor, can be derived in a similar fashion using eq. (4.59). The expression for acoustic pressure is given by

$$p(\mathbf{x},t) = \frac{B_2}{2} \sum_{m=-\infty}^{\infty} \sum_{k=-\infty}^{\infty} \sum_{n=0}^{\infty} \frac{J_\nu(\varkappa_{mn} r_x)}{\Gamma_{mn} k_{mn}} \exp\left\{ \mathrm{i}\omega_{km} t - \mathrm{i}\left(\frac{-M\kappa \pm k_{\nu,n}}{\beta^2} \right) x_1 - \mathrm{i}\nu\phi_x \right\}$$
$$\times \left[K_1^{\pm} \sin\alpha + \frac{\nu \cos\alpha}{r} \right] \int_{R_h}^{R_t} J_\nu(\varkappa_{mn} r_y)\, c\Psi_L \exp\{\mathrm{i}\phi_s\}\, \mathrm{d}r_y. \tag{4.74}$$

where now $\nu = mB_2 - kB_1$, $\omega = kB_1\Omega_1 + mB_2\Omega_2$ and Ψ_L is defined by eq. (4.61).

4.3 Analysis

Eqs. (4.49) and (4.70) are used to understand the impact of wind tunnel reverberation on the noise generated by rotating point dipoles. The equations are used to assess what effect the rigidity of the wind tunnel walls and the shape of the wind tunnel cross section may have on the reverberant noise field. This is a simplification of the problem of rotor tone noise in a wind tunnel environment. However it has been shown that in the free-field a source at a single, correctly identified, radial station is in most cases a great approximation for the field generated by a radial distribution of sources, and further to this, Peake and Boyd have shown that the near-field effects are also modelled suitably well by this approximation (Peake and Boyd, 1993), the importance of which will become apparent. The number of rotating point dipoles corresponds to the number of blades on the rotor being modelled and the dipole orientation corresponds to the direction of the loading force. In the following analyses, the force strength is arbitrarily set to 1.

The effect of tunnel wall impedance on the rotating point dipole noise field is demonstrated in Figure 4.3. The rectangular cross section wind tunnel model is used with a purely resistive impedance set equal to fluid impedance (i.e. $\Lambda = 1$). Note that there is no flow in the wind tunnel.

In Figure 4.3 the finite impedance tunnel model is compared to a free-field model (i.e. with no scattering objects present). The free-field pressure is expressed by

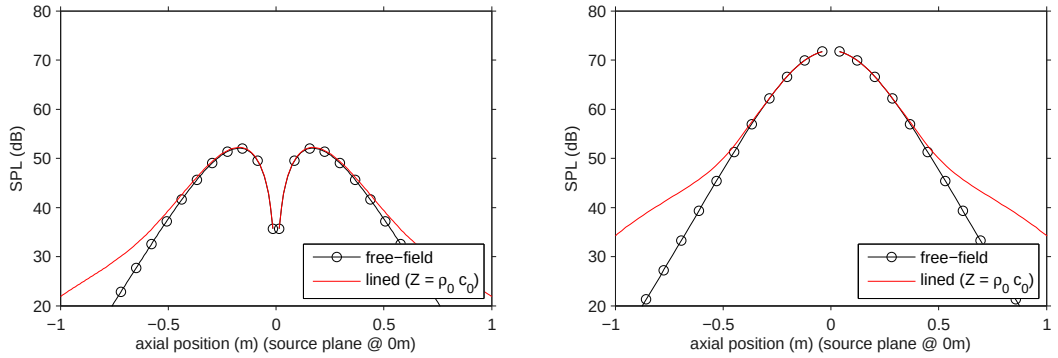

(A) (B)

FIGURE 4.3: Directivities produced by (a) axial point forces and (b) tangential point forces. Here, the specific acoustic impedance of the lined wind tunnel model (red) is set to 1 and compared with a free-field point force model (black).

$$p(\mathbf{x},t) = \frac{BF}{8\pi}\int_{-\infty}^{\infty}\left[k_1\sin\alpha - \frac{\nu\cos\alpha}{a}\right]J_\nu(k_r r_<)\,H_\nu^{(2)}(k_r r_>)$$
$$\times\exp\{\mathrm{i}\nu\Omega t + \mathrm{i}\nu\phi_x - \mathrm{i}k_1 x_1\}\,\mathrm{d}k_1 \quad (4.75)$$

where $\nu = mB$ (and m corresponds to the tone harmonic index), the radial wavenumber k_r is defined by the dispersion relation

$$k_r = \sqrt{(\kappa - k_1 M)^2 - k_1^2} \quad (4.76)$$

and $r_<$ is the smaller of the parameters r_x and r_y whilst $r_>$ corresponds to the larger of the two. Therefore these parameters depend on whether the observer is radially in- or outboard of the source. All the other parameters are consistent with previous definitions.

Figure 4.3 shows how, for both axially oriented rotating point dipoles (representing propeller thrust) and circumferentially oriented rotating point dipoles (representing propeller torque) in a wind tunnel, the field in the region of the source is a close match to that observed in the free-field. This is an expected result, since for incidence angles roughly normal to the wall the acoustic impedance is almost equivalent to the fluid impedance (as defined in eq. (4.15)). Therefore for this case measurements taken in a region close to the rotor disc plane would be free from contamination by the reverberant noise field.

Under ideal conditions, the acoustic liner insert designed for Open Rotor testing in the ARA wind tunnel would achieve similar results to the example case demonstrated in

Figure 4.3. However, at high flow speeds, it is believed that the refraction of noise in the tunnel wall boundary layer has an inhibiting effect on the performance of the acoustic liner, in particular upstream of the source, and results in a degradation of attenuation (P Murray, personal communication, 2014). The degradation is more notable at higher flow speeds ($M > 0.5$). However, the effect of the boundary layer is not modelled here due to the current assumption of plug flow. Degradation in the liner's performance at high flow speeds has also been noted in previous research (Kirker, 1990) and thus, as an initial approximation, the walls are modelled as rigid instead. McAlpine describes the validity of a similar approximation at high speed (and frequency) for the application of acoustic liners in mitigating buzz-saw tone noise (McAlpine et al., 2007).

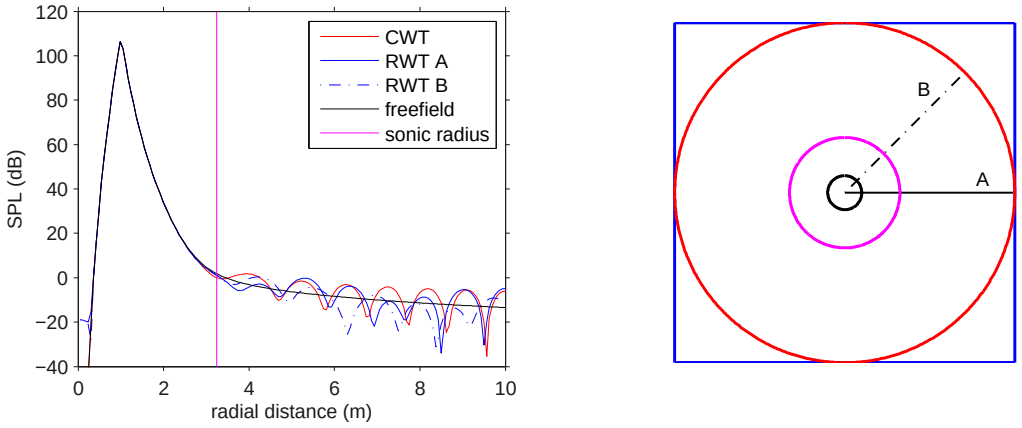

(A) (B)

FIGURE 4.4: Comparison of the rectangular (RWT) and circular (CWT) cross section wind tunnel models with a free-field model for the sound generated by rotating point dipoles, shown on (a). The dimensions for both tunnels are represented in (b) along with the source radius (black) and sonic radius of the source (magenta). The arrays on which the RWT model were evaluated are represented by the letters A and B. The fields generated by the CWT and free-field models are axisymmetric

Figure 4.4 shows a comparison between the rectangular and circular cross section wind tunnel models for rotating point dipoles. An equivalent free-field model is included in the comparison. A schematic of the wind tunnels setups is also given in Figure 4.4. The wind tunnels are sized so that a square cross section is compared to a circular one, where the width of the square is equal to the circle diameter. The axis of the rotating source (the path of the source is shown in the schematic as a black circle) is aligned to the centreline of both wind tunnels. The results presented in Figure 4.4 show radial variation of the sound pressure level as predicted by the two wind tunnel models and the free-field model. The results are almost in the plane of the source ($x_1 = 0.01$m, $y_1 = 0$m). Accurate calculation of the wind tunnel models in the source plane requires evaluation of the infinite modal sum, however as the observer-source axial distance increases the contribution from a larger number of cut-off modes diminishes. Therefore by increasing observer-source axial separation the number of terms to include in the sum can be exponentially reduced without significant impact on solution accuracy.

The results show that up to a certain radius the direct field of the source is dominant for the wind tunnel solutions and these are in agreement with the free-field solution. Outboard of this radius however, the impact of the tunnel's reverberant noise fields is noticeable and a reverberation pattern forms. This radius is consistent with the definition of the Mach radius r_m

$$r_m = \frac{a\sqrt{1 - M_x^2 \sin^2 \theta}}{M_s \sin \theta} \tag{4.77}$$

which, in the plane of the rotor, simplifies to the sonic radius

$$r_s = \frac{a\sqrt{1 - M_x^2}}{M_s} \tag{4.78}$$

where again, M is the (axial) flow Mach number and the variable M_s is the relative Mach number of the source. The polar observer angle, θ, has also been introduced.

Furthermore, when considering no flow, the sonic radius is simply R_t/M_t. Note that $M_t = a\Omega/c_0$ and is the rotational Mach number (a being the rotation radius of the source). The sonic radius is an important concept in rotor acoustics since it separates regions in which the noise field exhibits evanescent radiation (inboard) and sinusoidal radiation (outboard). Note how the field exhibits 'far-field' behaviour outboard of the sonic radius, where decay of the pressure amplitude is inversely proportional to the sideline distance. However inboard of the sonic radius the field exhibits 'near-field' behaviour and decay from the source radius occurs at a faster rate. Most importantly, the amplitude of acoustic pressure of the direct noise field is much larger than that of the reverberant field in the 'near-field' region, which is why a reverberation pattern fails to form in this region and the tunnel solutions are well matched to the free-field. The essentially uncontaminated field in the rotor's near-field may be used to accurately quantify the noise output of the rotor. This information may also be extrapolated to predict rotor noise at far-field positions. An extrapolation tool is described in Chapter 3, based on the work of Peake and Boyd (1993) and, as previously mentioned, this tool has already been applied to measurements from this test rig, further documented in Parry et al. (2012).

An obvious difference between both wind tunnel models is in the regularity in the reverberation pattern of the level and position of the lobes generated. The circular wind tunnel solution has a fairly regular pattern of lobes and since the field is axisymmetric this does not change with the azimuthal angle of the radial array. Similar observations are not true for the rectangular cross-section model. The pattern is affected by azimuthal angle (as seen by differences in the results generated at arrays A and B in Figure 4.4) and furthermore the regularity in the features of the lobes that is demonstrated in the circular wind tunnel solution is not present in the rectangular one, even for array A,

at which the tunnel wall is normal and at the same distance from the source as in the circular model. Array A and B are selected arbitrarily in this case and simply to demonstrate the variation caused by azimuthal angle for the field in the square cross-section wind tunnel. The reverberation pattern across the whole cross-section of a rectangular cross-section wind tunnel can be quite complex and is presented and discussed in the next section of this paper.

4.3.1 Simulation of the ARA's Transonic Wind Tunnel

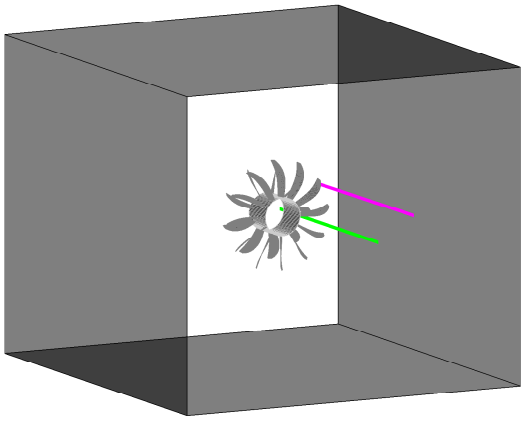

FIGURE 4.5: Diagram representing Rolls-Royce's Rig 145 in the ARA wind tunnel in Bedford. Measurement rails at typical puller and pusher sidelines have also been included.

Figure 4.5 is a simplified schematic of Rig 145 in ARA's Transonic Wind Tunnel test section (with the acoustic liner inserted). Also included in the figure are two measurement rails, which are placed at sideline distances equivalent to the aircraft passenger cabin distance for Open Rotor installations in both the pusher and puller configuration. Obtaining measurements at these sideline distances would be useful for predicting the level of noise inside the passenger cabin during cruise flight on an Open Rotor powered aircraft.

The contours in Figure 4.6 show the sound pressure level of a set of rotating dipoles in a rectangular cross section wind tunnel with rigid and finite impedance walls. The results simulate the sound pressure level of the [1,0] tone (i.e. the blade passing frequency tone of the first rotor) generated by Rig 145 in ARA's Transonic Wind Tunnel (as shown in Figure 4.5). The result for a rigid wall wind tunnel in Figure 4.6 (a) gives a visible indication of the complex reverberation pattern that is generated for rotating sources in a rectangular wind tunnel. A rotational symmetry of order 2 is noted on the cross-section, but other than this there is no obvious pattern to the reverberant field,

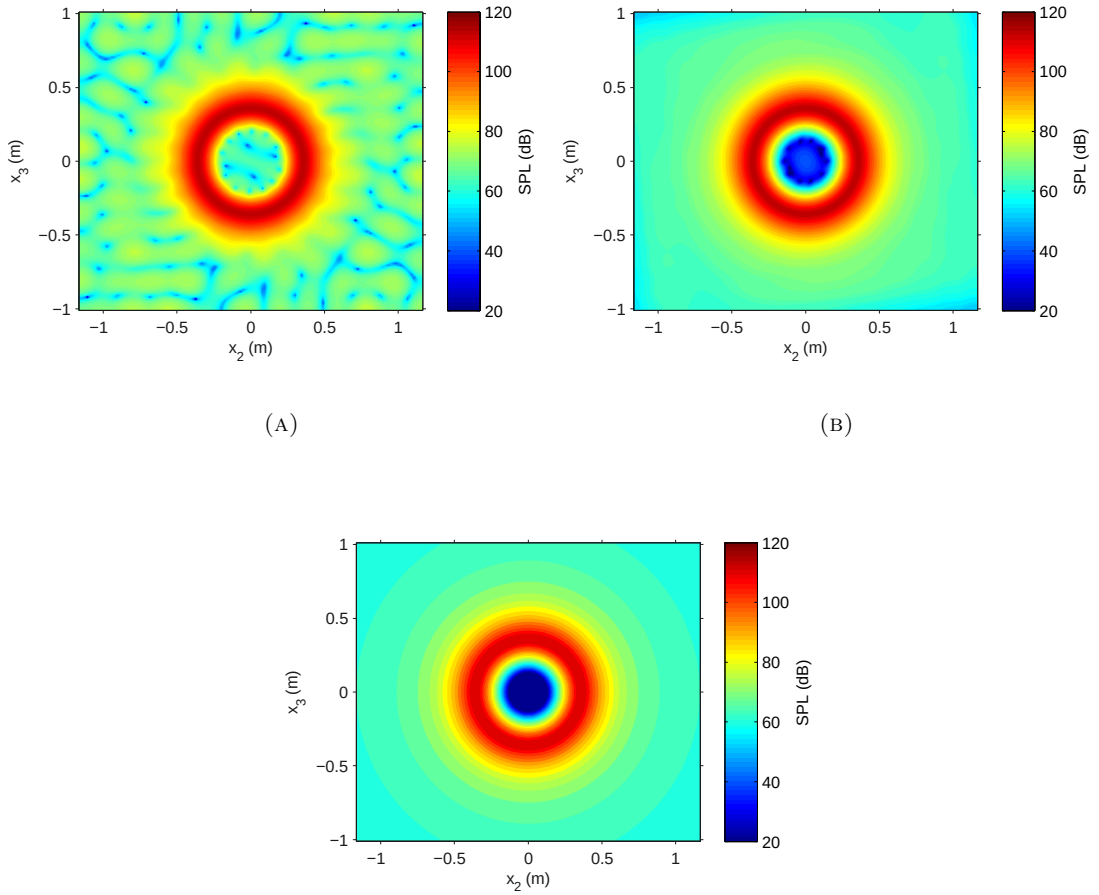

(A) (B)

(C)

FIGURE 4.6: Contours of the sound pressure level of a set of rotating point forces, on the cross section of ARA's transonic wind tunnel with (a) rigid walls and (b) walls with impedance $Z = \rho_0 c_0$. An equivalent solution using a free-field model is presented in (c). The contour plane ($x_1 = 0.01$m) is close to the source plane ($y_1 = 0$m), in order to assess near-field noise radiation in the tunnel.

which makes prediction of the impact of reverberation on the rotor noise field difficult. In contrast, imposing an impedance $Z = \rho_0 c_0$ on the walls, as in the contour shown in Figure 4.6 (b), significantly reduced the effect of reverberation. The field closely (but not precisely) resembles the noise field of the source in the free-field, which is axisymmetric. For reference the free-field result is shown in Figure 4.6 (c).

4.3.2 Simulations of ONERA's S1MA wind tunnel

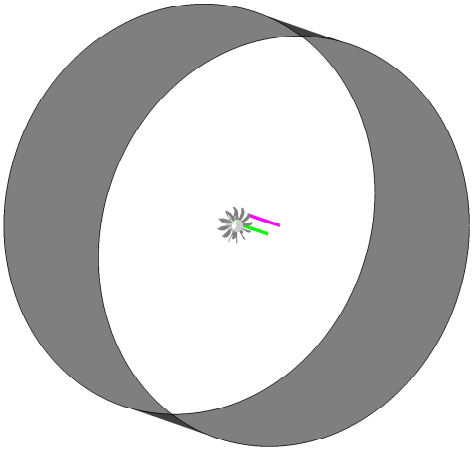

FIGURE 4.7: Diagram representing Rolls-Royce's Rig 145 in the S1MA wind tunnel in Modane. Measurement rails at typical puller and pusher sidelines have also been included.

Figure 4.7 is a schematic approximating the installation of Rig 145 in ONERA's S1MA wind tunnel test section. In this analysis the tunnel walls are assumed to be perfectly rigid and the test rig is installed exactly at the tunnel centreline. Note that to date, testing of Rig 145 has never been conducted in this wind tunnel. However the S1MA wind tunnel is also a possible choice for conducting high speed Open Rotor noise experiments, since it is capable of flow speeds up to Mach 1. The aim of this analysis is to derive simple estimates for the potential effect of reverberation on Open Rotor tone noise. Comparison of this schematic with Figure 4.5 indicates how much larger the cross section is in this wind tunnel. Again, two measurement rails corresponding to passenger cabin sideline distances for pusher and puller Open Rotor installation are included.

The sound pressure level contour in Figure 4.8 shows how in a perfectly cylindrical wind tunnel with rigid walls the field is axisymmetric. The reverberant pattern in the wind tunnel is much simpler in structure than that observed in a rectangular cross section wind tunnel (Figure 4.6). However it is still apparent that for this case at some radial distances outboard of the source, reverberation contaminates the field. In this case, the [1,0] tone generated by a cruise condition Open Rotor has been simulated and there is again no flow in the wind tunnel.

The circular wind tunnel results are also compared with a free-field solution in Figure 4.9, where results are instead shown along a radial path in the same plane ($x_1 = 0.01$m). The figure also includes the location of the measurement rails as well as the location of the sonic radius (eq. (4.78)). The figure shows that rail 1 is within the sonic radius and so for this case it seems the sound pressure level within the wind tunnel is equivalent to

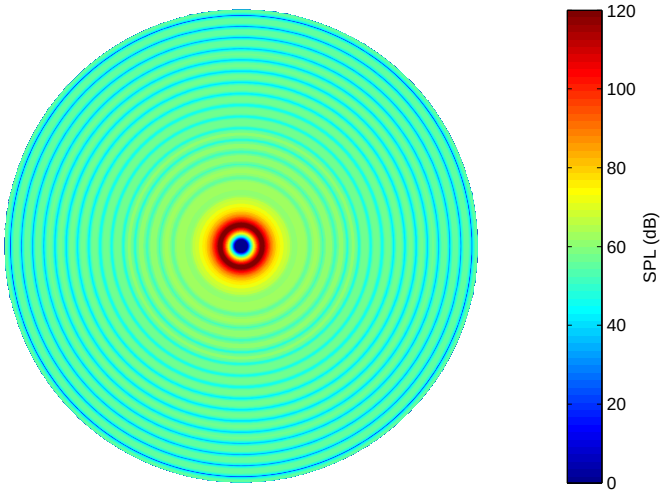

FIGURE 4.8: Contour of the sound pressure level of a set of rotating point forces, on the cross section of the S1MA wind tunnel. The contour plane ($x_1 = 0.01$m) is close to the source plane ($y_1 = 0$m), in order to assess near-field noise radiation in the tunnel.

the sound pressure level that would be expected in the free-field. Rail 2 is just outboard of the sonic radius, where the impact of the reverberant field starts, and in this case the two solutions seem to be fairly well matched at this point.

At the chosen operating conditions, the rotor speed is at the lower end of its typical operating range. This coupled with zero flow speed mean that the sonic radius is placed towards its outer limit for the operating conditions of this test rig. The wind tunnel solution does not match the free-field solution outboard of the sonic radius, however the levels are an almost perfect match inboard. The far-field levels of the two solutions are approximately similar, however it is quite clear that reverberation from the rigid tunnel walls has had an impact on the noise field in this outer region. The deviations in the wind tunnel prediction oscillate around the free-field solution, the range of which seems to expand towards the tunnel wall. This is believed to be due to interference between the direct and reflected sound fields, the levels of which are most comparable at the tunnel wall.

The conclusion then is that the sonic radius is a key factor in determining the extent of the reverberant field in a circular cross section wind tunnel. If the measurement rails are placed inboard of the sonic radius it may be expected that the result obtained in a wind tunnel may be consistent with that expected in the free-field. However the

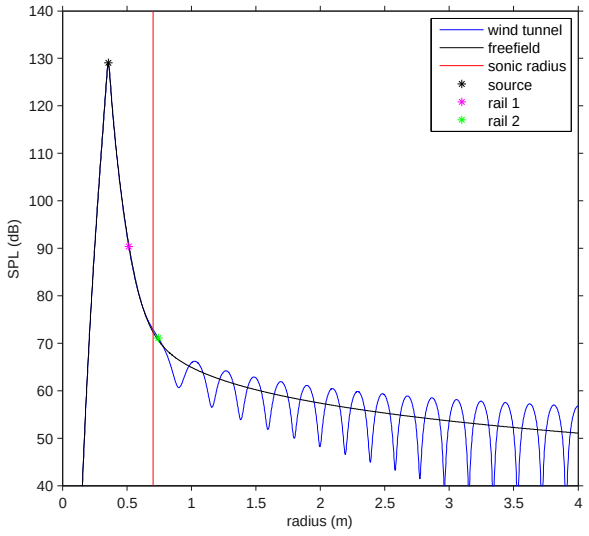

FIGURE 4.9: Simulations of the [1,0] tone generated by Rig 145 in the free-field and in the S1MA wind tunnel, with no flow. The results presented are radial directivities of the sound pressure level.

favourable conditions of this case mean that the sonic radius is near to its potential outer limit.

In Figure 4.10, it is shown that the reverberation pattern exists in the entire volume of the wind tunnel except in the near-field region, where the radiation is evanescent. Figure 4.10 shows a sound pressure level contour for the same case as before, however the contour plane has been rotated to span the tunnel radius and axis. Now, the contours represent the sound pressure level delta between the wind tunnel and free-field solutions. The contour focuses on the source region. The thick black line represents the radial extent of the source, whereas the region in white corresponds to where the wind tunnel solution was not evaluated due to computational expense. The red line indicates the boundary of the near-field region r_n defined by

$$r_n = \sqrt{r_m^2 - \frac{r_m^2 x_1^2}{r_m^2 - a^2}}. \tag{4.79}$$

This relation for the boundary was derived by analysis of the complex phase function in Prentice's rotor noise formulation and is discussed further in his paper (Prentice, 1993). It is shown that inboard of this boundary the radiation is evanescent whilst outboard radiation is sinusoidal. Again, the conclusion that can be drawn from this result is that the direct noise field of the source has a significantly larger amplitude in the rotor's 'near-field' region and so dominates the reverberant noise field. In the plane of the rotor source, the near-field boundary r_n is equivalent to the sonic radius r_m.

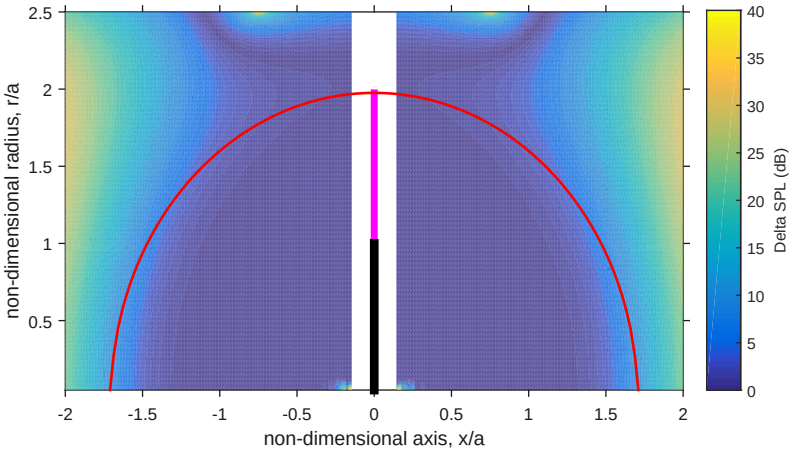

FIGURE 4.10: An axially and radially varying contour showing the delta in sound pressure level between wind tunnel and free-field solutions. The results simulate the [1,0] tone generated by Rig 145 and the S1MA wind tunnel. All distances have been made non-dimensional using the source radius, a. The red line indicates the near-field boundary of the rotor source, as predicted by eq (4.79).

The effect of flow is considered in Figure 4.11. The same parameters are chosen in this case except that now the flow Mach number $M = 0.7$, which is a typical cruise flight Mach number. The additional flow speed increases the relative Mach number of the source and thus reduces the sonic radius (see eq. (4.78)). As shown in Figure 4.11, the sonic radius is now inboard of both rail 1 and rail 2 and at these 'measurement' positions the impact of tunnel reverberation has resulted in the wind tunnel solution deviating from the free-field solution. This result suggests that at a typical cruise condition test point for Rig 145 in this wind tunnel setup, measurements made at these sideline distances should not be assumed to be equivalent to noise levels in the free-field.

Note that this case is at the lower end of operating rotor speeds for Rig 145 and an increase in rotor speed would draw the sonic radius further inboard. The source radius here is representative of the rotor tip radius and so it would not be possible to obtain measurements inboard of the source radius and near the source plane of the rotor due to the rotor's physical presence. It is possible then that during such Open Rotor test campaigns, obtaining measurements in the rotor near-field could be problematic.

The effects of reverberation on interaction tones have also been considered in Figure 4.12. The figure shows results simulating the [1,1] rotor-wake rotor interaction tone generated

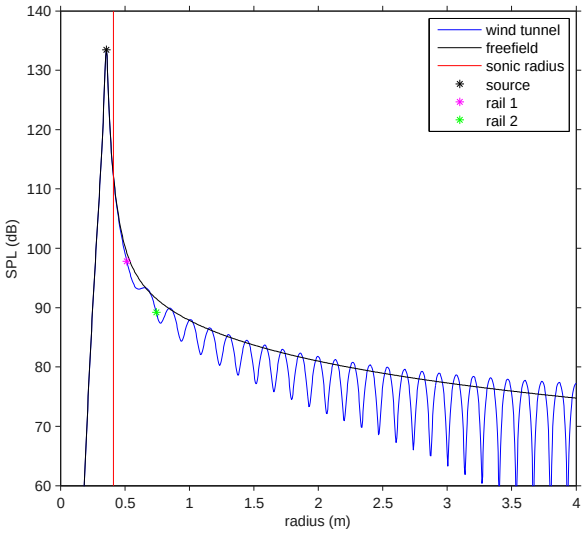

FIGURE 4.11: Simulations of the [1,0] tone generated by Rig 145 in the free-field and in the S1MA wind tunnel, with flow Mach number $M = 0.7$. The results presented are radial directivities of the sound pressure level.

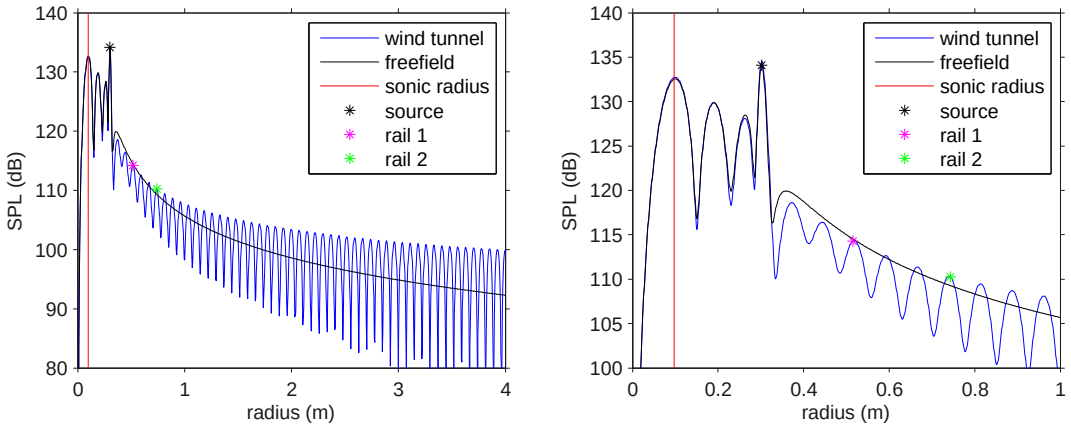

FIGURE 4.12: Simulations of the [1,1] interaction tone generated by Rig 145 in the free-field and in the S1MA wind tunnel, with flow Mach number $M = 0.7$. The results presented are radial directivities of the sound pressure level, where (a) show the directivity over the entire tunnel radius whilst (b) focuses on the source region.

by Rig 145, with results given for the rig in the S1MA wind tunnel and in the free-field. Note that for consistency the point forces have been placed at the rotor tip radius, which in terms of source propagation efficiency would not be the dominating radial station on the rotor blade for this tone. However the effects of the sonic radius are still captured effectively. The interaction tones of interest would have a higher mode phase speed caused by the counter rotation of the two propeller-fans on an open rotor. The sonic radius of an interaction tone would have to be calculated using an effective source rotation Mach number (Peake and Boyd, 1993) M'_s, defined as

$$M_s' = \frac{a\left(kB_k\Omega_k + mB_m\Omega_m\right)}{c_0\left(kB_k + mB_m\right)} \tag{4.80}$$

Note that technically, an interaction tone behaves like a rotor-locked tone that rotates with speed M_s', but with an effective tone harmonic index, ν', defined by

$$\nu' = kB_b - mB_m \tag{4.81}$$

where k and m respectively correspond to harmonics of the front and rear rotor and the subscript k and m to parameters of the front and rear rotor. The interaction tone sonic radius is shown in Figure 4.12. It is apparent from the figure that the reverberant noise field distorts the direct noise field right up to the source radius and so at any viable measurement position, interaction tones will always be affected by tunnel reverberation, in this setup. For typical open rotor operating conditions, the effective tip Mach number of interaction tones will always be highly supersonic and so it is plausible to suggest that interaction tone results in a rigid wall wind tunnel will never reflect those expected in the free-field.

4.4 Conclusions

This chapter has presented an investigation into the effect of wind tunnel reverberation on open rotor noise. The problem has been simplified to studying a rotating point force contained within a rectangular cross-section duct of infinite span. Furthermore, a technique for simplifying these expressions using Graf's addition theorem has also been presented and it is shown that this simplification greatly reduces the necessary computation time, when numerically evaluating the model. The walls are allowed varying impedance albeit currently only with no flow if the walls are not rigid. A circular cross-section model has also been implemented to present further analysis into tunnel reverberation. The effect that the walls have on the generated sound field are studied by comparison to results from equivalent free-field calculations. The conclusions can be generalised to show that acoustic observations made nearer to the rotor plane and further from the wind tunnel walls are the least affected by reverberation. More specifically, the analysis indicates that the sound pressure generated by an open rotor in a wind tunnel may not be physically similar to that generated in the free-field, unless measured in the acoustic near-field of the rotor source. This is an interesting result for the sponsor, as it suggests there is limited opportunity for acoustic measurement, if observations were only to be isolated to this 'near-field' region. In fact, for most open rotor tones generated at cruise conditions, which covers the majority of the wind tunnel experimental results, the near-field region is contained within the diameter of the propeller, where it would be practically impossible to mount microphones.

Common practice is to instead include acoustic treatments at the tunnel walls, to mitigate acoustic reflections. However, it is believed from the data analysis conducted as part of this work that when the flow Mach number is high such treatments become ineffective, or at least do not operate as intended by design. The current methods of acoustic treatment may therefore be unsuitable for cruise regime open rotor testing. Other possible options are the development of de-reverberation techniques or the use of beamforming methods, however these are not trivial for the setups explored here. In essence, the tunnel reverberation models could be a useful asset for the sponsor when designing future cruise regime experiments for their model scale test rig. Note that the models have been used to simulate the potential reverberant sound field that may develop in two existing wind tunnels; both tunnels have already been used for open rotor experimental campaigns and may again be options for future campaigns.

Appendices

4.A Method of Residues

Starting from Goldstein (1976, p64)

$$G_\omega\left(\mathbf{y}\,|\,\mathbf{x}\right) = \sum_m \sum_n f_{mn}\left(y_1\right) \Psi_{mn}\left(y_2, y_3\right) \tag{4.82}$$

where

$$\left(\beta_2 \frac{\mathrm{d}^2}{\mathrm{d}y_1^2} + 2\mathrm{i}M\kappa\frac{\mathrm{d}}{\mathrm{d}y_1} + \kappa^2 - k_{mn}^2\right) f_{mn} = -\frac{\Psi_{mn}^*\left(x_2, x_3\right)}{\Gamma_{mn}} \delta\left(x_1 - y_1\right) \tag{4.83}$$

and

$$\left(\frac{\partial^2}{\partial y_2^2} + \frac{\partial^2}{\partial y_3^2}\right) \Psi_{mn} = -k_{mn}^2 \Psi_{mn} \tag{4.84}$$

The Fourier transform of $f\left(y_1\right)$ is

$$f\left(k_1\right) = \frac{1}{2\pi} \int_{-\infty}^{\infty} f\left(y_1\right) \exp\left\{-\mathrm{i}k_1 y_1\right\} \mathrm{d}y_1 \tag{4.85}$$

and so the inverse is

$$f(y_1) = \int_{-\infty}^{\infty} f(k_1) \exp\{\mathrm{i}k_1 y_1\} \, \mathrm{d}k_1 \tag{4.86}$$

Take Fourier transform of eq. (4.83) which gives

$$\left(\beta^2 (\mathrm{i}k_1)^2 + 2\mathrm{i}M\kappa (\mathrm{i}k_1) + \kappa^2 - k_{mn}^2\right) \tilde{f}_{mn}(k_1) = - \frac{1}{2\pi} \int_{-\infty}^{\infty} \frac{\Psi_{mn}^*(x_2, x_3)}{\Gamma_{mn}} \exp\{-\mathrm{i}k_1 y_1\} \, \delta(x_1 - y_1) \, \mathrm{d}y_1 \tag{4.87}$$

$$\left(\kappa^2 - k_{mn}^2 - 2M\kappa k_1 - \beta^2 k_1^2\right) \tilde{f}_{mn} = -\frac{\Psi_{mn}^*(x_2, x_3)}{2\pi\Gamma_{mn}} \exp\{-\mathrm{i}k_1 x_1\} \tag{4.88}$$

$$\tilde{f}_{mn} = \frac{\Psi_{mn}^*(x_2, x_3) \exp\{-\mathrm{i}k_1 x_1\}}{2\pi\Gamma_{mn} \left(\beta^2 k_1^2 - \kappa^2 + k_{mn}^2 + 2M\kappa k_1\right)} \tag{4.89}$$

Now, taking the inverse Fourier transform yields

$$f_{mn} = \frac{\Psi_{mn}^*(x_2, x_3)}{2\pi\Gamma_{mn}} \int_{-\infty}^{\infty} \frac{\exp\{-\mathrm{i}k_1 (x_1 - y_1)\}}{\beta^2 k_1^2 + 2M\kappa k_1 - (\kappa^2 - k_{mn}^2)} \, \mathrm{d}k_1 \tag{4.90}$$

$$f_{mn} = \frac{\Psi_{mn}^*(x_2, x_3)}{2\pi\Gamma_{mn}\beta^2} \int_{-\infty}^{\infty} \frac{\exp\{-\mathrm{i}k_1 (x_1 - y_1)\}}{k_1^2 + 2M\kappa k_1/\beta^2 - (\kappa^2 - k_{mn}^2)/\beta^2} \, \mathrm{d}k_1 \tag{4.91}$$

The integral in k_1 $(= I_{k_1})$ is solved by contour integration. The denominator of the integrand is a quadratic in k_1, the solutions of which correspond to poles of the integrand in complex k_1 space. Therefore

$$k_1 = K^{\pm} = \frac{-M\kappa \pm \xi_{mn}}{\beta^2} \tag{4.92}$$

where

$$\xi_{mn} = \left(\kappa^2 - \beta^2 k_{mn}^2\right)^{\frac{1}{2}} \tag{4.93}$$

and

$$I_{k_1} = \int_{-\infty}^{\infty} \frac{\exp\left\{-\mathrm{i}k_1\left(x_1 - y_1\right)\right\}}{\left(k_1 - K^+\right)\left(k_1 - K^-\right)}\,\mathrm{d}k_1 \tag{4.94}$$

The integral I_{k_1} is solved by integrating over a closed contour and the direction in which to close the contour is selected by noting the relative value of x_1 and y_1 and the behaviour of the integrand on the complex k_1 plane.

Propagating Modes

Consider initially that we have purely real values for the infinite series of eigenvalues k_{mn}. For the values of k_{mn} which satisfy the inequality $\kappa^2 > \beta^2 k_{mn}^2$, k_1 would be purely real (for the hard wall case) and the associated acoustic mode is termed a cut-on or propagating mode. Each eigenvalue k_mn has tow propagating modes associated with it (i.e. $K^{\pm}$) and each is only considered valid (or causal) in each axial direction from the source (i.e. along negative or positive x_1). If a flow is present, the two directions are obviously termed upstream and downstream.

$K^{\pm}$ represents poles on the complex k_1 plane that lie on the real axis and the correct contour must be chosen to enclose each of these poles. Note that the exponential in the integrand changes behaviour depending on the relative values of x_1 and y_1, and that the exponential will either blow up or reduce to zero along at one of the infinities on the imaginary axis. The contour must be closed so that it passes through the infinity that reduces to zero. Therefore, all downstream oriented modes (i.e. when $x_1 > y_1$) should be contained in a clockwise contour passing through the lower half plane, whilst all upstream modes ($x_1 < y_1$) should instead be contained in an anti-clockwise contour in the lower half plane.

Now, determine if the axial wavenumbers $K^{\pm}$ correspond to either an up/downstream propagating wave by evaluating the mode group velocity,

$$\frac{\partial \omega}{\partial k_1} = c_0 \frac{\partial \kappa}{\partial k_1}. \tag{4.95}$$

To evaluate the group velocity, take

$$\beta^2 k_1^2 + 2M\kappa k_1 - \kappa^2 + k_{mn}^2 = 0 \tag{4.96}$$

and differentiate with respect to k_1, which gives

$$2\beta^2 k_1 + \left(2M\kappa + 2Mk_1 \frac{\partial \kappa}{\partial k_1}\right) - 2\kappa \frac{\partial \kappa}{\partial k_1} = 0 \tag{4.97}$$

or

$$\frac{\partial \kappa}{\partial k_1} = \frac{\beta^2 k_1 + M\kappa}{\kappa - M k_1} \tag{4.98}$$

By replacing $k_1 = K^{\pm}$ into the expression for group velocity it is possible to determine which pole corresponds to each mode.

For example, K^+ corresponds to a downstream propagating mode since

$$\frac{\partial \kappa}{\partial k_1} = \frac{\beta^2 \xi_{mn}}{\beta^2 \kappa - M\left(-M\kappa + \xi_{mn}\right)} \tag{4.99}$$

$$\frac{\partial \kappa}{\partial k_1} = \frac{\beta^2 \xi_{mn}}{\kappa - M\xi_{mn}} \tag{4.100}$$

which is positive (provided $\kappa/M > \xi_{mn}$).

In the same manner, K^- corresponds to an upstream propagating mode since

$$\frac{\partial \kappa}{\partial k_1} = \frac{-\beta^2 \xi_{mn}}{\beta^2 \kappa - M\left(-M\kappa - \xi_{mn}\right)} \tag{4.101}$$

$$\frac{\partial \kappa}{\partial k_1} = \frac{-\beta^2 \xi_{mn}}{\kappa + M\xi_{mn}} \tag{4.102}$$

which is negative (provided $\kappa/M > -\xi_{mn}$).

Thus, by noting the regions of space that $K^{\pm}$ are valid in, the axial phase exponential can be simplified into a single expression

$$\exp\left\{-\mathrm{i}K^{\pm}\left(x_1 - y_1\right)\right\} = \exp\left\{-\mathrm{i}\left[\frac{M\kappa}{\beta^2}\left(y_1 - x_1\right) + \frac{\xi_{mn}}{\beta^2}|x_1 - y_1|\right]\right\} \tag{4.103}$$

Evanescent Modes

Consider now the condition when $\kappa^2 < \beta^2 k_{mn}^2$. In order to match the convention set out by the previous condition, we require the downstream oriented modes, corresponding to K^+, to be contained in the clockwise directed contour which encircles the lower half plane. Conversely, if $x_1 < y_1$ and we consider upstream oriented waves, we require K^- poles to be situated in the upper half plane and encircled by an anti clockwise contour. This means that we select the negative imaginary root in the definition of k_1 when defining evanescent modes.

Frequency Domain Green's function

Finally, the contour integral can be evaluated by method of residues. For simple poles, likes the ones given by $K^{\pm}$, the residue of the function $f(x)$ at the pole X is evaluated as

$$\operatorname{Res}(f,x)=\lim_{x\to X}(x-X)\,f(x) \tag{4.104}$$

Here, let f represent the integrand of I_{k_1}. For a clockwise contour, which encloses the K^+ poles

$$I_{k_1}=-2\pi\mathrm{i}\operatorname{Res}\left(f,K^+\right) \tag{4.105}$$

$$I_{k_1}=-2\pi\mathrm{i}\frac{\exp\left\{-\mathrm{i}K^+(x_1-y_1)\right\}}{(K^+-K^-)} \tag{4.106}$$

$$I_{k_1}=-\frac{\mathrm{i}\pi\beta^2}{\sqrt{\kappa^2-\beta^2k_{mn}^2}}\exp\left\{-\mathrm{i}\left[\frac{M\kappa}{\beta^2}(y_1-x_1)+\frac{\xi_{mn}}{\beta^2}|x_1-y_1|\right]\right\} \tag{4.107}$$

and alternatively for the anti-clockwise contour encompassing the poles of the upstream modes

$$I_{k_1}=2\pi\mathrm{i}\operatorname{Res}(f,K^-) \tag{4.108}$$

$$I_{k_1}=2\pi\mathrm{i}\frac{\exp\left\{-\mathrm{i}K^-(x_1-y_1)\right\}}{(K^--K^+)} \tag{4.109}$$

which evaluates to the same expression as eq. (4.107). Finally, the expression for the frequency domain Green's function is therefore

$$G_\omega(\mathbf{y}\,|\,\mathbf{x})=-\frac{\mathrm{i}}{2}\sum_m\sum_n\frac{\Psi_{mn}^*(x_2,x_3)\,\Psi_{mn}(y_2,y_3)}{\Gamma_{mn}\xi_{mn}}\times\exp\left\{-\mathrm{i}\left[\frac{M\kappa}{\beta^2}(y_1-x_1)+\frac{\xi_{mn}}{\beta^2}|x_1-y_1|\right]\right\} \tag{4.110}$$

4.B Derivation of a Circular Wind Tunnel Green's Function

Start from

$$\left[\nabla_y^2 - \frac{1}{c_0^2}\left(\frac{\partial}{\partial\tau} + U\frac{\partial}{\partial y_1}\right)^2\right] G\left(\mathbf{y},\tau \,|\, \mathbf{x},t\right) = -\delta_3\left(\mathbf{x}-\mathbf{y}\right)\delta\left(t-\tau\right). \tag{4.111}$$

where

$$\mathbf{y} = \{y_1, \phi_y, r_y\} \tag{4.112}$$

$$\nabla_y^2 = \frac{1}{r_y^2}\frac{\partial^2}{\partial\phi_y^2} + \frac{1}{r_y}\frac{\partial}{\partial r_y} + \frac{\partial^2}{\partial r_y^2} + \frac{\partial^2}{\partial y_1^2} \tag{4.113}$$

$$\delta_3\left(\mathbf{x}-\mathbf{y}\right) = \delta\left(x_1-y_1\right)\delta\left(\phi_x-\phi_y\right)\frac{\delta\left(r_x-r_y\right)}{r_y} \tag{4.114}$$

To obtain a Green's function independent of time we use the following transform

$$G_\omega\left(\mathbf{y}\,|\,\mathbf{x}\right) = \int_{-\infty}^{\infty} G\exp\left\{-\mathrm{i}\omega\left(t-\tau\right)\right\}\,\mathrm{d}\tau. \tag{4.115}$$

the inverse of which is

$$G\left(\mathbf{y},\tau\,|\,\mathbf{x},t\right) = \int_{-\infty}^{\infty} G_\omega\frac{\exp\left\{\mathrm{i}\omega\left(t-\tau\right)\right\}}{2\pi}\,\mathrm{d}\omega \tag{4.116}$$

Using the above transform, the equation now becomes

$$\left[\frac{1}{r_y^2}\frac{\partial^2}{\partial\phi_y^2} + \frac{1}{r_y}\frac{\partial}{\partial r_y} + \frac{\partial^2}{\partial r_y^2} + \frac{\partial^2}{\partial y_1^2} - \left(-\mathrm{i}\kappa + M\frac{\partial}{\partial y_1}\right)^2\right] G_\omega\left(\mathbf{y}\,|\,\mathbf{x}\right) = -\delta\left(x_1-y_1\right)\delta\left(\phi_x-\phi_y\right)\frac{\delta\left(r_x-r_y\right)}{r_y} \tag{4.117}$$

where $\kappa = \omega/c_0$ and $M = U/c_0$ Defining the following Fourier transform in $\{y_1, k_1\}$ space

$$G_\omega^{100} = \int_{-\infty}^{\infty} G_\omega \frac{\exp\left\{-\mathrm{i}k_1 y_1\right\}}{2\pi}\,\mathrm{d}y_1 \tag{4.118}$$

along with its inverse

$$G_\omega = \int_{-\infty}^{\infty} G_\omega^{100} \exp\left\{\mathrm{i}k_1 y_1\right\}\,\mathrm{d}k_1 \tag{4.119}$$

yields the following transformed equation

$$\begin{aligned}\left[\frac{1}{r_y^2}\frac{\partial^2}{\partial\phi_y^2} + \frac{1}{r_y}\frac{\partial}{\partial r_y} + \frac{\partial^2}{\partial r_y^2} + (\mathrm{i}k_1)^2 - (-\mathrm{i}\kappa + \mathrm{i}k_1 M)^2\right] G_\omega^{100} \\ = -\int_{-\infty}^{\infty} \frac{\exp\left\{-\mathrm{i}k_1 y_1\right\}}{2\pi}\delta\left(x_1 - y_1\right)\delta\left(\phi_x - \phi_y\right)\frac{\delta\left(r_x - r_y\right)}{r_y}\,\mathrm{d}y_1\end{aligned} \tag{4.120}$$

Note that the Green's function can be further broken down into a Fourier series in ϕ_y where

$$G_\omega^{100} = \sum_{m=-\infty}^{\infty} G_\omega^{110} \exp\left\{\mathrm{i}m\phi_y\right\} \tag{4.121}$$

which is inverted by the following transform

$$G_\omega^{110} = \int_{-\infty}^{\infty} G_\omega^{100} \frac{\exp\left\{-\mathrm{i}m\phi_y\right\}}{2\pi}\,\mathrm{d}\phi_y \tag{4.122}$$

The Green's function, G_ω^{100} can be separated into the following functions

$$G_\omega^{100} = \sum_m \sum_n f_{mn} \Psi_{mn}\left(r_y, \phi_y\right) \tag{4.123}$$

$\Psi_{mn}\left(r_y, \phi_y\right)$ defines the eigenfunction on the face of the duct cross section which must satisfy the boundary conditions

$$\frac{\partial \Psi_{mn}}{\partial r_y} = 0; \tag{4.124}$$

and

$$\left[\frac{1}{r_y^2}\frac{\partial^2}{\partial\phi_y^2}+\frac{1}{r_y}\frac{\partial}{\partial r_y}+\frac{\partial^2}{\partial r_y^2}+k_{mn}^2\right]\Psi_{mn}\left(r_y,\phi_y\right)=0 \tag{4.125}$$

Rearranging this equation yields

$$\left[\frac{1}{r_y^2}\frac{\partial^2}{\partial\phi_y^2}+\frac{1}{r_y}\frac{\partial}{\partial r_y}+\frac{\partial^2}{\partial r_y^2}\right]\Psi_{mn}\left(r_y,\phi_y\right)=-k_{mn}^2\Psi_{mn}\left(r_y,\phi_y\right) \tag{4.126}$$

so

$$\sum_m\sum_n\left[\kappa^2-\beta^2k_1^2-2k_1M\kappa-k_{mn}^2\right]f_{mn}\Psi_{mn}=-\frac{\exp\left\{-\mathrm{i}k_1x_1\right\}}{2\pi r_y}\delta\left(\phi_x-\phi_y\right)\delta\left(r_x-r_y\right) \tag{4.127}$$

where $\beta^2=1-M^2$. Now multiply by $\Psi_{m'n'}^*\left(r_y,\phi_y\right)$ and integrate over the cross section of the duct.

$$\begin{aligned}\sum_m\sum_{m'}\int_0^{r_d}\int_0^{2\pi}&\left[\kappa^2-\beta^2k_1^2-2k_1M\kappa-k_{mn}^2\right]f_{mn}\Psi_{mn}\Psi_{m'n'}^*r_y\,\mathrm{d}\phi_y\,\mathrm{d}r_y\\&=\int_0^{r_d}\int_0^{2\pi}-\frac{\exp\left\{-\mathrm{i}k_1x_1\right\}}{2\pi}\delta\left(\phi_x-\phi_y\right)\frac{\delta\left(r_x-r_y\right)}{r_y}\Psi_{m'n'}^*\left(r_y,\phi_y\right)r_y\,\mathrm{d}\phi_y\,\mathrm{d}r_y\\&=-\frac{\exp\left\{-\mathrm{i}k_1x_1\right\}\Psi_{m'n'}^*\left(r_x,\phi_x\right)}{2\pi}\end{aligned} \tag{4.128}$$

Using orthogonality of the eigenfunction set it is clear that

$$\int_0^{r_d}\int_0^{2\pi}\Psi_{mn}\Psi_{m'n'}^*r_y\,\mathrm{d}\phi_y\,\mathrm{d}r_y=\begin{cases}\Gamma_{mn} & \text{when}\quad m=m'\text{ and }n=n'\\0 & \text{otherwise}\end{cases} \tag{4.129}$$

Now, to solve

$$\left[\frac{1}{r_y^2}\frac{\partial^2}{\partial\phi_y^2}+\frac{1}{r_y}\frac{\partial}{\partial r_y}+\frac{\partial^2}{\partial r_y^2}+k_{mn}^2\right]\Psi_{mn}\left(r_y,\phi_y\right)=0 \tag{4.130}$$

and assuming separable variables such that

$$\Psi_{mn}=R(r_y)\Phi(\phi_y) \tag{4.131}$$

means

$$\frac{R}{r_y^2}\frac{\partial^2\Phi}{\partial\phi_y^2}+\frac{\Phi}{r_y}\frac{\partial R}{\partial r_y}+\Phi\frac{\partial^2 R}{\partial r_y^2}+R\Phi k_{mn}^2=0 \tag{4.132}$$

$$\frac{1}{\Phi}\frac{\mathrm{d}^2\Phi}{\mathrm{d}\phi_y^2}+\frac{r_y}{R}\frac{\mathrm{d}R}{\mathrm{d}r_y}+\frac{r_y^2}{R}\frac{\mathrm{d}^2R}{\mathrm{d}r_y^2}+r_y^2k_{mn}^2=0 \tag{4.133}$$

$$\frac{1}{\Phi}\frac{\mathrm{d}^2\Phi}{\mathrm{d}\phi_y^2}=-m^2=-\left[\frac{r_y}{R}\frac{\mathrm{d}R}{\mathrm{d}r_y}+\frac{r_y^2}{R}\frac{\mathrm{d}^2R}{\mathrm{d}r_y^2}+r_y^2k_{mn}^2\right] \tag{4.134}$$

Therefore,

$$\Phi=\exp\left\{\mathrm{i}m\phi_y\right\} \tag{4.135}$$

and

$$\left[\frac{1}{r_y}\frac{\mathrm{d}}{\mathrm{d}r_y}+\frac{\mathrm{d}^2}{\mathrm{d}r_y^2}+k_{mn}^2-\frac{m^2}{r_y^2}\right]R=0 \tag{4.136}$$

which means

$$R=J_m\left(k_{mn}r_y\right). \tag{4.137}$$

k_{mn} must satisfy the rigid wall boundary condition

$$\frac{\partial\Psi_{mn}}{\partial\hat{\mathbf{n}}}=\frac{\mathrm{d}J_m\left(k_{mn}r_y\right)}{\mathrm{d}r_y}=J_m'\left(k_{mn}r_y\right)=0 \tag{4.138}$$

where for each order m there are infinite solutions to the above boundary condition, specified by the index n.

$$\int_0^{r_d}\int_0^{2\pi}J_m\left(k_{mn}r_y\right)J_{m'}^*\left(k_{mn}r_y\right)\exp\left\{\mathrm{i}\left(m-m'\right)\phi_y\right\}r_y\,\mathrm{d}\phi_y\,\mathrm{d}r_y \tag{4.139}$$

and since

$$\int_0^{2\pi}\exp\left\{\mathrm{i}\left(m-m'\right)\phi_y\right\}\,\mathrm{d}\phi_y=2\pi|_{m=m'} \tag{4.140}$$

and $J^*_{m'}(k_{mn}r_y) = J_{m'}(k^*_{mn}r_y)$ and all k_{mn} are real for the rigid wall boundary condition, we are left with (only when $m = m'$ and $n = n'$)

$$\begin{aligned}\Gamma_{mn} &= 2\pi \int_0^{r_d} J_m^2(k_{mn}r_y)\, r_y \,\mathrm{d}r_y \\ &= \left[\frac{r_y^2}{2}\left[J'_m(k_{mn}r_y)\right]^2 + \frac{r_y^2}{2}\left(1 - \frac{m^2}{(k_{mn}r_y)^2}\right)\left[J_m(k_{mn}r_y)\right]^2\right]_0^{r_d} \\ &= \frac{r_d^2}{2}\left(1 - \frac{m^2}{(k_{mn}r_d)^2}\right)\left[J_m(k_{mn}r_d)\right]^2 = \frac{r_d^2 k_{mn}^2 - m^2}{2k_{mn}^2}\left[J_m(k_{mn}r_d)\right]^2 \end{aligned} \tag{4.141}$$

Rearrange for f_{mn}

$$f_{mn} = -\frac{\exp\{-\mathrm{i}k_1x_1\}\,\Psi^*_{mn}(r_x,\phi_x)}{2\pi\Gamma_{mn}\left[\kappa^2 - \beta^2k_1^2 - 2k_1M\kappa - k_{mn}^2\right]} \tag{4.142}$$

means that

$$G_\omega^{100} = \sum_{m=-\infty}^{\infty}\sum_{n=0}^{\infty} -\frac{\exp\{-\mathrm{i}k_1x_1\}\,\Psi_{mn}(r_y,\phi_y)\,\Psi^*_{mn}(r_x,\phi_x)}{2\pi\Gamma_{mn}\left[\kappa^2 - \beta^2k_1^2 - 2k_1M\kappa - k_{mn}^2\right]} \tag{4.143}$$

so

$$G_\omega^{100} = \sum_{m=-\infty}^{\infty}\sum_{n=0}^{\infty} -\frac{\exp\{-\mathrm{i}k_1x_1 + \mathrm{i}m(\phi_y - \phi_x)\}\,J_m(k_{mn}r_y)\,J_m(k^*_{mn}r_x)}{2\pi\Gamma_{mn}\left[\kappa^2 - \beta^2k_1^2 - 2k_1M\kappa - k_{mn}^2\right]}. \tag{4.144}$$

Taking the inverse Fourier Transform yields

$$\begin{aligned}G_\omega = \sum_{m=-\infty}^{\infty}\sum_{n=0}^{\infty} -\frac{\exp\{\mathrm{i}m(\phi_y - \phi_x)\}\,J_m(k_{mn}r_y)\,J_m(k^*_{mn}r_x)}{2\pi\Gamma_{mn}} \\ \times \int_{-\infty}^{\infty} \frac{\exp\{-\mathrm{i}k_1(x_1 - y_1)\}}{\left[\kappa^2 - \beta^2k_1^2 - 2k_1M\kappa - k_{mn}^2\right]}\,\mathrm{d}k_1 \end{aligned} \tag{4.145}$$

$$I_{k_1} = \frac{-1}{\beta^2}\int_{-\infty}^{\infty} \frac{\exp\{-\mathrm{i}k_1(x_1 - y_1)\}}{\left[k_1^2 + 2k_1M\kappa/\beta^2 - (\kappa^2 - k_{mn}^2)/\beta^2\right]}\,\mathrm{d}k_1 \tag{4.146}$$

Set

$$I_{k_1} = \frac{-1}{\beta^2} \int_{-\infty}^{\infty} \frac{\exp\left\{-\mathrm{i}k_1\left(x_1 - y_1\right)\right\}}{\left(k_1 - K_1^+\right)\left(k_1 - K_1^-\right)} \,\mathrm{d}k_1 \tag{4.147}$$

where

$$K_1^{\pm} = \frac{-\kappa M \pm \xi_{mn}}{\beta^2} \tag{4.148}$$

and

$$\xi_{mn} = \left(\kappa^2 - \beta^2 k_{mn}^2\right)^{\frac{1}{2}} \tag{4.149}$$

Use contour integration to evaluate k_1 integral. For $x_1 > y_1$,

$$I_{k_1} = \frac{-1}{\beta^2}\left[\frac{-2\pi\mathrm{i}\exp\left\{-\mathrm{i}K_1^+\left(x_1 - y_1\right)\right\}}{K_1^+ - K_1^-}\right] = \frac{2\pi\mathrm{i}\exp\left\{-\mathrm{i}K_1^+\left(x_1 - y_1\right)\right\}}{\beta^2\left(K_1^+ - K_1^-\right)} \tag{4.150}$$

and for $x_1 < y_1$

$$I_{k_1} = \frac{-1}{\beta^2}\left[\frac{2\pi\mathrm{i}\exp\left\{-\mathrm{i}K_1^-\left(x_1 - y_1\right)\right\}}{K_1^- - K_1^+}\right] = \frac{-2\pi\mathrm{i}\exp\left\{-\mathrm{i}K_1^-\left(x_1 - y_1\right)\right\}}{\beta^2\left(K_1^- - K_1^+\right)} \tag{4.151}$$

The frequency domain Green's function can therefore be completely defined by the following, single expression

$$G_\omega\left(\mathbf{y}\,|\,\mathbf{x}\right) = -\frac{\mathrm{i}}{2}\sum_m\sum_n \frac{J_m\left(k_{mn}r_y\right)J_m\left(k_{mn}^* r_x\right)}{\xi_{mn}\Gamma_{mn}} \times \exp\left\{-\mathrm{i}\left[K^{\pm}\left(x_1 - y_1\right) - m\left(\phi_y - \phi_x\right)\right]\right\} \tag{4.152}$$

$$G_\omega\left(\mathbf{y}\,|\,\mathbf{x}\right) = -\frac{\mathrm{i}}{2}\sum_m\sum_n \frac{J_m\left(k_{mn}r_y\right)J_m\left(k_{mn}^* r_x\right)}{\Gamma_{mn}\xi_{mn}} \times \exp\left\{-\mathrm{i}\left[\frac{M\kappa}{\beta^2}\left(y_1 - x_1\right) + \frac{\xi_{mn}}{\beta^2}|x_1 - y_1| - m\left(\phi_y - \phi_x\right)\right]\right\} \tag{4.153}$$

4.B.1 Expressions for Loading Noise

$$p(\mathbf{x},t) = \int_{-T}^{T} \int_{S_{B_\tau}} \mathbf{f}(\mathbf{y},\tau)\, \nabla g(\mathbf{y},\tau \,|\, \mathbf{x},t)\, \mathrm{d}S(\mathbf{y})\, \mathrm{d}\tau \tag{4.154}$$

Integrate on each blade planform instead so that

$$p(\mathbf{x},t) = \sum_{b=1}^{B} \int_{-T}^{T} \int_{r_h}^{r_t} \int_{-c/2}^{c/2} \mathbf{f}^{(b)}(\mathbf{y},\tau)\, \nabla g(\mathbf{y},\tau \,|\, \mathbf{x},t)\, \mathrm{d}X\, \mathrm{d}r_y\, \mathrm{d}\tau. \tag{4.155}$$

Using the Green's function transform

$$p(\mathbf{x},t) = \sum_{b=1}^{B} \int_{-T}^{T} \int_{r_h}^{r_t} \int_{-c/2}^{c/2} \int_{-\infty}^{\infty} \mathbf{f}^{(b)}(\mathbf{y},\tau)\, \nabla G_\omega \frac{\exp\{\mathrm{i}\omega(t-\tau)\}}{2\pi}\, \mathrm{d}\omega\, \mathrm{d}X\, \mathrm{d}r_y\, \mathrm{d}\tau \tag{4.156}$$

and

$$\begin{aligned}\mathbf{f}^{(b)} &= \sum_{m'} \int_0^{2\pi} \delta\left(\phi_y - \Omega\tau - \frac{2\pi b}{B} - \frac{(s+X)\sin\alpha}{r} + 2\pi m'\right) \mathbf{f}_{m'}^{(b)}\, \mathrm{d}\phi \\ &= \sum_{m'} \int_0^{2\pi} \exp\left\{-\mathrm{i}m'\left(\phi_y - \Omega\tau - \frac{2\pi b}{B} - \frac{(s+X)\sin\alpha}{r}\right)\right\} \frac{\mathbf{f}_{m'}^{(b)}}{2\pi}\, \mathrm{d}\phi. \end{aligned} \tag{4.157}$$

Set

$$\mathbf{f}_{m'}^{(b)}(\mathbf{y},\tau) = L(X,r,\tau)\left[\hat{\mathbf{y}}_1 \sin\alpha + \hat{\phi}_y \cos\alpha\right] \tag{4.158}$$

so that

$$\begin{aligned}\mathbf{f}_{m'}^{(b)} \nabla G_\omega &= L(X,r,\tau)\left[\hat{\mathbf{y}}_1 \sin\alpha + \hat{\phi}_y \cos\alpha\right]\left[\mathrm{i}K_1^{\pm}\hat{\mathbf{y}}_1 + \frac{\mathrm{i}m}{r}\hat{\phi}_y + \hat{\mathbf{r}}_y \frac{\partial}{\partial r_y}\right] G_\omega \\ &= L(X,r,\tau)\left[\mathrm{i}K_1^{\pm}\sin\alpha + \frac{\mathrm{i}m\cos\alpha}{r}\right] G_\omega \end{aligned} \tag{4.159}$$

The Fourier transform of the periodic loading L is

$$\tilde{L}\left(X^{(b)}, r, \omega'\right) = \int_{-\infty}^{\infty} L\left(X^{(b)}, r, \tau\right) \frac{\exp\left\{-\mathrm{i}\omega'\tau\right\}}{2\pi}\,\mathrm{d}\tau \tag{4.160}$$

and the accompaniying inverse is

$$L\left(X^{(b)}, r, \tau\right) = \int_{-\infty}^{\infty} \tilde{L}\left(X^{(b)}, r, \omega'\right) \exp\left\{\mathrm{i}\omega'\tau\right\}\,\mathrm{d}\omega' \tag{4.161}$$

Therefore

$$\mathbf{f}_{m'}^{(b)} \nabla G_\omega = \int_{-\infty}^{\infty} \tilde{L}\left(X^{(b)}, r, \omega'\right) \exp\left\{\mathrm{i}\omega'\tau\right\} \left[\mathrm{i}K_1^{\pm} \sin\alpha + \frac{\mathrm{i}m\cos\alpha}{r}\right] G_\omega\,\mathrm{d}\omega' \tag{4.162}$$

and the equation for pressure is now

$$\begin{aligned} p\left(\mathbf{x}, t\right) = \sum_{b=1}^{B} \sum_{m'=-\infty}^{\infty} \int_{-T}^{T} \int_{r_h}^{r_t} \int_{-c/2}^{c/2} \int_{-\infty}^{\infty} \int_{0}^{2\pi} \mathbf{f}_{m'}^{(b)} \nabla G_\omega \\ \times \exp\left\{-\mathrm{i}m'\left(\phi_y - \Omega\tau - \frac{2\pi b}{B} - \frac{(s+X)\sin\alpha}{r}\right)\right\} \\ \times \frac{\exp\left\{\mathrm{i}\omega\left(t-\tau\right)\right\}}{4\pi^2}\,\mathrm{d}\phi_y\,\mathrm{d}\omega\,\mathrm{d}X\,\mathrm{d}r_y\,\mathrm{d}\tau \end{aligned} \tag{4.163}$$

or

$$\begin{aligned} p\left(\mathbf{x}, t\right) = \sum_{b=1}^{B} \sum_{m'=-\infty}^{\infty} \int_{-T}^{T} \int_{r_h}^{r_t} \int_{-c/2}^{c/2} \int_{-\infty}^{\infty} \int_{0}^{2\pi} \int_{-\infty}^{\infty} \frac{\tilde{L}\left(X^{(b)}, r, \omega'\right) G_\omega}{4\pi^2} \left[\mathrm{i}K_1^{\pm} \sin\alpha + \frac{\mathrm{i}m\cos\alpha}{r}\right] \\ \times \exp\left\{-\mathrm{i}m'\left(\phi_y - \Omega\tau - \frac{2\pi b}{B} - \frac{(s+X)\sin\alpha}{r}\right) + \mathrm{i}\omega\left(t-\tau\right) + \mathrm{i}\omega'\tau\right\} \\ \mathrm{d}\omega'\,\mathrm{d}\phi_y\,\mathrm{d}\omega\,\mathrm{d}X\,\mathrm{d}r_y\,\mathrm{d}\tau \end{aligned} \tag{4.164}$$

Evaluate the τ integral (assuming $T \to \infty$)

$$\int_{-\infty}^{\infty} \exp\left\{\mathrm{i}\left(\omega' - \left(\omega - m'\Omega\right)\right)\tau\right\}\,\mathrm{d}\tau = 2\pi\delta\left(\omega' - \left(\omega - m'\Omega\right)\right) \tag{4.165}$$

then evaluating the ω' integral yields

$$2\pi \int_{-\infty}^{\infty} \delta\left(\omega' - (\omega - m'\Omega)\right) \tilde{L}\left(X^{(b)}, r, \omega'\right) \mathrm{d}\omega' = 2\pi \tilde{L}\left(X^{(b)}, r, \omega - m'\Omega\right) \tag{4.166}$$

and so, expanding the Green's function

$$\begin{aligned} p\left(\mathbf{x}, t\right) = -\frac{\mathrm{i}}{2} \sum_{b=1}^{B} \sum_{m'=-\infty}^{\infty} \sum_{m=-\infty}^{\infty} \sum_{n=0}^{\infty} \int_{r_h}^{r_t} \int_{-c/2}^{c/2} \int_{-\infty}^{\infty} \int_{0}^{2\pi} \frac{\tilde{L}\left(X^{(b)}, r, \omega - m'\Omega\right)}{2\pi} \\ \times \left[\mathrm{i}K_1^{\pm} \sin\alpha + \frac{\mathrm{i}m\cos\alpha}{r}\right] \frac{J_m\left(k_{mn} r_y\right) J_m\left(k_{mn}^* r_x\right)}{\xi_{mn} \Gamma_{mn}} \\ \times \exp\left\{\mathrm{i}\omega t - \mathrm{i}m'\phi_y + \frac{2\pi \mathrm{i} b m'}{B} + \frac{\mathrm{i}m'(s+X)\sin\alpha}{r} - \mathrm{i}K^{\pm}\left(x_1 - y_1\right) + \mathrm{i}m\left(\phi_y - \phi_x\right)\right\} \\ \mathrm{d}\phi_y \, \mathrm{d}\omega \, \mathrm{d}X \, \mathrm{d}r_y. \end{aligned} \tag{4.167}$$

Then, evaluating ϕ_y integral yields

$$\sum_{m=-\infty}^{\infty} \sum_{m'=-\infty}^{\infty} \int_{0}^{2\pi} \exp\left\{\mathrm{i}\left(m - m'\right)\phi_y\right\} \mathrm{d}\phi_y = 2\pi|_{m'=m}. \tag{4.168}$$

Therefore

$$\begin{aligned} p\left(\mathbf{x}, t\right) = \frac{1}{2} \sum_{b=1}^{B} \sum_{m=-\infty}^{\infty} \sum_{n=0}^{\infty} \int_{r_h}^{r_t} \int_{-c/2}^{c/2} \int_{-\infty}^{\infty} \left[K_1^{\pm} \sin\alpha + \frac{m\cos\alpha}{r}\right] \\ \times \frac{\tilde{L}\left(X^{(b)}, r, \omega - m\Omega\right) J_m\left(k_{mn} r_y\right) J_m\left(k_{mn}^* r_x\right)}{\xi_{mn} \Gamma_{mn}} \\ \times \exp\left\{\mathrm{i}\omega t + \frac{2\pi \mathrm{i} b m}{B} + \frac{\mathrm{i}m(s + X^{(b)})\sin\alpha}{r} - \mathrm{i}K^{\pm}\left(x_1 - y_1\right) - \mathrm{i}m\phi_x\right\} \\ \mathrm{d}\omega \, \mathrm{d}X \, \mathrm{d}r_y \end{aligned} \tag{4.169}$$

This is a general loading expression. Evaluating the summation in b yields

$$\sum_{b=1}^{B} \sum_{m=-\infty}^{\infty} \exp\left\{\frac{2\pi \mathrm{i} b m}{B}\right\} f\left(m\right) = B \sum_{m=-\infty}^{\infty} f\left(\nu\right) \tag{4.170}$$

where $\nu = mB$, so

$$p\left(\mathbf{x},t\right)=\frac{B}{2}\sum_{m=-\infty}^{\infty}\sum_{n=0}^{\infty}\int_{r_h}^{r_t}\int_{-c/2}^{c/2}\int_{-\infty}^{\infty}\left[K_1^{\pm}\sin\alpha+\frac{\nu\cos\alpha}{r}\right]$$
$$\times\frac{\tilde{L}\left(X,r,\omega-\nu\Omega\right)J_\nu\left(k_{mn}r_y\right)J_\nu\left(k_{mn}^{*}r_x\right)}{\xi_{mn}\Gamma_{mn}}$$
$$\times\exp\left\{\mathrm{i}\omega t+\frac{\mathrm{i}\nu(s+X)\sin\alpha}{r}-\mathrm{i}K^{\pm}\left(x_1-y_1\right)-\mathrm{i}\nu\phi_x\right\}\mathrm{d}\omega\,\mathrm{d}X\,\mathrm{d}r_y \quad (4.171)$$

This is a general steady loading expression. For a rotating point force, set s = 0 (zero sweep) and set

$$\tilde{L}\left(X,r,\omega-\nu\Omega\right)=F\delta\left(X\right)\delta\left(r_y-a\right)\delta\left(\omega-\nu\Omega\right) \quad (4.172)$$

Then, solving the remaining integrals (and $y_1=0$) means that

$$p\left(\mathbf{x},t\right)=\sum_{m=-\infty}^{\infty}p_m\exp\left\{\mathrm{i}\nu\Omega t\right\} \quad (4.173)$$

$$p_m=\frac{BF}{2}\sum_{n=0}^{\infty}\left[K_1^{\pm}\sin\alpha+\frac{\nu\cos\alpha}{a}\right]\frac{J_\nu\left(k_{mn}a\right)J_\nu\left(k_{mn}^{*}r_x\right)}{\xi_{mn}\Gamma_{mn}}$$
$$\times\exp\left\{-\mathrm{i}K^{\pm}x_1-\mathrm{i}\nu\phi_x\right\} \quad (4.174)$$

Distributed source

For steady loading noise we use the following expression to characterise the pressure jump over the blades

$$\tilde{L}\left(X^{(m)},r,\omega-\nu\Omega\right)=\frac{1}{2}\rho_0U_r^2C_Lf\left(X\right)\delta\left(\omega\right) \quad (4.175)$$

Also for blades define

$$y_1=(s+X)\cos\alpha \quad (4.176)$$

Replace into eq. (4.171) to obtain

$$p_m = \frac{B\rho_0}{4}\sum_{n=0}^{\infty}\int_{r_h}^{r_t}\int_{-c/2}^{c/2}\left[K_1^{\pm}\sin\alpha + \frac{\nu\cos\alpha}{r_y}\right]\frac{J_\nu\left(k_{mn}r_y\right)J_\nu\left(k_{mn}^{*}r_x\right)}{\xi_{mn}\Gamma_{mn}}\exp\left\{-\mathrm{i}K^{\pm}x_1 - \mathrm{i}\nu\phi_x\right\}$$
$$\times\exp\left\{\mathrm{i}\left[K^{\pm}\cos\alpha + \frac{\nu\sin\alpha}{r_y}\right](s+X)\right\}U_r^2C_Lf\left(X\right)\,\mathrm{d}X\,\mathrm{d}r_y \quad (4.177)$$

Define a non-dimensional chordwise variable

$$\bar{X} = \frac{X}{c} \quad (4.178)$$

and substitute into the chordwise integral to define a non-compact blade 'loading' function

$$\int_{-c/2}^{c/2} f\left(X\right)\exp\left\{\mathrm{i}\left[K^{\pm}\cos\alpha + \frac{\nu\sin\alpha}{r_y}\right]X\right\}\mathrm{d}X$$
$$= c\int_{-1/2}^{1/2} f\left(X\right)\exp\left\{\mathrm{i}k_c\bar{X}\right\}\mathrm{d}\bar{X} = c\Psi_L \quad (4.179)$$

where

$$k_c = \left[K^{\pm}\cos\alpha + \frac{\nu\sin\alpha}{r_y}\right]c. \quad (4.180)$$

Therefore,

$$p_m = \frac{B\rho_0}{4}\sum_{n=0}^{\infty}\int_{r_h}^{r_t}\left[K_1^{\pm}\sin\alpha + \frac{\nu\cos\alpha}{r_y}\right]\frac{J_\nu\left(k_{mn}r_y\right)J_\nu\left(k_{mn}^{*}r_x\right)}{\xi_{mn}\Gamma_{mn}}$$
$$\times\exp\left\{\mathrm{i}\phi_s - \mathrm{i}\nu\phi_x - \mathrm{i}K^{\pm}x_1\right\}U_r^2C_L\Psi_L\,\mathrm{d}r_y \quad (4.181)$$

where $\phi_s = k_c s/c$.

Periodic Unsteady Loading

The loading function for periodic unsteady loading on 0^{th} blade is given by the Fourier series

$$L^{(0)}\left(X^{(0)},r,\tau\right)=\sum_{k=-\infty}^{\infty}L_k^0\left(X^{(0)},r\right)\exp\left\{\mathrm{i}kB_1\left(\Omega_1+\Omega_2\right)\tau\right\} \tag{4.182}$$

which may be inversted by the transform

$$L_k^{(0)}\left(X^{(0)},r\right)=\frac{1}{T}\int_0^T L^{(0)}\left(X^{(0)},r,\tau\right)\exp\left\{-\mathrm{i}kB_1\left(\Omega_1+\Omega_2\right)\tau\right\}\,\mathrm{d}\tau \tag{4.183}$$

where the period $T=2\pi/\left(B_1\left(\Omega_1+\Omega_2\right)\right)$. The series is generalised to all blades from the loading on the reference blade by accounting for the time delay

$$\begin{aligned}L^{(b)}\left(X^{(b)},r,\tau\right)&=L^{(0)}\left(X^{(b)},r,\tau+\frac{2\pi b}{B_2\left(\Omega_1+\Omega_2\right)}\right)\\&=\sum_{k=-\infty}^{\infty}L_k^{(0)}\left(X^{(b)},r\right)\exp\left\{\mathrm{i}kB_1\left(\Omega_1+\Omega_2\right)\tau+2\pi\mathrm{i}\frac{bkB_1}{B_2}\right\}\end{aligned} \tag{4.184}$$

and the Fourier transform of this loading function is defined in the usual way

$$\begin{aligned}\tilde{L}^{(b)}\left(X^{(b)},r,\omega\right)&=\frac{1}{2\pi}\int_{-\infty}^{\infty}\sum_{k=-\infty}^{\infty}L_k^{(0)}\left(X^{(b)},r\right)\\&\quad\times\exp\left\{-\mathrm{i}\omega\tau+\mathrm{i}kB_1\left(\Omega_1+\Omega_2\right)\tau+2\pi\mathrm{i}\frac{bkB_1}{B_2}\right\}\,\mathrm{d}\tau\\&=\sum_{k=-\infty}^{\infty}L_k^{(0)}\left(X^{(b)},r\right)\exp\left\{2\pi\mathrm{i}\frac{bkB_1}{B_2}\right\}\delta\left(\omega-kB_1\left(\Omega_1+\Omega_2\right)\right)\end{aligned} \tag{4.185}$$

Now, evaluating the summation in b yields (some terms borrowed from expression for pressure)

$$\sum_{b=1}^{B_2}\sum_{m=-\infty}^{\infty}\sum_{k=-\infty}^{\infty}\exp\left\{2\pi\mathrm{i}b\left(\frac{kB_1+m}{B_2}\right)\right\}f\left(m,k\right)=B_2\sum_{m=-\infty}^{\infty}\sum_{k=-\infty}^{\infty}f\left(\nu,k\right) \tag{4.186}$$

where $\nu = mB_2 - kB_1$. Repacing these terms into the general loading expression and solving the ω integral yields

$$p\left(\mathbf{x},t\right) = \frac{B_2}{2}\sum_{m=-\infty}^{\infty}\sum_{k=-\infty}^{\infty}\sum_{n=0}^{\infty}\int_{r_h}^{r_t}\int_{-c/2}^{c/2}\left[K_1^{\pm}\sin\alpha + \frac{\nu\cos\alpha}{r}\right] \times L_k^{(0)}\left(X^{(b)},r\right)\frac{J_\nu\left(k_{mn}r_y\right)J_\nu\left(k_{mn}^{*}r_x\right)}{\xi_{mn}\Gamma_{mn}} \times \exp\left\{\mathrm{i}\omega_{km}t + \frac{\mathrm{i}m(s+X^{(b)})\sin\alpha}{r} - \mathrm{i}K^{\pm}\left(x_1-y_1\right) - \mathrm{i}\nu\phi_x\right\}\mathrm{d}X\,\mathrm{d}r_y \quad (4.187)$$

where $\omega_{km} = kB_1\Omega_1 + mB_2\Omega_2$. Expanding y_1 as before gives a final expression for noise generated in a circular wind tunnel by periodic unsteady loading of a rotor

$$p\left(\mathbf{x},t\right) = \frac{B_2}{2}\sum_{m=-\infty}^{\infty}\sum_{k=-\infty}^{\infty}\sum_{n=0}^{\infty}\int_{r_h}^{r_t}\left[K_1^{\pm}\sin\alpha + \frac{\nu\cos\alpha}{r}\right]\frac{J_\nu\left(k_{mn}r_y\right)J_\nu\left(k_{mn}^{*}r_x\right)}{\xi_{mn}\Gamma_{mn}} \times \exp\left\{\mathrm{i}\omega_{km}t + \mathrm{i}\phi_s - \mathrm{i}K^{\pm}x_1 - \mathrm{i}\nu\phi_x\right\}c\Psi_L\,\mathrm{d}r_y \quad (4.188)$$

where

$$\Psi_L = \int_{-1/2}^{1/2} L_k^{(0)}\left(X^{(b)},r\right)\exp\left\{-\mathrm{i}k_c\bar{X}^{(b)}\right\}\mathrm{d}\bar{X}^{(b)} \quad (4.189)$$

and k_c and ϕ_s are defined as before.

Chapter 5

Centrebody Scattering

This chapter describes research into open rotor centrebody scattering. Although this work was not initially in the scope of the research project, it proved to be an interesting application into the effects of near-field open rotor noise. Originally, work in this area was conducted by the primary supervisor to this research project, and so the following work is a collaborative effort between the supervisor and thesis author and has previously been published (Kingan and Sureshkumar, 2014). Analyses in this chapter concerning the near-field propagation of rotor noise and models for its prediction have been produced by the thesis author. The original models for centrebody scattering, including extensions for forward flight and realistic 'blade' source distributions have been published in previous work, highlighted in the following literature survey. The addition of the impedance boundary condition at the 'centrebody' surface to the model, which is at the conclusion of this chapter, is the original work of the thesis supervisor, but this has been verified separately by the thesis author, who has further contributed to the resulting analysis.

The centrebody of the open rotor houses the engine core and is similar in function to the engine core of a turbofan aero-engine. It houses a number of compressor stages, a combustion chamber and turbine stages, which drive the compressors and the counter rotating open rotors outboard of the centrebody. Investigations into open rotor near-field noise have lead to research into the phenomenon of centrebody scattering. In this chapter it will be demonstrated how, at certain operating conditions, the tone noise generated by open rotors may scatter from the centrebody surface.

An initial analysis of centrebody scattering was conducted by Glegg (1991). The propeller was modelled as a rotating point force, the centrebody was modelled as an infinite rigid cylinder and the effect of forward flight was not considered. Glegg showed that for a subsonic propeller, scattering from the centrebody surface had a negligible effect on rotor-alone tones, but could have a significant effect on 'interaction tones' produced

by an impulsive force on the rotating blade. Kingan et al. (2010) performed a relatively simple extension of Glegg's formulae to include the effect of forward flight and distributed sources. They then analysed the tonal noise produced by the open rotor aero-engine and were able to show that certain tones produced by the interaction of the front-rotor wake with the rear rotor were significantly affected by scattering from the centrebody.

The models of Glegg, Kingan et al. and those presented here make the assumption that the centrebody can be represented by an infinite, rigid circular cylinder; a necessary assumption in order to allow the simple theoretical analyses presented in this chapter. Of course, the fact that the assumed and actual geometries do not match will introduce some error. Although modelling the centrebody as an infinite circular cylinder may be somewhat crude, the analyses of Glegg (1991), Kingan et al. (2010) and that presented here highlight the importance of considering scattering from the centrebody and provide useful simple methods for describing and understanding the physics which govern the behaviour of the incident and scattered acoustic fields. In this chapter we analyse the acoustic field produced by an open rotor and investigate the mechanism governing centrebody scattering. Both the near- and far-fields are analysed. In Section 5.1, a rotating point force model, equivalent to that developed by Glegg (1991) is used to investigate the near-field pressure and intensity fields produced by both subsonic and supersonic propellers. It is shown that for supersonic propellers, there is significant acoustic radiation inboard of the source radius towards the centrebody. Because of this inboard radiation, centrebody scattering is important for highly supersonic rotor alone tones. Because some of the rotor-rotor interaction tones produced by the open rotor are acoustically equivalent to supersonic rotor-alone tones, centrebody scattering is also important for these tones.

The near-field contour plots presented in this chapter were inspired by those presented in Chapman (1990, 1993) and Carley (1999, 2000), however the analysis and method used for generating them are different. Chapman (1990) investigated the nature of the field produced by rotating sources and in a subsequent publication Chapman (1993) developed a novel method for the fast numerical calculation of the near-field produced by a radial distribution of multipole sources. The analysis was restricted to a stationary propeller with an even number of blades and it was assumed that the source strength was constant along the blade radius. Carley (1999) extended Chapman's analysis to include the effect of forward flight and odd blade number and in a subsequent paper (Carley, 2000), to include arbitrary radial source distributions. However, it should be noted that Carley's method does not appear to make provision for effects such as blade lean/sweep and chordwise source distributions which are important features required for the accurate prediction of high-speed rotor noise - particularly in the near-field. Also, the inspiration for investigating the acoustic intensity produced by the open rotor came from a paper published by Prentice (1993) who developed asymptotic formulae

for calculating the near-field produced by a subsonic rotating point source. Once again, the analysis and method presented by Prentice is very different to that presented here, however, both methods of analysis must necessarily yield identical results.

5.1 Rotating Point Force Model

The analysis presented in this section will follow that of Glegg (1991). Each blade is modelled as a rotating point force which is located in a still atmosphere and does not translate. Although these are very simple assumptions, the goal of this section was to investigate the fundamental mechanisms of open rotor centrebody scattering. The analysis will be extended to include axial flow and distributed sources in Section 5.2.

The propeller blades are represented by point forces which rotate in the $x = 0$ plane at radius $r = r_s$ and with rotational speed Ω rad/s in the positive ϕ direction. The centrebody is modelled as an infinite rigid cylinder of radius r_h. The analysis will make use of cylindrical coordinates $\mathbf{x} = \{r, \phi, x\}$ and the observer position will be denoted by a subscript o.

The frequency domain pressure $\tilde{p}$ at observer position $\mathbf{x}_o$ and frequency ω produced by an arbitrary force per unit volume distribution $\mathbf{f}(\mathbf{x}, \tau)$ within a fluid which occupies volume v is given by

$$\tilde{p}(\mathbf{x}_o, \omega) = \int_v \tilde{\mathbf{f}}(\mathbf{x}, \omega) \cdot \nabla_{\mathbf{x}} \tilde{G}(\mathbf{x}|\mathbf{x}_o, \omega)\, \mathrm{d}\mathbf{x} \tag{5.1}$$

where the time domain pressure, p, and force per unit volume, $\mathbf{f}$, are converted to frequency domain expressions $\tilde{p}$ and $\tilde{\mathbf{f}}$ using the following Fourier transform convention

$$\tilde{p}(\mathbf{x}_o, \omega) = \frac{1}{2\pi} \int_{-\infty}^{\infty} p(\mathbf{x}_o, t) \exp\{-i\omega t\}\, \mathrm{d}t$$

$\tilde{G}(\mathbf{x}|\mathbf{x}_o, \omega)$ is a frequency domain Green's function which satisfies eq. (5.47) and the rigid boundary condition on the surface of the cylinder. $\tilde{G}(\mathbf{x}|\mathbf{x}_o, \omega)$ is the sum of incident, $\tilde{G}^i(\mathbf{x}|\mathbf{x}_o, \omega)$, and scattered, $\tilde{G}^s(\mathbf{x}|\mathbf{x}_o, \omega)$, components which are defined in eqs. (5.2) and (5.3) below. $\tilde{G}^i$ represents the Green's function for free-field radiation and can thus be thought of as representing the 'incident' field. $\tilde{G}^s$ is the scattered portion of the field which when added to $\tilde{G}^i$ satisfies the rigid-wall boundary condition on the surface of the cylinder at radius r_h.

$$\tilde{G}^i(\mathbf{x}|\mathbf{x}_o,\omega) = -\frac{i}{8\pi}\sum_{n=-\infty}^{\infty}\exp\{in(\phi-\phi_o)\}\int_{-\infty}^{\infty}J_n(\gamma r_<)H_n^{(2)}(\gamma r_>)\exp\{ik_x(x-x_o)\}\mathrm{d}k_x \tag{5.2}$$

$$\tilde{G}^s(\mathbf{x}|\mathbf{x}_o,\omega) = \frac{i}{8\pi}\sum_{n=-\infty}^{\infty}\exp\{in(\phi-\phi_o)\}\int_{-\infty}^{\infty}\frac{J_n'(\gamma r_h)}{H_n^{(2)\prime}(\gamma r_h)}H_n^{(2)}(\gamma r_<)H_n^{(2)}(\gamma r_>) \times\exp\{ik_x(x-x_o)\}\mathrm{d}k_x \tag{5.3}$$

Note that $\kappa = \omega/c_0$, and the radial wavenumber γ and radial coordinates $r_<$ and $r_>$ are defined below.

$$\gamma = \mathrm{sgn}(\kappa)\sqrt{\kappa^2 - {k_x}^2}, {k_x}^2 < \kappa^2; \tag{5.4a}$$

$$\gamma = -i\sqrt{{k_x}^2 - \kappa^2}, {k_x}^2 > \kappa^2, \tag{5.4b}$$

$$r_< = r_s, r_> = r_o \text{ for } r_o > r_s; \tag{5.5a}$$

$$r_< = r_o, r_> = r_s \text{ for } r_o < r_s. \tag{5.5b}$$

The Hankel function has a branch cut along the negative real axis and thus the solution which approaches the real axis from the negative imaginary side should be selected. In eq. (5.4) above it is implied that the positive real root of the term beneath the square root is taken. Note that this expression for the Green's function is slightly different to that used by Glegg (even once the complex conjugate of Glegg's expression has been taken due to the different time conventions in the Fourier transforms). The derivation of the expression used in this chapter is detailed in Kingan et al. (2010).

Each propeller blade is represented by a point force $\mathbf{F}$, which has axial and tangential components $-L$ and D which are defined in cylindrical coordinates such that $\mathbf{F} = \{0, D, -L\}$. There are B evenly spaced point forces which rotate in the $x = 0$ plane at radius r_s and with rotational speed Ω rad/s in the positive ϕ direction. The force per unit volume is thus

$$\mathbf{f}(\mathbf{x},\tau) = \sum_{m=-\infty}^{\infty}\mathbf{F}\delta(x)\frac{\delta(r-r_s)}{r_s}\delta\left(\phi - \Omega\tau + \frac{2\pi m}{B}\right) \tag{5.6}$$

Taking the Fourier transform of this expression, substituting the result along with eqs. (5.2) and (5.3) into eq. (5.1) and then taking the inverse Fourier transform in time yields the following expression for the radiated pressure field.

$$p(\mathbf{x}_o,t) = -\frac{B}{8\pi}\sum_{m=-\infty}^{\infty}\exp\{imB(\Omega t-\phi_o)\}\int_{-\infty}^{\infty}\left[k_xL-\frac{mBD}{r_s}\right]\times \left[J_{mB}(\gamma r_<)-\frac{J'_{mB}(\gamma r_h)}{H^{(2)}_{mB}{}'(\gamma r_h)}H^{(2)}_{mB}(\gamma r_<)\right]H^{(2)}_{mB}(\gamma r_>)\exp\{-ik_xx_o\}\mathrm{d}k_x \tag{5.7}$$

The integration over k_x was performed using Matlab's 'quadgk', an adaptive quadrature routine which can handle moderate singularities at the endpoints. The integration was truncated at points $k_x = K_x^{\pm}$ where the integrand had become sufficiently small (which was determined automatically by the quadgk function). Because of the Hankel functions, the integrand may contain an integrable singularity at $k_x = \pm\kappa$. The integral was thus evaluated by splitting it into three sections: (1) $K_x^- < k_x < -\kappa$, (2) $-\kappa < k_x < \kappa$, (3) $\kappa < k_x < K_x^+$ and summing the contribution from each section.

In the far-field, the k_x integral in eq. (5.7) can be evaluated using the method of stationary phase which yields

$$p(\mathbf{x}_o,t) \sim -\frac{iB}{4\pi R_o}\sum_{m=-\infty}^{\infty}\exp\left\{imB\Omega\left(t-\frac{R_o}{c_0}\right)-imB\left(\phi_o-\frac{\pi}{2}\right)\right\}\left[\kappa L\cos\theta-\frac{mBD}{r_s}\right] \times\left[J_{mB}\left(\kappa r_s\sin\theta\right)-\frac{J'_{mB}\left(\kappa r_h\sin\theta\right)}{H^{(2)}_{mB}{}'\left(\kappa r_h\sin\theta\right)}H^{(2)}_{mB}\left(\kappa r_s\sin\theta\right)\right] \tag{5.8}$$

where $x_o = R_o\cos\theta$, $r_o = R_o\sin\theta$ and $\kappa = mB\Omega/c_0$. Applying the method of stationary phase for rotor noise is outlined in Section 2.C.

Glegg (1991) defines a 'free-field correction term' S_c which is a multiplicative factor used to correct far-field, free-field harmonic pressure predictions in order to account for centrebody scattering. S_c is thus defined by eq. (5.9) below.

$$S_c = 1-\frac{J'_{mB}\left(\kappa r_h\sin\theta\right)H^{(2)}_{mB}\left(\kappa r_s\sin\theta\right)}{H^{(2)}_{mB}{}'\left(\kappa r_h\sin\theta\right)J_{mB}\left(\kappa r_s\sin\theta\right)} \tag{5.9}$$

For subsonic source motion ($M_s \equiv \Omega r_s/c_o \ll 1$) and for $mB \to \infty$, the Bessel and Hankel functions in eq. (5.9) may be approximated by their large order principle asymptotic forms (Abramowitz and Stegun (1972), eq. 9.3.1) and the scattering correction factor simplifies to

$$S_c \sim 1+\left(\frac{r_h}{r_s}\right)^{2mB} \tag{5.10}$$

which shows that the contribution of the scattered field to the total field becomes negligible in comparison to the incident field as the harmonic number increases.

For highly supersonic source motion ($M_s \gg 1$), a similar approximation can be derived. When $M_s >> 1$ and the observer is not too close to the propeller axis, the Bessel and Hankel functions may be approximated by their large order asymptotic forms (Abramowitz and Stegun (1972), 9.3.15-16)

$$J_\nu(\nu\sigma) \sim \sqrt{\frac{2}{\pi\nu\tan\lambda}}\cos\left(\nu\left[\tan\lambda-\lambda\right]-\frac{\pi}{4}\right), \nu\to\infty,$$
$$H_\nu^{(2)}(\nu\sigma) \sim \sqrt{\frac{2}{\pi\nu\tan\lambda}}\exp\left\{-i\nu\left[\tan\lambda-\lambda\right]+i\frac{\pi}{4}\right\}, \nu\to\infty,$$

where $\sigma = \sec\lambda$. These expressions are valid for ν large and positive and $\nu^{-1/3} \ll \lambda < \pi/2$. Thus, when $\lambda_h \gg \nu^{-1/3}$ the correction factor can be approximated by

$$S_c \sim 1 + \frac{\exp\left\{2imB\left(\tan\lambda_h-\lambda_h\right)-i\pi/2\right\}-1}{\exp\left\{2imB\left(\tan\lambda_s-\lambda_s\right)-i\pi/2\right\}+1} \tag{5.11}$$

In eq. (5.11), the subscripts s and h respectively indicate that λ is evaluated at either the source (point force) or hub radius. This result indicates that the scattered field can be of the same order as the incident field for highly supersonic forces and therefore centrebody scattering must be taken into account when calculating the total acoustic field. It is important to note that the asymptotic expressions derived above are only valid for rotating point forces. In Section 5.2 it will be shown that for a real propeller, where sources are distributed across the blade span, the radius which contributes most to the centrebody scattered field is not necessarily the same as that which contributes most to the incident field. The concept of the 'sonic radius' is again useful here. The sonic radius is the radius at which the maximum speed in the direction of the observer of an object with the same rotational speed as the rotating force being considered is precisely sonic. The sonic radius is denoted r^* and will also be defined in terms of a non-dimensional radius $z^* = r^*/r_s$.

For a non-translating, rotating force immersed in a stationary fluid and in the plane of the rotor, $z^* = 1/M_s$. Eq. (5.11) is only valid for highly supersonic sources where the sonic radius lies well inboard of the hub radius. This is unlikely to happen for a practical propeller as a source located at the tip of a modern open rotor with a hub to tip ratio of 40% would be required to have a rotational Mach number well in excess of 2.5. However, Peake and Boyd (1993) point out that the acoustic field produced by a rotor-rotor interaction tone is equivalent in nature to that produced by a rotor-alone tone. They show that the n_2^{th} harmonic of the noise produced by the interaction of the downstream blades with the n_1^{th} Fourier component of the upstream blade wake, for a

$B_1 \times B_2$ bladed contra-rotating open rotor, is equivalent to the m^{th} harmonic of steady loading noise produced by a single B-bladed rotor but with and adjusted mode speed ω, harmonic number ν and effective tip Mach number M_t':

$$\omega = mB\Omega \rightarrow \omega = n_1 B_1 \Omega_1 + n_2 B_2 \Omega_2, \tag{5.12}$$

$$\nu = -mB \rightarrow \nu = n_1 B_1 - n_2 B_2, \tag{5.13}$$

$$M_t' = -\frac{\omega R_t}{c_0 \nu}. \tag{5.14}$$

For practical open rotor geometries, it is not uncommon for the 'sonic radius' of some interaction tones to lie inboard of the rotor hub, meaning that centrebody scattering is important for these tones.

Acoustic Intensity

The acoustic particle velocity can be calculated relatively easily by substituting eq. (5.7) into the linearized momentum equation below and evaluating the resulting expression using the same numerical method employed to calculate the pressure field.

$$\frac{\partial \mathbf{u}}{\partial t} = -\frac{1}{\rho} \nabla_{\mathbf{x}_o} p \tag{5.15}$$

Note that the expressions for pressure and particle velocity both contain infinite summations over a harmonic number m. Summation terms for which $m > 0$ are the complex conjugate of the corresponding $m < 0$ term. Thus, the pressure and velocity fields can be expressed

$$p = \sum_{m=-\infty}^{\infty} P_{mB} \exp\{imB\Omega t\} = P_0 + \sum_{m=1}^{\infty} 2|P_{mB}| \cos\left(mB\Omega t + \Phi_{mB}^{p}\right), \tag{5.16}$$

$$u = \sum_{m=-\infty}^{\infty} U_{mB} \exp\{imB\Omega t\} = U_0 + \sum_{m=1}^{\infty} 2|U_{mB}| \cos\left(mB\Omega t + \Phi_{mB}^{u}\right), \tag{5.17}$$

where $\Phi_{mB}^{p} = \arg\left(P_{mB}\right)$ and $\Phi_{mB}^{u} = \arg\left(U_{mB}\right)$. These expressions are useful for calculating acoustic intensity $\mathbf{I}$ which for no mean flow is defined $\mathbf{I} = p\mathbf{u}*$. It is relatively straightforward to show that a component of the time averaged acoustic intensity vector for a single tone is given by the following expression

$$\overline{I}_{mB} = 2|P_{mB}||U_{mB}| \cos\left(\Phi^p_{mB} - \Phi^u_{mB}\right). \tag{5.18}$$

The phase speed of the pressure field for a single tone is given by

$$\nu_p = \frac{2c_0^2 \overline{V}_{mB}}{|\overline{\mathbf{I}}_{mB}|}, \tag{5.19}$$

where $\overline{V}_{mB}$ is the time averaged potential energy per unit volume which is defined

$$\overline{V}_{mB} = \frac{1}{\rho c_0^2}|P_{mB}|^2. \tag{5.20}$$

Near-field Acoustic Contours

Figure 5.1 plots contours of instantaneous pressure in the $x = 0$ plane for the first harmonic of the incident field produced by 12 evenly spaced rotating tangential point forces. The point forces are located at radius $r = 1$m and four separate cases are considered in which the forces rotate at Mach numbers $M_s = 0.5, 1, 1.33$ and 5 respectively. A single acoustic streamline, which is everywhere tangent to the local intensity vector, is also plotted inboard of the source radius for each case. This streamline is denoted by a dashed line. In this case and in the plane of rotation the axial component of time averaged intensity is zero everywhere except at the source radius, thus the streamline is confined to the source plane.

For all four cases, at radii well inboard of the sonic radius, $z^* = 1/M_s$, (depicted as a blue circle) the contours of constant instantaneous pressure are approximately radial and resemble the 'cross-section of an orange'. A similar pattern has been observed by Chapman (1993) and Carley (1999, 2000). These papers present similar plots of harmonics of the instantaneous field produced by radial distributions of various multipole sources. The phase velocity and intensity have a direction normal to the lines of constant phase (qualitatively similar to those created by contours of instantaneous pressure). Therefore at radii inboard of the sonic radius the direction of phase velocity (and intensity) is almost tangential. In this region, the magnitude of the pressure field also rapidly decays in a radial direction inboard from the sonic radius. Since the harmonic field rotates at the same speed as the point forces, the phase velocity inboard of the sonic radius must be subsonic, decaying in a linear fashion when considering the variation moving radially inwards towards the axis of rotation. As noted by Prentice (1993), this subsonic phase velocity and rapid decay in magnitude is typical of an evanescent field.

As previously stated, the time averaged acoustic intensity vector is normal to the contours of constant phase. In each subplot of Figure 5.1, inboard of the sonic radius, the

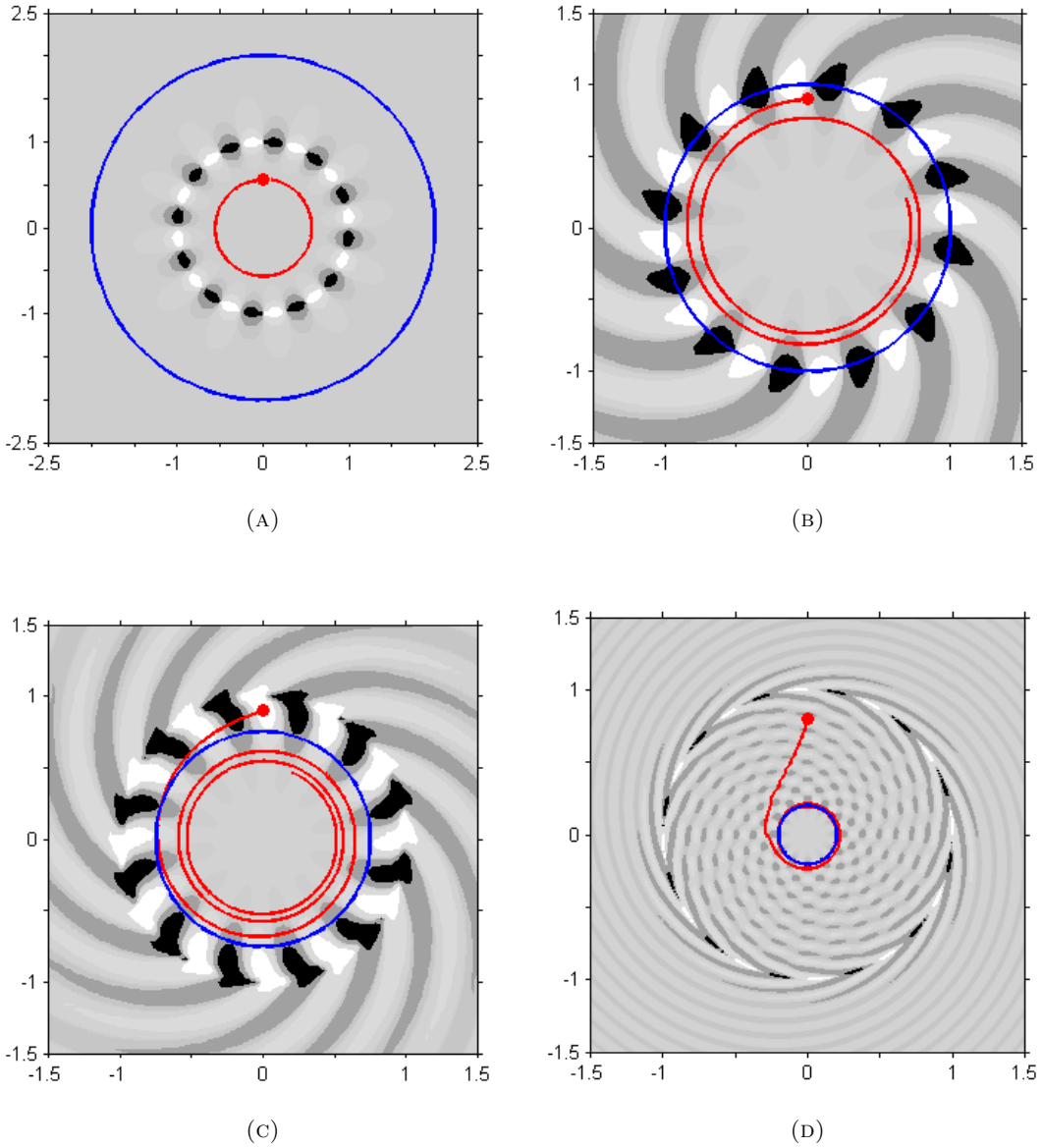

FIGURE 5.1: Contours of instantaneous acoustic pressure in the $x = 0$ plane for the first harmonic of the incident field produced by 12 rotating tangential point forces located at radius $r = 1$m. Note that contours are spaced logarithmically and are different for each case. The rotational Mach number of the forces is (a) 0.5, (b) 1, (c) 1.33 and (d) 5. The forces rotate about the origin and the horizontal and vertical axes have units of metres.

streamline is observed to propagate inwards in an increasingly tight spiral as it moves through the evanescent region. This observation is in agreement with the asymptotic theory of Prentice (1993). Note that for the hypersonic source, where $M_s = 5$, the streamline propagates inwards in an approximately straight radially-aligned direction until it transitions inboard of the sonic radius whereupon it begins to spiral inwards, as for the other cases.

In the plane of the rotor, at radii outboard of the sonic radius, acoustic propagation is

very efficient. At radii well outboard of both the source and sonic radii, the phase velocity is almost sonic. Since the harmonic field has the same rotational speed as the point forces, and beacuse the phase speed remains roughly sonic, the contours of instantaneous pressure (which are qualitatively similar to those of constant phase) sweep back to form a spiral pattern. Figure 5.2 is an expanded version of Figure 5.1 and so again plots contours of instantaneous acoustic pressure for the first harmonic of the field produced by 12 evenly spaced tangential point forces with different rotational Mach numbers. For each case, a number of acoustic streamlines are 'launched' at radii outboard of the source position. These streamlines propagate in a straight line normal to the local pressure phase contours and appear to be tangential to the circle with radius equal to r^* (shown by a dark circle). This is an interesting result as the propagating acoustic radiation outboard of the source appears to emanate from the sonic radius rather than the source radius. When the sonic radius lies well inboard of the source radius, streamlines outboard of the source radius propagate almost radially. As the observer position moves further outboard, the intensity vector tends towards the radial direction and thus the tangential component of intensity becomes negligible, as expected in the far-field of the rotating source Prentice (1993). As the source Mach number decreases and the sonic radius moves outboard, the intensity vectors have a greater tangential component. Thus, when compared to supersonic sources, the rotor acoustic near-field effects at radii outboard of the source are expected to be more prominent for subsonic sources.

The scattered field also rotates at the same speed as the point forces, meaning that the sonic radius of the scattered field is equal to that of the incident field. For cases where the sonic radius is located outboard of the centrebody, incident sound inboard of the source radius must 'burrow' through an evanescent region. This significantly reduces the magnitude of the field incident on the centrebody and thus by extension the magnitude of the sound field scattered from the rigid centrebody. This scattered field must burrow back out through the evanescent region, further reducing the magnitude of the scattered field, before finally transitioning through the sonic radius where propagation becomes relatively efficient. For the 'hypersonic' case, where the sonic radius lies inboard of the centrebody, in the plane of rotation, the incident and scattered fields are never evanescent and thus the centrebody scattered field can be of a similar magnitude to that of the incident field. In such a case the scattered field is no longer likely to be negligible and should be accounted for. This is shown clearly in Figure 5.3 which plots contours of instantaneous pressure in the $\phi = 0°$ plane of the first harmonic of the incident and scattered fields, produced by 12 supersonic ($M_s = 1.33$ and $M_s = 5$) tangential point forces.

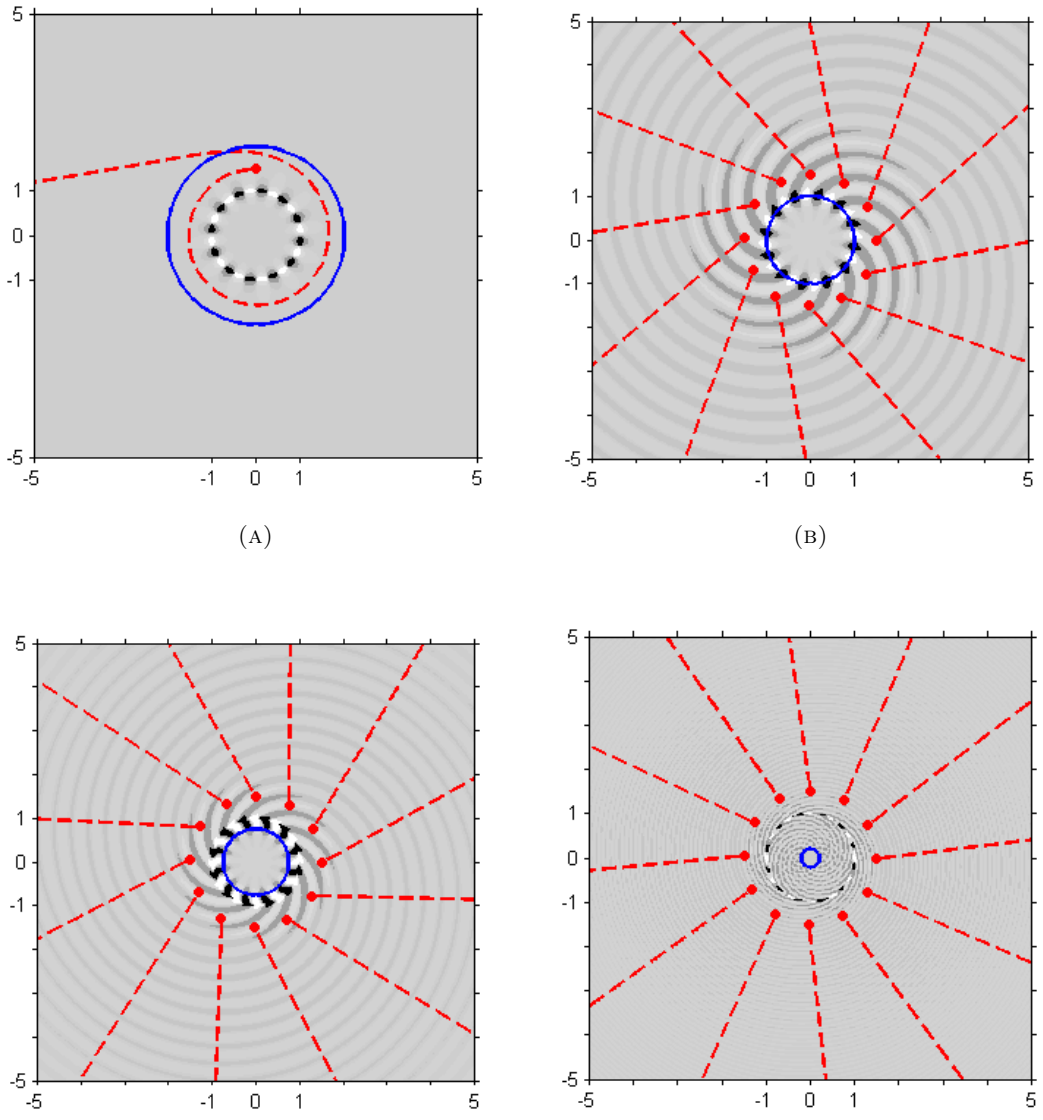

(A) (B)

(C) (D)

FIGURE 5.2: Contours of instantaneous acoustic pressure in the $x = 0$ plane for the first harmonic of the incident field produced by 12 rotating tangential point forces located at radius $r = 1$m. Note that contours are spaced logarithmically and are different for each case. The rotational Mach number of the forces is (a) 0.5, (b) 1, (c) 1.33 and (d) 5. The forces rotate about the origin and the horizontal and vertical axes have units of metres.

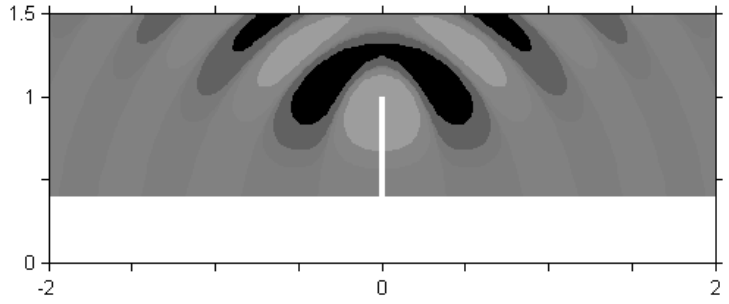

(A)

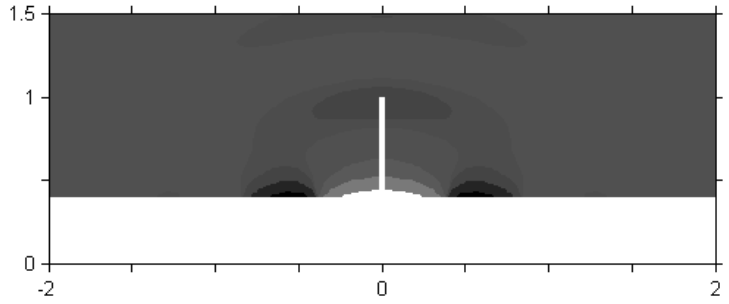

(B)

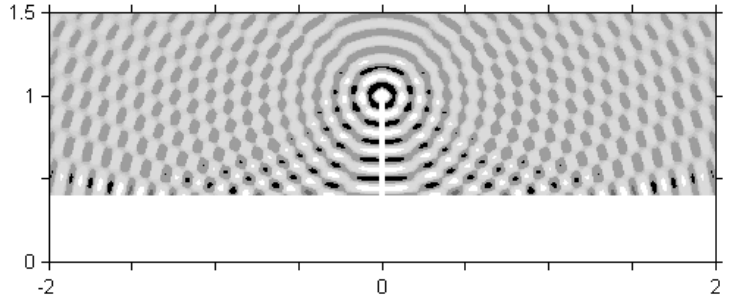

(C)

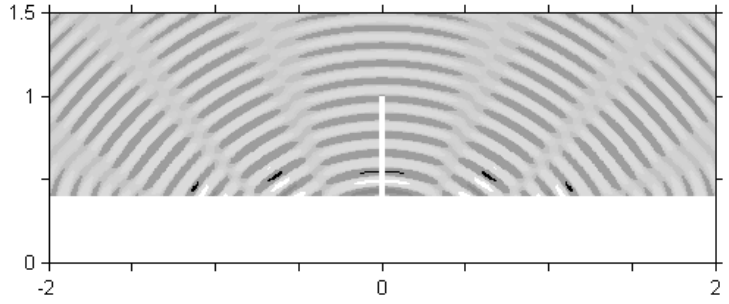

(D)

FIGURE 5.3: Contours of instantaneous acoustic pressure in the $\phi = 0°$ plane for the first harmonic of the field produced by 12 rotating tangential point forces located at radius $r = 1$m. Note that contours are spaced logarithmically and are different for each case, but identical for corresponding incident and scattered fields. (a) Incident field, $M_s = 1.33$, (b) Scattered field, $M_s = 1.33$, (c) Incident field, $M_s = 5$ and (d) Scattered field, $M_s = 5$. The horizontal axis is the x_o axis and the vertical axis is the r_o axis. Both axes have units of metres.

5.2 Distributed Source Model

In this section, the point force analysis is extended to include the effects of translation and of a distribution of sources across the rotor blade surface.

The far-field incident tone pressure produced by the downstream rotor of an advanced open rotor is given by eqs. (5.21) - (5.25) below. These expressions were first derived by Hanson (1985*b*). The front and rear rotor blade counts are denoted B_1 and B_2, the rotor and observer are stationary yet immersed in a flow of Mach number M_x parallel to the engine axis. The fluid has density ρ and speed of sound c_0 and the downstream rotor has a tip radius R_t and a centrebody/hub radius r_h. The observer location is expressed in emission coordinates where R_e is the emission radius, θ_e is the emission polar angle and ϕ_0 is the azimuthal angle of the observer. The free-field acoustic pressure is thus given by

$$p^i\left(\mathbf{x}_o, t\right) = \sum_{n_1=-\infty}^{\infty} \sum_{n_2=-\infty}^{\infty} \frac{-\rho c_0^2 B_2 R_t}{4\pi R_e \left(1 - M_x \cos\theta\right)} \times \exp\left\{ i\omega \left(t - R_e/c_0\right) + i\nu \left(\phi_o + \frac{\pi}{2}\right)\right\} P^i_{n_1,n_2} \quad (5.21)$$

where the mode speed, ω, and harmonic number, ν, are given by eqs. (5.12) and (5.13). $P^i_{n_1,n_2}$ is a radial integral which is defined as

$$P^i_{n_1,n_2} = \int_{z_h}^{1} S\left(z\right) J_\nu \left(\nu \frac{z}{z^*}\right) \mathrm{d}z, \quad (5.22)$$

where z^*, the non-dimensional sonic radius, is

$$z^* = \frac{\left(1 - M_x \cos\theta\right)}{\sin\theta} \frac{\nu c_0}{\omega R_t}. \quad (5.23)$$

Only straight rotor blades will be considered and the effects of chordwise non-compactness and drag forces will be neglected. Under these assumptions $S(z)$ is defined

$$S(z) = M_{r_2}^2 i k_y \frac{C_{L_2}^{(n_1)}}{2}, \quad (5.24)$$

where M_{r_2} is the local Mach number of the downstream rotor blade relative to the fluid, $C_{L_2}^{(n_1)}$ is the n_1^{th} harmonic of the unsteady lift coefficient on the downstream rotor blade and the wavenumber k_y is defined

$$k_y = \frac{c_2}{M_{r_2}}\left[\frac{\omega/c_0}{1 - M_x\cos\theta}M_{t_2}z\cos\theta + \frac{\nu}{zR_t}M_x\right]. \tag{5.25}$$

M_{t_2} is the rotational tip Mach number of the downstream rotor blade. Note that the $n_1 = 0$ terms in eq. (5.21) correspond to the noise produced by the steady component of loading on the rotor blades and thus these expressions could also be used to calculate the steady loading component of the rear-rotor rotor-alone tones. In the analysis presented below it is always assumed that $\nu > 0$. For cases where $\nu < 0$, Abramowitz and Stegun (1972, eqs. 9.1.5-6) can be used to convert eqs. (5.21) through (5.25) to a suitable form. Thus cases where $\nu = 0$ are not considered here.

For subsonic rotor-alone tones and interaction tones for which the sonic radius lies outboard of the blade tip and such that $\lambda \gg \nu^{-1/3}$ (where $z = z^*\mathrm{sech}\lambda$) the Bessel function in eq. (5.22) may be approximated by

$$J_v\left(\nu\mathrm{sech}\lambda\right) \sim \frac{\exp\left\{\nu\left(\tanh\lambda - \lambda\right)\right\}}{\sqrt{2\pi\nu\tanh\lambda}}, \nu \to \infty.$$

If $S(z)$ does not vary exponentially rapidly with ν, the integrand in eq. (5.22) is dominated by the behaviour of the Bessel function which increases exponentially towards the tip. The radial integral may thus be evaluated using Laplace's method. Parry (1988), and Parry and Crighton (1989) show that $P^i_{n_1,n_2}$ may be approximated by the following expression

$$P^i_{n_1,n_2} \sim \frac{S\left(1\right)\exp\left\{\nu\left(\tanh\lambda_t - \lambda_t\right)\right\}}{\sqrt{2\pi}\left(\nu\tanh\lambda_t\right)^{3/2}}. \tag{5.26}$$

where the subscript t indicates that λ is evaluated at the blade tip.

Kingan et al. (2010) show that the centrebody scattered field is given by eqs. (5.21) through (5.25) but with $P^i_{n_1,n_2}$ replaced by $P^s_{n_1,n_2}$, which is defined as

$$P^s_{n_1,n_2} = -\frac{J'_\nu\left(\nu\frac{z_h}{z^*}\right)}{H^{(2)\prime}_\nu\left(\nu\frac{z_h}{z^*}\right)}\int_{z_h}^{1} S(z)H^{(2)}_\nu\left(\nu\frac{z}{z^*}\right)\mathrm{d}z. \tag{5.27}$$

Note that Kingan et al. (2010) rather confusingly denoted the emission radius as $|\mathbf{x}_o|$. In this work the expressions have been converted to be similar to the notation of Hanson (1985*b*) and Parry (1988). The radial integral in $P^s_{n_1,n_2}$ can be evaluated in a similar fashion to that in $P^i_{n_1,n_2}$. Provided that $\lambda \gg \nu^{-1/3}$, the Hankel function in the integral in eq. (5.27) may be approximated by

$$H^{(2)}_\nu\left(\nu\mathrm{sech}\lambda\right) \sim i\sqrt{\frac{2}{\pi\nu\tanh\lambda}}\exp\left\{-\nu\left(\tanh\lambda - \lambda\right)\right\}, \nu \to \infty.$$

In this case the Hankel function increases exponentially towards the hub rather than the tip. Thus the scattered field is dominated by contributions from the hub region (rather than the tip). Substituting the asymptotic expression for the Hankel function into eq. (5.27), making use of the equivalent asymptotic expressions for the derivatives of the Bessel and Hankel functions and evaluating the integral using Laplace's method yields

$$P^s_{n_1,n_2} \sim \frac{z_h S(z_h)}{\sqrt{2\pi}} \frac{\exp\{\nu(\tanh\lambda_h - \lambda_h)\}}{(\nu\tanh\lambda_h)^{3/2}}. \tag{5.28}$$

Eqs. (5.26) and (5.28) can be used to calculate the following expression, equivalent in form to Glegg's correction factor S_c, which can be used for adjusting free-field predictions to account for centrebody scattering, for distributed source rotor-rotor interaction noise.

$$S_c \sim 1 + z_h \frac{S(z_h)}{S(1)} \left(\frac{\tanh\lambda_t}{\tanh\lambda_h}\right)^{3/2} \frac{\exp\{\nu(\tanh\lambda_h - \lambda_h)\}}{\exp\{\nu(\tanh\lambda_t - \lambda_t)\}} \tag{5.29}$$

Note that this expression is valid for cases where the sonic radius lies well outboard of the tips and ν is large.

In Figure 5.4, the magnitude of the incident and scattered fields at polar angle $\theta = 90°$ is plotted against harmonic number for the steady loading component of the rotor-alone tones produced by a 9-bladed rotor. The figure shows the fields calculated using eqs. (5.22) and (5.27) which require a numerical integration along the blade span. The open rotor has a tip Mach number of $M_t = 0.7$ and is immersed in a flow of Mach number $M_x = 0.2$. The rotor blades are straight and the effect of chordwise non-compactness has been neglected. As expected, the centrebody scattered field makes a negligible contribution to the total sound field relative to the incident component. Also, this contribution becomes more negligible as harmonic number increases. The difference between the full numerical solutions (eqs. (5.22) and (5.27)) and the asymptotic expressions (eqs. (5.26) and (5.28)) for the incident and scattered fields is shown in Figure 5.5 below. It is observed that the agreement between the numerical and asymptotic expressions is very good, validating the accuracy of these expressions.

For 'hyper-sonic' rotor rotor-alone tones and interaction tones for which the sonic radius lies inboard of the centrebody such that $\nu^{-1/3} \ll \lambda < \pi/2$, where $z = z^* \sec\lambda$, the Bessel function in eq. (5.22) may be approximated by eq. (9.3.15) in Abramowitz and Stegun (1972) and the radial integral may be evaluated using the method of stationary phase. Parry (1988) and Crighton and Parry (1991) show that to leading order in ν, $P^i_{n_1,n_2}$ may be approximated by the following expression

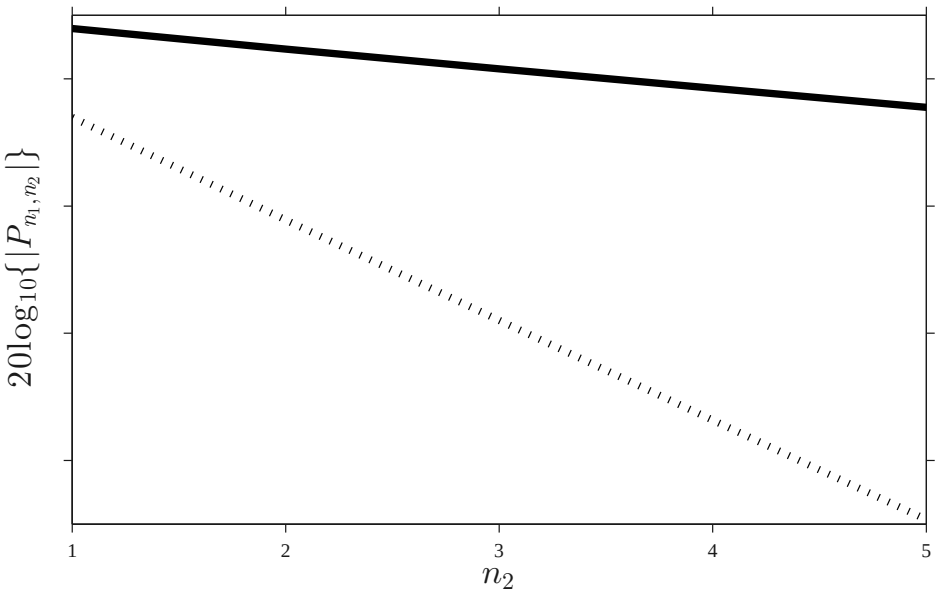

FIGURE 5.4: Plot of incident and scattered field magnitude at $\theta = 90°$ versus harmonic number (full numerical calculation). Incident field (solid line), scattered (dashed line). 100dB per vertical tick. Subsonic rotor ($M_t = 0.7$, $M_x = 0.2$, $n_1 = 0$).

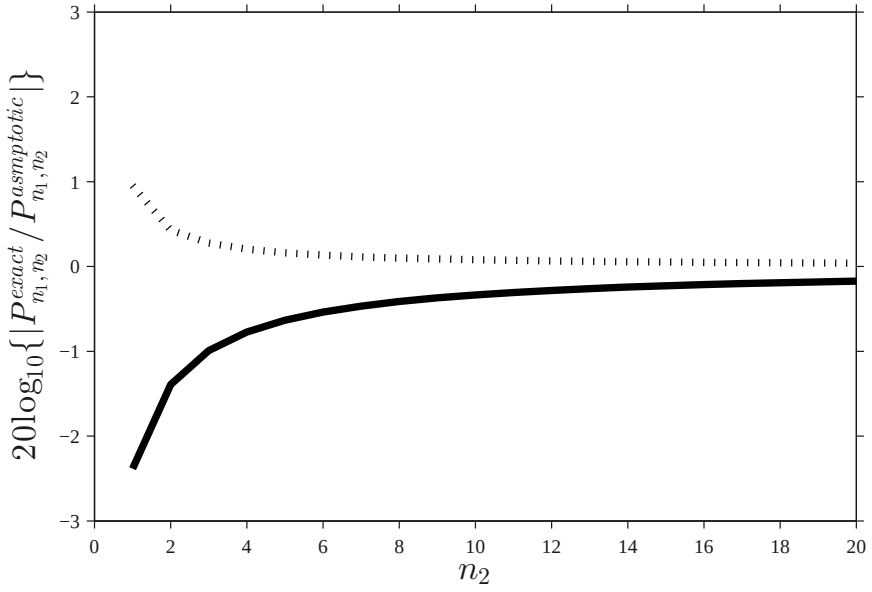

FIGURE 5.5: Plot of difference between full numerical and asymptotic solution as a function of harmonic number at $\theta = 90°$ for the same case considered in Figure 5.4. Incident field (solid line), scattered field (dashed line).

$$P^i_{n_1,n_2} \sim \left[\left(\frac{2}{\pi\nu\tan\lambda}\right)^{1/2} \frac{z^* S\left(z^*\sec\lambda\right)}{\nu\sin\lambda} \sin\left(\nu\left(\tan\lambda-\lambda\right)-\frac{\pi}{4}\right)\right]_{\lambda=\lambda_h}^{\lambda=\lambda_t} \tag{5.30}$$

where the subscripts h and t respectively indicate evaluation at the hub and tip radii. Thus, the free-field solution contains contributions from both the hub and tip regions. Consider now the centrebody scattered field of such tones. If the sonic radius lies well inboard of the open rotor hub, such that $\nu^{-1/3} \ll \lambda < \pi/2$, where $z = z^*\sec\lambda$, the Hankel function in the integral of $P^s_{n_1,n_2}$ (eq. (5.27)) may be approximated using Abramowitz and Stegun (1972, eqs. 9.3.15-16). Making this substitution and changing integration variables yields

$$P^s_{n_1,n_2} \sim -\frac{J_\nu'\left(\nu\frac{z_h}{z^*}\right)}{H_\nu^{(2)\prime}\left(\nu\frac{z_h}{z^*}\right)} \int_{\lambda_h}^{\lambda_t} S\left(z^*\sec\lambda\right)\sqrt{\frac{2}{\pi\nu\tan\lambda}} \times \exp\left\{-i\nu\left[\tan\lambda-\lambda\right]+i\frac{\pi}{4}\right\} z^*\tan\lambda\sec\lambda\,\mathrm{d}\lambda. \tag{5.31}$$

As for the incident field, the integral may be evaluated using the method of stationary phase provided that $S(z)$ is not a strong function of z (which is the case for a straight blade under the assumption of chordwise compact loading).

Defining

$$f(\lambda) = \tan\lambda - \lambda,$$

$$f'(\lambda) = \tan^2\lambda,$$

a stationary phase point exists at $\lambda = 0$, which corresponds to $z = z^*$. This lies outside the range of integration and thus the main contribution to the integral comes from the endpoints at the blade hub and tip. Applying the method of stationary phase yields the following expression for $P^s_{n_1,n_2}$ which is accurate to leading order in ν.

$$P^s_{n_1,n_2} \sim -i\frac{J_\nu'\left(\nu\frac{z_h}{z^*}\right)}{H_\nu^{(2)\prime}\left(\nu\frac{z_h}{z^*}\right)} \times \left[\sqrt{\frac{2}{\pi\nu\tan\lambda}}\frac{z^* S\left(z^*\sec\lambda\right)}{\nu\sin\lambda} \exp\left\{-i\nu\left[\tan\lambda-\lambda\right]+i\frac{\pi}{4}\right\}\right]_{\lambda=\lambda_h}^{\lambda=\lambda_t} \tag{5.32}$$

In Figure 5.6, the magnitude of the incident and scattered pressure fields at $\theta = 90°$ is plotted against harmonic number for the steady loading component of the rotor alone tones produced by a 9-bladed rotor. The figure shows the fields calculated using eqs. (5.22) and (5.27) which require a numerical integration along the blade span as well as the fields calculated using the asymptotic expressions given by eqs. (5.30) and (5.32). The rotor has a tip Mach number of 4 and is immersed in a flow with Mach number 0.2. Note that such a rotor is physically unrealistic, the purpose of this plot being to show the accuracy of the asymptotic expressions, which appears to be excellent. As in the subsonic rotor case, the rotor blades are straight, and chordwise non-compactness effects have been neglected. Also note that for supersonic rotors, effects such as chordwise non-compactness and blade sweep are significant and in reality should be included in any prediction scheme. However, using the methods described in Parry (1988), Parry and Crighton (1989), and Crighton and Parry (1991, 1992), it should be straightforward to extend the asymptotic expressions presented in this chapter to include such effects.

In Figure 5.7 the polar directivity of the $\{n_1, n_2\} = \{1, 1\}$ and $\{1, 2\}$ interaction tones produced by a 12×9 bladed contra-rotating open rotor are plotted. The incident and scattered fields are calculated using both the full numerical as well as asymptotic formulae. The agreement between both calculation methods is reasonable. As before, the rotor blades are straight and chordwise non-compactness effects were not included in the calculation. The rotor tip and translational Mach numbers are listed in the figure caption. The unsteady blade loading was calculated using the same method as that described in Kingan et al. (2010) and only interactions of the viscous wake from the upstream rotor with the downstream rotor blades is included (i.e. potential field interactions are neglected).

5.3 Noise reduction by lining the centrebody

Until this point, the effect of rigid centrebody scattering has been investigated. It is shown that scattering from a rigid centrebody can be important for hypersonic rotor rotor-alone tones and (of more practical use) rotor-rotor interaction tones, where the sonic radius lies inboard of the rotor hub. For these particular tones a significant proportion of the acoustic field propagates inboard and is reflected off the centrebody. A logical way to reduce the magnitude of the scattered field, and thus the magnitude of the total field, is to apply an acoustic liner on the surface of the centrebody. Acoustic liners are commonly used to line the tip casing of bypass ducts and intakes of modern turbofan engines, however, their possible application to propellers and open rotors does not appear to have been considered previously. Presumably, this is because lining the centrebody surface will not significantly affect the rotor-alone tones produced by an isolated single propeller design.

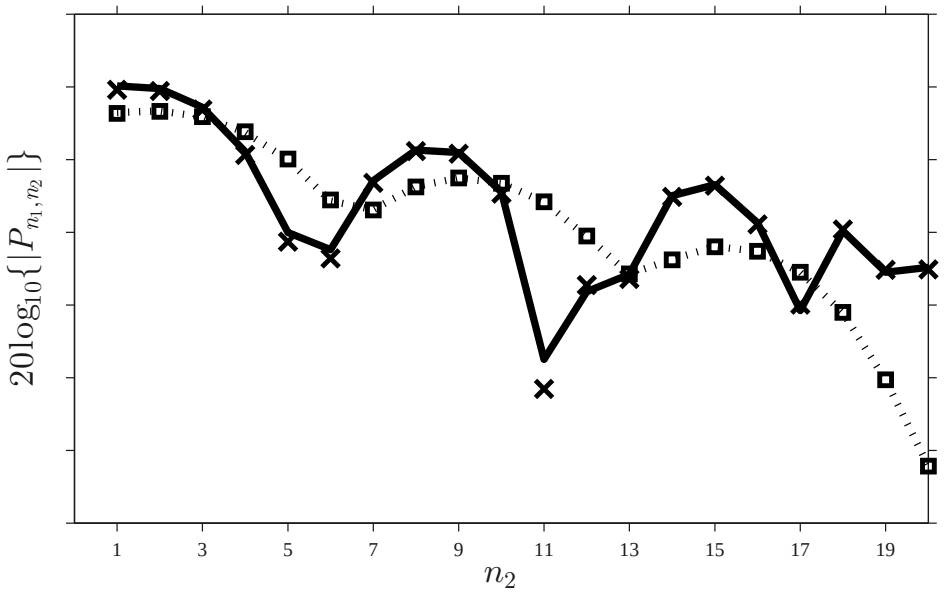

FIGURE 5.6: Plot of sound pressure level at $\theta = 90°$ versus harmonic number. Incident field full numerical calculation (solid line) and asymptotic expression (crosses). Scattered field full numerical calculation (dashed line) and asymptotic expression (squares). 10dB per vertical tick spacing. $B = 9$, $M_t = 4$, $M_x = 0.2$.

The analysis here generally follows that presented in Glegg (1991, pp. 574-5) who considered the scattering of sound from an impulsive point force by a rigid cylindrical centrebody. In this section, the scattering of this sound field by a centrebody of constant impedance is considered. The analysis is only meant to demonstrate the potential of acoustic liner treatments and as such is very simple. The blades are approximated as rotating axial point forces and the effect of propeller translation or axial flow is neglected.

For this case the axial loading on each blade is allowed to vary as a function of azimuthal position. Only the axial component of loading is considered and for the sake of simplicity, the blade loading, L, is assumed to be a function of azimuthal angle ϕ only. This loading might be thought of as being equivalent to the loading produced by a rotor blade interacting with a stationary flow disturbance at $\phi = 0°$. Glegg (1991) models this 'impulsive' type loading using the function

$$L(\phi) = \frac{\phi_s}{2} \sum_{k=-\infty}^{\infty} \exp\{-i\phi - |k|\phi_s\} \tag{5.33}$$

where $\phi_s = 0.065$rad.

The frequency domain Green's function $\tilde{G}(\mathbf{x}_0|\mathbf{x}, \omega)$ can be derived in a straightforward manner by following the method described in Appendix B of Kingan et al. (2010) or in Morfey et al. (2011) to obtain

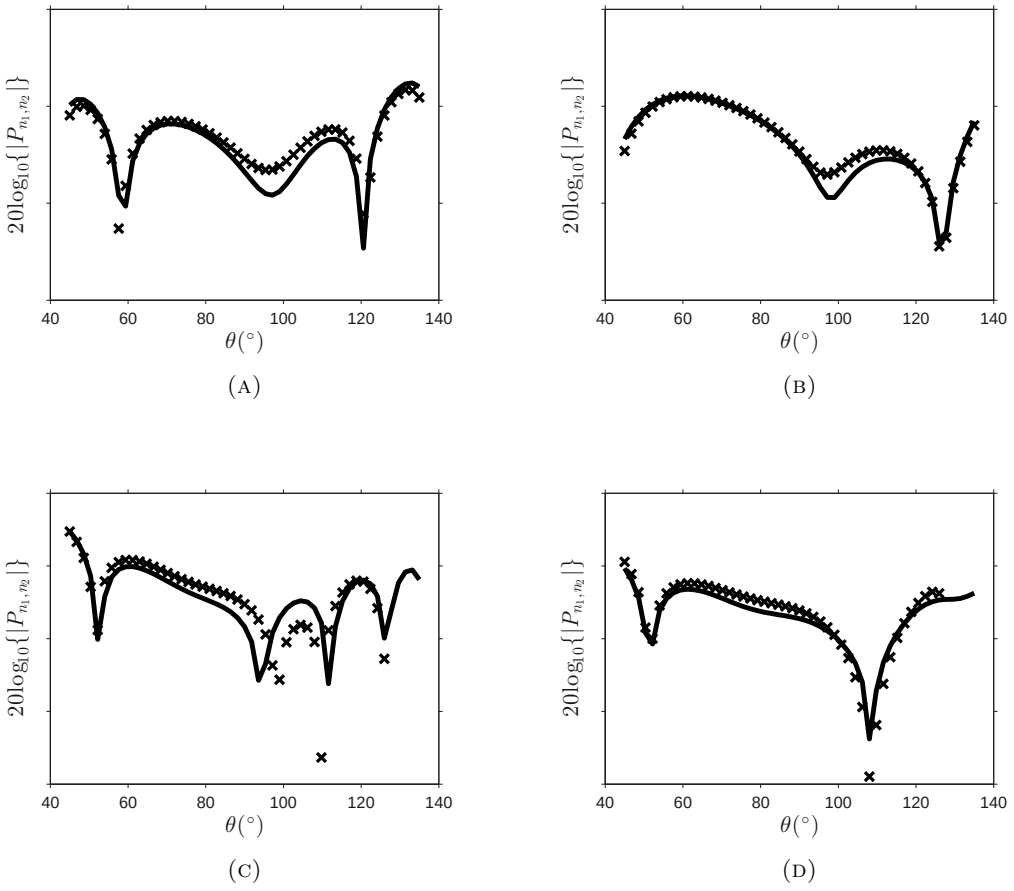

FIGURE 5.7: Plot of sound pressure level versus polar angle θ. (a) incident field and (b) scattered field of the $\{1,1\}$ rotor-rotor interaction tone. (c) incident field and (d) scattered field of the $\{1,2\}$ rotor-rotor interaction tone. Full numerical solutions are plotted using a solid line whereas asymptotic solutions are plotted using crosses. 10dB per vertical tick spacing. $B_1 = 12$, $B_2 = 9$, $M_{t_1} = 0.68$, $M_{t_2} = 0.7$, $M_x = 0.2$.

$$\tilde{G}\left(\mathbf{x}|\mathbf{x}_o,\omega\right) = -\frac{i}{8\pi}\sum_{n=-\infty}^{\infty}\exp\left\{in\left(\phi-\phi_o\right)\right\}\int_{-\infty}^{\infty}\exp\left\{ik_x(x-x_o)\right\} \left[J_n\left(\gamma r\right) - A\right]H_n^{(2)}\left(\gamma r_o\right)\,\mathrm{d}k_x, \qquad r_o > r, \quad (5.34)$$

where

$$A = \frac{\kappa J_n\left(\gamma r_h\right) + i\tilde{z}\gamma {J_n}'\left(\gamma r_h\right)}{\kappa H_n^{(2)}\left(\gamma r_h\right) + i\tilde{z}\gamma {H_n^{(2)}}'\left(\gamma r_h\right)} H_n^{(2)}\left(\gamma r\right) \quad (5.35)$$

and $\tilde{z}$ is the acoustic impedance of the lining on the centrebody surface which is assumed to be constant.

Following the same analysis as presented in Section 5.1 yields the following expression for the far-field sound pressure

$$p\left(\mathbf{x}_o, t\right) = \sum_{m=1}^{\infty} p_m\left(\mathbf{x}_o, t\right) \tag{5.36}$$

$$p_m\left(\mathbf{x}_o, t\right) = \frac{mB^2\Omega\phi_s}{4\pi c_0 R_o}\cos\theta\left|C_{mB}\right|\sin\left(mB\Omega\left(t - \frac{R_o}{c_0}\right) - mB\left(\phi_o - \frac{\pi}{2}\right) + \gamma_s\right) \tag{5.37}$$

where

$$C_{mB} = \sum_{k=-\infty}^{\infty} D\exp\left\{ik\left(\phi_o - \frac{\pi}{2}\right) - |k|\phi_s\right\}, \tag{5.38}$$

$$\gamma_s = \arg\left(C_{mB}\right), \tag{5.39}$$

$$\begin{aligned} D = {} & J_{mB-k}\left(\kappa_m r_s \sin\theta\right) \\ & - \frac{J_{mB-k}\left(\kappa_m r_h \sin\theta\right) + i\tilde{z}\sin\theta J_{mB-k}{}'\left(\kappa_m r_h \sin\theta\right)}{H^{(2)}_{mB-k}\left(\kappa_m r_h \sin\theta\right) + i\tilde{z}\sin\theta H^{(2)}_{mB-k}{}'\left(\kappa_m r_h \sin\theta\right)} H^{(2)}_{mB-k}\left(\kappa_m r_s \sin\theta\right) \end{aligned} \tag{5.40}$$

where $\kappa_m = \frac{mB\Omega}{c_0}$ The mean square sound pressure of the m^{th} tone is given by

$$\overline{p_m^2} = \frac{1}{2}\left(\frac{mB^2\Omega\phi_s}{4\pi c_0 R_o}\right)^2 \cos^2\theta |C_{mB}|^2. \tag{5.41}$$

In Figure 5.8, the sound pressure at a location on the same side of the centrebody as the impulsive force ($\phi_o = 0°$), produced by a one-bladed propeller with $r_h/r_s = 0.3$ and source Mach number 0.7, is plotted as a function of time for three different cases. The first case assumes a lined centrebody with surface impedance $\tilde{z} = 1$, the second case assumes a rigid centrebody, while the third case assumes no scattering from the centrebody. All three predictions show an almost identical acoustic pulse associated with a direct wave propagating from the impulsive force. The rigid and lined centrebody predictions show secondary acoustic pulses associated with reflections from the centrebody. As might be expected, the amplitude of the reflected pulse from the lined centrebody is substantially weaker than that from the rigid centrebody.

Figure 5.9 plots the sound pressure at an observer location on the opposite side of the centrebody to the impulsive force ($\phi_o = 180°$). Relative to the free-field prediction, the

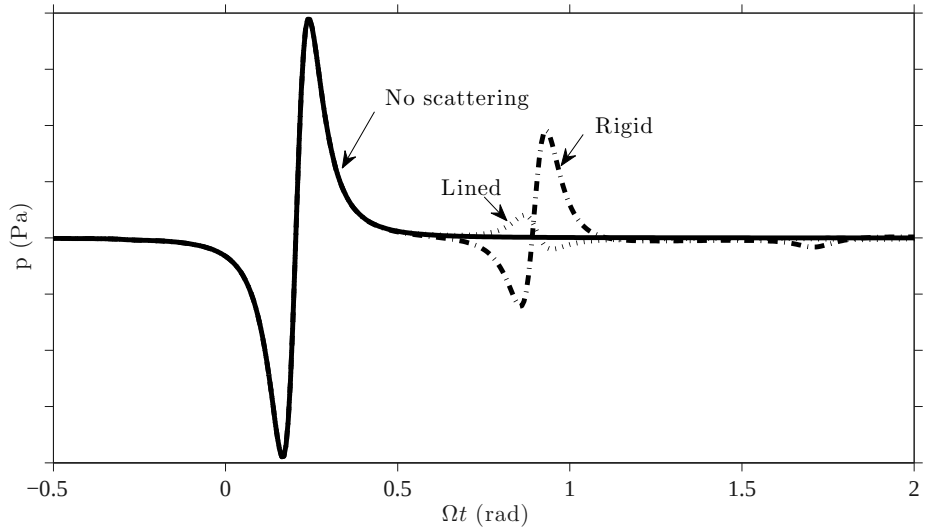

FIGURE 5.8: Plot of pressure time history at $\phi_o = 0°$, $\theta = 45°$ for a one-bladed propeller with $r_h/r_s = 0.3$.

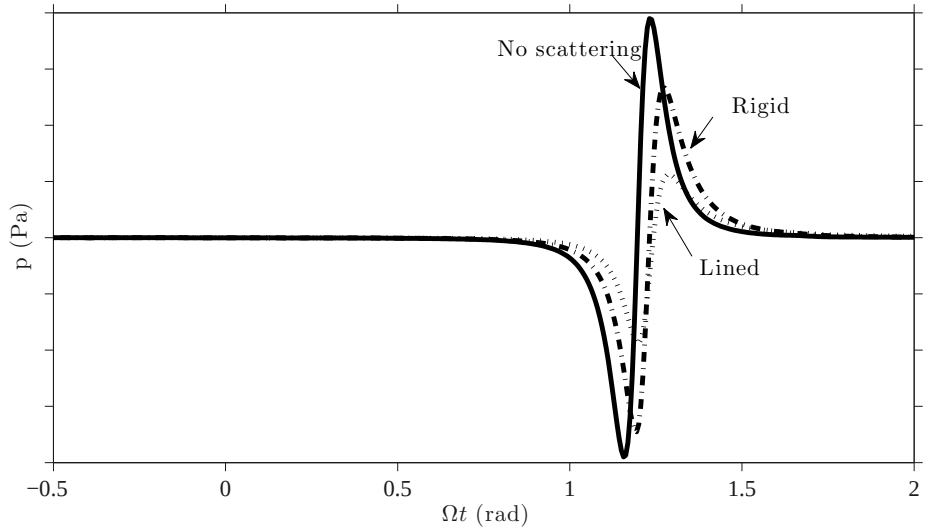

FIGURE 5.9: Plot of pressure time history at $\phi_o = 180°$, $\theta = 45°$ for a one-bladed propeller with $r_h/r_s = 0.3$.

rigid centrebody prediction shows a slight reduction in the amplitude of the acoustic pulse. This is presumably due to the 'shielding' provided by the centrebody. For the case with a lined centrebody there is a substantial reduction in the amplitude of the pulse.

The acoustic spectra for the lined, rigid and free-field cases are also plotted in figures 5.10 and 5.11. When the observer lies on the same side of the cylinder as the impulsive force (figure 5.10) the rigid centrebody appears to drastically alter the sound pressure spectrum relative to a free-field prediction. The rigid centrebody appears to have the effect of modulating the amplitude of the tones about the free-field prediction.

The lined centrebody prediction has a similar tone spectrum to the rigid centrebody prediction, except the 'modulation' of the tones relative to the free-field prediction is much smaller. This is due to the relatively small (compared to the rigid hub) reflected acoustic pulse at this particular observer position. For the case of an observer on the opposite side of the centrebody (Figure 5.11), relative to a free-field prediction, a prediction which includes scattering from the rigid centrebody has little effect on the amplitude of the low frequency acoustic harmonics, however higher harmonics are reduced by $\sim$ 4dB. There is a significant reduction in the amplitude of all tones for the lined centrebody case at this position.

5.4 Conclusions

Scattering from the open rotor centrebody has been investigated in this chapter. Much of the analysis is simplified by considering a single rotating point force. It is shown that centrebody scattering is a phenomenon that exists only for 'highly supersonic' tones, where the sonic radius is inboard of the centrebody or hub radius. Some interaction tones are known to comply with this condition and in these cases, centrebody scattering could be of the same order as the incident field and so should not be neglected. For tones where the sonic radius lies outboard of the blade tips (a category that most single propeller tones fall into) centrebody scattering can generally be neglected. For this case, asymptotic formulae have been presented which show that the incident field is dominated by contributions from the tip region of the blades whereas the centrebody scattered field is dominated by contributions from the hub region. It has also been shown in this work that lining the open rotor hub with an acoustically absorbent material appears to be an effective method of reducing the level of tones which suffer the centrebody scattered component. This research outcome is a useful finding for the sponsor and this preliminary work has led to further investigation and culminated in a patent application by the sponsor, relating to lining the open rotor centrebody exterior surface with acoustically absorbent material. Further work is needed to establish the practicality of such a noise mitigation technique.

Appendices

5.A Scattering by a Rigid Surface

The acoustic pressure $p(\mathbf{x}_o, t)$ within a volume of fluid v, with density ρ_0 and speed of sound c_0 satisfies the following wave equation.

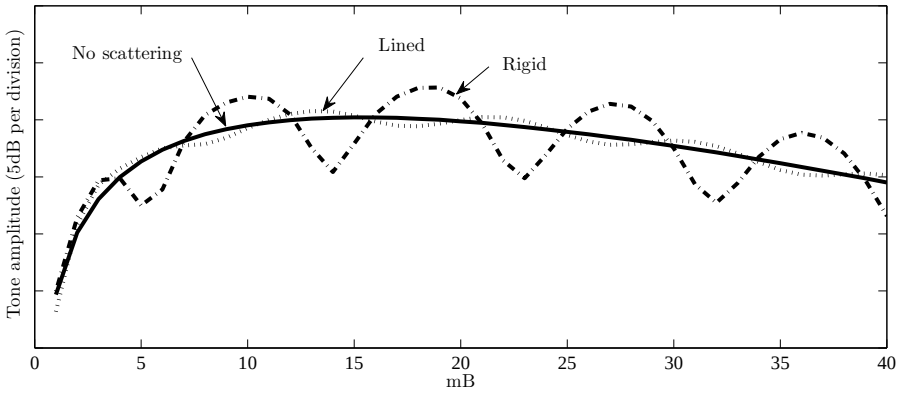

FIGURE 5.10: Plot of tone amplitude versus mB at $\phi_o = 0°$, $\theta = 45°$ for a one-bladed propeller with $r_h/r_s = 0.3$.

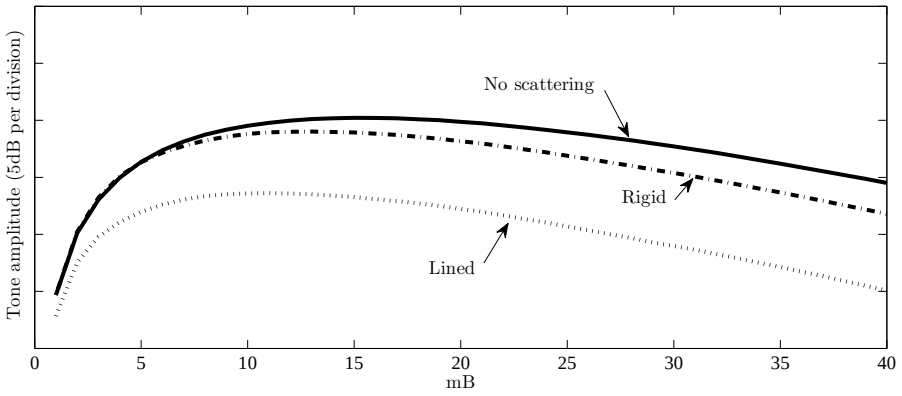

FIGURE 5.11: Plot of tone amplitude versus mB at $\phi_o = 180°$, $\theta = 45°$ for a one-bladed propeller with $r_h/r_s = 0.3$.

$$L\left(\mathbf{x}_o, t\right) p\left(\mathbf{x}_o, t\right) = \nabla_{\mathbf{x}_o} \cdot \mathbf{f}\left(\mathbf{x}_o, t\right), \tag{5.42}$$

where $\mathbf{f}$ is the force per unit volume exerted on the fluid and

$$L\left(\mathbf{x}_o, t\right) = \nabla^2_{\mathbf{x}_o} - \frac{1}{c_0^2} \frac{\partial^2}{\partial t^2}. \tag{5.43}$$

Ignoring the effect of any boundaries, the solution to eq. (5.42) is given by

$$p\left(\mathbf{x}_o, t\right) = \int_{-\infty}^{\infty} \int_{v} \mathbf{f}\left(\mathbf{x}, \tau\right) \cdot \nabla_{\mathbf{x}} g\left(\mathbf{x}, \tau \,|\, \mathbf{x}_o, t\right) \, \mathrm{d}\mathbf{x} \, \mathrm{d}\tau, \tag{5.44}$$

where $g\left(\mathbf{x}, \tau \,|\, \mathbf{x}_o, t\right)$ satisfies the following convected wave equation

$$L\left(\mathbf{x}_o, t\right) g\left(\mathbf{x}, \tau \,|\, \mathbf{x}_o, t\right) = -\delta\left(t-\tau\right)\delta\left(\mathbf{x}_o - \mathbf{x}\right) \tag{5.45}$$

and a causality condition, which requires that

$$g\left(\mathbf{x}, \tau \,|\, \mathbf{x}_o, t\right) = 0 \quad \text{for} \quad t < \tau. \tag{5.46}$$

The validity of eq. (5.44) can be checked by applying the operator defined in eq. (5.43) to eq. (5.44) and making use of eq. (5.45) to yield eq. (5.42).

From inspection of eq.(5.44) we see that if the pressure satisfies any boundary conditions on the stationary surfaces surrounding the volume of fluid, then in order for eq. (5.44) to satisfy these conditions, the Green's function must also satisfy the same boundary condition. For example, for scattering by a rigid cylinder, the boundary condition on the rigid surface requires that the normal derivative of pressure $\partial p/\partial n_{\mathbf{x}_o} = 0$. For this case we require that the Green's function also satisfies $\partial g/\partial n_{\mathbf{x}_o} = 0$ on the surface of the cylinder. The causality condition ensures that the solution decays at large distances from the source.

Taking the Fourier transform of eq. (5.45) and then defining $\tilde{G} = 2\pi\tilde{g}\exp\left\{\mathrm{i}\omega\tau\right\}$ yields the following equation which defines $\tilde{G}$.

$$\nabla^2_{\mathbf{x}_o}\tilde{G} + \kappa^2\tilde{G} = -\delta\left(\mathbf{x}_o - \mathbf{x}\right), \tag{5.47}$$

where $\tilde{G}$ is related to g by the following expression

$$g\left(\mathbf{x}, \tau \,|\, \mathbf{x}_o, t\right) = \frac{1}{2\pi}\int_{-\infty}^{\infty} \tilde{G}\left(\mathbf{x} \,|\, \mathbf{x}_o, \omega\right)\exp\left\{\mathrm{i}\omega(t-\tau)\right\}\,\mathrm{d}\omega \tag{5.48}$$

Note that because g is real, we expect that $\tilde{G}\left(\mathbf{x} \,|\, \mathbf{x}_o, -\omega\right) = \tilde{G}^*\left(\mathbf{x} \,|\, \mathbf{x}_o, \omega\right)$, where the asterisk denotes the complex conjugate.

Also, for scattering by a rigid surface, $\tilde{p}\left(\mathbf{x}_o, \omega\right)$ and $\tilde{G}\left(\mathbf{x} \,|\, \mathbf{x}_o, \omega\right)$ must satisfy a rigid boundary condition i.e. $\partial\tilde{p}/\partial n_{\mathbf{x}_o} = 0$ and $\partial\tilde{G}/\partial n_{\mathbf{x}_o} = 0$ for $\mathbf{x}_o$ on the rigid surface.

Substituting eqs. (5.47) and (5.48) into eq. (5.44) and utilising the Fourier transform of $\mathbf{f}\left(\mathbf{x}, \tau\right)$ and evaluating the integrals yields

$$\tilde{p}\left(\mathbf{x}_o, \omega\right) = \int_v \tilde{\mathbf{f}}\left(\mathbf{x}, \omega\right)\cdot\nabla_{\mathbf{x}}\tilde{G}\left(\mathbf{x} \,|\, \mathbf{x}_o, \omega\right)\,\mathrm{d}\mathbf{x} \tag{5.49}$$

5.B Scattering by a Lined Surface

The boundary condition on a lined surface is defined in terms of $\tilde{p}(\mathbf{x}_o, \omega)$

$$\tilde{p}(\mathbf{x}_o, \omega) = \rho c_o \tilde{z}(\mathbf{x}_o, \omega)\, \tilde{\mathbf{u}}(\mathbf{x}_o, \omega) \cdot \mathbf{n}_{\mathbf{x}_o} \tag{5.50}$$

where $\mathbf{n}_{\mathbf{x}_o}$ is the outward (from the fluid) unit vector normal to the surface and $\tilde{z}(\mathbf{x}_o, \omega)$ is a frequency domain impedance which is related to a time domain impedance via its Fourier transform

$$\tilde{z}(\mathbf{x}_o, \omega) = \frac{1}{2\pi} \int_{-\infty}^{\infty} z(\mathbf{x}_o, t) \exp\{-\mathrm{i}\omega t\}\, \mathrm{d}t. \tag{5.51}$$

Note that if time domain pressure $p(\mathbf{x}_o, t)$ and velocity $\mathbf{u}(\mathbf{x}_o, t)$ are both real then $\tilde{z}(\mathbf{x}_o, \omega)$ must satisfy a reality condition which requires that $\tilde{z}(\mathbf{x}_o, \omega) = \tilde{z}^*(\mathbf{x}_o, -\omega)$ and a causality condition $z(\mathbf{x}_o, t) = 0$ for $t < 0$. Note that the value of impedance used in this paper, $\tilde{z} = 1$, satisfies both these conditions.

The normal velocity on the scattering surface can be calculated from the frequency domain version of the linearised momentum equation.

$$\tilde{u} \cdot \mathbf{n}_{\mathbf{x}_o} = -\frac{1}{\rho \mathrm{i}\omega} \frac{\partial \tilde{p}}{\partial n_{\mathbf{x}_o}} \tag{5.52}$$

Substituting eq. (5.52) into eq. (5.50) and rearranging yields

$$\frac{\partial \tilde{p}}{\partial n_{\mathbf{x}_o}} = -\frac{\mathrm{i}\kappa}{\tilde{z}} \tilde{p}. \tag{5.53}$$

Thus we require that $\tilde{G}$ satisfies the following boundary condition on the scattering surface.

$$\frac{\partial}{\partial n_{\mathbf{x}_o}} \tilde{G}(\mathbf{x} \,|\, \mathbf{x}_o, \omega) = -\frac{\mathrm{i}\kappa}{\tilde{z}(\mathbf{x}_o, \omega)} \tilde{G}(\mathbf{x} \,|\, \mathbf{x}_o, \omega). \tag{5.54}$$

In order to investigate the effectiveness of applying a liner to a propeller centrebody we consider the absorption of sound produced by a force which acts in the negative x direction, with a magnitude which varies as a function of azimuthal angle. For this case, we assume that the loading can be expressed as a Fourier series

$$L(\phi) = \sum_{k=-\infty}^{\infty} L_k \exp\{\mathrm{i}k\phi\}. \tag{5.55}$$

This gives a frequency domain force per unit volume of

$$\tilde{\mathbf{f}}\left(\mathbf{x},\omega\right)=-\hat{\mathbf{x}}\delta\left(x\right)\frac{\delta\left(r-r_{s}\right)}{2\pi r}\sum_{m}\sum_{k}L_{k}\exp\left\{\mathrm{i}(k-m)\phi\right\}\delta\left(\omega-m\Omega\right). \tag{5.56}$$

Chapter 6

Conclusions

The work in this thesis has concerned the prediction and assessment of the noise in the near-field of the open rotor aero-engine concept. In particular the analysis has been in aid of the assessment of acoustic measurements of a model scale open rotor. The work in this thesis contributes towards an Engineering Doctorate and as such has been conducted as part of a collaborative effort with the project sponsor, *Rolls-Royce plc.*

A number of key research outcomes have been generated through this body of work and will now be summarised. In order to provide context to the work, any direct benefits to the project sponsor will also be highlighted alongside the summaries. The chapter concludes with a number of suggestions which may be potential avenues for future work.

6.1 Summary of Research Outcomes

Achieving beneficial and novel outcomes for the sponsor were a significant influence on the direction of the work presented. The research outcomes for each body of work presented in this thesis have been outlined at the conclusion of each chapter. A brief synopsis of these outcomes is provided here, highlighting collaborative work with and benefit to project sponsor.

The initial work focused on the characterisation of simple near-field models suited for predicting open rotor noise in a free-field environment. This extended previous analysis conducted by the sponsor which is predominantly using far-field models - most test campaign results to date have been collected at far-field microphones and far-field prediction models compute several times quicker than typical near-field models. The simple near-field models were developed in conjunction with data analysis conducted on a number of near- and far-field noise data sets, collected from open rotor test campaigns previously

run by the project sponsor. Comparisons of free-field prediction models and experimental results indicated the contamination of acoustic data, either by other sources of noise or propagation effects. Establishing the theory behind some of these unknown effects on the experimental data has directed the work in this thesis. Also, conducting data analyses from several different campaigns on behalf of the sponsor led to the need for an extrapolation method for noise at different observer locations. Such a method has been proposed in this work, which in turn proved quite useful for the sponsor, as the method experimentally established the benefit of its aeroacoustically optimised open rotor blade design.

Features of open rotor near-field tone noise that were found to be interesting to investigate were the presence of centrebody scattering of open rotor tones and reverberation in a closed cross section wind tunnel of very limited extent. Quite interestingly, the behaviour of both phenomena seem to be linked to the sonic radius (or Mach radius off the source plane) - as is the extent of the near-field region itself. Simplified, analytic analysis of wind tunnel reverberation indicates that it can significantly contaminate the measured noise field from an open rotor, irrespective of tunnel geometry. Correcting for reverberation can be complicated, however it is shown with some consistency that the reverberant field is less capable of contaminating the noise field in the near-field of the open rotor, where the direct noise field is relatively much higher in level than the reverberant noise field. Thus, using the idea of the sonic radius, it is possible to predict what observation points could be used to quantify open rotor noise without contamination during measurement campaigns. It is also shown that in many cases it may be impossible to accurately measure uncontaminated open rotor noise in a wind tunnel, because the near-field is contained in a region in which it might be challenging to install the relevant telemetry equipment. Such conclusions are useful to the project sponsor because they can quite clearly aid in the design of any future open rotor test campaigns. For centrebody scattering, the strength of the scattered field is dependent on whether the scattering surface may efficiently radiate noise, which it cannot do whilst contained within the evanescent, near-field region. Interaction tones push the near-field region within the centrebody, allowing for the scattered field to become a potentially significant contribution to the radiated noise field of that tone. This insight led to further investigation of using an acoustically absorbent lining on the exterior surface of the centrebody, an idea which has since been patented by the project sponsor.

6.2 Further Research

Further avenues of research which could arise from the work in this thesis are now suggested.

The most immediately apparent area of further research is the continued development of the tunnel reverberation model. It is speculated that the depreciation in performance of the acoustic liner may be due to the presence of tunnel wall boundary layers and so removing the plug flow assumption used in the models may provide a more accurate prediction. This speculation is based on the idea that the noise would refract through shear flow and so performance depreciation is clearly dependant on frequency and flow gradients. A model that simultaneously accounts for stratified flow in and wall impedance of a wind tunnel would allow for the study of possible shielding on the acoustic liner, an effect which would certainly have an impact on noise measurements. The improved understanding from such work could translate to more accurate predictions of cruise regime noise of open rotor powered aircraft. The introduction of complex flows and the absence of further experimental data sets mean that a coupled, numerical aerodynamic and acoustic simulation could be a consideration for a high fidelity solution. In terms of computational power, such an approach would be plausible for tunnel cross-sections of a smaller size, perhaps where the extent of the cross-section was limited to the near-field of the open rotor.

It would be interesting to test the validity of modelling an open rotor centrebody as an infinite cylinder. A numerical approach may also be used in this case to establish a prediction for near-field open rotor noise with a realistic geometry for an open rotor centrebody included. The impact of acoustic lining of the centrebody could also be established with such an approach and a comparison of both methods could determine whether an infinite cylinder assumption is appropriate and how much computation time the analytic model could save in comparison to the equivalent numerical calculation.

Another possible topic of research is improved source modelling for the analytic models. The models presented are semi-analytic and require blade aerodynamic performance parameters as input. Currently, for the most part, simplistic predictions for the blade aerodynamics are fed into the acoustic models. It would be interesting to investigate how improvements in the aerodynamic model affect accuracy of the final noise prediction, which could be significant. Using a more advanced prediction tool would provide a better description of the blade force distributions, which for example would improve the source descriptions for steady loading and rotor-wake interaction noise. For tone noise prediction, an unsteady Reynolds-Averaged Navier-Stokes (URANS) solver would be sufficient and could be used to establish the steady and unsteady loading distribution on the blade surface in high resolution. Numerical aerodynamic and acoustic simulations could again be used to make near-field acoustic predictions in more complicated flow regimes and comparison of numerical computations to the analytic models presented here may provide insight into the accuracy and range of validity of the simple analytic models, presuming use of a validated numerical code.

Finally and more generally, there are a number of other modelling parameters that could be incorporated in some of the analytic models. One such parameter is flow angle of attack - currently all models consider purely axial and uniform flow. Another modelling parameter that could be considered is the effect of swirling flow (there are lower levels of swirl encountered in an open rotor when compared to a turbofan, however it is potentially still significant) (Peake and Parry, 2012).

References

Abramowitz, M. and Stegun, I. A. (1972), *Handbook of Mathematical Functions*, National Bureau of Standards.

ACARE (2001), European Aeronautics: A Vision for 2020, Technical report, Advisory Council for Aeronautics Research in Europe (ACARE).

Alonso, J. S. and Burdisso, R. a. (2007), 'Green's Functions for the Acoustic Field in Lined Ducts with Uniform Flow', *AIAA Journal* **45**(11), 2677–2687.
URL: *http://arc.aiaa.org/doi/abs/10.2514/1.29872*

Amiet, R. K. (1974), 'Compressibility Effects in Unsteady Thin-Airfoil Theory', *AIAA Journal* **12**(2), 252–255.
URL: *http://arc.aiaa.org/doi/abs/10.2514/3.49212*

Amiet, R. K. (1977), 'Noise Produced by Turbulent Flow into a Propeller or Helicopter Rotor', *AIAA Journal* **15**(3), 307–308.
URL: *http://doi.aiaa.org/10.2514/3.63237*

Amiet, R. K. (1989), *Noise produced by turbulent flow into a rotor: theory manual for noise calculation*, NASA contractor report ; NASA CR-181788., National Aeronautics and Space Administration, Langley Research Center, Hampton, Va.

Blandeau, V. P. and Joseph, P. F. (2010), 'Broadband Noise Due to Rotor-Wake/Rotor Interaction in Contra-Rotating Open Rotors', *AIAA Journal* **48**(11), 2674–2686.
URL: *http://arc.aiaa.org/doi/abs/10.2514/1.J050566*

Brambley, E. and Peake, N. (2006), 'Classification of aeroacoustically relevant surface modes in cylindrical lined ducts', *Wave Motion* **43**(4), 301–310.
URL: *http://linkinghub.elsevier.com/retrieve/pii/S0165212506000023*

Brouwer, H. (2010), 'Analytic description of the noise radiation from single and contra-rotating propellers', pp. 1–6.

CAA (2014), Managing Aviation Noise, Technical report, Civil Aviation Authority.

Carley, M. (1999), 'Sound Radiation From Propellers in Forward Flight', *Journal of Sound and Vibration* **225**(2), 353–374.
URL: *http://linkinghub.elsevier.com/retrieve/pii/S0022460X99922848*

Carley, M. (2000), 'Propeller Noise Fields', *Journal of Sound and Vibration* **233**(2), 255–277.
URL: *http://linkinghub.elsevier.com/retrieve/pii/S0022460X99927979*

Chapman, C. J. (1990), 'The Spiral Green Function in Acoustics and Electromagnetism', *Proceedings of the Royal Society A: Mathematical, Physical and Engineering Sciences* **431**(1881), 157–167.
URL: *http://rspa.royalsocietypublishing.org/cgi/doi/10.1098/rspa.1990.0124*

Chapman, C. J. (1993), 'The Structure of Rotating Sound Fields', *Proceedings of the Royal Society A: Mathematical, Physical and Engineering Sciences* **440**(1909), 257–271.
URL: *http://rspa.royalsocietypublishing.org/cgi/doi/10.1098/rspa.1993.0015*

Colin, Y., Blanc, F., Caruelle, B., Barrois, F. and Djordjevic, N. (2012), Computational strategy for predicting CROR noise at low-speed Part II: investigation of the noise sources computation with the chorochronic method, *in* '18th AIAA/CEAS Aeroacoustics Conference (33rd AIAA Aeroacoustics Conference)', American Institute of Aeronautics and Astronautics, Reston, Virigina.
URL: *http://arc.aiaa.org/doi/abs/10.2514/6.2012-2222*

Colin, Y., Carazo, A., Caruelle, B., Node-Langlois, T. and Parry, A. (2012), Computational strategy for predicting CROR noise at low-speed Part I: review of the numerical methods, *in* '18th AIAA/CEAS Aeroacoustics Conference (33rd AIAA Aeroacoustics Conference)', American Institute of Aeronautics and Astronautics, Reston, Virigina.
URL: *http://arc.aiaa.org/doi/abs/10.2514/6.2012-2221*

Colin, Y., Caruelle, B. and Parry, A. (2012), Computational strategy for predicting CROR noise at low-speed Part III: investigation of noise radiation with the Ffowcs-Williams Hawkings analogy, *in* '18th AIAA/CEAS Aeroacoustics Conference (33rd AIAA Aeroacoustics Conference)', American Institute of Aeronautics and Astronautics, Reston, Virigina.
URL: *http://arc.aiaa.org/doi/abs/10.2514/6.2012-2223*

Crighton, D. G. and Parry, A. B. (1991), 'Asymptotic theory of propeller noise. II - Supersonic single-rotation propeller', *AIAA Journal* **29**(12), 2031–2037.
URL: *http://doi.aiaa.org/10.2514/3.10838*

Crighton, D. G. and Parry, A. B. (1992), 'Higher Approximations in the Asymptotic Theory of Propeller Noise', *AIAA Journal* **30**(1), 23–28.
URL: *http://doi.aiaa.org/10.2514/3.59977*

Dickson, N. (2013), 'ICAO Noise Standards'.

Envia, E. (2015), 'Aeroacoustic analysis of a high-speed open rotor', *International Journal of Aeroacoustics* **14**(3), 569–606.

Farassat, F. (1981), 'Linear Acoustic Formulas for Calculation of Rotating Blade Noise', *AIAA Journal* **19**(9), 1122–1130.
URL: *http://doi.aiaa.org/10.2514/3.60051*

Farassat, F. (1986), 'Prediction of advanced propeller noise in the time domain', *AIAA Journal* **24**(4), 578–584.
URL: *http://doi.aiaa.org/10.2514/3.9310*

Farassat, F. and Brentner, K. S. (1998), 'The acoustic analogy and the prediction of the noise of rotating blades', *Theoretical and Computational Fluid Dynamics* **10**(1-4), 155–170.

Farassat, F., Dunn, M. H. and Spence, P. L. (1992), 'Advanced propeller noise prediction in the time domain', *AIAA Journal* **30**(9), 2337–2340.
URL: *http://doi.aiaa.org/10.2514/3.11224*

Farassat, F. and Myers, M. K. (1987), Extension of Kirchhoff's formula to radiation from moving surfaces, Technical report, NASA Langley Research Center; Hampton, VA, United States.

Ffowcs-Williams, J. E. and Hawkings, D. L. (1969), 'Sound Generation by Turbulence and Surfaces in Arbitrary Motion', *Philosophical Transactions of the Royal Society of London. Series A, Mathematical and Physical Sciences* **264**(1151), 321–342.
URL: *http://www.jstor.org/stable/73790*

Garrick, I. and Watkins, C. (1954), A theoretical study of the effect of forward speed on the free-space sound-pressure field around propellers, Technical report, NACA.

Glegg, S. A. L. (1991), 'Effect of centerbody scattering on propeller noise', *AIAA Journal* **29**(4), 572–576.
URL: *http://doi.aiaa.org/10.2514/3.10622*

Goldstein, M. (1976), *Aeroacoustics*, McGraw-Hill International Book Company.
URL: *https://books.google.co.uk/books?id=HY1TAAAAMAAJ*

Gutin, L. (1936), 'On the Sound Field of a rotating propeller.', *Physik Z der Sowjetunion (Translated as 1948 NACA Tech Memo 1195)* .

Hanson, D. B. (1980*a*), 'Helicoidal Surface Theory for Harmonic Noise of Propellers in the Far Field', *AIAA Journal* **18**(10), 1213–1220.
URL: *http://arc.aiaa.org/doi/abs/10.2514/3.50873*

Hanson, D. B. (1980*b*), 'Influence of Propeller Design Parameters on Far-Field Harmonic Noise in Forward Flight', *AIAA Journal* **18**(11), 1313–1319.

Hanson, D. B. (1983), 'Compressible Helicoidal Surface Theory for Propeller Aerodynamics and Noise', *AIAA Journal* **21**(6), 881–889.
URL: *http://doi.aiaa.org/10.2514/3.60132*

Hanson, D. B. (1985*a*), 'Nearfield Frequency-Domain Theory for Propeller Noise', *AIAA Journal* **23**(4).

Hanson, D. B. (1985*b*), 'Noise of counter-rotation propellers', *Journal of Aircraft* **22**, 609–617.
URL: *http://adsabs.harvard.edu/abs/1985JAir...22..609H*

Hanson, D. B. (1992), 'Direct frequency domain calculation of open rotor noise', *AIAA Journal* **30**(9), 2334–2337.
URL: *http://doi.aiaa.org/10.2514/3.11223*

Hubbard, H. and Regier, A. (1950), *Free-space oscillating pressures near the tips of rotating propellers*, National Advisory Committee for Aeronautics.
URL: *http://naca.central.cranfield.ac.uk/reports/1950/naca-report-996.pdf*

IATA (2004), Noise Certification Standards, *in* 'IATA Environmental Review', Vol. I, p. 9.

Kim, Y. N. and George, A. R. (1982), 'Trailing-Edge Noise from Hovering Rotors', *AIAA Journal* **20**(9), 1167–1174.
URL: *http://arc.aiaa.org/doi/abs/10.2514/3.51176*

Kingan, M. J. (2012), Open Rotor Broadband Interaction Noise, *in* '18th AIAA/CEAS Aeroacoustics Conference (33rd AIAA Aeroacoustics Conference)', Aeroacoustics Conferences, American Institute of Aeronautics and Astronautics.
URL: *http://dx.doi.org/10.2514/6.2012-2304*

Kingan, M. J., Powles, C. and Self, R. H. (2010), 'Effect of centrebody scattering on advanced open rotor noise', *AIAA Journal* **48**, 975–980.

Kingan, M. J. and Self, R. H. (2011), Open Rotor Tone Scattering, *in* '17th AIAA/CEAS Aeroacoustics Conference2'.

Kingan, M. J. and Sureshkumar, P. (2014), 'Open Rotor Centrebody Scattering', *Journal of Sound and Vibration* **333**, 418–433.

Kirker, T. J. (1990), Procurement and testing of a 1/5 scale advanced counter rotating propfan model, *in* '13th AIAA Aeroacoustics Conference'.

Majumdar, S. J. and Peake, N. (1998), 'Noise generation by the interaction between ingested turbulence and a rotating fan', *Journal of Fluid Mechanics* **359**, S0022112097008318.
URL: *http://www.journals.cambridge.org/abstract_S0022112097008318*

McAlpine, A., Fisher, M. and Tester, B. (2007), 'Buzz-saw noise: A comparison of modal measurements with an improved prediction method', *Journal of Sound and Vibration* **306**, 419–443.

McAlpine, A. and Wright, M. (2006), 'Acoustic scattering by a spliced turbofan inlet duct liner at supersonic fan speeds', *Journal of Sound and Vibration* **292**(3-5), 911–934.
URL: *http://linkinghub.elsevier.com/retrieve/pii/S0022460X05006577*

Metzger, F. B. and Rohrbach, C. (1979), 'Aeroacoustic Design of the propfan', *AIAA* .

Morfey, C. L., Powles, C. J. and Wright, M. C. M. (2011), 'Green's functions in computational aeroacoustics', *International Journal of Aeroacoustics* **10**(2), 117–160.

Parker, R. (2011), Green Aeroengines, Technical report, Rolls-Royce.

Parry, A. B. (1988), Theoretical Prediction of Counter-Rotating Propeller Noise, PhD thesis, University of Leeds.

Parry, A. B., Britchford, K., Kingan, M. J. and Sureshkumar, P. (2012), Aeroacoustic Tests of Isolated Open Rotors at High Speed, *in* '18th AIAA Aeroacoustics Conference'.

Parry, A. B. and Crighton, D. G. (1989), 'Asymptotic theory of propeller noise. I - Subsonic single-rotation propeller', *AIAA Journal* **27**(9), 1184–1190.
URL: *http://doi.aiaa.org/10.2514/3.10244*

Parry, A. B., Kingan, M. J. and Tester, B. J. (2011), 'Relative importance of open rotor tone and broadband noise sources', *17th AIAA/CEAS Aeroacoustics Conference* .

Parry, A. and Vianello, S. (2012), 'A project study of open rotor noise', *International Journal of Aeroacoustics* **11**(2), 247–258.
URL: *http://multi-science.atypon.com/doi/10.1260/1475-472X.11.2.247*

Paterson, R. and Amiet, R. (1982), 'Noise of a model helicopter rotor due to ingestion of isotropic turbulence', *Journal of Sound and Vibration* **85**(4), 551–577.
URL: *http://linkinghub.elsevier.com/retrieve/pii/0022460X82903236*

Peake, N. and Boyd, W. (1993), 'Approximate Method for the Prediction of Propeller Noise Nearfield Effects', *Journal of Aircraft* **30**(5).

Peake, N. and Crighton, D. G. (1991), 'An asymptotic theory of near-field propeller acoustics', *Journal of Fluid Mechanics* **232**(-1), 285.
URL: *http://www.journals.cambridge.org/abstract_S0022112091003695*

Peake, N. and Parry, A. B. (2012), 'Modern Challenges Facing Turbomachinery Aeroacoustics', *Annual Review of Fluid Mechanics* **44**(1), 227–248.
URL: *http://www.annualreviews.org/doi/abs/10.1146/annurev-fluid-120710-101231*

Prentice, P. R. (1993), 'Energy transport in rotating sound fields', *Proceedings: Mathematical and Physical Sciences* **441**, 83–96.

Rienstra, S. W. and Tester, B. J. (2008), 'An analytic Green's function for a lined circular duct containing uniform mean flow', *Journal of Sound and Vibration* **317**(3-5), 994–1016.
URL: *http://linkinghub.elsevier.com/retrieve/pii/S0022460X08002836*

Sears, W. R. (1941), 'Some Aspects of Non-Stationary Airfoil Theory and Its Practical Application', *Journal of the Aeronautical Sciences* **8**(3), 104–108.
URL: *http://arc.aiaa.org/doi/10.2514/8.10655*

Sharma, A. and Chen, H.-N. (2013), 'Prediction of aerodynamic tonal noise from open rotors', *Journal of Sound and Vibration* **332**(16), 3832–3845.
URL: *http://linkinghub.elsevier.com/retrieve/pii/S0022460X13001806*

Sinayoko, S., Kingan, M. J. and Agarwal, A. (2013), 'Trailing edge noise theory for rotating blades in uniform flow', *Proceedings of the Royal Society A: Mathematical, Physical and Engineering Sciences* **469**(2157), 20130065–20130065.
URL: *http://rspa.royalsocietypublishing.org/cgi/doi/10.1098/rspa.2013.0065*

Sureshkumar, P. and Kingan, M. J. (2012), Open Rotor Tone Acoustics: Near-field Prediction & Projection, *in* '18th AIAA Aeroacoustics Conference'.

Tyler, J. M. and Sofrin, T. G. (1962), Axial Flow Compressor Noise Studies, Technical report.
URL: *http://www.sae.org/technical/papers/620532*

Watkins, C. E. and Durling, B. J. (1956), 'A method for cacluation of free space sound pressures near a propeller in flight including considerations of the chordwise blade loading', *NACA Tech Note 3809* .

Whitfield, C. E., Mani, R. and Gliebe, P. R. (1990), High speed turboprop aeroacoustic study (counterrotation). Volume 1: Model development, Technical report, NASA.

Wood, M. E. and Newman, D. A. (1990), 'The design and commissioning of an acoustic liner for propeller noise testing in the ARA transonic wind tunnel', *IMechE* .

Zhou, Q. and Joseph, P. (2006), 'Frequency-Domain Method for Rotor Self-Noise Prediction', *AIAA Journal* **44**(6), 1197–1206.
URL: *http://dx.doi.org/10.2514/1.16176*